

AD-A045 240

ADVISORY GROUP FOR AEROSPACE RESEARCH AND DEVELOPMENT--ETC F/G 17/8
LASER OPTICAL MEASUREMENT METHODS FOR AERO ENGINE RESEARCH AND --ETC(U)
JUL 77

UNCLASSIFIED

AGARD-LS-90

NL

1 OF 2
AD
A045 240



COPIED
1 OF 2
AD
A045 240



AGARD-LS-90

AGARD-LS-90

AD A 045240

AGARD

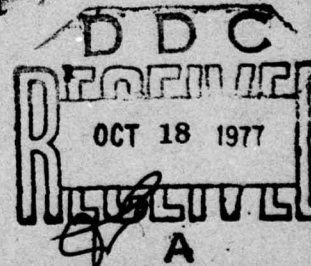
ADVISORY GROUP FOR AEROSPACE RESEARCH & DEVELOPMENT

7 RUE ANCELLE 92200 NEUILLY SUR SEINE FRANCE

A008 586
587
A001 980

AGARD LECTURE SERIES No. 90

Laser Optical Measurement Methods for Aero Engine Research and Development



NORTH ATLANTIC TREATY ORGANIZATION



DISTRIBUTION AND AVAILABILITY
ON BACK COVER

DISTRIBUTION STATEMENT A

Approved for public release;
Distribution Unlimited

DDC FILE COPY

NORTH ATLANTIC TREATY ORGANIZATION
ADVISORY GROUP FOR AEROSPACE RESEARCH AND DEVELOPMENT
(ORGANISATION DU TRAITE DE L'ATLANTIQUE NORD)

11 Jul 77

12 164p.

9

AGARD Lecture Series No. 90

6

LASER OPTICAL MEASUREMENT METHODS FOR
AERO ENGINE RESEARCH AND DEVELOPMENT,

DDC
REFILED
OCT 18 1977
A

DISTRIBUTION STATEMENT A
Approved for public release
Distribution Unlimited

The material in this publication was assembled to support a Lecture Series under the sponsorship of the Propulsion and Energetics Panel and the Consultant and Exchange Programme of AGARD presented on 25-26 August 1977 Trenton, New Jersey, USA, 30-31 August 1977 London, UK, and 5-6 September 1977 Urbino, Italy.

400043

Amec

THE MISSION OF AGARD

The mission of AGARD is to bring together the leading personalities of the NATO nations in the fields of science and technology relating to aerospace for the following purposes:

- Exchanging of scientific and technical information;
- Continuously stimulating advances in the aerospace sciences relevant to strengthening the common defence posture;
- Improving the co-operation among member nations in aerospace research and development;
- Providing scientific and technical advice and assistance to the North Atlantic Military Committee in the field of aerospace research and development;
- Rendering scientific and technical assistance, as requested, to other NATO bodies and to member nations in connection with research and development problems in the aerospace field;
- Providing assistance to member nations for the purpose of increasing their scientific and technical potential;
- Recommending effective ways for the member nations to use their research and development capabilities for the common benefit of the NATO community.

The highest authority within AGARD is the National Delegates Board consisting of officially appointed senior representatives from each member nation. The mission of AGARD is carried out through the Panels which are composed of experts appointed by the National Delegates, the Consultant and Exchange Program and the Aerospace Applications Studies Program. The results of AGARD work are reported to the member nations and the NATO Authorities through the AGARD series of publications of which this is one.

Participation in AGARD activities is by invitation only and is normally limited to citizens of the NATO nations.

The content of this publication has been reproduced directly from material supplied by AGARD or the author.

ACCESSION 127	
NTIS	White Section <input checked="" type="checkbox"/>
DOC	Ball Section <input type="checkbox"/>
UNANNOUNCED	<input type="checkbox"/>
IDENTIFICATION	
BY DISTRIBUTION/AVAILABILITY CODES	
RAT. EXPL. AND/OR SPECIAL	
A	

Published July 1977

Copyright © AGARD 1977

All Rights Reserved

ISBN 92-835-1248-0



Printed by Technical Editing and Reproduction Ltd
Harford House, 7-9 Charlotte St, London, W1P 1HD

PREFACE

This Lecture Series was recommended by the Propulsion and Energetics Panel of AGARD and is implemented under the Consultant and Exchange Programme.

In recent years many optical measuring methods, most using lasers, for determining flow velocity (with turbulence and fluctuations), temperature, and species concentration have been studied. The main advantage is that the flow is not disturbed. They are of great value for research and development on engines and components and for the understanding of fundamental flow processes.

The Lecture Series will inform propulsion specialists of the techniques that are currently available, how to use them and their limitations. It will review experience to date in practical applications. Laser-velocimetry will be emphasized since it is the only technique which has achieved practical importance up until now. Raman scattering and holography interferometry will also be addressed. Commonly-used techniques and qualitative type methods such as infrared for surface temperature and Schlieren techniques will not be addressed.

Dr Ing. H.B.WEYER
Lecture Series Director

LIST OF SPEAKERS

Lecture Series Director: Dr-Ing. H.B.Weyer
DFVLR
Institut für Luftstrahlantriebe
Cologne
F.R.G.

Dr A.E.Lennert
ARO, Inc
Arnold Air Force Station
Tennessee 37389
USA

Dipl -Ing R.Schodl
DFVLR
Institut für Luftstrahlantriebe
Cologne
Germany

Dr A.E.Smart
Rolls Royce Limited
Derby Engine Division
Derby
UK

Monsieur C.Veret
ONERA
Châtillon-sous-Bagneux
France

Dr D.C.Wisler
General Electric Company
Cincinnati, Ohio
USA

CONTENTS

	Page
PREFACE	iii
LIST OF SPEAKERS	iv
	Reference
REQUIREMENTS OF AERO-ENGINE DEVELOPMENT TO ADVANCED EXPERIMENTAL TECHNIQUES by H.B.Weyer	1
REVIEW OF OPTICAL TECHNIQUES WITH RESPECT TO AERO ENGINE APPLICATIONS by C.Véret	2
FUNDAMENTALS OF LASER DOPPLER VELOCIMETRY by A.E. Lennert	3
LASER-TWO-FOCUS VELOCIMETRY (L2F) FOR USE IN AERO ENGINES by R.Schodl	4
PRACTICAL APPLICATION OF LV SYSTEMS TO AERO ENGINE RESEARCH AND DEVELOPMENT by D.C.Wisler and P.W.Mossey	5
SPECIAL PROBLEMS OF LASER ANEMOMETRY IN DIFFICULT APPLICATIONS by A.E.Smart	6
BIBLIOGRAPHY	B

REQUIREMENTS OF AERO-ENGINE DEVELOPMENT TO ADVANCED EXPERIMENTAL TECHNIQUES

By

H.B. Weyer

DFVLR-Institut für Luftstrahlantriebe
Linder Höhe, 5 Köln 90, W.Germany

ABSTRACT

The development of an new aero engine needs today always a very long time and requires an extremely high budget of money, because in each case a lot of individual problems (aero-thermodynamic design, materials, structures, a.s.o.) must be solved.

Concerning the aero-thermodynamic design of aero-engines worldwide efforts are focused on lowering the developmental costs by improving the calculation techniques for designing the various engine components - more reliability and more general validity are demanded. However the activities are also - aimed at increasing the performance capability and the efficiency of the engine. In order to arrive at satisfactory solutions it is necessary to learn - by detailed experimental studies - more about the complex flow patterns, about the combustion processes, and about the cooling phenomena in real engines and their components.

In this paper the attempt will be made to expose the primary problems of the aero-thermodynamic design, to outline the requirements to adequate experimental studies and to the corresponding testing techniques.

INTRODUCTION

A main aspect of aero-engine research and development was always to provide reliable measuring and testing techniques appropriate for the detailed experimental study of flow, of materials, of machine dynamics a.s.o. Qualified experimental data will contribute in the future to realizing the next steps of performance increase, of efficiency improvement, of life-time extension, and of reducing the extremely high developmental costs by refining the today's design and off-design calculation techniques.

Excellent reviews of the past efforts in the field of developing appropriate measuring techniques are given in ref.1 and 2. Although being aware of the very serious materials and vibration problems in aero-engines the Lecture Series on "Laser Optical Measurement Methods" will only deal with the aero-thermodynamic R and D aspects focused on non-intrusive optical methods which allow to measure the flow velocity and direction, the flow turbulence and fluctuations, the temperature, and the species concentrations without disturbing the flow. These new methods enable measurements which up to now could not be or not easily be performed, such as measurements inside the rotating blade channels of turbomachines, interstage measurements of multistage machines, or inside combustors. The use of such techniques in engine R and D will provide a better understanding of the fundamental flow phenomena in the different engine components. Thus they offer great possibilities to achieve more confidential data for component design and to prove respectively to improve theoretical flow models.

Some of these techniques are still in the development phase in laboratories, others have already become appropriate for application in engine R and D. The objective of this Lecture Series is to inform propulsion specialists in research and development which techniques are presently available for the use in engine and component test rigs and how to handle these methods.

A critical review of all optical techniques being presently under development shows that today only the laser velocimetry has achieved practical importance. Therefore, these methods including their practical application in engine R and D are covered with particular emphasis. Other methods (such as Raman scattering, holography, interferometry) are treated in a review lecture paying attention to their status of development and their promises for engine R and D.

Before opening the series of the expert lectures I would like to comment briefly upon some fundamental aero-thermodynamic aspects of engine research and development particularly upon the status of today's engine technology, its future trends, and their requirements to advanced experimental techniques.

AERO-ENGINE TECHNOLOGY AND TRENDS

As in the past also the development of future aircraft engines will be dictated primarily by the following fundamental requirements:

- Low Specific Fuel Consumption
- High Specific Thrust or Power
- Minimum Weight and Dimensions

Due to quite different operational missions of civil and military aircrafts, helicopters and RPV's additional requirements exist for each engine category:

Civil Aircraft Engines	Milit.Aircraft Engines	Helicopter Engines	RPV Engines
- Long Life Endurance	- Multi Mission-Capability	- Low Price	- Extreme Low Price
- Long Time between Overhaul	- Max. Reliability	- High Acceleration Capability	- Very Small Overall Dimensions
- Low Noise Level	- Short Duration Maxim.Thrust Capability	- High Emergency Power	

The development of military aircraft engines has always revealed the most advanced engine and component technology associated however by relatively short life cycles. This technology has then been transferred into the field of civil aircraft engines and has been modified to meet the special demands of common civil aircraft missions as for instance longer life times (ref.3).

Armstrong from NGTE published in the Aeronautical Journal an excellent review paper on the conventional aero-engine and its progress over the last three decades since World War II (ref.4). The following set of figures was taken from this paper to demonstrate here - more or less completely - the today's engine technology and its future trends. Fig.1 illustrates the considerable increase in thrust-to-weight ratio of military engines from about 2 in 1945 to about 8 in 1975. The physical boundary is obviously not yet arrived as indicated by the arrow. Further increase seems to be attainable by augmenting the aerodynamic blade loading which may lead to a reduced number of blades or even stages, and by introducing new materials and structures.

Fig.2 emphasizes the great progress in civil engine equivalent power that has grown since 1945 by more than one magnitude with no effective size limit in sight. The figure reveals also the great superiority of turbo-engines against piston engines. As shown in Fig.3 the overall pressure ratio of both civil and military engines are now approaching a value of 30. A remarkable increase in aerodynamic stage loading since 1945 has led to this figure without increasing the total number of engine stages - compressor plus turbine. Armstrong outlines that progress is by no means exhausted; considerably higher pressure ratios than 30 may be expected in 20-stage engines with current efficiency levels.

To give an idea on the performance situation of modern axial compressors the polytropic efficiency is plotted against the mean stage pressure ratio in Fig.4. The trend of falling efficiency with increasing pressure ratio is evident as expected. The single-stage fans at the right-hand side of the diagram now used in advanced civil turbofan engines are operating at relative tip Mach numbers of about 1.5; they produce considerable pressure ratios up to 1.7 at an acceptable efficiency of about 83 %. However, further great progress is indicated in the diagram by the "research units" incorporating all research experience which is today available but not yet applied to engines, because a lot of still existing research and developmental problems must be solved before.

The last figure (Fig.5) taken from Armstrong's paper is concerned with the turbine inlet temperature, its past progression, and its future prospect. The large stepwise increase in the fifties was achieved by introducing cooling techniques; however, since there again a steady progression is observed with data between 1 400 and 1 600 K presently used in both civil and military engines. The entry temperatures of 1985 are assumed to be around 1 600 to 1 800 K. Today's research turbines are running at temperatures considerably higher than realized in engines indicating that already research experience on more advanced cooling techniques and high temperature materials is available which will be applied to real engines - after a further period of research and development.

The following more fundamental conclusion can be drawn from Armstrong's paper: in spite of the enormous progress in aero-engine technology over the last three decades today the physical boundary is by no means in sight; the capabilities assumed to be still inherent promise a similar progression for at least the next decade.

It is now the point to study the effects which the technology progress will probably have in the sense of the aforementioned requirements to future aircraft engines. Thereby the term "technology" comprehends cycle and component optimisation in conventional engines as shown in the preceding figures as well as the application of new unconventional concepts as variable cycle, variable geometry, heat-exchangers, and so on, which offer additional great possibilities to push forward the performance and economy of aero-engines. The possible improvement of engine specific fuel consumption (SFC) has been selected here as an example to illustrate the above mentioned effects. Fig.6 demonstrates - for a large civil fan engine - the step-by-step SFC improvement process attainable with the introduction of more and more advanced technologies. The diagram originally published by Denning and Miller in ref.5 presents - for the Rolls Royce RB-211 - the estimated SFC

improvement as a percentage of the basic engine (211-22) datum. The data are plotted - against the cruise specific thrust. An overall SFC gain of about 25 % could be achieved by incorporating different technology steps into the engine design as (ref.5):

1. refinement of current engine components;
2. increase of propulsive efficiency by increasing the total engine air flow;
3. optimising the component geometry to produce maximum efficiency from current technology standards;
4. general component technology objectives;
5. new design concepts.

Concerning the small turbo engines (mass flow: 0.5 to 7 kg/s) the "Small Turbine Advanced Gas Generator" (STAGG) program has revealed the possibility of a considerable reduction in specific fuel consumption for this engine class by applying advanced technologies as shown in Fig.7. An overall improvement of SFC between 20 and 35 % - depending on the shaft horsepower - seems realistic to be gained. The STAGG-program was initiated in 1971 with high risk goals because small engines were "unable to utilize directly the advanced technology from large engine research and development due to inherent geometry and size limitations" according to Johnsson and Elliot.

This brief survey on current engine technology, its future progress, and its influence on engine economy does not claim for completeness; it just should emphasize the potentials still inherent with the aero-engine to justify and stimulate further research and development activities.

ENGINE RESEARCH AND DEVELOPMENT

In the following only those research and development activities to meet the fundamental requirements to aero-engines are summarized which - as previously mentioned - are exclusively concerned with the engine aero- and thermodynamics. The synopsis does not differentiate between the various engine categories; only those problems have been included which are similar for all engines, and which - in the case of successful solution - promise great progress in aerodynamic component technology. New concepts as variable cycle or geometry are not considered due to their very early stage.

From that a research and development program on aero-engines results with the following aero- and thermodynamic objectives:

COMPRESSOR AND TURBINE

- Increase of Aerodynamic Loading
- Improvement of Efficiency
- Increase of Stall Margin
- Improvement of Blade Cooling Techniques
- Reduce of Noise Emission
- Development of Reliable Design and Off-Design Calculation Techniques

COMBUSTION CHAMBER

- Aero-Thermodynamic Optimization of Primary and Dilution Zones
- Improvement of Combustor Liner Cooling Techniques
- Development of New Combustor Concepts for Reduced Exhaust Gas Emissions
- Development of Reliable Calculation Techniques

COMPRESSORS

Current research activities on compressors are focused on increasing the performance capability and on improving the design techniques; they include both extensive experimental investigations and theoretical efforts to develop reliable calculation methods. However, the complete theoretical treatment always suffers from a lack in detailed information on real flow effects as compressibility, three-dimensionality, viscosity, and unsteadiness. Some of these flow phenomena are normally not considered in the flow models but are approached by empirical correlations, for instance the estimation of flow losses, flow turning, boundary-layer and secondary flow effects.

In transonic axial compressors additional problems arise due to the three-dimensional shock waves and their interactions with wall and blade boundary-layers; in radial compressors the well-known jet-wake flow pattern plays a dominant role jointly with the strong flow fluctuations, the high streamline curvature, and the field force effects.

The basic compressor flow equations are often - for practical purposes - drastically simplified by assuming the flow being steady, inviscid, two-dimensional, and even incompressible. In order to improve the knowledge and understanding of the real flow phenomena for compressor performance, efficiency, and stall margin optimization as well as to accomplish the theoretical flow models, detailed experimental investigations of the complex internal compressor flow are absolutely necessary addressed to the following objectives:

- Optimization of blade profiles with respect to high aerodynamic loading and low flow losses.
- Analysis of the 3-dimensional nature of compressor flow; effects of annulus

- geometry; 3-dimensional shock waves; secondary flows; gap flows; boundary-layer movement.
- Particularities of 3-dimensional flow in radial compressors; effect of strong streamline curvature and flow fluctuations; flow separation, secondary flows and jet-wake flow pattern.
- Study of particular flow processes in multi-stage / multi-spool compressors; stage matching; onset of instabilities and surge.
- Analysis of unsteady flow phenomena; blade wake interaction; rotating stall; effects of inlet flow distortion.

Optimisation of Blade Profiles

Today single-stage transonic compressors have achieved high levels of pressure ratios around 2:1 while maintaining quite high efficiencies. For supersonic inlet flow (rotor tip sections) the blade profile design must carefully take into account the Mach number distribution ahead of the shock wave, the shock-boundary layer interaction, the shock induced or even subsonic flow separation, and subsonic diffusion. Suction surface curvature, throat area, cascade solidity, and stagger angle are therefore the main design principles according to ref.7.

Fig.8 presents a typical profile as it is presently used for tip section of transonic rotors. It consists of a series of circular arcs to meet the above mentioned design philosophy. The blade Mach number distribution corresponds to an inlet Mach number of 1.23, to a static pressure ratio of 1.39, and to an axial velocity density ratio of 1.28. It clearly identifies the shock wave impingement on the blade suction side (ref.8).

For high subsonic inlet velocities occurring in the hub sections of transonic rotors, in stators of transonic stages, and in HP compressors the supercritical airfoil is going to be used promising great increase of aerodynamic loading and considerable decrease of flow losses. Fig.9 taken from ref.9 shows such an airfoil and its optimum blade Mach number distribution. As indicated in the diagrams supercritical profiles have a high turning capability which however is expected in the future to exceed 30 deg. considerably.

Another tool to improve the performance of high-turning subsonic airfoils and to increase their stable operating range is suction surface boundary-layer treatment. Fottner (ref.10) reports on very successful cascade measurements with suction side boundary-layer energized by bleeding; thereby flow turning over 60 deg. has been achieved.

In order to deal completely with the aerodynamic potentials of these advanced blade configurations for practical use and in order to develop coincidentally reliable design techniques a still deeper understanding of the fundamental flow processes is required which only can be obtained by detailed experimental studies. Future measurements must provide complete informations particularly on:

- Intensity and position of shock waves depending on inlet flow, back-pressure, profile shape, and cascade geometry,
- Shock-boundary-layer interaction, boundary-layer growth and separation, boundary-layer treatment effects,
- Local distribution of flow losses and turning inside the blade channels,
- Blade wake shape and mixing,
- Turbulence and/or fluctuation of cascade internal flow.

For the clarification of the aforementioned subjects testing techniques are needed which allow to analyse locally the flow velocity and flow direction as well as the pressures and temperatures or fluid densities; thereby the steady-state values and the unsteady components of these flow quantities must be determined.

Three-Dimensional Compressor Flow

High-pressure ratio axial compressors have always a converging annulus to adapt the flow cross-section to the increasing static pressure, as illustrated in Fig.10 for a single-stage compressor. The convergence induces more or less strong radial flow components effecting the flow on adjacent blade sections.

Another very important feature of transonic compressors is the appearance of 3-dimensional shock waves extending over the blade height in the rotor entrance portion. Fig.11 demonstrates this situation for a transonic rotor operating at 430 m/s tip speed with a relative inlet tip Mach number of 1.4 and a pressure ratio over 1.5. The entrance shock wave is shown at 45, 63 and 89 % blade height with respect to the corresponding profiles at right stagger to give an idea on the complicated 3-d shock wave surface.

Inlet and outlet flow conditions, blade and cascade geometry varying over the blade height initiate this flow pattern which obviously leads to strong radial gradients of the static pressure and to strong radial components of the flow vectors behind the shock wave. Thus the radial equilibrium of the rotor flow is more complex than predicted

by today's usual theories which do not account for these flow phenomena (ref.11).

Stream tube convergence and 3-dimensional shock waves cause a severe deterioration of the stream surfaces within the blade row; and this deviation from axis-symmetric flow is still amplified by strong secondary flows. Streamwise vorticity associated with flow deflection, wall boundary-layer development, blade boundary-layer movement, and other phenomena lead to a very complex secondary flow pattern in compressors which often is aggravated by leakage flows at rotor tip and stator hub with and without relatively moving walls (ref.12). Fig.12 presents a rough qualitative scheme of secondary and gap flow just to demonstrate its complexity.

Quantitative details of the 3-dimensional flow pattern in compressors are today rather unknown. Experimental research on compressors should therefore be aligned to provide accurate and detailed data on:

- Local position of the 3-dimensional shock wave and its local intensity,
- Radial flow components, local loss and turning distribution,
- Secondary and leakage flow phenomena,
- Wall boundary-layer development with and without moving walls,
- Blade boundary-layer growth and movement,
- Blade wake flows and downstream mixing.

Experimental techniques must be available to measure locally the prime steady and unsteady flow quantities, as pressure, temperature or density, fluid velocity, and flow direction, even within the 3-d boundary layers. Additional methods are required to analyse accurately the gaps between the bladings and the walls. Techniques to determine the precise cascade geometry under operating conditions are also of high practical interest.

Particularities of Radial Compressor Flow

The basic flow in radial compressors is characterized by a pronounced jet-wake discharge flow at the impeller outlet. Fig.13 illustrates the flow field in the rear part of the rotor. The relative velocity distribution at impeller discharge always appears to be rather different from the ideal one calculated on the basis of inviscid theory and steady-state boundary-layer techniques.

Low-energetic fluid accumulates along the blade suction surface very often preceding flow separation and the formation of a wake region. This finally shifts the main flow (jet) towards the blade pressure side. The flow separation impairs the diffusion potential and leads to a highly distorted velocity field at the impeller discharge, which causes a considerable reduction of stage efficiency due to additional mixing losses and unsteady flow in the subsequent diffuser.

Primarily two flow mechanisms have been identified to be of decisive importance for flow separation and wake development; these are secondary flows and turbulence stabilization effects due to streamline curvature and system's rotation (ref.13).

As experimentally verified (ref.14) the wake increases rapidly downstream of the separation point, due to strong secondary and tip leakage flow feeding low-energy fluid material into the wake. The wake area covering more than 30 % of the blade channel is characterized by a low mass-flow component (≈ 15 % of total mass-flow), by a high fluctuation intensity (RMS: ≈ 20 % of mean velocity), and by a steep, relatively stable velocity gradient to the surrounding jet flow. This illustrates the separation of high- and low-energetic fluid material and the suppression of turbulent mixing along the jet/wake shear layer due to effects of the Coriolis force and meridional channel curvature.

Further experimental investigations of various impeller configurations at different speeds and operating points must help to clarify - besides the questions described in the preceding chapter:

- Which viscous flow effects initiate the flow separation and dominate the position and development of the wake,
- Which flow phenomena govern the interaction between jet and wake areas.

The experimental procedures are the same as for the analysis of the 3-dimensional flow in axial compressors.

Flow Processes in Multi-stage/Multi-spool Compressors

Experiences on any stage interactions that may limit the application of single-stage results to multi-stage compressors are not yet available as much as desired for design purposes. In such machines additional very characteristic phenomena arise which only can be investigated in fuel multi-stage and/or multi-spool compressors:

- Aerodynamic matching of stages, e.g. fan and core compressor,

- Development of wall boundary-layers particularly with the effect of relative wall movement
- Structure of flow fluctuation and turbulence, effect of low Reynolds number (high altitude, ref.3),
- Effects of tip clearance and associated leakage flows.

L.H. Smith reports in ref.15 for example on the difficulties of matching fans and core compressors while meeting the requirement of a high bypass stream pressure ratio in the range of 1.5 to 1.8. The blade speed near the hub of a low hub/tip radius ratio fan is substantially less than near the tip; thus the high pressure ratio cannot be maintained in the fan hub region revealing problems of fan design and stage matching particularly at engine off-design operation. Fig.14, drawn from ref.15, shows various concepts of fan arrangement demonstrating its very complexity from an aerodynamic point of view. Measurements - at least in the core compressors - are difficult to be carried out, because the inner flow ducts are practically inaccessible.

Wall boundary layers, flow fluctuations and low Reynolds number effects at high altitude are believed to contribute considerably to the onset of flow instabilities preceding surge. No reliable informations are available today, which stages of a multi-stage compressor first induce instabilities, how they propagate in the compressor, and how they lead to stall. Detailed interstage measurements of flow quantities will help to clarify these phenomena. Non-intrusive techniques are well-appropriate for this task, while the narrow spacing between the blade rows does not allow to immerse hard-ware probes.

Tip clearance leakage flow has been identified as a major problem in the last stages of high-pressure compressors because of the very small blades (around 15 mm span). Minimum tip clearances are required to maintain high efficiencies and satisfactory stall margin.

Further improvement of performance, efficiency, and stall margin of multi-stage, multi-spool compressors require experimental investigations as outlined in the preceding chapters, however with particular emphasis of

- Tip clearance control especially in the rear stages of HP compressors.
- Detailed interstage measurements of flow quantities and wall boundary-layer measurements to localize the onset of flow instabilities.

Analysis of Unsteady Flow Phenomena

The 46th meeting of AGARD Propulsion and Energetics-Panel reviewed in great detail the unsteady flow phenomena in turbomachinery with the following general conclusions: unsteady flow have a strong impact on efficiency, aerodynamic stability, aeroelastic stability, and noise generation. A better understanding and improved prediction techniques for unsteady flow effects will contribute in the future to the design of more efficient, low-noise turbomachinery. Even in turbomachines with uniform and steady inlet flow large periodic fluctuations are generated by wake cutting, by viscous vortices shed from blade tip, by cross flows at the endwalls, or by potential field interactions between stator and rotor blade rows (ref.16). These effects require a proper selection of rotor-stator spacing and other design concepts. The main fluctuation component is induced by wake cutting. Fig.15 taken from ref.16 presents the basic flow model. The rotor wake fluid enters the stator passage and is transported-due to its slip velocity (sketch at top of Fig.15) - towards the stator blade pressure side. Thus the wake fluid is collected near pressure surface and tends to appear in the stator wakes.

Non-uniform steady or unsteady flow entering a turbomachine always initiates complicated dynamic flow processes as unsteady blade loading particularly in the rotor blading. This leads to strong flow fluctuations in all stages, to part stall conditions, and to unsteady losses (a.o ref.17 and 18). Fig.16 shows a basic example of inlet distortion. The flow in a subsonic engine intake separates at the nose due to cross-wind situation producing a non-uniform pressure distribution ahead of the compressor (right hand side sketch). Inlet distortion like this always cause a decrease in the stall margin (diagr. at bottom) which may be critical in engine operation. The flow phenomena associated with upstream distortions are today not fully understood; current, very intense R and D activities are aimed at developing distortion tolerant compressors.

Rotating stall is another important unsteady phenomenon in axial compressors involving rapid pressure and lift variations on the rotor blades (ref.19), which up to now could not be studied experimentally because the appropriate testing techniques were missed. Rotating stall is characterized by regions of retarded flow which move circumferentially around a rotor blade row affecting the compressor in two ways: in the region of retarded flow the maximum possible pressure rise is not achieved resulting in an overall performance decrease; second, the stall cells rotating around the blade row cause periodic loading of the blades.

Better understanding of the unsteady phenomena to gain adequate design rules require particularly interstage measurements of the fluctuating flow quantities, require procedures to measure the unsteady blade pressures and to discover the rotating stall cells.

TURBINES

The fundamental flow processes in turbines do not differ in principal from those in compressors. Thus, in order to meet the previously mentioned R and D goals of turbine technology an experimental program very similar to that of compressors has to be formulated for the analysis of the turbine flow field, however with main emphasis of cooling air bleeding effects on the turbine aerodynamics, of secondary - and clearance leakage flows. The last mentioned flow processes play a major role in turbines than in compressors due to the considerably higher aerodynamic loading of turbine stages.

Concerning the measuring techniques quite different requirements exist because of the very high gas temperatures at turbine inlet. The application of hard-ware probes particularly of high-natural frequency transducers for fluctuating pressure measurements are rather limited due to their allowable operating temperature range. Non-intrusive optical techniques are believed to be most easily suited for turbine flow field studies. Additionally, flow visualization techniques may come into question to investigate - at least qualitatively - the phenomena of cooling air bleeding into main streams.

COMBUSTORS

Combustors for presentday's and future aero-engines are subject to very stringent requirements which are partly contradictory and which cannot be met without better knowledge of the physical processes within combustors. Increasing thrust-to-weight ratio of aero-engines requires extremely short combustors with decreased residence times of the gas flow. A comparison between a standard and an advanced flame tube is shown in Fig.17. Optimum use has to be made of the available combustor volume with respect to minimum times for fuel distribution and evaporation, mixing, and combustion. Furthermore, the control of combustion process is aggravated by the omission of the intermediate zone air admission holes.

A similar optimisation is also necessary for the processes in the dilution zone. The achievement of a suitable temperature distribution at the combustor outlet is vital for high-pressure turbine life. However, the increasing demand for flame tube cooling air - which results from higher primary zone temperatures and from a decreased cooling capacity of the cooling air tends to decrease the available amount of dilution air. Therefore, optimum use has to be made of the dilution air in the mixing zone.

Advanced combustors have to fulfill the air pollution standards set by the U.S. Environmental Protection Agency. The contemporary decrease of carbon monoxid, unburnt hydrocarbons and nitric oxides necessitates the development of new combustor concepts, using features like prevaporization and premixing, controlled air admission to the primary zone by means of variable geometry and staged combustion. In order to fulfill the emission standards it is not only necessary to have a direct diagnostic access to the chemical reaction processes but also to develop and to use advanced modelling techniques for the calculation of the combustion process. It seems to be unavoidable to use simplified computation models the validity of which has to be checked against experimental evidence.

Within the next 10 or 20 years the aviation fuel situation will be characterized by decreasing availability and rising prices. This will lead to the introduction of wide-specification-fuels, which are specified through higher boiling ranges and also higher c/h-ratios. Therefore further requirements will arise with respect to enhancement of fuel evaporation and suppression of soot and smoke formation. Many of the above tendencies apply directly to after burners, too.

For the successful treatment of these problems, the combustion engineer needs advanced measuring techniques which enable direct access to the primary zone itself, without disturbing the combustion process by the presence of probes. Informations are needed of flow velocity, density, temperature, gas composition including pollutants and radicals. The development of realistic calculation models needs information not only on average but also on fluctuating quantities. The optimization of droplet evaporation needs procedures for measuring droplet distributions inside of primary zones and their change with time. Improved techniques for measuring soot and smoke particles are needed, too. Non-intrusive optical techniques are believed to be well-suited to yield the necessary informations.

CONCLUDING REMARKS ON REQUIREMENTS TO MEASURING TECHNIQUES

The preceding sections deal briefly with the main aerodynamic research and development problems of aero-engine components and give a rough survey on the flow quantities which have to be analysed experimentally for an adequate solution. To study the flow in compressors, combustors, and turbines already well-known experimental techniques may be used so far they can successfully adapted to the extreme standards of aero-engine applications. In detail the following steps must be done:

- Refinement of conventional pressure, temperature, and air angle measuring methods for the analysis of the mean steady flow in all components (particular attention has to be paid to the probe integrating effects in fluctuating flows and to the radiation effects in hot gas sections).
- Application of miniaturised high-natural frequency transducers for the measurement of unsteady wall, total, and blade surface pressures (extension of

transducer's operating range to higher temperatures is desired).

- Improvement of pulsed laser holography for the analysis of 3-dimensional shock patterns in rotor and stator blading.
- Further development of Raman spectroscopy for the local measurement of temperature, density, and species concentration.
- Examination of the capability of gaseous fluorescent techniques for fluid density analysis.
- Extension of laser velocimetry to the local analysis of three flow components and to the measurement of wall and blade boundary-layers.
- Refinement of clearance measuring devices (ref.21) particularly for the application in hot gas turbine sections.
- Development of techniques for rotating stall detection, e.g. on hot-wire basis.
- Improvement of infrared pyrometry for the measurement of turbine blade temperature fields.

The efficient application of these measuring techniques to aerodynamic testing of engine components however depends largely upon the availability of appropriate electronic systems which take real advantage of the methods themselves and which may help to save time and man power during the tests. On the other side, adequate evaluation techniques have to be provided in order to interpret fully the extensive experimental data.

Now, the subsequent expert lectures will primarily cover the relatively small area - with respect to the preceding list - of laser anemometry, a new field, however, which opens very promising prospects for aero-engine research and development.

REFERENCES

- 1 Fuhs, A.E., Kingery, M.: Instrumentation for Airbreathing Propulsion. Progress in Astronautics and Aeronautics, Vol.34, MJT Press (1974).
- 2 Pianko, M. Modern Methods of Testing Rotating Components of Turbomachines. AGARD-AG-207 (1975).
- 3 Heilmann, W., Winterfeld, G.: Neuere Beiträge aus Forschung und Entwicklung auf dem Gebiet der Turboflugtriebwerke. 8. DGLR-Jahrestagung, Bonn-Bad Godesberg, Sept.1975.
- 4 Armstrong, F.W.: The Aero Engine and its Progress - Fifty Years after Griffith. The Aeronautical Journal, Vol.80, No.792, Dec.1976.
- 5 Denning, R.M., Miller, S.C.: Future Trends in Aero Gas Turbine Design - Conventional Engines, Part 1. The Aeronautical Journal, Vol.80, No.788, Aug.1976.
- 6 Johnson, E.T., Graydon, A.E.: Small Turbine Advanced Gas Generators for Future Engine Requirements. American Helicopter Society, 30th Annual National Forum, May 1974, Reprint No.872.
- 7 Hartmann, M.J., Benser, W.A., Hauser, C.H., Ruggeri, R.S.: Fan and Compressor Technology, in: NASA SP-259 (1970).
- 8 Schreiber, H.A.: Comparison between Flows in Cascade and Rotors in the Transonic Range. VKI-Lecture Series on Transonic Blade-to-Blade Flows in Turbomachinery, Febr.1976.
- 9 Korn, D.G.: Numerical Design of Transonic Cascades. ERDA Research and Development Report. C00-3077-72 (1975).
- 10 Fottner, L.: Aerodynamisch hochbelastete Verdichterbeschaufelung mit Grenzschichtbeeinflussung. Forschungsberichte aus der Wehrtechnik, BMVg FBWT 77-4 (1977).
- 11 Weyer, H., Dunker, R.: Dual Beam Laser Anemometry Study of the Flow Field in a Transonic Compressor. 49th AGARD-PEP Specialists Meeting, The Hague, March 1977, to be published.
- 12 Horlock, J.H.: Recent Development in Secondary Flow. 49th AGARD-PEP Specialists Meeting, The Hague, March 1977, to be published.
- 13 Eckardt, D., Schodl, R.: Three-Dimensional Flow Studies in a High-Speed Centrifugal Compressor Impeller Using a Laser Velocimeter, in: Improvements in Fluid Machines and Systems for Energy Conversion, Vol.IV, U. Hoepli Press, Milano (1976).
- 14 Eckardt, D.: Detailed Flow Investigations within a High-Speed Centrifugal Compressor. Tr.ASME, J.of Fluids Engineering, Series I, Vol.98 (1976).
- 15 Smith, L.H.: Some Aerodynamic Design Considerations for High Bypass Ratio Fans. 2nd ISABE, held at Sheffield, U.K., March 1974.

- 16 Mikolajczak, A.A.: The Practical Importance of Unsteady Flow. AGARD-CP-177 (1975).
- 17 Mazzawy, R.S.: Multiple Segment Parallel Compressor Model for Circumferential Flow Distortion. AGARD-CP-177 (1975).
- 18 Lecht, M., Weyer, H.: On the Unsteady Aerodynamic Rotor Blade Loading in a Transonic Axial Flow Compressor with Steady-State Inlet Distortion. U.T.A.M.-Symposium on Aeroelasticity in Turbomachines, Paris, Oct.1976.
- 19 Sexton, M.R., O'Brien, W.F., Moses, H.L.: An On-Rotor Investigation of Rotating Stall in an Axial-Flow Compressor. AGARD-CP-177 (1975).
- 20 Gastebois, P., Caruel, J.: Chambre de combustion anti NO_x à écoulement aérodynamique variable pour turboréacteur. AGARD-CP-205 (1976).
- 21 Ford, M.J., Hildebrand, J.R., Prosser, J.C.: Design, Fabrication, and Demonstration of a Miniaturized Tip Clearance Measuring Device. USA AMRDL-TR-74-67 (1974).

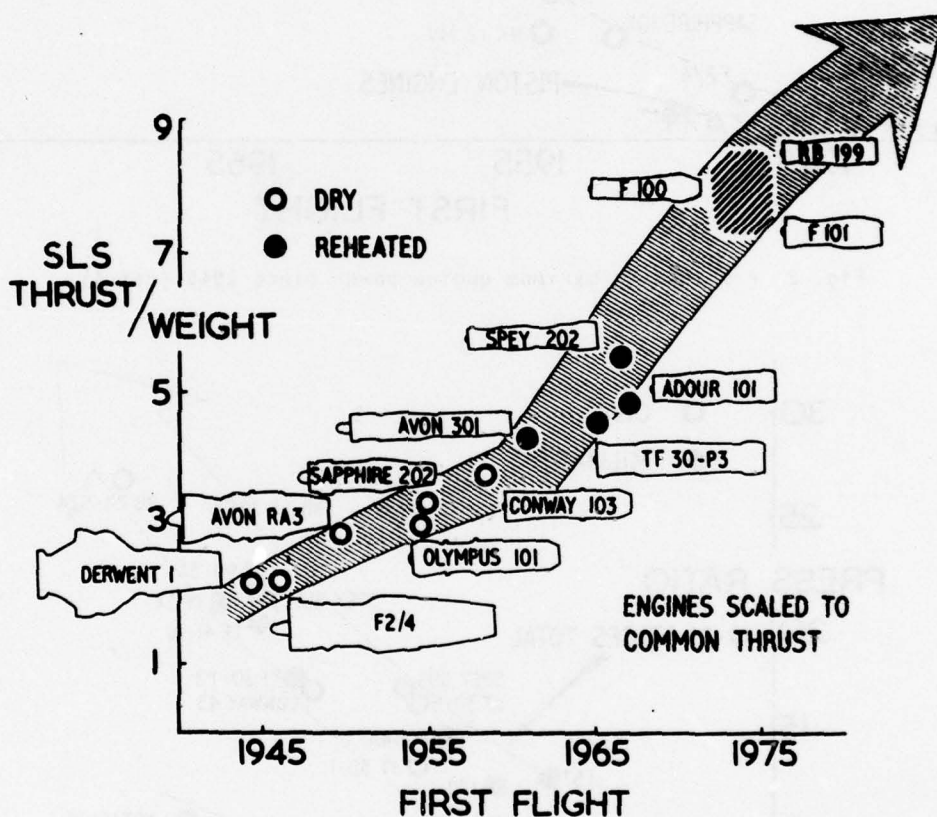


Fig. 1 Progress in military engines since 1945 (ref.4).

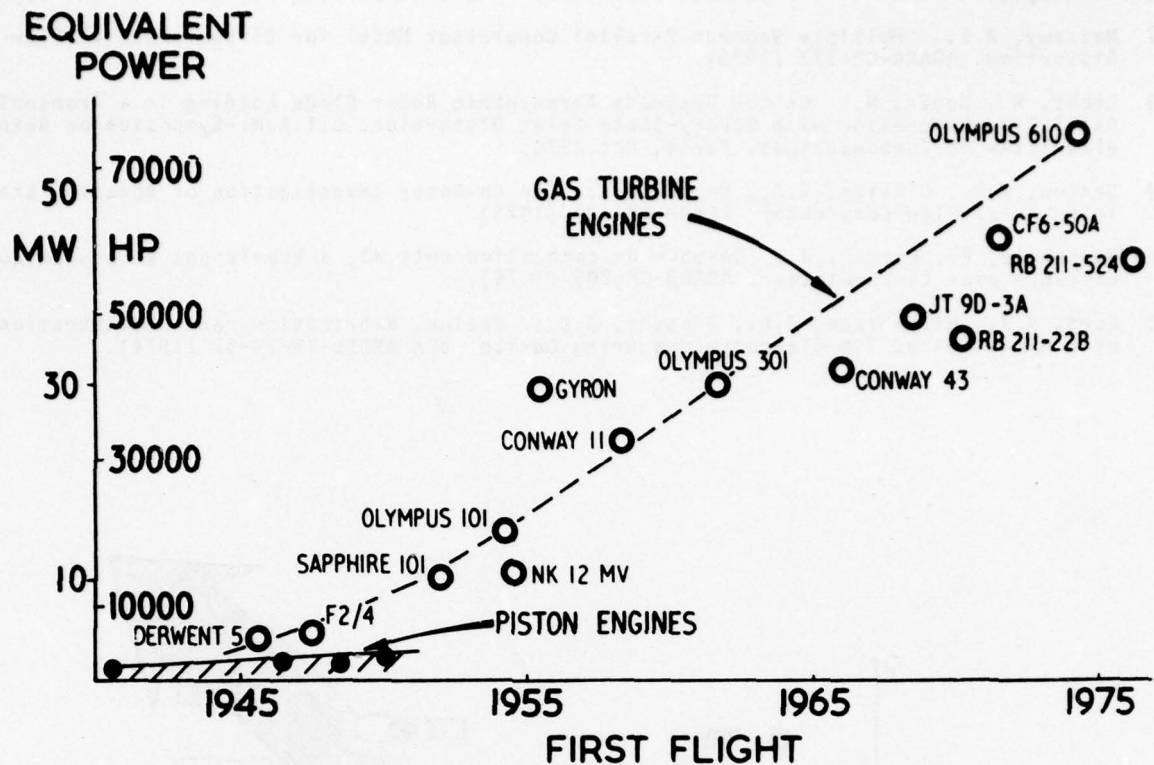


Fig. 2 Progress in maximum engine power since 1945 (ref.4)

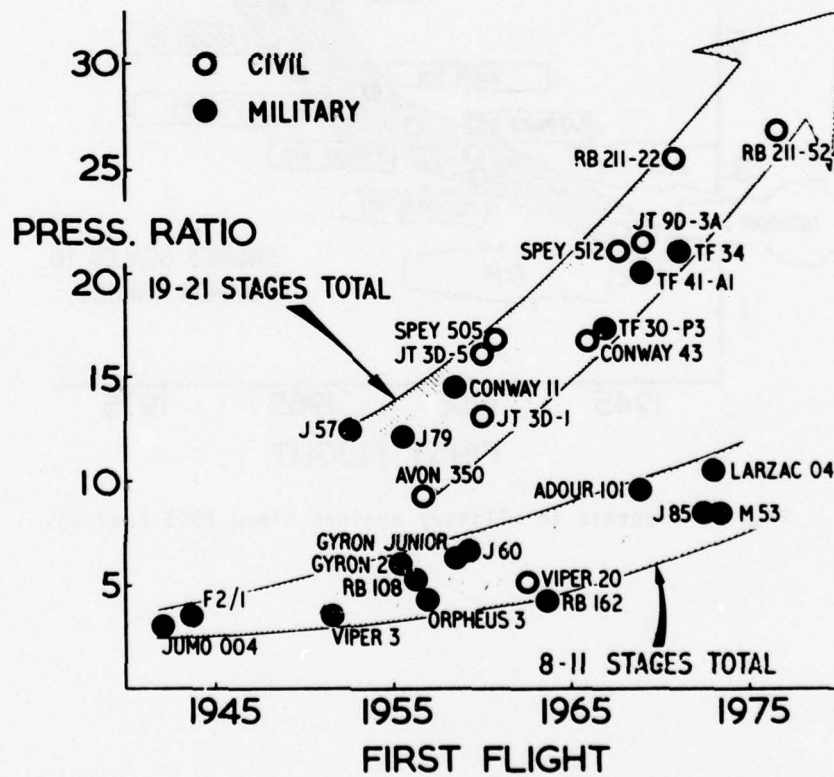


Fig. 3 Increase in cycle pressure ratio since 1945 (ref.4)

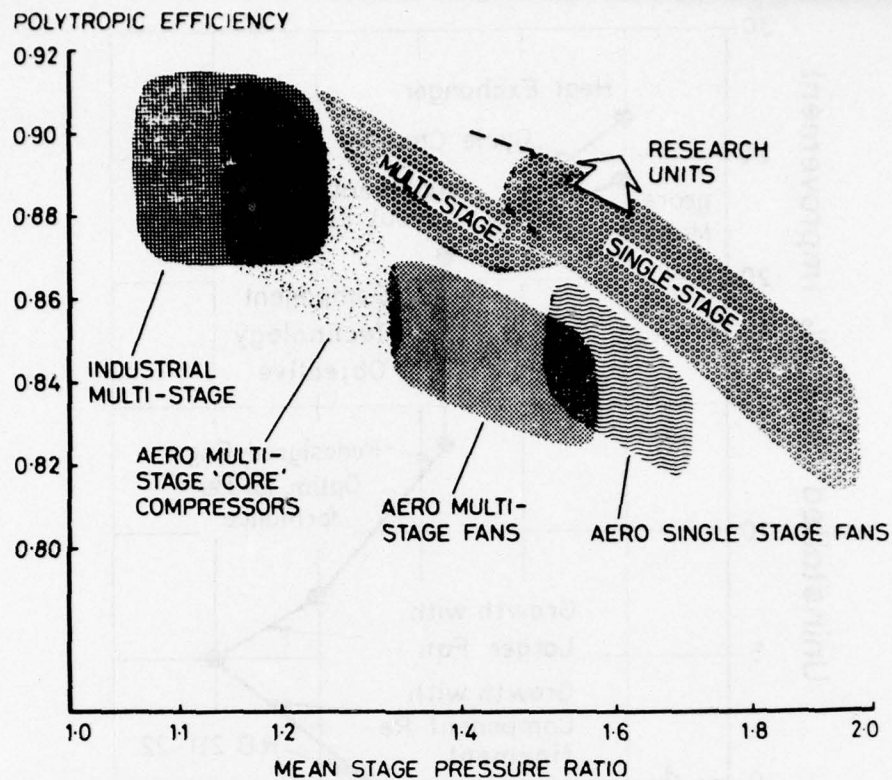


Fig. 4 Current compressor efficiency versus stage pressure ratio (ref.4)

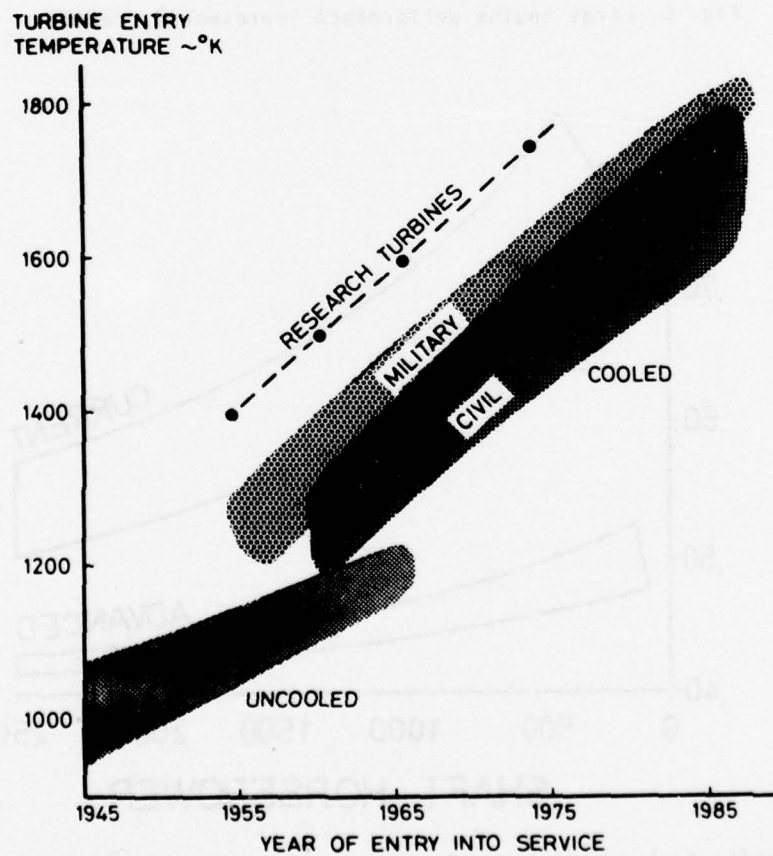


Fig. 5 Progress in turbine entry temperature since 1945 (ref.4)

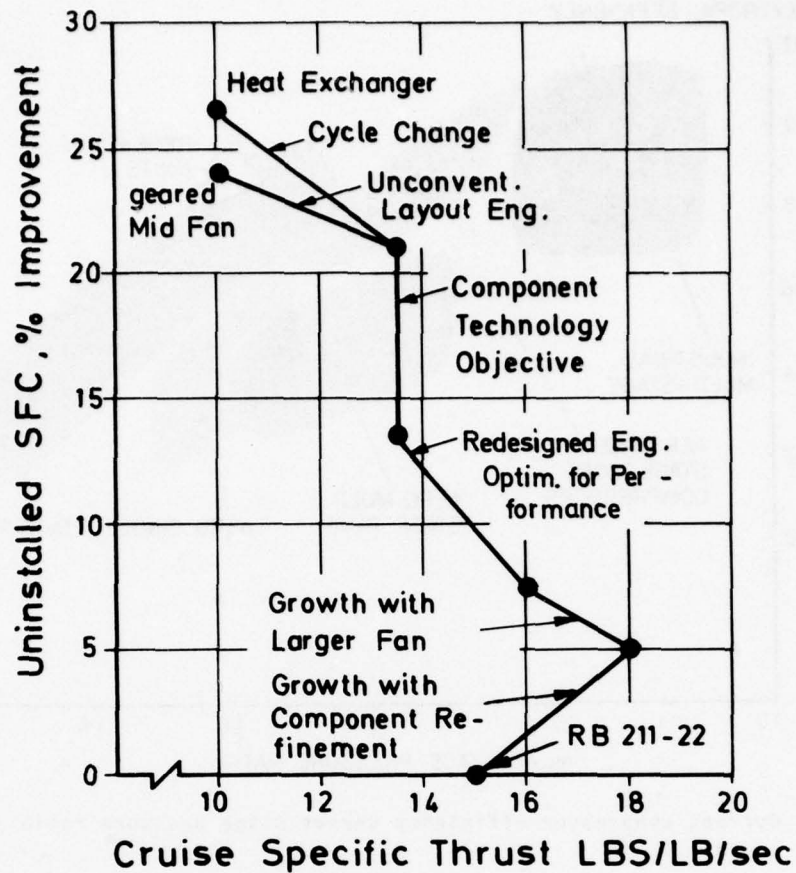


Fig. 6 Large engine performance improvement (ref.5).

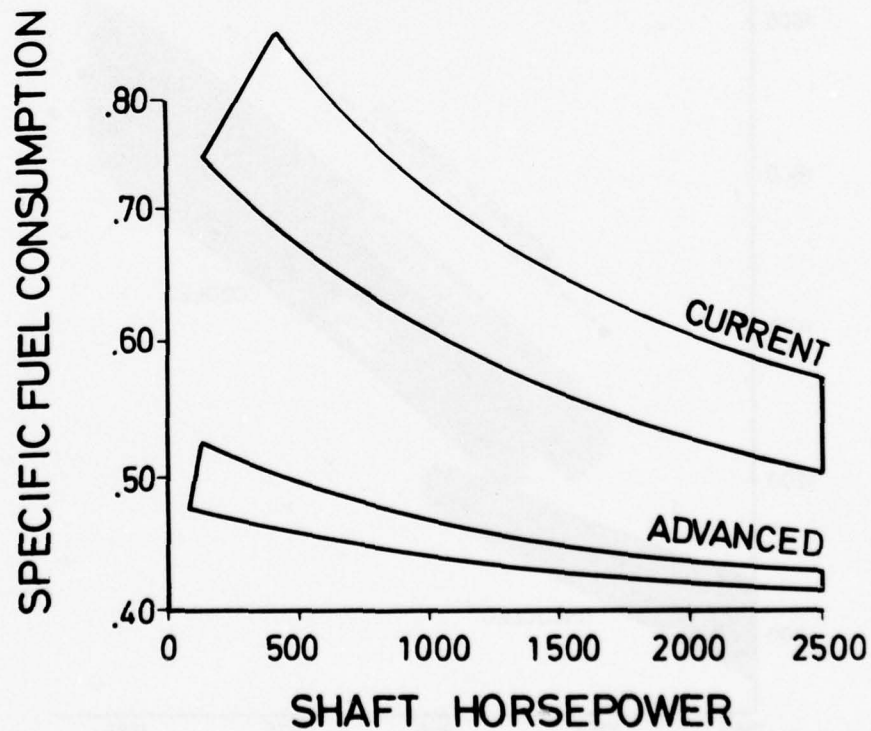


Fig. 7 Specific fuel consumption of current and advanced small engines (ref.6)

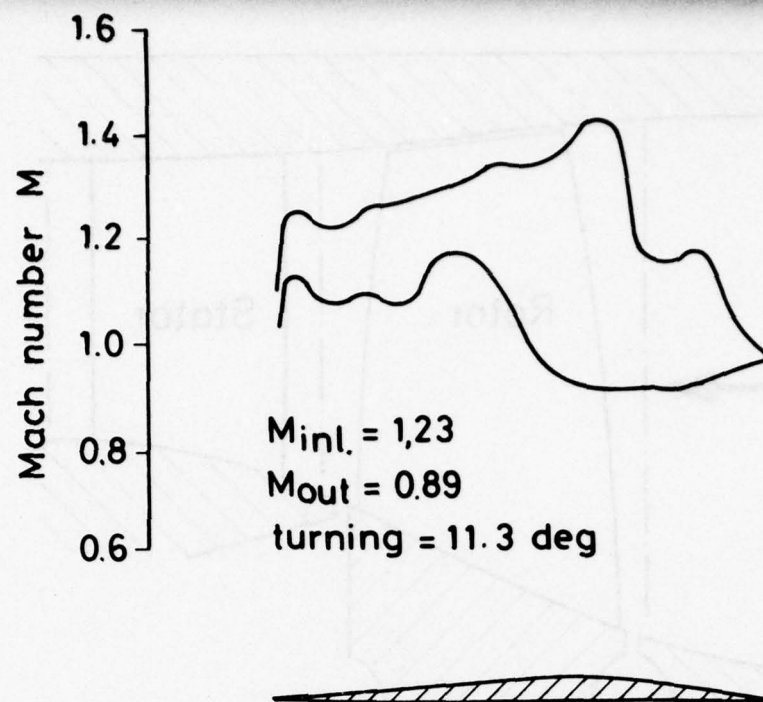


Fig. 8 Multiple-circular-arc (MCA) blade profile for transonic inlet velocity and typical blade Mach number distribution.

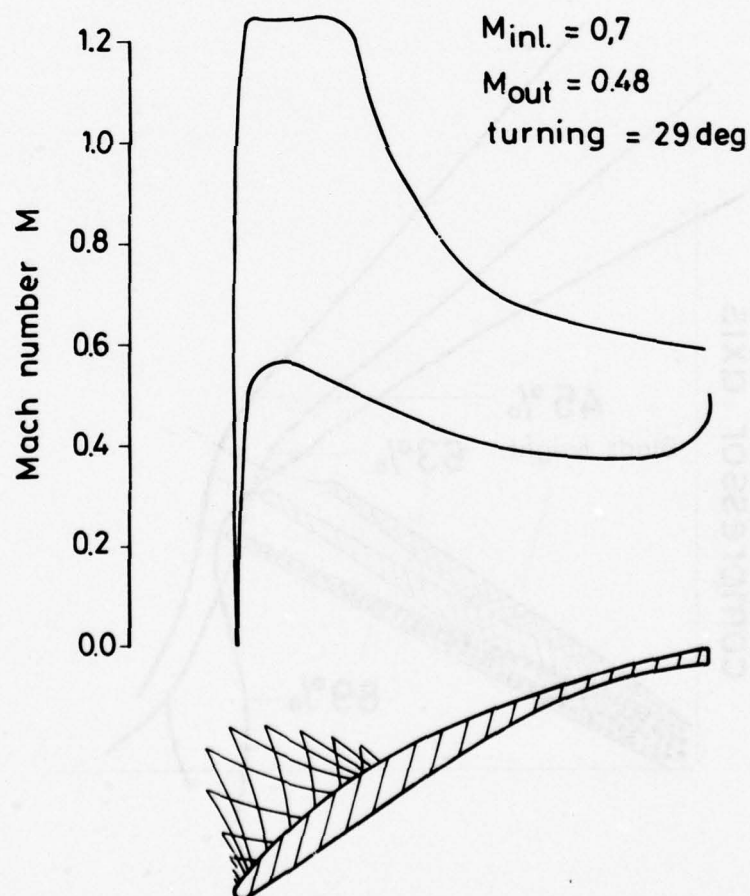


Fig. 9 Supercritical airfoil for high-subsonic inlet velocity and typical blade Mach number distribution (ref.9).

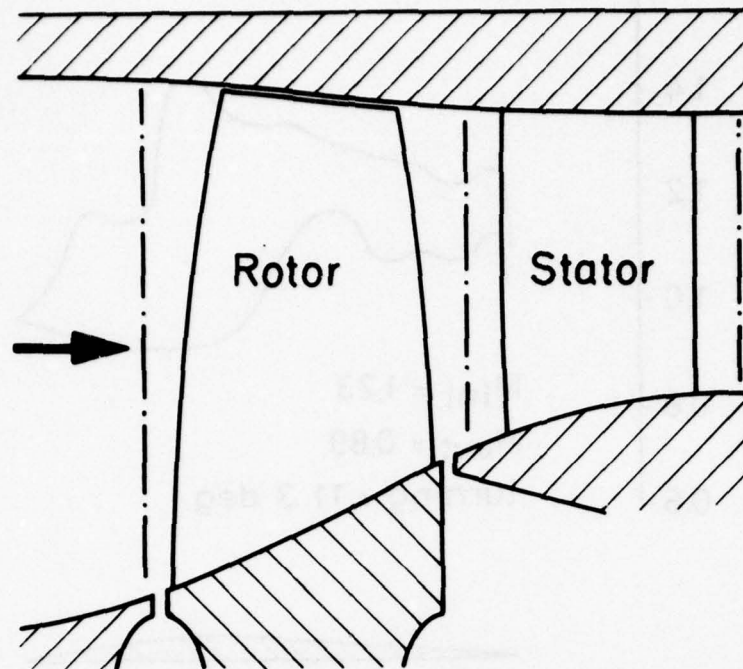


Fig.10 Cross-section view of a transonic compressor stage

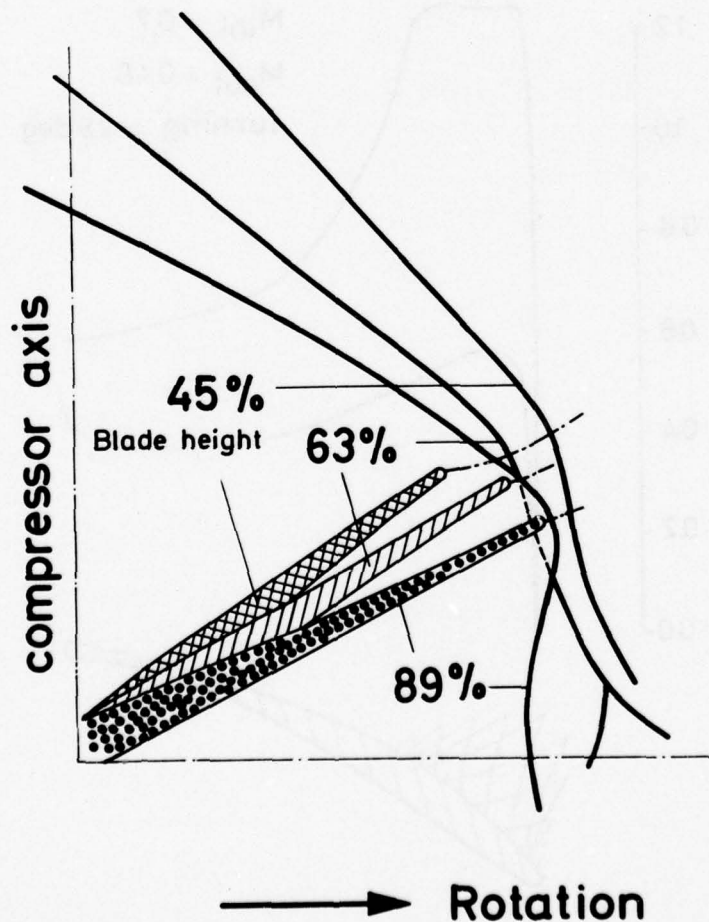


Fig.11 Three-dimensional shock wave pattern at a transonic rotor inlet (100 % speed, max. efficiency).

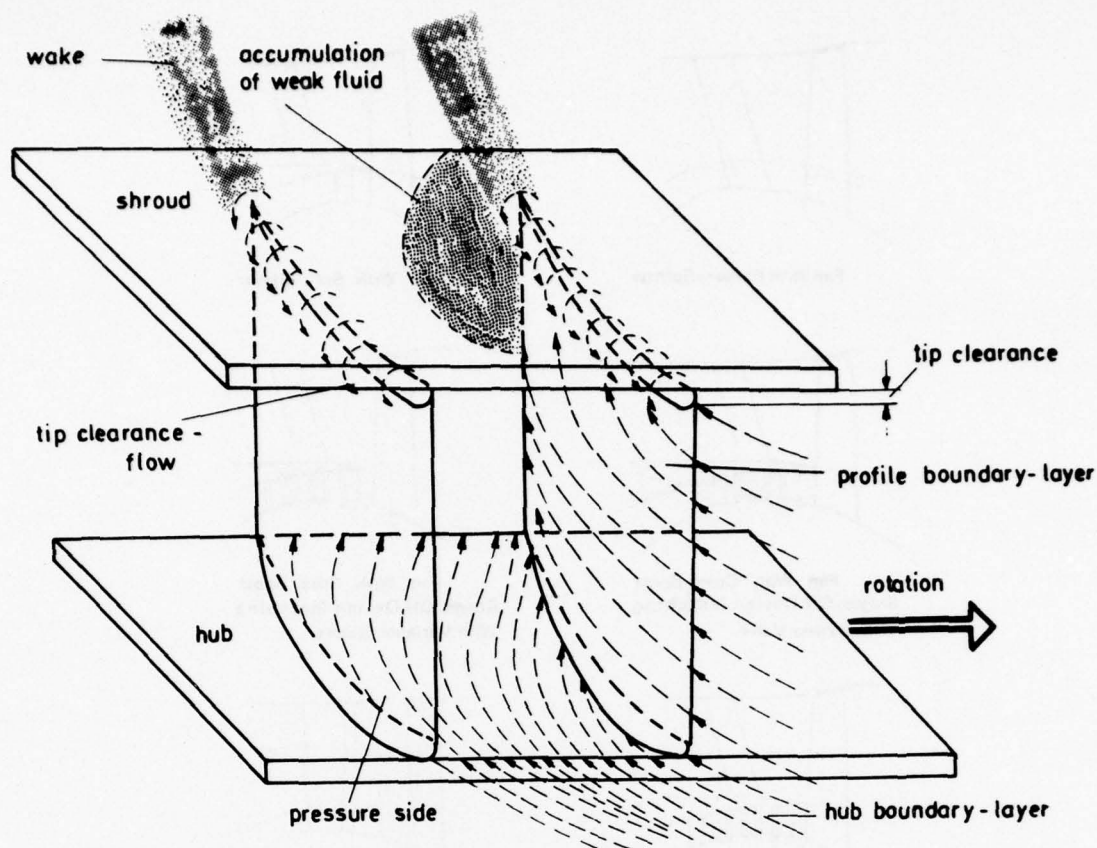


Fig.12 Schematic view of secondary and leakage flow in an axial compressor blading.

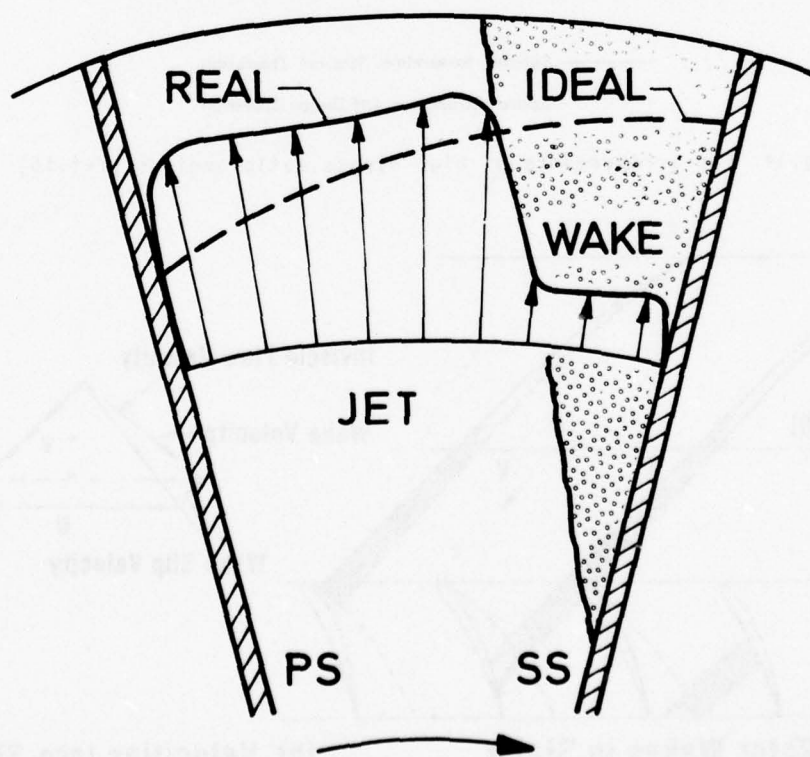


Fig.13 Centrifugal impeller flow near rotor exit (PS = pressure side; SS = suction side).

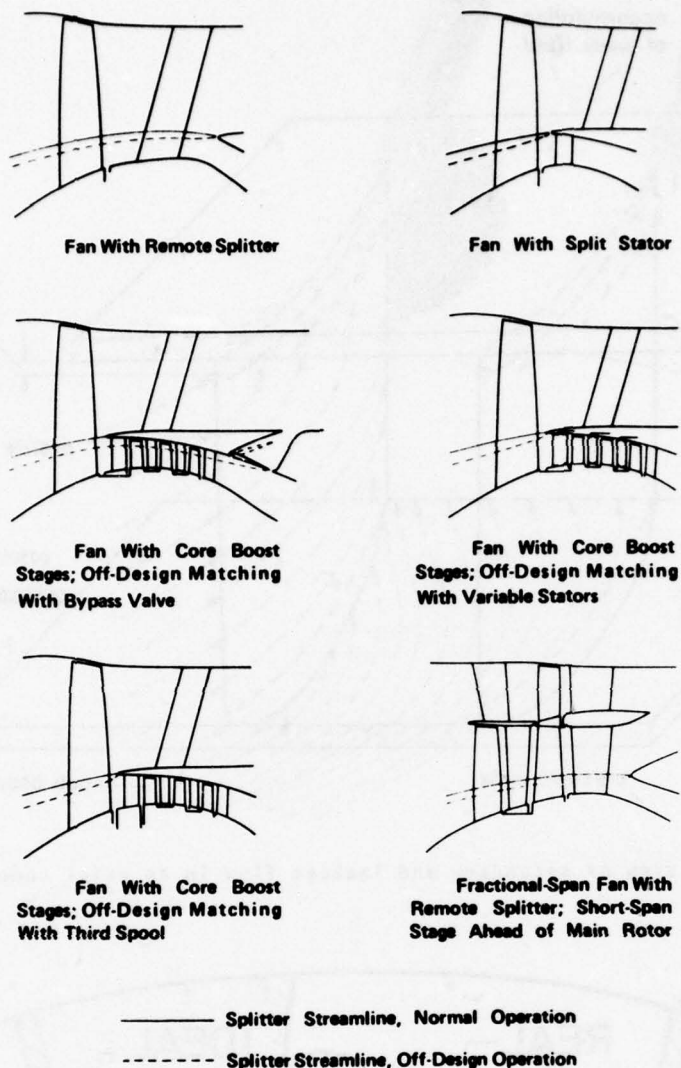


Fig.14 Fan arrangements of high bypass ratio engines (ref.15)

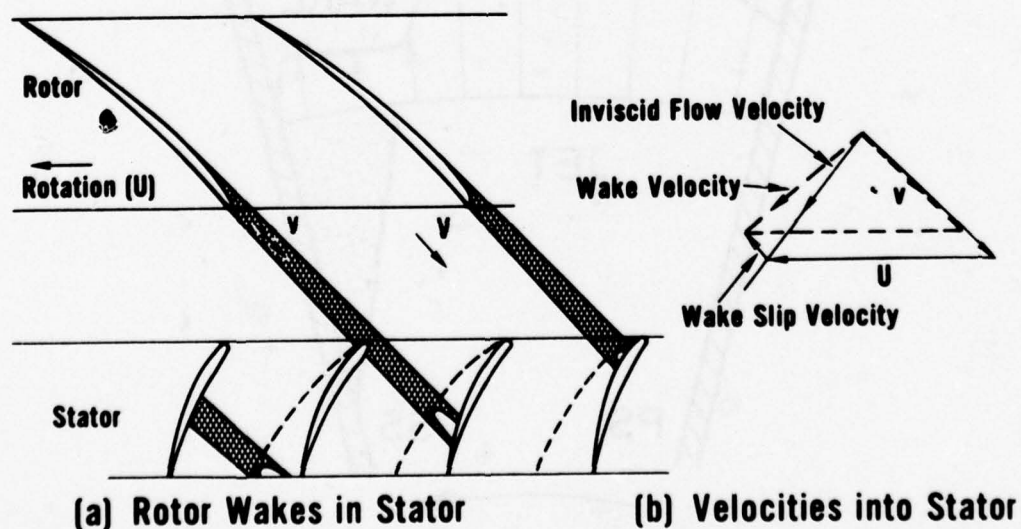


Fig.15 Basic model of rotor blade wake cutting (ref.16)

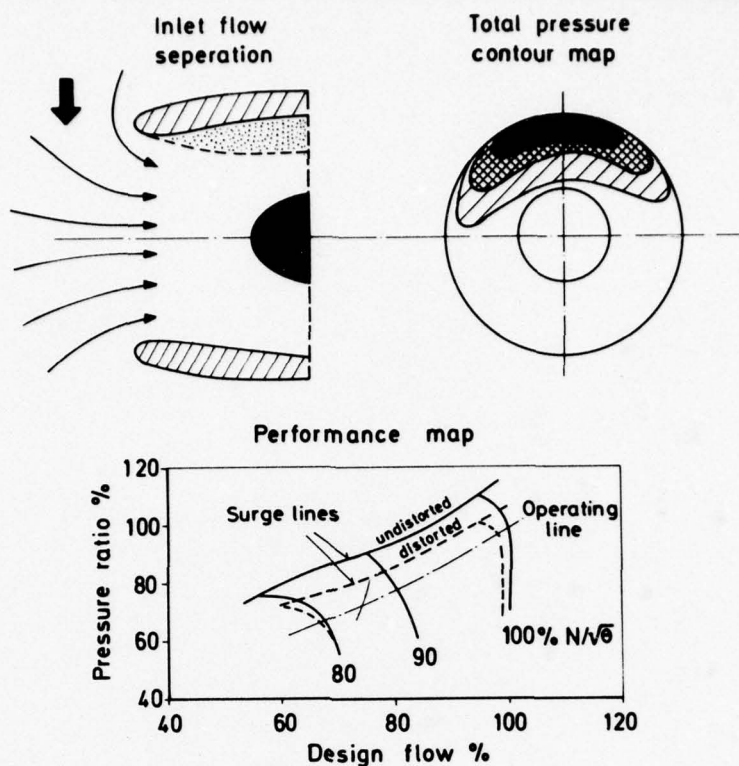


Fig.16 Schematic of compressor inlet flow distortion and performance map of distorted and undistorted compressor.

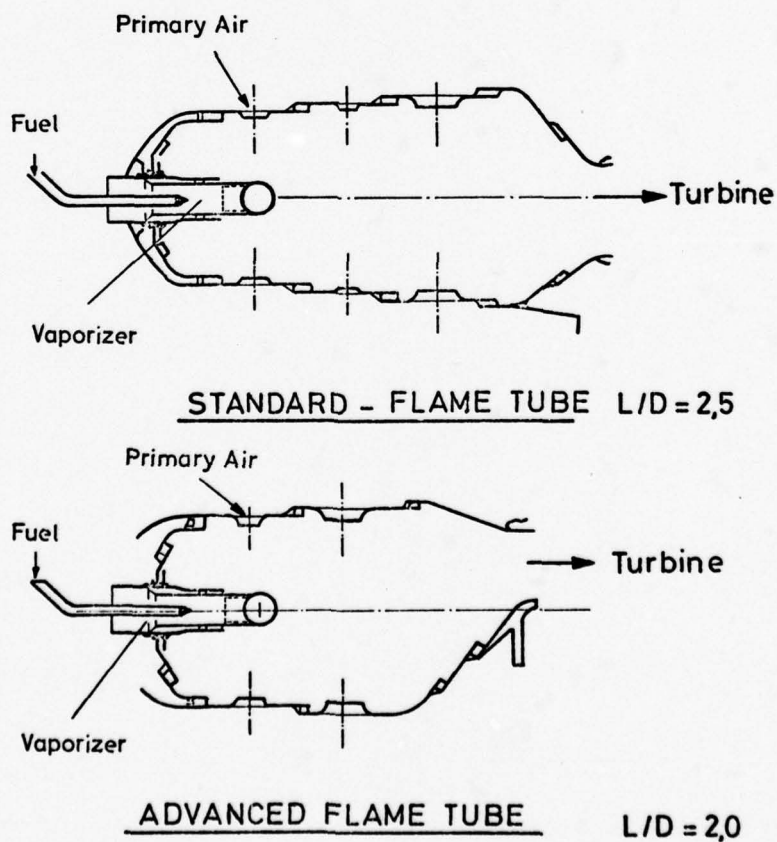


Fig.17 Comparison of standard and advanced flame tubes (ref.20).

REVIEW OF OPTICAL TECHNIQUES WITH RESPECT TO AERO-ENGINE APPLICATIONS

by Claude VÉRET

Office National d'Etudes et de Recherches Aéronautiques (ONERA)
92320 Châtillon (France)

SUMMARY

With the exception of laser doppler velocimeter measurement techniques which will be covered during another session, the main optical methods providing quantitative information on gas flows are presented in this paper.

Are concerned :

- Those usable in compressible flow, based on the deformation of a light wave crossing a medium (interferometry) or light rays deviations accompanying these deformations (schlieren technique and shadowgraphy). These methods allow to measure either shock pattern shape in transsonic and supersonic flows or, in some cases, gas density fields. A few examples on stationary or rotating blade cascade flows will be given and holography advantages to get interferograms will be shown.
- Spontaneous or stimulated Raman scattering which provides original means to determine the concentrations and temperatures of given components within the flame itself.

It is difficult to apply most of these methods to the engines themselves. Their use on test rigs simulating the conditions to be encountered in engines is described.

1 - Introduction

Optical methods are commonly used in aerodynamic research, not only for flow visualization, but also for density or temperature distribution measurement.

The main advantage of these methods lies in the fact that the interaction between the gas flow and the light beam does not generate any flow disturbances.

However, the application of these methods to the study of the inner flow of a real aero-engine is very often difficult, if not impossible. As a matter of fact, no window can be made for the penetration of a light beam into the part of the engine to be investigated, i.e. rotor carrying blades, combustion chamber, etc. Therefore, optical methods are mainly used at the research stage, on experimental set-ups simulating partial engines, the design of which includes optical windows.

The principles governing the use of interferometry for the measurement of flow density fields and the use of Raman scattering for temperature measurements in hot gases will be covered to illustrate the applications of optical methods. These operational means of measurement have been recently developed as a result of the use of laser sources providing both monochromatic light and high power density.

2 - Interferometry

2.1 - Principle

Interferometry is the basic optical method permitting visualization and density measurements in a flow field, which has been applied since the inception of aerodynamic studies [1]. Although the Mach-Zehnder type interferometer is the most highly developed instrument for use in wind tunnels, the principles of interferometry will be demonstrated with a Michelson type interferometer, as this type is much easier to use in aero-engine research.

The main optical parts of a Michelson interferometer are a beam splitter and two mirrors, as shown on figure 1.

The light beam coming out of a laser is expanded by means of a telescopic optical system including a diverging lens L_1 and a converging lens L_2 . The beam splitter S receiving the beam, transmits a part of the incident light to the plane mirror M_1 and reflects the other part of this light to the plane mirror M_2 .

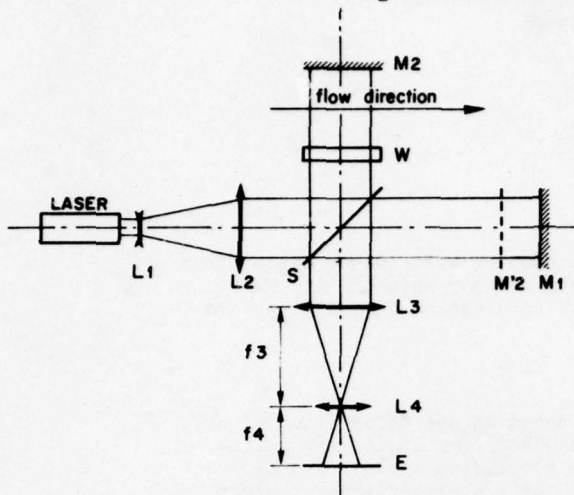


Figure 1 - Michelson interferometer optical diagram.

One face of the beam splitter is coated with a thin dielectric layer in order to get about half the light transmitted and about the other half reflected.

The light reflected by M_1 is then reflected by the beam splitter S towards the lens L_3 , and the light reflected by M_2 is transmitted to the same lens L_3 . The latter is a converging lens and the light falls on the screen E .

The test chamber for the aerodynamic flow is located between the plane mirror M_2 and a plane glass window W , so that the direction of propagation of the light is perpendicular to the flow. Finally, a lens L_4 sends an image of the test chamber towards the screen E .

A given point P of the screen receives two rays of light from the same laser source, one ray is transmitted by S , reflected by M_1 , reflected by S and transmitted by L_3 and L_4 ; the other ray is reflected by S , transmitted by W , reflected by M_2 , transmitted by W , then S , L_3 and L_4 . These two rays can interfere with each other. At the point P , the resulting intensity I is given by the relation :

$$I = I_0 (1 + \cos \varphi) \quad (1)$$

where :

I_0 : Incident intensity on the beam splitter S (the coating on S is supposed to have 50% transmission, 50% reflection and no absorption)

φ : Phase difference between the waves corresponding to the two rays.

The phase difference can be expressed as follows :

$$\varphi = \frac{2\pi \delta}{\lambda} \quad (2)$$

where :

λ : Light wavelength

δ : Optical path difference between the two rays.

The optical path is the product of the geometrical length L travelled by the light from one point to another, and the refractive index n .

$$\Delta = nL \quad (3)$$

n being the ratio of the speed of light in the vacuum to the speed of light in the medium, this optical path is the length that the light would have covered while propagating in the vacuum during the same period of time.

With air in the test chamber, the refractive index n is the same at all points along both light paths $L_1 = SM_1S$ and $L_2 = SM_2S$. Then, the optical path difference is given by :

$$\delta = \Delta_1 - \Delta_2 = n(L_1 - L_2) \quad (4)$$

Let us consider a virtual mirror M'_2 which is the image of the mirror M_2 produced by the reflection on the coated face of the beam splitter S . If M_1 and M'_2 are parallel, the optical path difference is the same for all the rays of the incident light beam. Thus, the optical path difference δ is the same for each point P on the screen. Therefore, the phase difference φ is a constant, as well as the intensity I , given by (1), over the whole screen; this condition is called "infinite fringe width alignment". The intensity value is a function of φ or $\delta = \lambda \varphi / 2\pi$:

maximum for $\varphi = 2k\pi$ or $\delta = k\lambda$: bright fringe

minimum for $\varphi = \pi + 2k\pi$ or $\delta = \frac{\lambda}{2} + k\lambda$: dark fringe

where k is an integer (positive or negative) or zero. The screen appears uniformly bright.

For a small rotation ϵ of the mirror M_1 the reflected ray of light rotates by 2ϵ , and the two interfering rays cross each other on the screen at an angle η given by :

$$\eta = 2\epsilon \frac{f_3}{f_4} \quad (5)$$

The phase difference φ becomes a linear function of the distance along a direction x and a fringe pattern appears on the screen. Fringes of such a pattern are equidistant, parallel to each other and perpendicular to the direction x . The direction x is parallel to the line of intersection of two planes : one of them contains the two interfering rays and the other is that of the screen E .

The constant fringe spacing is given by :

$$i = \frac{\lambda}{\eta} = \frac{\lambda}{2\epsilon} \frac{f_4}{f_3} \quad (6)$$

In conclusion, the fringe spacing can be varied with the value of the angle ϵ , and the fringe direction with the direction of the axis of rotation of the mirror M_1 . This

configuration is called "finite fringe width alignment".

2.2 - Application to aerodynamics flows

2.2.1 - General case

In the case of light propagating in a gas, the refractive index n depends on the physical state of the gas (pressure and temperature). The Gladstone-Dale relation is the following :

$$n - 1 = k \rho \quad (7)$$

where :

K : molecular refractivity (dependent on the gas mixture)

ρ : gas density

with, for a perfect gas :

$$\rho = \frac{M}{R_0} \frac{p}{T} \quad (8)$$

M : molecular mass

R : gas constant per mole

p : pressure

T : temperature

In an high speed aerodynamic flow around a model, the gas density ρ varies from one point to another with the pressure and the temperature due to the compressibility effect. Thus, the optical path along a ray propagating in this medium is given by :

$$\Delta = \int n_i dl \quad (9)$$

n_i : refractive index at a point i

dl : elementary geometrical path

Let us consider again the interferometer shown on figure 1. Between the glass W and the mirror M_2 , the rays of light propagate perpendicularly to the flow.

Without a flow, the optical path in the chamber is :

$$\Delta_0 = 2n_0e \quad (10)$$

n : refractive index in the chamber

e : distance between W and M_2

Including relation (4), the optical path difference in the interferogram on the screen becomes :

$$\delta_o = \delta_a + 2(n_0 - n_a)e \quad (11)$$

where :

n_a : air refractive index outside the chamber

δ_a : optical path difference with air in the chamber.

With a flow, taking relation (9) into account, the optical path difference becomes :

$$\begin{aligned} \delta_1 &= \delta_a - 2n_ae + \int_{A_1}^{A_2} n_i dz \\ &= \delta_0 - 2n_0e + \int_{A_1}^{A_2} n_i dz \quad (12) \end{aligned}$$

The integration limits A_1 and A_2

correspond respectively to the point of incidence in the flow and to the point of emergence out of the flow, after reflection by the mirror M_2 .

With the infinite fringe width alignment, δ_o is a constant over the screen, as stated above, and the fringes observed on the screen are lines of equal optical path difference in the flow (fig.2).

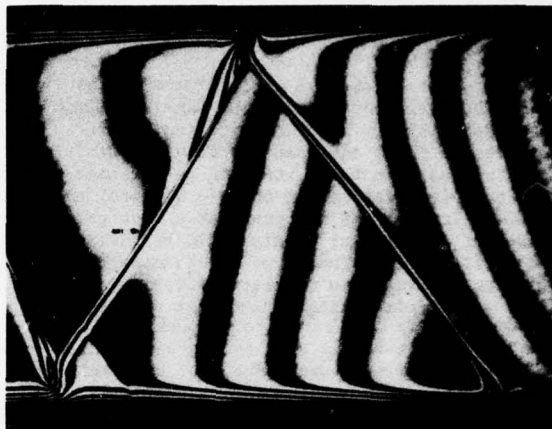


Figure 2 - Transonic flow in wind tunnel test chamber along a half profile mounted on the lower wall. The shock wave is attached to the model trailing edge and successively reflected on the upper and lower wall. Infinite fringe interferogram.

With a finite fringe width alignment, parallel and equidistant fringes, corresponding to the linear variation of δ_o in a given direction, are distorted by the propagation of light through the flow (fig.3).

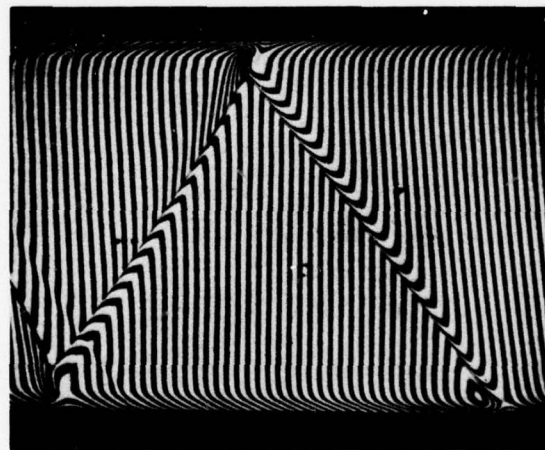


Figure 3 - Same flow conditions as for figure 2. Finite fringe interferogram.

In order to get the values n_i at each point $P(x,y)$ on the screen plane, it is necessary to know a relation of the variation of n_i along the direction of propagation of light z . This is only possible in a few cases; the two main ones, which will be considered are : two dimensional flows and axisymmetrical flows.

2.2.2 - Two-dimensional flows

A flow is called two-dimensional when it may be assumed that the gas density ρ (and also, according to (7), the refractive index n) is a constant along a ray of light, in the direction z .

Then, relation (12) becomes :

$$\delta_{1P} = \delta_0 + 2(n_P - n_0)e \quad (13)$$

n_P : refractive index at a point $P(x, y)$ on the screen.

Let us observe again figures 2 and 3 which are interferograms of the same aerodynamic flow, respectively with infinite and finite fringes. We first see that the former contains less fringes than the latter. If we consider that numerical values can only be obtained along the dark fringes, it appears that a much greater number of measurement points could be given by the finite fringe. This type of adjustment offers additional advantages for data processing. In fact, with finite fringes, the sign of the difference from one fringe to the next is unambiguous; it is the same in the whole interferogram, along the same direction. With infinite fringes, it is not possible to know if this difference is increasing or decreasing. Also, when fringes are submitted to a rapid density change as in a shock wave, only the finite fringe width alignment makes it possible to follow the same fringe from one side to the other.

For these reasons, finite fringe interferograms are not often used for data processing purposes. Let us consider again relation (13). In this case, the refractive index without a flow n_0 is a constant but δ_0 is a function of the position of the point P in the field.

$$\delta_{1P} = \delta_{0P} + 2(n_P - n_0)e \quad (14)$$

The interferogram, recorded on a photographic plate, is processed along lines crossing all the fringes, with a microdensitometer connected with a microprocessor in order to determine the maximum optical density (bright fringe) and the minimum density (dark fringe) abscissis [2].

The absolute values of δ_{1P} and δ_{0P} are unknown; therefore, we consider a reference point R in the field, where the gas density is ρ_R and the refractive index n_R . For this reference point, we derive from (14) :

$$\delta_{1R} = \delta_{0R} + 2(n_R - n_0)e \quad (15)$$

Subtracting (15) from (14), we get :

$$\delta_{1P} - \delta_{1R} = \delta_{0P} - \delta_{0R} + 2(n_P - n_R)e \quad (16)$$

Let us consider the first member of this relation. We know that, from one fringe to the next, the optical path difference is one wavelength; therefore :

$$\delta_{1P} - \delta_{1R} = N_{1PR} \lambda \quad (17)$$

N_{1PR} : fringe number between R and P measured on the interferogram with a flow. A fractional part of this number is obtained by interpolation between the two nearest fringes located at either side of a point (R or P).

Let us consider now the $\delta_{0P} - \delta_{0R}$ term of the (16) second member. Its value is obtained from the interferogram without a flow on which the fringe spacing ι_0 is a constant everywhere, so that :

$$\delta_{0P} - \delta_{0R} = N_{0PR} \lambda = \frac{x_P - x_R}{\iota_0} \lambda \quad (18)$$

Finally, from the Gladstone-Dale relation (7), we get :

$$n_P - n_R = K(\rho_P - \rho_R) \quad (19)$$

Substituting (17), (18) and (19) in (16), we get :

$$N_{1PR} = \frac{x_P - x_R}{\iota_0} + \frac{2Ke}{\lambda} (\rho_P - \rho_R) \quad (20)$$

Or :

$$\rho_P - \rho_R = \frac{\lambda}{2Ke} \left(N_{1PR} - \frac{x_P - x_R}{\iota_0} \right) \quad (21)$$

Measuring N_{1PR} on the interferogram with a flow, N_{0PR} or $x_P - x_R$ and ι_0 on the interferogram without a flow and knowing λ , K and e , we obtain the difference in gas density between the points R and P .

It is often easy to get the value of the gas density at a given reference point R , for example, by Pitot gauge measurements; therefore the absolute value ρ_R is deduced from relation (21).

2.2.3 - Axisymmetrical flow

In this case, we consider that the flow has an axis of revolution, as around a conical or cylindrical model, the flow direction being parallel to this axis.

An axisymmetrical flow around a spherical model is shown on figure 4; we see that the revolution part is bounded by the shock wave. Outside of the shock, the refractive index is a constant n . Inside the shock, the refractive index is constant along circles the centers of which are on axis of revolution, but varies with the radii of the circles.

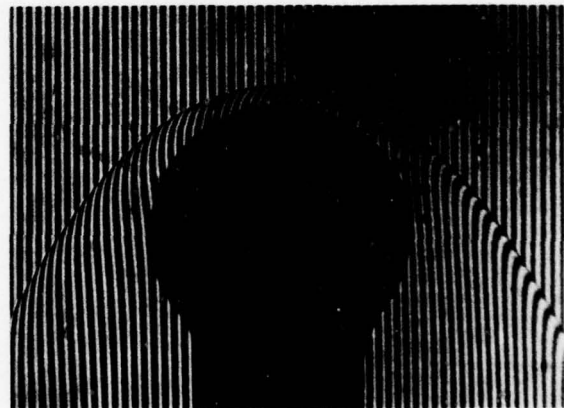


Figure 4 - Supersonic flow around a spherical model; finite fringe interferogram.

Axisymmetrical flow interferograms can be processed by several methods. One simple method will be considered here. Let us consider figure 5, showing rays of light propagating in a plane perpendicular to the flow. Each ray is designated by a subscript i (integer). The refractive index is n_i between circles of radii r and r

(respectively the shock wave and a circle tangent to the ray i); it is n_{i-1} between circles of radii r_i and r_{i-1} , and so on.

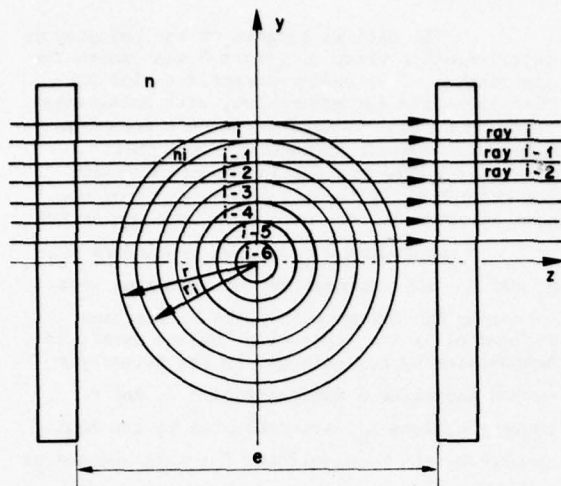


Figure 5 - Rays of light through an axisymmetrical flow; section of a plane perpendicular to the flow direction.

For each ray, the optical path between the windows are :

$$\begin{aligned}\Delta_i &= \Delta + 2(n_i - n) \sqrt{r_i^2 - z_i^2} \\ \Delta_{i-1} &= \Delta + 2(n_i - n) \sqrt{r_i^2 - z_{i-1}^2} + 2(n_{i-1} - n_i) \sqrt{r_{i-1}^2 - z_{i-1}^2} \\ \Delta_{i-2} &= \Delta + 2(n_i - n) \sqrt{r_i^2 - z_{i-2}^2} + 2(n_{i-1} - n_i) \sqrt{r_{i-1}^2 - z_{i-1}^2} \\ &\quad + 2(n_{i-2} - n_{i-1}) \sqrt{r_{i-2}^2 - z_{i-2}^2} \\ \Delta_{i-m} &= \Delta + 2(n_i - n) \sqrt{r_i^2 - z_{i-m}^2} + 2(n_{i-1} - n_i) \sqrt{r_{i-1}^2 - z_{i-1}^2} \\ &\quad + 2(n_{i-2} - n_{i-1}) \sqrt{r_{i-2}^2 - z_{i-2}^2} + \dots + 2(n_{i-m} - n_{i-m+1}) \sqrt{r_{i-m}^2 - z_{i-m}^2}\end{aligned}$$

: optical path outside the axisymmetrical flow, therefore :

$$\Delta = n e \quad (23)$$

The interferograms, obtained with an interferometer of the Michelson type (figure 1), are processed with a microdensitometer like two-dimensional interferograms. At a given position x along the axis of revolution (x parallel to the flow direction), the values of δ_i versus those of r_i in the direction y are obtained. According to (12), the path difference δ_i at a point P corresponding to the ray i , is given by :

$$\delta_i = \delta_{0P} - 2n_0 e + 2 \Delta_i \quad (24)$$

where the subscript 0 corresponds to the condition without a flow.

Taking (22) into account, we have :

$$\delta_i = \delta_{0P} + 2(n - n_0)e + 4(n_i - n) \sqrt{r_i^2 - z_i^2} \quad (25)$$

For a reference point R in the field,

we get :

$$\delta_R = \delta_{0R} + 2(n - n_0)e \quad (26)$$

Subtracting (25) and (26), we obtain :

$$N_{iPR} \lambda = N_{0PR} \lambda + 4(n_i - n) \sqrt{r_i^2 - z_i^2} \quad (27)$$

where :

N_{iPR} : fringe number measured on the interferogram with a flow.

N_{0PR} : fringe number measured on the interferogram without a flow.

The refractive index n_i is deduced from relation (27) and enable us to obtain the corresponding gas density ρ_i according to the Gladstone-Dale relation (7).

Then, using the other equations in (22) we can obtain the other values of n_{i-m} corresponding to different point P_{i-m} .

3 - Holographic Interferometry

3.1 - Introductory remarks

I do not intend to describe the principle of holography. This has been done recently very successfully by J.D. Trolinger in Agardograph n°186 on "Laser Instrumentation for Flow Field Diagnostics" to which you should refer for basic information [3]. I would only like to show here how the use of interferometry in the aerodynamic field is improved by this new technique. As to classical interferometry dealt with in chapter 2, it will be assumed that, for aero-engine applications, investigations have to be carried out in a cavity which can be close by one window on a single side.

3.2 - How to modify Michelson interferometer for holographic purposes

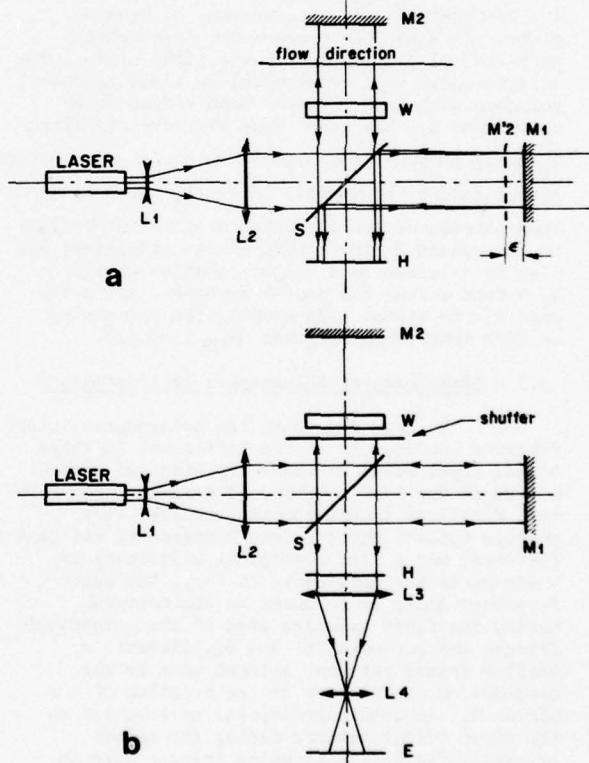


Figure 6 - Holographic interferometer optical diagram derived from a Michelson.

- a) Hologram recording
- b) Interferogram reconstruction.

Let us consider, on figure 6a, an interferometer of the Michelson type, similar to that shown on figure 1, but from which lenses L_3 and L_4 have been removed. Mirror M_2 is

adjusted in order to achieve finite fringes, that is to say mirror M_1 is not parallel to image mirror M'_2 and they are set at an angle ϵ . On a plane H , 2ϵ is the angle between the two light waves issuing respectively from M_1 and M'_2 ; thus we get a parallel fringe pattern, the fringe spacing of which is $\lambda/2\epsilon$. This fringe pattern, recorded on a photographic plate, constitutes a hologram.

This kind of interferometer can be used in two ways : stored beam holographic interferometry and double exposure holographic interferometry.

3.2.1 - Stored beam holographic interferometry

The hologram is first recorded on the photographic plate without a flow. After exposure, the plate is removed from the plate holder to be developed and put back exactly in the same place in the plate holder. Then, lenses L_2 and L_4 (fig. 6b) are introduced again; an infinite fringe interferogram of the chamber is obtained on the screen E . A finite fringe interferogram can be obtained just by rotating mirror M_1 (change of the value ϵ). With a flow, the fringes obtained on the screen are distorted and by processing this interferogram, we get N_{IPR} directly as given by relation (20).

3.2.2 - Double exposure holographic interferometry.

Both exposures, without and with a flow, are successively made on the same holographic plate, which is then removed for development purposes and placed back in the plate holder. The interferogram is reconstructed by lighting the hologram with the reference beam reflected by the mirror M_1 , the other beam reflected by mirror M_2 being stopped, for example by means of a shutter placed before the window. Lenses L_3 and L_4 are then introduced and the interferogram is obtained on the screen E . The finite fringe adjustment can also be obtained by a slight rotation of mirror M_1 before making the second exposure. As in the case of the stored beam method, the processing of this interferogram gives N_{IPR} directly.

3.3 - Advantages of holographic interferometry

We have seen that the holographic interferogram corresponds to the difference in shape of the light waves successively with and without a flow in the test chamber. As a result, contrary to a Michelson interferometer, neither very precise optical parts (glass homogeneity and face flatness) nor a fine mechanical adjustment of these parts are necessary. In fact, the interferometer state is recorded on the hologram during the first exposure even if the holographic fringes are not parallel and equidistant. A similar fringe pattern, altered only by the presence of the flow or by the rotation of the mirror M_1 , is then superimposed or recorded on the first fringe pattern during the second exposure. The resulting moiré fringes make it possible to obtain the interferogram on the screen. It may be said that the interferometer state, with its imperfections, was set in memory by the first exposure. Considerable advantages result from these features : as the optical part are less precise and the mechanism simpler, the device is much cheaper, as well as easier to operate. In addition, holographic interferometry offers a great advantage : not only the mirror M_2 in the test chamber does not require a precise optical surface, but it can

even be unpolished, scattering reflected light. This is very useful for aero-engine applications in which it is often difficult, not to say impossible, to introduce an optical surface inside a cavity.

The optical diagram of the holographic interferometer shown on figure 6 was chosen for the purpose of an easier comparison with the Michelson interferometer. But, with holography, there is no need to expand the reference beam. Many other optical arrangements are thus possible; figure 7 shows an example thereof. The laser beam is divided in two parts by the beam splitter S_1 . The reference beam, reflected by S_1 is successively reflected by mirrors M_2 , M_3 and M_4 , and enlarged by the diverging lens D towards the holographic plate H . The beam designated by the expression "object beam", is transmitted by S_1 , enlarged by the telescopic system including a diverging lens L_1 and a converging lens L_2 , and reflected to the test chamber by the beam splitter S_2 ; this chamber is closed, on one side, by the transparent window W and, on the other by the mirror M_1 . The "object beam", reflected by the latter mirror is transmitted through the window and through the beam splitter S_2 and falls on the holographic plate where it interferes with the "reference beam" to form the holographic fringe pattern. The stored beam and the double exposure methods are both possible with this interferometer and lenses L_3 and L_4 make it possible to obtain real time or reconstructed interferograms on the screen E .

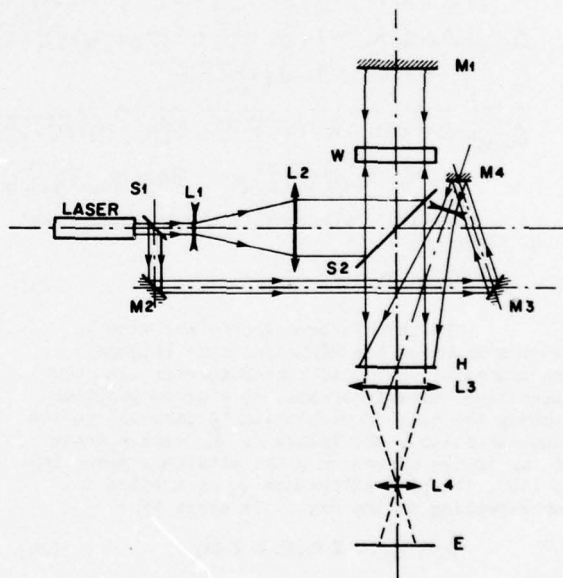


Figure 7 - Holographic interferometer with an unexpanded reference beam.

4 - Application in the Field of Aero-Engine Studies.

The main modern aero-engines are turbo-machines including compressors within which the flow velocity gets increasingly higher, reaching transonic and supersonic domains. It becomes very difficult, if not impossible, to use classical probes for aerodynamic measurements (pressure, temperature, flow velocity) without creating disturbances. In spite of difficulties

due to environmental conditions (vibrational and thermal noises, difficult access), considerable efforts were made to develop optical methods, mainly because they are non-intrusive [4].

In such flows, gas compressibility effects, leading to density changes, require the use of optical methods based on the determination of refractive index variations (interferometry), or of the associated refraction of rays of light (shadowgraphy and schlieren). As a first attempt to study the flow field near and between the blades, experiments were conducted on plane stationary blade cascades [4], [5]. In such cascades, the flow is approximately two-dimensional and all the optical methods can be used as easily as in wind tunnels. An example of such a flow field is shown on figure 8. Visualization is achieved by schlieren methods; coloured schlieren pictures were used but the photograph reproduced here is in black and white. Such a picture provides a means to measure the shape and the angle of incidence of the shock wave and to deduce the Mach number in some points. The limits of the transition between the laminar and the turbulent flow can also be seen. With the flow velocity or the mass flow rate as a parameter, the stability regimes are determined. Besides, as the conditions are two-dimensional, interferometry makes it possible to measure the density flow field.



Figure 8 - Schlieren photograph of the flow field in a plane stationary blade cascade.

However, such a model takes no account of the helicoidal flow effect occurring in a real compressor. Therefore, additional experiments were conducted on an annular stationary blade cascade [6]. The hub carrying the blade is a polished cylinder; visualization is effected in front of a window with cylindrical faces concentric with the hub. A special schlieren device with cylindrical lenses makes it possible to get coloured or black and white flow field pictures as shown on figure 9. It is also possible to use a holographic interferometer, even with an unpolished hub, which would make it possible to measure the approximately two-dimensional density field. However, difficulties are created by the thermal effects appearing on the hub during the run [7]. The dilatation of the unpolished hub surface is such that it is impossible to use double exposure holographic interferometry, making the first exposure before starting the flow and the second during the run.

To reduce these thermal disturbance effects, two other methods can be applied, using a pulse laser (Q-switched ruby laser) as a light source. The first method consists in making both exposures immediately one after the other during

the run. As the flow is not perfectly stationary, the shock wave positions are slightly different for each exposure, and reconstructed differential interferogram shows the shock wave and the turbulent region of the flow. With the other method, the first exposure is made during the run. Then the flow is rapidly stopped and the other exposure is made afterwards.



Figure 9 - Schlieren photograph of the flow field in an annular stationary blade cascade.

The following step is the study of a single rotor with short blades where the flow is approximately two-dimensional. In this case, visualization was achieved with a cylindrical schlieren system [8]. A small part of the rotor was polished and a pulse light source, synchronized with the position of this polished part, was used. Schlieren pictures can be taken for different positions of the rotor in front of the window, by means of a delay line. For various flow conditions, the bow shock, the interblade shock and the turbulent regions can be seen. Pulsed laser holographic interferometry could be used for measurements of the density field but this possibility was not investigated.

Schlieren pictures of a rotor in freon gas are shown on figure 10, and figure 11 shows the flow within the stationary diffuser of a centrifugal compressor.

Finally, experiments were conducted on rotors with long helicoidal blades. In this case, the flow is essentially three-dimensional and even by resorting to interferometry, it is impossible to reconstruct the flow density field. However, the observation of shock waves and turbulent regions remains a very important objective.

A special device was built by ONERA to study the flow inside a rotor rotating in freon gas. Bow shocks near the leading edges of the blades are visualized by shadowgraphy, shock shadows being projected on a screen (scotchlite) glued on the interblade face of the rotating hub. With a special dual channel shadowgraph using spark lamps, two images can be made from two viewing angles in order to reconstruct the bow shock shape stereoscopically [9]. Such a pair of stereoscopic images is shown on figure 12. Interesting experiments were also conducted with real compressor by several U.S. teams on behalf of NASA. They built a holographic interferometer

with a double pulse light source. This source is a Q-switched ruby laser with a 10 microsecond pulse interval. Each pulse produces a hologram on the photographic plate, the blades being slightly shifted by the rotor motion. As the laser light is reflected on the diffuse face of a stationary hub, it is possible to reconstruct several differential interferograms from the hologram illuminated with a helium neon laser. These interferograms show the bow shocks generated by the blade leading edges, from different viewing angles. The three-dimensional shape of the shock waves can then be reconstructed.

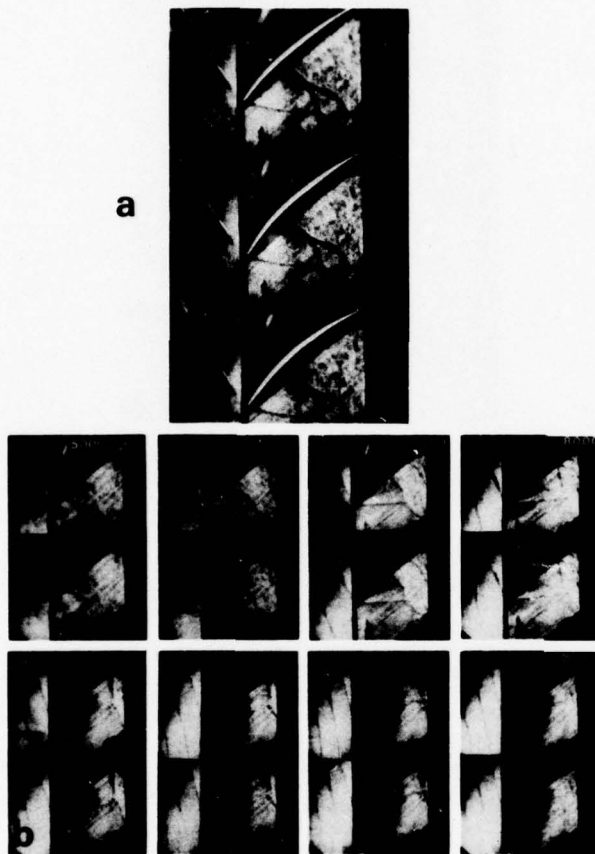


Figure 10 - Schlieren photograph of the flow field in a rotating blade cascade in freon gas.

- a) Supersonic flow. Rotation speed 6000 r.p.m.
- b) Sequence of pictures for different rotation speed.

5 - Optical Measurements in Flames

5.1 - Introductory remarks

Physical and chemical measurements in hot reactive media, such as flames, are difficult to perform. The use of material probes such as thermocouples, pressure gauges, sampling probes is generally ruled out not only because they could be rapidly destroyed, but also because they disturb hot gas flows and chemical compositions. The non-intrusive nature of optical methods, due to the weak interaction between light and gases, is therefore appreciated in this domain.

Interferometric methods could be applied to



Figure 11 - Schlieren photographs of the flow field in the stationary diffuser of a centrifugal compressor. Constant rotation speed : 8000 r.p.m., variable mass flow rate.

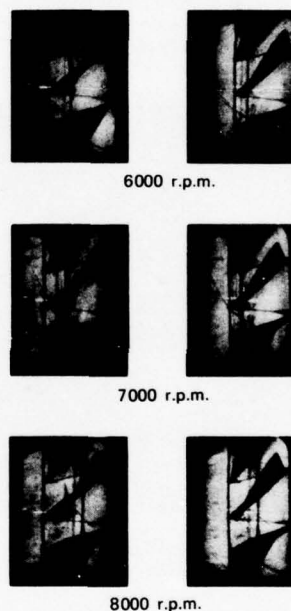


Figure 12 - Stereoscopic images couple from which bow shock shape can be reconstructed.

determine density distribution, but their disadvantage lies in the fact that they provide only integrated values along the light path within the flow which is most often three-dimensional.

Scattering optical methods provide means to carry out local measurements inside a medium, and are therefore suited to this field of research.

5.2 - Light scattering in a gas medium

An intense light beam propagating in the air becomes visible from all directions, due to scattering. The main part of the scattered light has the same colour as the incident light beam itself : one part, called Mie scattering,

originates from particles (dust or liquid droplets) present in the air, and another Rayleigh scattering, from gas molecules. Most often, in unfiltered gas, Mie scattering is several orders of magnitude higher than the Rayleigh scattering. Spectral analysis, conducted with a spectrograph (fig.13), shows weak lines appearing on each side of the Mie and Rayleigh intense lines. These Raman lines which are less intense than the latter by several orders of magnitude, are caused by molecular vibrations.

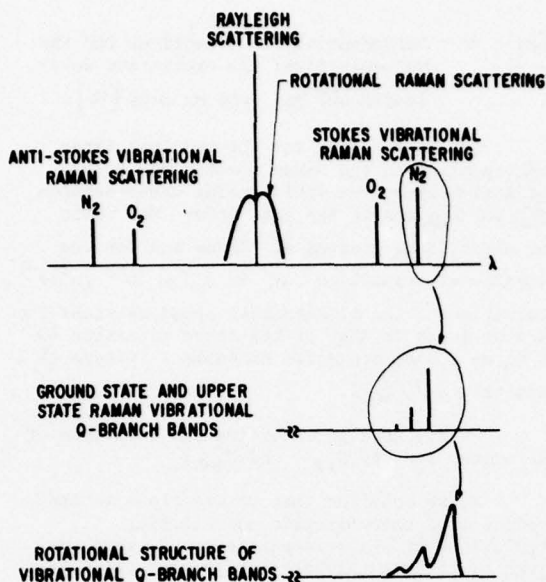


Figure 13 - Schematic of Rayleigh, rotational Raman, and vibrational Raman scattering. Shown in detail is the splitting of the vibrational Stokes Raman signal for nitrogen into a series of fundamental vibrational bands (ground state band, first upper state or "hot" band, second upper state band, etc.). Also shown is the spreading out of this fundamental vibrational band series due to rotational structure, as would be viewed by a typical laboratory double monochromator. From M. Lapp [4].

A high dispersive spectrograph shows that each line is resolved in several components: the rotation Raman lines. If we take the wavenumber (reciprocal of the wavelength commonly measured in cm) as the spectral measuring scale, the Mie and Rayleigh scattered lights have the same wavenumber as the incident light. For a given gas, the vibration Raman lines have (Stokes line) and (Anti-Stokes line) as wavenumbers; characterizes the gas molecule.

A number of values are given on table 1 (fig.14) for several molecular gases; these values range approximately from 1000 to 4000 cm^{-1} . The spacing between the rotation lines is of the order of 10 cm^{-1} or less.

MOLECULE	$\Delta\nu$ cm^{-1}	λ pour $\lambda_0 = 488$ (nm)	Rotational constant B cm^{-1}	σ/σ_{N_2}
N_2	2 331	550.6	2.010	1.0
O_2	1 556	528.1	1.4456	1.3
H_2	4 161	612.3	60.8	2.4
CO	2 145	545.1	1.931	1.0
NO	1 877	537.2	1.7046	0.27
CO_2 (ν_1)	1 388	523.5	0.390	1.4
CO_2 ($2\nu_2$)	1 286	520.7		0.89
SO_2 (ν_1)	1 151	517.0		5.2
SO_2 (ν_2)	519	500.7		0.12
N_2O (ν_1)	1 285	520.6		2.2
N_2O (ν_3)	2 224	547.4	0.419	0.51
H_2S	2 611	559.3		6.4
NH_3	3 334	582.8		5.0
ND_3	2 420	553.3		3.0
CH_4	2 914	568.9		6.0
C_2H_6	993	512.9		1.6
C_6H_6 (ν_1)	3 062	573.7		7.0
C_6H_6 (ν_2)	992	512.8		9.1

Figure 14 - Table of the Raman characteristics of various species.

$\Delta\nu$: Raman wavenumber shift.

λ : Raman wavelength of the Stokes vibrational line with an excitation radiation at 488 nm.

B : Rotational constant.

σ/σ_{N_2} : Ratios of differential lines to that of the ν_1 vibration in N_2 at 488 nm.

Let us consider (fig.15) a light beam, whose power is P, propagating in the gas to be analysed. If A designates the beam cross section, each molecule receiving the power density P/A acts as a light source whose intensity is given by :

$$i = \frac{P}{A} \frac{d\sigma}{d\Omega} = \frac{P}{A} \sigma \quad (5.1)$$

$\frac{d\sigma}{d\Omega}$: differential scattering cross section, designated, more simply, by σ .

Assuming that the medium is optically thin, for all the molecules contained in a volume V of

the beam, the total intensity I_T is given by :

$$I_T = iNV = iNAL \\ = PLN\sigma \quad (5.2)$$

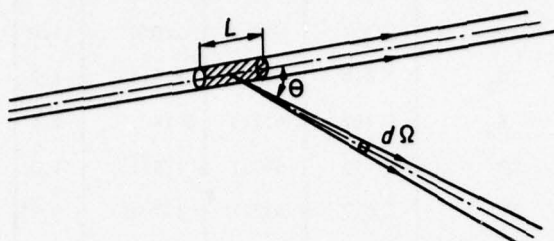


Figure 15 - Diagram of the scattered light.

In this relation, $N\sigma$ includes all the interaction processes between light and the gas, that is to say, $N\sigma$ is the sum of the following terms :

$$N\sigma = N_{RAY}\sigma_{RAY} + N_{SR}\sigma_{SR} + N_{ASR}\sigma_{ASR} \quad (5.3)$$

representing respectively each of the following processes : Rayleigh, Stokes Raman, Anti-Stokes Raman.

The first of these terms is the highest, not only because the differential Rayleigh cross section is higher than the Raman one, but also because the number density corresponding to the Rayleigh scattering is higher than that of Raman : the transition probability for $\Delta v = 0$ is higher than for $\Delta v = \pm 1$ (figure 16).

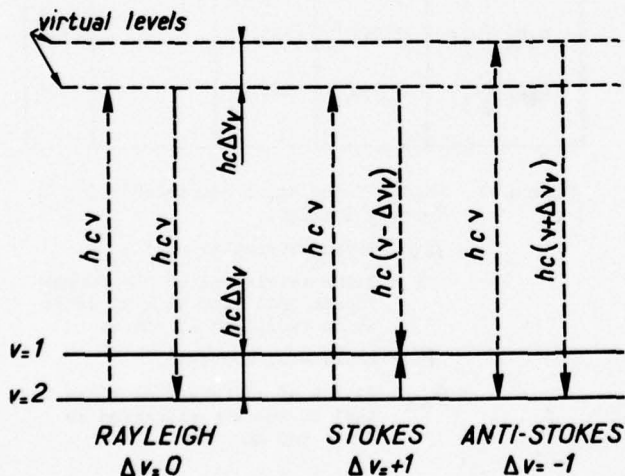


Figure 16 - Energy diagram of the vibrational transitions for Rayleigh and Raman scattering.

All the quantities σ are strongly wavenumber dependent; they vary as the fourth power of the wavenumber. We can then introduce in relation (5.3) a factor q which is the ratio of the wavenumber considered to the wavenumber for which was measured :

$$N\sigma = q_{RAY}^4 N_{RAY}\sigma_{RAY} + q_{SR}^4 N_{SR}\sigma_{SR} + q_{ASR}^4 N_{ASR}\sigma_{ASR} \quad (5.4)$$

The table on figure 17 gives as example the approximate magnitudes of the differential

cross sections for molecule N_2 excited by an ionised argon laser on the blue line ($\lambda = 488 \text{ nm}$, $\nu = 20,492 \text{ cm}^{-1}$).

Rayleigh	- $10^{-27} \text{ cm}^2/\text{sr}$
Rotational Raman (all lines)	- 10^{-29}
Rotational Raman (strong line, including fractional population factor at room temperature)	- 6×10^{-31}
Vibrational Raman (Stokes Q-branch)	- 5×10^{-31}

Figure 17 - Differential cross-sections for the molecule N_2 at the excitation wavelength 488 nm. From M. Lapp [14].

Let us consider now the two last terms corresponding to the Raman scattering: Stokes and Anti-Stokes. The differential cross-section σ_{SR} and σ_{ASR} are of the same order. The value for molecule N_2 excited at 488 nm and for the vibrational transition ν_1 is $3.3 \times 10^{-31} \text{ cm}^2 \text{ sr}^{-1}$. The ratios of the differential cross-sections for various gases to that of the above vibration ν_1 in N_2 at 488 nm are given on table 1 (figure 14, last column σ/σ_{N_2}).

We now have to determine the influence of the number density N_{SR} and N_{ASR} .

If we consider that we are close to the condition of thermodynamic equilibrium, populations of the different energy levels are given by the Maxwell-Boltzmann distribution law. If we relate the vibration, population N_ν of the ν level to the population N_0 of the lowest level ($\nu = 0$), we have :

$$N_\nu = N_0 e^{-\Delta E/kT_\nu} = N_0 e^{-G(\nu)hc/kT_\nu} \quad (5.5)$$

with :

- h : Plank constant
- c : light velocity
- k : Boltzmann constant
- T : absolute vibration temperature

and :

$$G_0(\nu) = a\nu - b\nu^2 \quad (5.6)$$

The total molecule number N corresponds to the sum of the populations for all the vibration states. With the populations N_0 of the lowest level, as a reference, it is called partition function Q_ν and is given by :

$$\frac{N}{N_0} = Q_\nu = 1 + e^{-\frac{G_1(\nu)hc}{kT_\nu}} + e^{-\frac{G_2(\nu)hc}{kT_\nu}} + \dots \quad (5.7)$$

Therefore, the number of molecules N_ν in a state ν is :

$$N_\nu = \frac{N}{Q_\nu} e^{-\frac{G_\nu(\nu)hc}{kT_\nu}} \quad (5.8)$$

The diatomic molecule vibrations can be considered, in a first approximation, as those of an harmonic oscillator. In this case, relation (5.6) to (5.8) become :

$$G_0(\nu) = \nu \Delta \nu_\nu \quad (5.9)$$

$\Delta\nu_v$: wavenumber vibration Raman shift

$$Q_v = (1 - e^{-hc\Delta\nu_v/kT_v})^{-1} \quad (5.10)$$

$$N_v = N e^{-\frac{v h c \Delta\nu_v}{k T_v}} (1 - e^{-\frac{h c \Delta\nu_v}{k T_v}}) \quad (5.11)$$

Several rotation levels correspond to each vibration level. Then, the number of molecules $N_{v,J}$ of a vibration level v is distributed over the rotation levels in such a manner that the population of a level J is :

$$N_{v,J} = \frac{N_v}{Q_r} (2J+1) e^{-BJ(J+1)hc/kT_r} \quad (5.12)$$

Where the rotation partition function Q_r has the approximate value :

$$Q_r = \frac{kT_r}{hcB} \quad (5.13)$$

T_r : absolute rotation temperature

B : rotation constant.

Therefore, the population of a vibration-rotation level $N_{v,J}$ is given by :

$$N_{v,J} = \frac{N(2J+1)hcB}{kT_r} e^{-\frac{hc\Delta\nu_v}{kT_v}} e^{-\frac{BJ(J+1)hc}{kT_r}} \quad (5.14)$$

The number densities $N_{v,R}$ and $N_{v,S,R}$ appearing in relations (5.3) and (5.4) correspond to the number of energy transition per unit volume from a lower state to an upper state as far as the first one is concerned and, inversely, from the upper to the lower state, as far as the second one is concerned; the former, $N_{v,R}$, is proportional to the population of the lower state and the latter, $N_{v,S,R}$, is proportional to the population of the upper state.

As regards the vibration transitions $v=0$ to $v=1$, which are about the only ones created at temperatures less than 1000°K, we get the Stokes and Anti-Stokes intensities according to (5.2), (5.4) and (5.11)

$$I_s = CPL \left(\frac{v - \Delta\nu_v}{v_0} \right)^4 \sigma_0 N (1 - e^{-hc\Delta\nu_v/kT_v}) \quad (5.15)$$

$$I_{AS} = CPL \left(\frac{v + \Delta\nu_v}{v_0} \right)^4 \sigma_0 N e^{-\frac{hc\Delta\nu_v}{kT_v}} (1 - e^{-\frac{hc\Delta\nu_v}{kT_v}}) \quad (5.16)$$

C : proportionality constant

σ_0 : differential Raman cross-section measured for $v = v_0$.

Then, the Stokes and Anti-Stokes intensity ratio is :

$$\frac{I_s}{I_{AS}} = \left(\frac{v - \Delta\nu_v}{v + \Delta\nu_v} \right)^4 e^{\frac{hc\Delta\nu_v}{kT_v}} \quad (5.17)$$

Let us now consider the rotation transitions which are only allowed by selection rules for $\Delta J = 0$ (Q -branch) and $\Delta J = \pm 2$ (S and O branches). The rotational Raman shift would be cancelled for all the transitions $\Delta J = 0$ if B was a constant. However, due to the vibration-rotation coupling, B is a function

of v given by :

$$B_v = B_e - \alpha_e \left(v + \frac{1}{2} \right) \quad (5.18)$$

Where the constant α_e is small compared to the constant B_e . For the Stokes transition $v=0$ to $v=1$, the Raman rotation shift, corresponding to the branch is :

$$\Delta\nu_v = (B_1 - B_0) J(J+1) = -\alpha_e J(J+1) \quad (5.19)$$

This corresponds to a series of lines for all the values J whose intensities, according to (5.2), (5.4) are :

$$I_s(0,J) = CPL \left(\frac{v - \Delta\nu_v}{v_0} \right)^4 \sigma_0 N_{0,J} \quad (5.20)$$

With, according to (5.14) :

$$N_{0,J} = \frac{N(2J+1)hcB(1 - e^{-\frac{hc\Delta\nu_v}{kT_v}}) e^{-\frac{BJ(J+1)hc}{kT_r}}}{kT_r} \quad (5.21)$$

On figure 18, an example is given for the molecule N_2 at temperatures 300°K, 1000°K and 3000°K. We see that the envelope curve of the lines reaches a peak value whose spectral position is temperature dependent, and that the spectral half-width of this curve is also a function of the temperature.

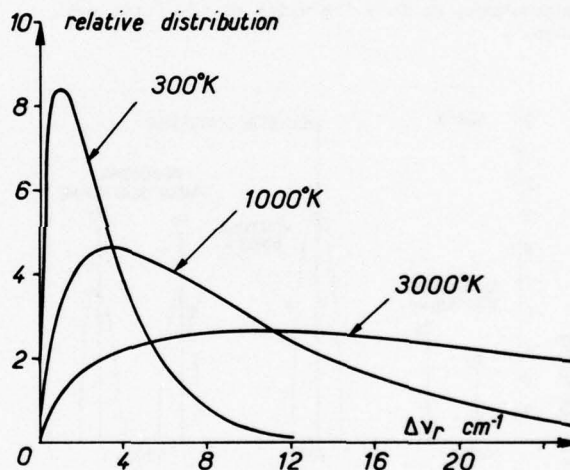


Figure 18 - Relative distribution of the rotational levels for $B = 2.01 \text{ cm}^{-1}$ (molecule N_2) and $T = 300^\circ\text{K}$, 1000°K and 3000°K .

As for the other allowed transitions $\Delta J = \pm 2$, we get a line series on each side of the Rayleigh line ($\Delta v = 0$) and Raman lines ($\Delta v = \pm 1$). The wavenumber shifts for each series are given by :

$$|\Delta\nu_r| = F(J+2) - F(J) = 4B(J + \frac{3}{2}) \quad (5.22)$$

with :

$$F(J) = BJ(J+1) \quad (5.23)$$

The intensity value for the lines J of each series are given by :

- Stokes rotation wing of the Rayleigh line.

$$\left| \begin{aligned} \nu_s(0,J) &= \nu_{ex} - 4B(J + \frac{3}{2}) \\ I_{rs}(0,J) &= CPL \sigma_{RAY} N_{0,J} \end{aligned} \right. \quad (5.24)$$

: wavenumber of the excitation line.

- Anti-Stokes rotation wing of the Rayleigh line.

$$\begin{cases} \nu_{AS}(0,J) = \nu_e + 4B(J + \frac{1}{2}) \\ I_{AS}(0,J) = CPL \sigma_{RAY} N_{0,J+2} \end{cases} \quad (5.25)$$

- Stokes rotation wing of the Stokes line $\nu = 1$:

$$\begin{cases} \nu_s(1,J) = \nu_e - \Delta\nu_v - 4B(J + \frac{1}{2}) \\ I_{sS}(1,J) = CPL \left(\frac{\nu_e - \Delta\nu_v}{\nu_e} \right)^4 \sigma_0 N_{0,J} \end{cases} \quad (5.26)$$

- Anti-Stokes rotation wing of the Stokes line $\nu = 1$:

$$\begin{cases} \nu_{AS}(1,J) = \nu_e - \Delta\nu_v + 4B(J + \frac{1}{2}) \\ I_{AS}(1,J) = CPL \left(\frac{\nu_e - \Delta\nu_v}{\nu_e} \right)^4 \sigma_0 N_{1,J+2} \end{cases} \quad (5.27)$$

and so on for the wings of the Anti-Stokes vibration line.

Figure 19 shows, schematically, the Raman and Rayleigh scattering lines for molecules N_2 and O_2 observed in the air at two different temperatures 300°K and 1000°K. On each side of the Rayleigh and vibration Raman lines, the envelope curves of the rotation lines are drawn. We see that the Anti-Stokes-to-Stokes vibration lines intensity ratio increases with the temperature; so does the width of the rotational wings.

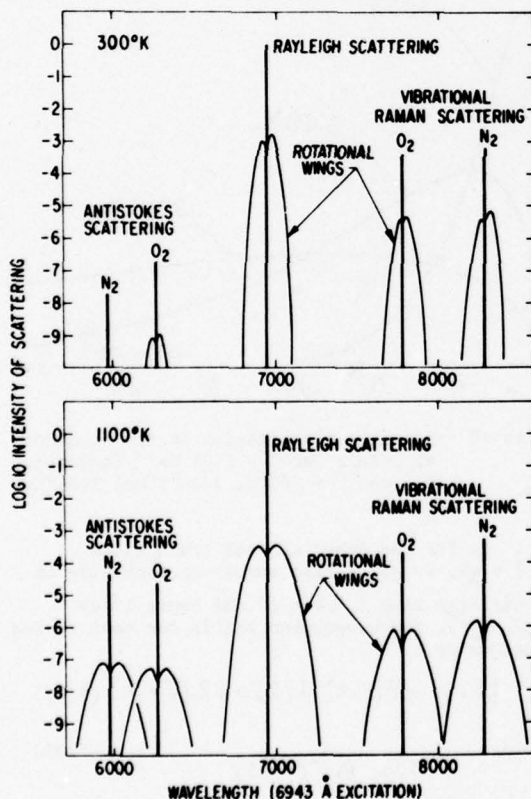


Figure 19 - Raman and Rayleigh scattering for air, drawn roughly to scale, at room temperature and 1100°K. To the scale of this drawing, ground state and upper state fundamental vibrational Raman bands are not distinguishable. From M. Lapp [14].

As mentioned above, at low temperatures, the populations of vibration levels higher than $\nu = 1$ are negligible. For higher temperature (about >1500°K) the populations of vibration levels $\nu = 2, \nu = 3, \dots$ become significant. Thus, if we apply the selection rule $\Delta\nu = +1$, we have to take account of other transitions such as $\nu = 1$ to $\nu = 2$, $\nu = 2$ to $\nu = 3$ and so on, each of them being associated with the rotation series. For example, for the rotation Q branch ($\Delta J = 0$) and Stokes vibration transition $\nu = 1$ to $\nu = 2$, we obtain from (5.6), (5.14) and (5.19):

$$\begin{cases} \nu_{sQ}(1,J) = \nu_e - \alpha + 3\beta + \alpha_e J(J+1) \\ I_{sQ}(1,J) = CPL \left(\frac{\nu_e - \Delta\nu_v}{\nu_e} \right)^4 \sigma_0 N_{1,J} \end{cases} \quad (5.28)$$

Figure 20A shows the envelope curves of the N_2 Q-branch at a temperature of 2000°K, calculated for successive lower levels 0,1,2,3, and figure 20B shows the resulting envelope curve of the whole Q-branch, when analysed with a finite resolution spectrograph. The influence of temperature on the shape of this envelope curve is shown on figure 21, for temperatures ranging from 300°K to 3500°K.

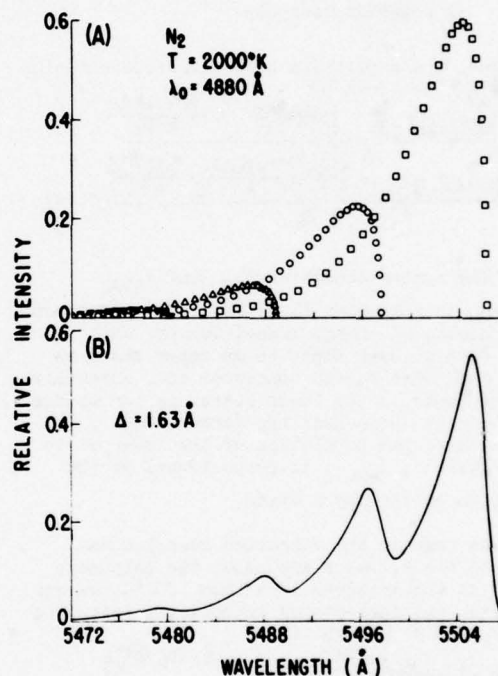


Figure 20 - Calculated Stokes vibrational Q-branch intensity at 2000°K for nitrogen. (A) Alternate "strong" line intensities. The square data points correspond to the ground state band, the circular points to the first upper state band, the open triangular points to the second upper state band, etc. (B) Triangular slit function convoluted profile, where Δ is the spectral slit width (FWHM). From M. Lapp [14].

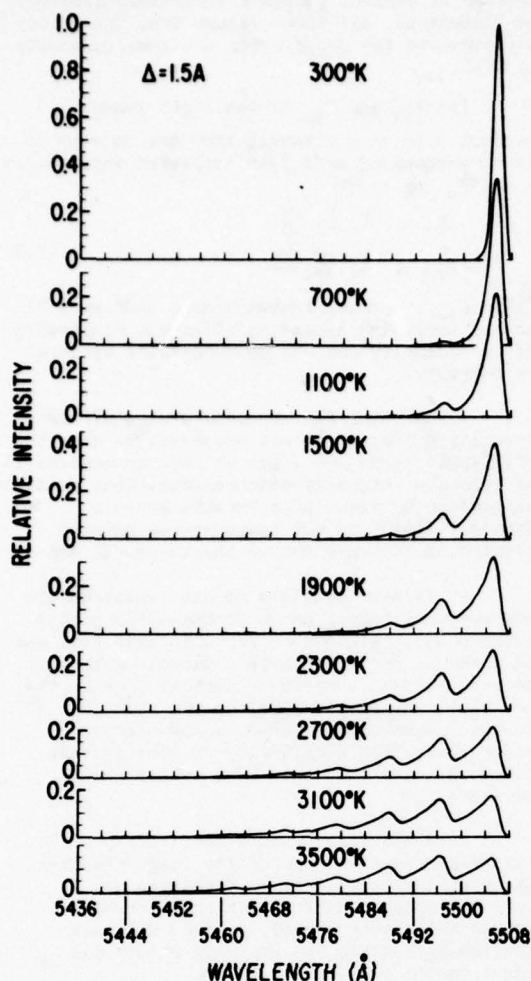


Figure 21 - Calculates Stokes vibrational Q-branch intensity for nitrogen from 300°K to 3500°K.

5.3 - Potential use of Raman scattering for temperature and density measurements

As explained above, all the Raman intensities are both temperature- and density-dependent. Therefore, they could be used to measure these quantities. But, unless one of them is otherwise known, which is difficult in hot gases, we have to find means to separate these two values. Let us review some of these means.

5.3.1 - Rotational wings of the Rayleigh line

Among all the rotational line series, both Stokes and Anti-Stokes wings of the Rayleigh line are the most intense as they are the nearest to the ground state (figure 19).

By selecting two lines in the same wing (S. or A.S.) and measuring their intensity ratio, we obtain values which are only functions of the rotational temperature. Then, based on these values and on the measurement of the integrated intensity of the whole band, we can deduce the number density.

This method requires a high resolution dispersive set-up (spectrograph or filters) to resolve the rotation lines, and then the measured intensities are very low. In fact, it is not

absolutely necessary to resolve these lines. If we select two spectral bands including several lines, we can obtain their intensity ratio, and the measured intensities are higher. By means of a spectrograph, it is also possible to record the whole unresolved band and to determine the shape, width or peak intensity spectral positions which are all functions of the rotational temperature.

Though it seems attractive, this method requires very selective filters or a spectrograph without spray light, to select spectral bands very efficiently blocked to the excitation wavelength side, for the near Rayleigh and Mie radiations are much more intense.

This method can only be used with a pure gas. In the case of a gas mixture, the rotational bands are very near each other and even overlap. Then, it becomes difficult to find two separate spectral bands, characteristic of a given gas, permitting temperature measurements without interference with another gas, and due to this overlapping, number density measurements for each species become impossible.

Sometimes, fluorescent species are mixed in the gas. In this case, it is better to use both spectral bands for temperature measurement and the whole band for density measurement on the A.S. side of the Rayleigh line; the fluorescent light is mainly dispersed to the S. side.

5.3.2 - Vibrational-rotational Raman bands

Vibrational-rotational bands for different species are more distant from each other than the rotational bands of the Rayleigh line; therefore, for common gases, the overlapping is less frequent.

As they are further from the excitation line, the intensities are smaller, but the spectral blocking is much easier. Since, in addition, the spectral bandwidths are larger, the spectral purity requirement of the dispersive set-ups (spectrograph or filters) is not so strong, therefore, the transmittance is improved which compensates partially for the intensity lost.

At low temperatures the A.S. side bands are so weak that they are useless (figure 19).

Then, let us consider the Stokes band whose Q-branch is the most intense. As shown on figure 21, even if each rotation line is unresolved, the envelope curve of this Q-branch varies with the temperature in shape, spectral extension, and number of peaks. All these properties may lead to the implementation of a temperature measuring method.

At low temperatures ($< 1000^{\circ}\text{K}$), vibrational transitions other than from $v=0$ to $v=1$ are negligible: a single peak appears. Methods related to the shape of the curve are used: half intensity width determination or measurement of the curve slope near the half-height. Vibrational temperatures are thus obtained either by comparison with calculated results or by experimental calibration, for different known temperatures. In this temperature range (0 to 1000°K), the integrated light intensity received through a filter which is approximately 16 Å wide (between 5492 and 5508 Å for nitrogen, as shown on figure 21) is independent of the temperature; this intensity can be used to measure the number density.

At higher temperatures, on the one hand, the A.S. band intensity becomes significant,

and on the other hand, the number of transitions $\nu = 1$ to $\nu = 2$, $\nu = 2$ to $\nu = 3$,... (hot bands) increases, and additional peaks appear in the Q-branch.

Through filters transmitting the whole bands, S. and A.S. intensities are measured, whose ratio I_S / I_{AS} is a function of the vibrational temperature as given by (5.16). The S. band measured intensity is independent of the temperature and permits the determination of the number density. As shown on figure 21, in the case of nitrogen, the filter bandpass has to be about 30 Å for temperatures less than 2000°K and about 50 Å for temperatures less than 3500°K.

Another method of determining temperatures consists in the intensity ratio of the two highest peaks in the Q-branch. But this method necessitates very narrow filters (about 2 Å wide for nitrogen, as shown on figure 20), so that the measured intensities are much lower than with the previous method.

5.4 - Application to studies on hot gases and reactive media

An experimental system for Raman scattering application is schematically shown on figure 22.

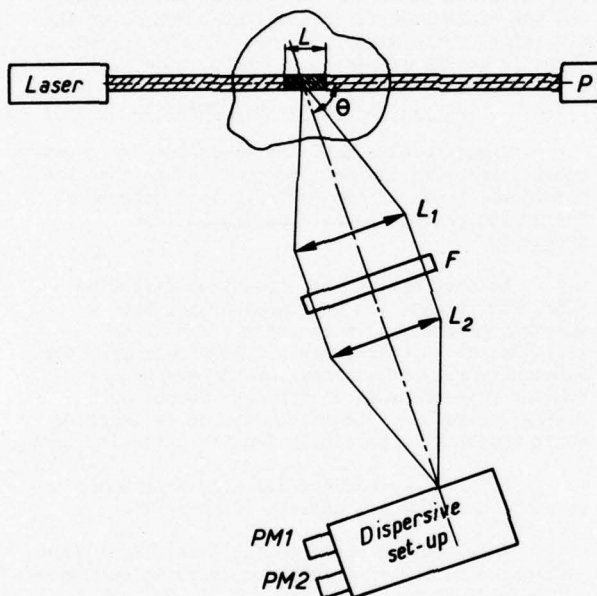


Figure 22 - Optical diagram of a spontaneous Raman scattering device.

A laser beam crosses the gas medium to be analyzed. An optical system, whose axis forms an angle θ with the incident light beam, collects the scattered light inside a solid angle Ω . A prefilter F, introduced between lenses L_1 and L_2 , rejects part of the unwanted light coming from luminous surroundings, gas emissions, Rayleigh and Mie scattering, fluorescence... An image of the laser beam is formed on the dispersive set-up entrance slit; its width determines the suitable beam interaction length L. The dispersive set-up may be a prism or a grating spectrograph, interferential filters or even, if necessary, for high resolution, a Fabry-Pérot interferometer. Two bandwidths (or more) are selected, the spectral light from each of them being respectively collected on the photoreceivers PM_1 and PM_2 . A laser power meter P measures the incident light

in order to correct possible variations during the experiment. All three values from the photoreceivers and the power meter are simultaneously recorded.

Let P_{R1} and P_{R2} be the light powers received from each channel; they are related to the corresponding efficient scattered intensities I_1 and I_2 , by :

$$\begin{aligned} P_{R1} &= \tau_1 I_1 \Omega \\ P_{R2} &= \tau_2 I_2 \Omega \end{aligned} \quad (5.29)$$

τ_1 and τ_2 : optical transmittance over each channel including lenses, prefilters, dispersive set-up transmittance and photodetector spectral responsivity.

We see that for measurements requiring an intensity ratio, it is not necessary to know the solid angle value Ω ; but we have to measure it for absolute intensity measurements. When possible, calibration by means of reference gases at different densities and temperatures permits avoiding the measurement of the values τ and Ω .

It is also possible to use spectrograph with spectrum recording on photographic plates. Suitable spectral domains are then selected, and the plate is processed with a microdensitometer. The main advantage of these methods lies in the fact that they permit simultaneous recording of all the traces of species in a gas mixture. Nevertheless, the sensitivity of photographic plates is lower than that of the best photoreceiver.

To avoid this loss of sensitivity while preserving the advantage of the image receiver, highly efficient television tubes can now be used. The image can be either transferred to a monitor and photographed, or recorded on a magnetoscope; also, the scanning electrical signal can be sent to a recorder.

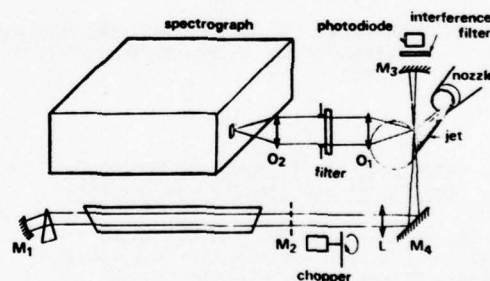


Figure 23 - Lay-out with the measuring volume inside the laser cavity. The plane mirror M_2 of the laser cavity is removed and replaced by a system including the lens L, the folding mirror M_4 and the spherical mirror M_3 . From S. Druet and al. [17].

As regards the laser source, since the scattered light is weak, very intense lasers are needed. Owing to the strong dependence of the differential cross-section on the excitation radiation wavelength, the shortest wavelength seems to be the best. But, when the violet and ultraviolet spectral regions are reached, more species become highly fluorescent and some of them emissive. Thus, these unwanted lights degrade the signal-to-noise ratio. If we take account of the photoreceiver or photographic spectral sensitivity

and of the rejection of the unwanted light, the best spectral region for the excitation laser is near the blue and green. Among continuous lasers, it is the argon ionised laser with its 488 nm blue and 514.5 nm green lines which produces powers over 10 W. With such a continuous laser, the useful power can be still improved if we remove one of the cavity reflectors, and replace it by a lens and a mirror on each side of the measuring volume (figure 23). Thus, a power gain of more than 10 is obtained within the interaction field.

For a pulse laser with very high power and short pulses, a frequency doubled ruby (347 nm) and a frequency doubled neodymium (530 nm) are the most commonly used.

Continuous or pulsed dye lasers are now commonly used for every wavelength required.

5.5 - Coherent Anti-Stokes Raman scattering

The main experimental difficulty encountered in spontaneous Raman scattering, as described above, arises from the weakness of the efficient light power as compared to the incident power: not only the interaction process is weak but also the light is scattered in every direction and can only be collected in a finite solid angle.

A new method, called "Coherent Anti-Stokes Raman Scattering" improves the efficiency by several orders of magnitudes. Two monochromatic beams of respective wavenumbers ν_1 and ν_2 ($\nu_1 > \nu_2$) are mixed by means of a beamsplitter S (figure 24) in order that they may be exactly superimposed and propagate in the same direction. The resulting two-frequency beam is focused by the lens L_1 on the gas to be analysed, crosses the lens L_2 , the filter F and falls on a photoreceiver.

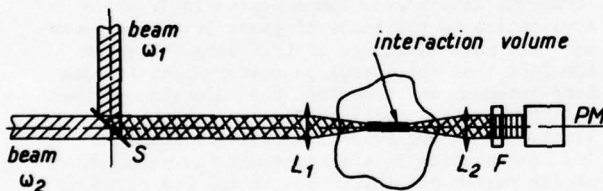


Figure 24 - Experimental lay-out of a "coherent Anti-Stokes Raman scattering" system to measure the local temperature and number density in a gas mixture.

As the gas contains a species whose vibrational transition ($\nu = 0$ to $\nu = 1$) is exactly $\nu_\nu = \nu_1 - \nu_2$, a strong interaction process occurs, mainly near the focus of the lens L_1 , where the power density is the highest; a new light wave is generated whose wavenumber is $\nu_3 = 2\nu_1 - \nu_2 = \nu_1 + \nu_\nu$; it propagates in the same direction as both incident waves. Through the filter F, radiations ν_1 and ν_2 are rejected and ν_3 is transmitted, and falls on the photodetector. If ν_1 is considered as the excitation radiation in a Raman scattering process ($\nu_1 = \nu_2$), ν_2 is in the position of the Stokes line ν_3 and ν_3 in the position of the Anti-Stokes line ν_{AS} .

If P_{ex} and P_S are the respective incident powers for the excitation and Stokes radiations, the Anti-Stokes power P_{AS} received by the photodetector is given by

$$P_{AS} = \tau \left(\frac{16\pi^3 \nu_{ex} \nu_{AS}}{c} \right)^2 P_{ex}^2 P_S |\chi|^2 \quad (5.30)$$

τ : filter transmittance

χ : nonlinear susceptibility including two terms such as:

$$\chi = \chi_R + \chi_{NR} \quad (5.31)$$

χ_R : resonant part of the susceptibility, only contributive near a vibrational-rotational resonance.

χ_{NR} : non-resonant, quasi-constant, part representing the contribution from the electrons and remote resonances.

The resonant susceptibility is a complex quantity; it is a sum of terms for all the vibrational-rotational transitions j involved in the interaction process, given by:

$$\chi_R = \frac{N}{4\pi^3 \nu_{ex} \nu_S^2} \sum_j \Delta_j g_j \sigma_j \frac{\nu_j}{2\pi c [\nu_j^2 - (\nu_2 - \nu_1)^2 - \nu_j(\nu_2 - \nu_1)]} \quad (5.32)$$

Δ_j : average population difference per molecule between the lower vibration-rotation level (ν_j, J_j) and the upper one.

ν_j : wavenumber difference between these levels.

σ_j : corresponding differential scattering cross-section.

g_j : weighting factor ($g_j = \nu_j + 1$ for a Q-branch line).

γ_j : transition linewidth.

Relations (5.30) shows that P_{AS} is proportional to the square of the excitation radiation power P_{ex} ; therefore the interaction is stronger near the focus of lens L_1 , where the power density is higher. As a result, local measurements are made within this near cylindrical volume, a few microns in diameter and a few millimeters in length.

The A.S. generated power propagates within the same beam as both excitation radiations; the whole generated light is then collected on the photodetector and as the collecting solid angle is much smaller than for spontaneous Raman scattering, the unwanted light power from the background (spray light, fluorescence or emission) is also smaller; a much higher signal-to-noise ratio is easy to obtain, even with a lower excitation power.

Let us now consider resonant and non-resonant susceptibility contribution.

Relation (5.32) shows that χ_R is at its maximum when $\nu_j = \nu_{ex} - \nu_S$; the excitation radiation wavenumber ν_{ex} remaining constant, the shifting of the wavenumber ν_S makes it possible to take into account successive values j . By tuning ν_S in a given spectral domain, it is then possible to record vibration-rotation spectra as with the spontaneous Raman method and to deduce from them the temperature and number density. The Q-branch profile is generally used for these measurements as it is the most intense, with a weak interference between the spectra of different species.

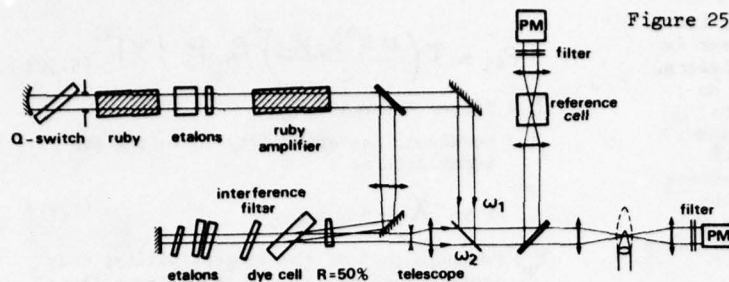


Figure 25 - "Coherent Anti-Stokes Raman scattering". Generation of the two radiations, one by means of a Q-switch ruby laser, the other by means of a dye laser excited by the former. The beam with the reference cell is for calibration purposes. From S. Druet and al. [17].

The non-resonant part χ_{NR} of the susceptibility, which is independent of the wavelength, increases with the total number density for all the species. It has the same effect as a stray-light, that is to say sensitivity limitations for low partial number density: typical minimum detectable mixing ratio about 1000 p.p.m.

Continuous or pulse lasers can be used as light sources. The optical diagram of a CARS set-up is shown in figure 25 with a pulse Q-switched ruby laser. In order to obtain small linewidths, spatial and spectral filters are placed in the cavity and a passive Q-switching is performed by a cryptocyanine in ethanol cell. The output power is about 1 MW in 8 ns; the linewidth is less than 0.01 cm^{-1} . The shot frequency is 3 pulses per minute. The beam diameter is 2 mm. A ruby amplifier increases the power to 5 MW. A beam splitter transmits part of the emitted light as the excitation radiation at frequency ω_1 and reflects the other part to a dye laser cell, in order to generate the other radiation, with a frequency ω_2 . The frequency adjustment is made by tilting a Fabry-Perot etalon placed in the laser cavity. Both beams ω_1 and ω_2 are mixed by means of a second beam splitter. A third beam splitter is used to separate the beam in two ways: 80% are focused on the sample (flame, gas cells), 20% are focused on a reference cell filled with 40 atm. of argon. The signal ratio of the two detectors is recorded in such a way that the laser power variations from pulse to pulse are cancelled. Considerable care has to be taken in order to avoid an unwanted wavelength shift resulting mainly from temperature variations. As mentioned for the spontaneous Raman method, it is also possible to use a broad linewidth for the Stokes frequency and to obtain the Anti-Stokes spectrum with a spectrograph. The spectrum recorded on a photographic plate or with a television equipment can then be processed to obtain the desired measurements.

6 - Work in Progress for Flame Studies

It appears increasingly necessary to improve the aero-engine performance in order to reduce fuel consumption and the pollution due to unburnt gases and solid particles generation. Therefore, it becomes essential to study the chemical reaction and the species distribution inside the flame itself without the creation of disturbances. Only the optical methods can do this. Among them, the methods based on Raman scattering are the most attractive because they permit remote local measurements of temperatures and number densities of specific species, even if these are not in thermodynamic equilibrium in every point. Nevertheless, the application of these methods is difficult because of the very low scattered intensities as compared to the excitation power.

The recent advances of the laser technology permit the production of directive,

selective, stable and intense light sources; all these properties are required for the use of the Raman scattering method. These lasers are essential for the Raman methods to be used for applied physical measurements. Other problems, such as those concerning stray light rejections, light detection and spectral filtering with an efficient blocking should not be overlooked but they are of secondary importance in comparison with the essential necessity of a suitable light source.

Approximately ten years ago, the main teams I know in USA and Europe undertook fundamental studies. Their interesting results were reported in publications, the bibliographic reference numbers of which are [14] to [17].

However, classical Raman scattering is limited as regards both accuracy and the possibility of detecting species at a low concentration in a mixture. These limitations are mainly due to the presence of unwanted light, mixed with the useful scattered light, which it is very often difficult to eliminate.

Some of these difficulties can be overcome by the use of the new method designated as "Coherent Anti-Stokes Raman Scattering", whose application to the study of gases began six years ago. The main advantage of this method lies in the fact that the useful generated light is much more intense, and therefore the rejection of the unwanted light is easier. However, another limitation to the detection of a species at a low concentration in a mixture and the measurement of its number density is due to the non-resonant part of the susceptibility (molecular quenching), which is proportional to the total number density of the mixture.

Promising results have already been obtained. However, the improvement of this method requires two-wavelength stable lasers, one of these wavelengths being accurately tunable with respect to the other. Considerable efforts were devoted to the development of this kind of lasers and some devices are now in the production stage but they are still expensive.

7 - Conclusion

The optical methods appear particularly attractive to perform physical and chemical measurements within the gas flow of an aero-engine because they are specifically non-intrusive. As it is often very difficult, if not impossible, to use them on a real engine, they are mostly used on models simulating parts of engines.

Like similar optical methods, such as shadowgraphy and schlieren, interferometry has been used for flow visualization since the beginning of experimental aerodynamics. This method permits density measurements within aerodynamic flows, provided that specific

conditions, such as two-dimensional or axisymmetrical, be met. The advent of the laser permitted the development of a new kind of interferometer: the holographic interferometer. It is easier to build and use, and less sensitive to environmental conditions created in the vicinity of a machine (heat, vibrations). Thus, it can be applied to density distribution measurements in fixed or rotating blade cascades, in cold or hot gas flows, even in flames.

The Raman scattering methods are particularly interesting to perform local temperature measurements and local concentration measurements on specific species in a mixture of hot and reactive gases. Their application to flames studies is extremely important because there are no other convenient methods of determining the physical and chemical characteristics in these media.

However, the implementation of the optical methods requires the building of complex and expensive devices. These devices have to be handled with great care by experienced technicians in order to obtain unquestionable results.

Data processing is generally a time-consuming operation. Therefore, considerable efforts are still required to improve this phase of work, and the advantages offered by the connection of these devices with microprocessors should be fully used, in order that optical methods may become operational.

BIBLIOGRAPHY

Interferometry

- [1] - W. Merzkirch - Current Problems of Optical Interferometry Used in Experimental Gas Dynamics - AGARDograph n°193 (1976).
- [2] - J. Delerey, J. Surget, J.P. Lacharme - Interférométrie Holographique Quantitative en Ecoulement Transsonique Bidimensionnel - La Recherche Aéronautique n°1977-2, p. 89-101.
- [3] - J.D. Trolinger - Laser Instrumentation for Flow Field Diagnostics - AGARDograph n°186 (1974).
- [4] - M. Pianko - Modern Methods of Testing Rotating Components of Turbomachines (Instrumentation) - AGARDograph n°207 (1975).
- [5] - R. Fuchs - Work cited in the reference 4, section I on Aerodynamic Measurements in Cascades.
- [6] - M. Philbert et G. Fertin - Dispositif de Visualisation pour Soufflerie de Grilles Annulaires Fixes ou Tournantes. La Recherche Aéronautique n°141 (mars-avril 1971) p. 109-118.
- [7] - Jean-Marie Caussignac - Visualisation d'Ecoulements Aérodynamiques dans les Compresseurs par Interférométrie Holographique - Note Technique ONERA n°190 (1972).
- [8] - M. Philbert et G. Fertin - Schlieren Systems for Flow Visualization in Axial and Radial Flow Compressors. Asme Publication - Paper n°74-GT-49 (1974).

- [9] - G. Fertin - Visualisation de l'Ecoulement dans un Compresseur Axial Supersonique à Aubes Longues. La Recherche Aéronautique n°166 (1975-3) p. 165-168. Visualisation des Ondes Choc - Mesures n°4 avril 1977 p. 57-69.
- [10] - R.G. Hantman, R.J. Burr, W.G. Alwang and M.C. Williams - The Application of Holography to the Visualization of Shock Patterns in a Transonic Compressor - AIAA Paper n°74-637 (July 1974).
- [11] - Ralph F. Wierker - Holographic Interferometry - Proceedings of the ICO Conference, Tokyo (August 1974)-Japan J. Appl. Phys. 14 (1975) Suppl. 14-1.
- [12] - W.A. Benser, E.E. Bailey and T.F. Gelder - Holographic Studies of Shock Waves within Transonic Fan Rotors - Journal of Engineering for Power (January 1975) p. 75-84.

Raman Scattering

- [13] - G. Herzberg - Spectra of Diatomic Molecules - Second Edition - D. Van Nostrand Co- Inc., Princeton 1950.
- [14] - M. Lapp and C.M. Penney - Laser Raman Diagnostics - Plenum Press - New-York and London 1974, containing many papers written by the main teams working in the field in USA and Europe.
- [15] - W.F. Fenner, H.A. Hyatt, J.M. Kellam and S.P.S. Porto - Raman Cross Section of Some Simple Gases - J.O.S.A. vol. 63, n°1 January 1973.
- [16] - W. Stricker (DFVLR, Stuttgart) - Local Temperature Measurements in Flames by Laser Raman Spectroscopy. Combustion and Flame 27, 133-136 (1976) - Published by American Elsevier Publishing Co- Inc.
- [17] - AGARD-CP-n°193 - Applications of Non-Intrusive Instrumentation in Fluid Flow Research (1976), containing :
 - R. Goulard - Optical Measurements of Thermodynamic Properties in Flow Fields.
 - S. Druet, R. Bailly, M. Péalat and J.P. Taran - Techniques Raman d'Etude des Ecoulements et des Flammes.
 - A. Hirth - Mesure Locale et Continue de la Densité d'un Ecoulement Gazeux par Diffusion Cohérente Raman Anti-Stokes.

FUNDAMENTALS OF LASER DOPPLER VELOCIMETRY

by

A. E. Lennert
 Supervisor, Advanced Concepts Staff
 ARO, Inc.
 Arnold AF Station, Tennessee 37389 USA

SUMMARY

The basic principles of the laser Doppler velocimeter (LDV or LV) an instrument being utilized in many laboratories for measurements of fluid flow, is treated in detail. The development includes one, two and three-dimensional simultaneous measurements using both forward and backscatter techniques. Conventional laser velocimeters determine speed only; therefore, ambiguities exist when attempting to measure turbulence, flow angularities, and flow circulation. With the inclusion of a Bragg cell, or other modulation techniques, the ambiguities are resolved. The characteristics of the Bragg cell system, both one- and two-component types, is presented. Several counting techniques are reviewed and a "real time" processor evaluated. Of the various data acquisition and processing mechanisms only the direct-counting techniques are favorably considered for aircraft engine applications. Included are discussions concerning pertinent parameters affecting LV design for engine application and finally several LV systems used in wind tunnel environments are described.

I. INTRODUCTION

Conventional devices that are used for performing flow field diagnostics comprise material-type probes such as hot-wire anemometers, rakes, pitot tubes, and others. The basic shortcomings of such devices are that they substantially perturb the medium that is being measured; hence, correction factors must be introduced to re-establish the free-stream, unperturbed conditions. None of these devices measures velocity directly. Most are quite sluggish insofar as frequency response is concerned. It is very difficult to acquire accurate transient and/or turbulent flow measurements; the physical sizes of the instruments are such that the spatial resolution is relatively poor. In the case of plasma diagnostics where the flow fields are extremely energetic, material-type probes have the failing of either rupturing or disintegrating. It is not an understatement to say that conventional diagnostic techniques leave much to be desired.

The previous lecturers have introduced and discussed the importance of utilizing non-perturbation-type instrumentation as diagnostic tools for engine development. One of these techniques--the laser velocimeter--will be treated in this session. In general the LV measures fluid velocities indirectly by determining the velocities of the particles moving with the flow field. If the particles are small in size (less than $0.5\mu\text{m}$) then accurate measurements of gas velocities over a wide range of flow and turbulent conditions can be obtained. Often particles are inherent in the flow medium as impurities. In some cases the impurities are large in size such that particle lag problems are experienced. In other cases the impurities may be too low in number density and experimenters must resort to artificially seeding the flow.

This artificial particle environment can offer debilitating effects upon the desired data and on engine components. In addition to these instrumentation problems, fundamental problems that must be resolved before the LV becomes a routine tool, in particular, for the altitude performance testing and aero-engine development, are associated with the complex geometries of wind tunnels, compressors, combustion and exhaust chambers, where the volume that can be probed is restricted. Additionally, the combustor environment results in high temperatures, high velocity, and high turbulent flow conditions which preclude theoretical analyses without introducing simplifying assumptions.

In what follows, attention will be focused upon the basic operational principles of operational LV. The two major types of LV, the self-aligned reference beam and the two beam, dual scatter (or differential Doppler) systems, will be evaluated. The fundamental problems, which are inherent errors and limitations of the LV aircraft engine application will be discussed. Since the successful application of the LV is strongly dependent upon the data acquisition and processing techniques, conventional electronic devices will be briefly reviewed and the techniques that are seriously being developed for improving the data acquisition, both in quantity and quality, will be discussed.

II. THEORETICAL CONSIDERATIONS

A. Introduction

The basic equations will be derived for determining the frequency of light scattered from a moving object. The derivation is equally applicable to light reflected, refracted, or scattered from a moving surface. The essential factor involved is that the moving object re-emits, or scatters, the wave-fronts instantaneously.

B. Doppler Shift Relationships

In Fig. 1-a a small particle at P is assumed moving with a velocity v in an environment of refractive index n . A stationary light source of frequency f_0 and free-space wavelength λ_0 illuminates the region. Upon entering the refractive region, the

the frequency of the light is not changed, but its wavelength, λ_i , and the velocity, v_i , are reduced to $\lambda_i = \lambda_o/\eta$ and c/η , respectively. Light scattered from the particle is of wavelength λ_s , of velocity c/η , and of frequency f_s ; exterior to the refractive region the scattered light is of wavelength λ_s , velocity c , and identical frequency f_s . The rate at which wavefronts intercept the moving particle is v .

$$f' = \left(\frac{c}{\eta} - \vec{v} \cdot \hat{e}_i \right) = f_o - \vec{v} \cdot \frac{\hat{e}_i}{\lambda_o} \quad (2-1)$$

where the \hat{e}_i represents the unit vector of the incident beam propagation vector.

In Fig. 1-b a particle is assumed to have scattered a wavefront when at position 1. The particle then moves to position 2 before it scatters another wavefront. A time $1/f'$ elapses between points 1 and 2 during which the initial wavefront travels a distance $c\hat{e}_s/\eta f'$ toward the observer, and the particle travels a distance \vec{v}/f' ; \hat{e}_s is the unit vector in the scattered direction. Then:

$$\lambda_s = \frac{c}{\eta f'} - \frac{\vec{v} \cdot \hat{e}_s}{f'} \quad (2-2)$$

Substituting Eq. (2-1) for f' and solving for f_s yields:

$$f_s = \frac{c}{\eta \lambda_s} = \left(\frac{f_o - \frac{1}{\lambda_i} \vec{v} \cdot \hat{e}_i}{1 - \frac{\eta}{c} \vec{v} \cdot \hat{e}_s} \right) \quad (2-3)$$

In the nonrelativistic limit ($v \ll c$), eq. (2-3) can be simplified by expanding the denominator in a binomial expansion. Retaining only the first three terms then,

$$f_s = \left(f_o - \frac{1}{\lambda_i} \vec{v} \cdot \hat{e}_i \right) \left(1 + \frac{\eta}{c} \vec{v} \cdot \hat{e}_s \right) = f_o + \vec{v} \cdot \left(\frac{f_o \eta \hat{e}_s}{c} - \frac{\hat{e}_i}{\lambda_i} \right) \quad (2-4)$$

Substituting $\lambda_i = \lambda_o/\eta$ and $f_o = c/\eta \lambda_i$ yields

$$f_s = f_o + \frac{\eta}{\lambda_o} \left[\vec{v} \cdot (\hat{e}_s - \hat{e}_i) \right] \quad (2-5)$$

Equation (2-5) expresses the frequency of the light scattered by a particle moving in an environment of refractive index η . The Doppler frequency shift can be expressed as

$$f_D = f_s - f_o = \frac{\eta \vec{v}}{\lambda_o} \cdot (\hat{e}_s - \hat{e}_i) \quad (2-6)$$

or using the alternative form

$$f_D = \frac{\eta \vec{v}}{2\pi} \cdot (\vec{k}_s - \vec{k}_i) \quad (2-7)$$

Where $\vec{k}_i = \frac{2\pi}{\lambda_i}$ and $\vec{k}_s = \frac{2\pi}{\lambda_s}$ are the incident and scattered propagation vectors.

The magnitude of the scattered propagation vector \vec{k}_s is essentially equal (to within one part in 10^7) to the magnitude of the reference vector \vec{k}_o . Since $\vec{k} = \frac{2\pi}{\lambda} = \frac{2\pi \eta f}{c}$ when the frequency of a wave changes a small amount of $df = f_D$ its propagation constant changes by an amount

$$d\vec{k} = \vec{k}_D = \left(\frac{2\pi \eta}{c} \right) df = \left(\frac{2\pi \eta}{c} \right) f_D \quad (2-8)$$

Thus, the propagation constant of the scattered light is:

$$\vec{k}_s = \vec{k}_i + \vec{k}_D = \frac{2\pi \eta}{\lambda_o} + \left(\frac{2\pi \eta}{c} \right) f_D \quad (2-9)$$

The ratio of \vec{k}_D/\vec{k}_i is given by:

$$\frac{\vec{k}_D}{\vec{k}_i} = \frac{f_D}{c} = \frac{f_D}{f_o} = \frac{10^8}{5 \times 10^{14}} = 5 \times 10^{-7} \quad (2-10)$$

where typical values of $f_D = 100$ MHz and $f_o = 5 \times 10^{14}$ Hz have been assumed. Thus, $\vec{k}_s = \vec{k}_i$ and $\lambda_s = \lambda_i$ within better than seven place accuracy.

C. Detection of One Velocity Component

The Doppler frequency shift relationship will be applied to show that only one component of the velocity of a moving semitransparent medium is detected. In Fig. 2 an incident light beam of wave vector \vec{k}_i , located in the x-y plane and at an angle $\theta/2$ with the x-axis, passes through and scatters light from a moving semitransparent medium. Only that light scattered from the origin of wave vector \vec{k}_s is detected by the combination of the lens L2, the aperture, and the PM tube. The detected scattered light is oriented at an angle $\theta/2$ with the x-axis and an angle θ with the incident beam. The wave vectors \vec{k}_s and \vec{k}_i are of approximately equal magnitude. \vec{k}_s and \vec{k}_i are indicated emerging away from the scatter point so that the tail of each vector is located at the scatter point and the vector difference, $\vec{k}_s - \vec{k}_i$, is from the tip of one vector to the tip of the other. Since $k_s = k_i = 2\pi\eta/\lambda_o$.

$$\left| \vec{k}_s - \vec{k}_i \right| = 2k_i \sin \theta/2 = \frac{4\pi\eta}{\lambda_o} \sin \theta/2 \quad (2-11)$$

and

$$\vec{k}_s - \vec{k}_i = \frac{4\pi\eta}{\lambda_o} \sin \theta/2 \hat{e}_y \quad (2-12)$$

Since $\eta = 1.00^+$ for air, it may safely be neglected in the following discussion. However, in media other than air η must be included. The Doppler frequency shift of the scattered light k_s is given by

$$\begin{aligned} f_D &= \frac{1}{2\pi} \vec{v} \cdot (\vec{k}_s - \vec{k}_i) \\ &= \frac{1}{2\pi} (\vec{v}_x \hat{e}_x + \vec{v}_y \hat{e}_y + \vec{v}_z \hat{e}_z) \frac{4}{\lambda_o} \sin \theta/2 \hat{e}_y \\ &= \frac{2\vec{v}_y}{\lambda_o} \sin \theta/2 \end{aligned} \quad (2-13)$$

For small θ , $\sin \theta/2 \approx \theta/2$. Solving for \vec{v}_y yields:

$$\vec{v}_y = \frac{f_D \lambda_o}{\theta} \quad (2-14)$$

Thus, by selecting the direction of the incident light and of the detected scattered light so that the vector difference of their propagation vectors is parallel to one chosen component of velocity, only that chosen component of velocity will contribute to the frequency shift of the detected scattered light.

D. Fringe Analysis of Dual Scattered LV

There is, however, an alternative, and simpler analysis of the velocimeter which will be discussed since it presents a much clearer phenomenological picture of the events that occur when the particle traverses the probe volume. As in the previous cases, the laser source is split into two beams (Fig. 3) one for each of the two velocity components, and focused a diffraction-limited region where the Gaussian intensity consists essentially of planar wavefronts of radiation. Because of the coherence of the source, the beams will interfere constructively and destructively to establish a set of closely spaced, planar, stationary interference fringes at the beam or crossover focal region. The peak-to-peak fringe spacing; δ , is

$$\delta = \frac{\lambda}{2 \sin \theta/2} \quad (2-15)$$

the $1/e^2$ diameter of the focal region is given by

$$2b_o = \frac{4}{\pi} \lambda \frac{F.L.}{d_B} \quad (2-16)$$

where F.L. is the focal length of the lens and d_B the diameter of the beam at that lens. The number of fringes N contained in the focal volume can be determined by dividing the peak-to-peak fringe spacing into the focal diameter as follows:

$$N_s = \frac{8 F.L.}{\pi d_B} \sin \theta/2 \quad (2-17)$$

This can be simplified by assuming $\theta/2$ is much less than unity such that $2 \sin \theta/2$ is approximately equal to θ where θ is the separation of the two beams, d_s , at the transmitter lens divided by the focal length. With this approximation:

$$N_s = \frac{4}{\pi} \frac{d_s}{d_B} \quad (2-18)$$

As a particle traverses the focal volume at a velocity \vec{v} , the interference fringes are cut at a rate equal to

$$f_D = \frac{2v}{\lambda} \sin \theta/2 \quad (2-19)$$

which is equal to the Doppler frequency. Since the particles traversing the fringes repetitively scatter light, they generate an alternating, fluctuating, current in the photodetector with a frequency proportional to the rate at which the particles intercept the fringes. Although the fringe explanation is relatively simple to understand it cannot be used to analyze the scattered radiation in detail. This is attributed to the complicated nature of the particle scattering process that is dependent upon the ratio of particle size to the wavelength of light, the index of refraction of the particle, the angle of incidence of the light beam, etc.

III. LASER VELOCIMETER ANALYSIS

A. Introduction

The reference beam LDV was the first type unit constructed and placed into operation. The initial LV system (Ref. 1) was a forward scatter non self-aligning LDV unit. After several years of operation in which alignment difficulties were experienced, self-aligning units were developed. Operational difficulties were still evidenced and the dual scatter or differential type LV units emerged from the development laboratories. In these latter units the radiation that impinges upon the detection system is light scattered away from the incident beam. The resulting improvement centered upon minimizing the so-called broadening effects inherent with the reference beam systems. The basic problem with the reference beam system is that a large number of particles, or scattering centers, is required for operation.

In the present section the two main types of LDV systems will be discussed and representative examples displayed. Although only one operational principle is described, a number of different modifications exist. The analysis, however, is generally valid. Both forward and back-scattered LV techniques will be discussed.

B. Forward Scatter LDV

The reference beam LDV can readily be analyzed with recourse to Fig. 2a and Eq. (2-14). Two laser beams coming from one source are made to cross and to focus to a common point in space. One of the beams is a low power reference beam (1% of the total beam power) and intercepts the photocathode surface of the PM tube. The Doppler shifted frequency for light scattered from the main beam is

$$f_o = \frac{\vec{v}}{2\pi} (\vec{k}_s - \vec{k}_o) = \frac{2}{\lambda_o} \sin \theta/2 \vec{v} \quad (3-1)$$

The reference low power beam impinging upon the phototube is mostly unscattered, and therefore, is not frequency shifted. Furthermore, any frequency shift of this very low intensity light scattered from the reference beam is essentially zero since in Eq. (3-1) $\theta \approx 0$. The reference beam and the Doppler shifted scattered beam interfere, however, at the PM tube and generate an electronic (Doppler) current of frequency f_D . The generated Doppler current will continually increase and decrease in amplitude as the scatterer moves toward and away from the axis of the focused reference beam because of radiation alignment effects. In addition, variations in illuminating beam intensity (i.e., the Gaussian beam profile) will also affect the Doppler signal current amplitude. Both radiation alignment and illuminating intensity effects combine to produce an effective probe volume. The probe volume is defined to be the region where the laser beam intensity is at least $1/e \approx 0.37$ of the maximum possible current amplitude which occurs when a scatter center passes through the geometrical focus P.

The Doppler current generated by a single scatterer is not of a unique frequency f_D but is dispersed slightly about the mean frequency f_D . This frequency dispersion is caused by the finite angle $\Delta\theta$ (Fig. 2a) of the scattered radiation which is superimposed upon and aligned with the reference beam at the photocathode surface. This angle is essentially constant at points remote from the geometrical focus, P. The net frequency dispersion Δf_D attributable to a finite $\Delta\theta_s$ is determined from Eq. (3-1) to be

$$\begin{aligned}
 \frac{\Delta f_D}{f_D} &= \frac{\Delta \theta}{2} \cot \theta/2 \\
 &= \frac{\Delta \theta}{\theta} \quad (\text{for small } \theta) \\
 &= 0 \text{ at } 180^\circ
 \end{aligned}
 \tag{3-2}$$

For small angle frontscattered light the angle $\Delta \theta$ is made much smaller than θ to minimize signal frequency dispersion and provide a very accurate Doppler frequency measurement. A value of $\Delta f_D/f_D - \Delta \theta/\theta = 0.05$ will provide a velocity measurement accuracy of approximately one percent for f_D either a spectrum analyzer or direct-recording frequency readout. A small θ has a limiting effect on the signal power and the S/N ratio as the effective solid collection angle of scattered radiation, $\Delta \Omega = \Delta \theta^2$, is restricted. However, for submicron particles and small θ , the scattered intensity is very large, and this limitation is not severe, provided a sufficient seed density exists.

In practice the reference beam, or local oscillator, systems are self-aligning and several means are used in splitting the laser beam into components. One technique uses path compensating (Fig. 2a) glass blocks whereas other techniques utilize various type prisms. A photograph of a compact two component block system is shown in Fig. 2b and Fig. 2c. A number of these devices have been analyzed in detail for performance (Ref. 2).

C. Backscatter, Reference Beam, LV

If backscattered light ($\theta = 180$ deg) is heterodyned with reference light, the relative frequency dispersion is negligible i.e., $\Delta f_D/f_D = 0$, as $\sin(\theta/2)$ is essentially constant for $\theta = 180$ deg so long as $\Delta \theta \ll \theta$. Such considerations permit substantially more backscattered radiation power to be collected and aligned with reference radiation without adversely affecting the relative frequency dispersion. Also, for fractional micron-sized scatterers, the backscattered light intensity (Refs. 3, 4, 5, and 6) is much reduced in comparison to that of small angle frontscattering. Thus, to obtain signals comparable to those of frontscattering, substantially more radiation must be collected and aligned without adversely affecting the relative frequency dispersion $\Delta f_D/f_D$.

The frequency to velocity conversion for the backscatter system where $\theta = 180$ deg is given by:

$$\frac{f_D}{\vec{v} \cdot \vec{e}_\perp} = \frac{2}{\lambda}
 \tag{3-3}$$

where \vec{e}_\perp is the unit vector orthogonal to the vertical and horizontal components - or in the direction of the incoming laser beam.

$$\therefore f_D = \frac{2v}{\lambda} \cos \theta/2 \approx v/\theta \quad \text{for small } \theta$$

This result implies that the frequency to velocity conversion factor is large for backscattered light and approximately one order of magnitude greater than for the front-scattering case.

By extending the techniques two and three orthogonal components of velocity, using a single laser source, may be measured. Such a three component system would comprise one laser, three sets of optics that are orthogonal to each other, and three photodetectors such as photomultiplier tubes or photodiodes. The advantage of utilizing an orthogonal set of optics is that subsequent algebraic manipulation of the data is not required to extract individual velocity components as the output frequency of each photomultiplier tube will be proportional to only one orthogonal component of velocity.

An optical arrangement for measuring three orthogonal reference beam systems is shown in Fig. 4. On the backscattered component, path length equalization mirrors were employed as the laser did not include an etalon to extend its coherence length and permit detection with large optical path differences. Note that the performance of the backscatter component detection scheme is also vibration insensitive because the illuminating and collecting optics are closely positioned in space and are very stable with respect to one another.

D. Dual Scatter LDV

Velocity components can also be detected by heterodyning two wavefronts emanating from a common scatter center illuminated by two beams. This is accomplished (Fig. 5) by simultaneously illuminating the object from two input directions (\hat{e}_{i1} and \hat{e}_{i2}) and detecting the difference frequency of two superimposed rays generated by a common scatter center and propagated in a common direction (\hat{e}_s). One ray is scattered from the \hat{e}_{i1} beam and the other from the \hat{e}_{i2} beam. Light scattered from \hat{e}_{i1} and in the direction \hat{e}_s is of frequency

$$f_{s1} = f_0 + \frac{v}{\lambda} \cdot (\hat{e}_s \cdot \hat{e}_{i1})
 \tag{3-4}$$

whereas light scattered from the \hat{e}_{i2} beam and in the same direction as \hat{e}_s is of frequency.

$$f_{s_2} = f_0 + \frac{v}{\lambda} \cdot (\hat{e}_s - \hat{e}_{i2}) \quad (3-5)$$

As both wavefronts originate at a common scatter center, they are precisely aligned. When they intercept a photodetector simultaneously, they will generate a Doppler current of frequency

$$f_D = f_{s_1} - f_{s_2} = \frac{v}{\lambda} \cdot (\hat{e}_{i2} - \hat{e}_{i1}) = \frac{2 \sin \theta/2}{\lambda} \cdot \hat{v} \cdot \hat{e}_\perp \quad (3-6)$$

which is independent of the viewing direction \hat{e}_s and sensitive only to the velocity component $\hat{v} \cdot \hat{e}_\perp$. θ is now the angle between the two illuminating directions \hat{e}_{i1} and \hat{e}_{i2} , and \hat{e}_\perp is now a unit vector orthogonal to the mean illuminating direction, i.e., orthogonal to $\hat{e}_{i1} + \hat{e}_{i2}$ (Fig. 4). f_D of Eq. (4-1) is independent of the observation direction \hat{e}_s because as \hat{e}_s is varied, each individual scattered frequency (f_{s_1} or f_{s_2}) increases (or decreases) an identical amount such that the difference frequency $f_D = f_{s_1} - f_{s_2}$ remains constant. An inherent advantage of the two-beam, dual-scatter system (in comparison to the reference beam) is that a large solid angle of scattered radiation can be collected without introducing signal frequency broadening, thus, enhanced S/N ratio is provided. Also, Eq. (4-3) predicts that f_D should be a unique frequency, providing \hat{v} , \hat{e}_{i1} and \hat{e}_{i2} are uniquely defined.

A frontscatter arrangement of the two-beam, dual-scatter system is shown in Fig. 4. Two Gaussian illuminating beams focus to a common point P. The radiation wavefronts are planar near P, and therefore \hat{e}_{i1} and \hat{e}_{i2} are uniquely defined. The inherent signal frequency dispersion is thus zero, i.e.

$$\frac{\Delta f_D}{f_D} = 0 \quad (3-7)$$

and is independent of both $\Delta\theta$ and θ . Thus $\Delta\theta$ can be increased at will to provide enhanced values of S/N ratio.

Experimentally the two-beam, dual-scatter system performs satisfactorily with low laser powers and low seed density. Using approximately 15 mw at 4880 Å, the system has been used in the frontscatter mode to measure 300 m/sec velocities in a free-jet turbulent flow, using only atmospheric impurities (dust, etc.) (Ref. 8).

A self-aligning, backscatter, two-beam LV unit is schematically shown in Fig. 6. This system, has been used to measure a 300-m/sec velocity component in a free-jet turbulent flow using smoke (partially oxidized mineral oil) as a seed material, with a laser power of only 20 mw at $\lambda = 4800\text{-}\text{\AA}$. With higher laser power, $P_0 = 0.5$ watts, artificial seeding was not required.

IV. BRAGG CELL VECTOR VELOCIMETER

A. Introduction

Self-aligning laser velocimeters using the dual-scatter or differential Doppler techniques have been used successfully in a number of applications (Refs. 7, 8, 9, and 10). For measurements of one velocity component, such instruments are simple to construct and straightforward to use. All that is required is a beam splitter of reasonably high quality, a laser, lenses, and a signal detector. A self-aligning velocimeter capable of measuring two velocity components is considerably more difficult to construct, especially since care must be taken to eliminate the so-called cross-talk between components and to match optical paths in the transmitting portion of the instrument to maintain a high signal-to-noise ratio. Furthermore, some complex means such as polarization separation must be used to separate the signals for each velocity component and then direct the respective signals to two different detectors (Ref. 11). Such velocimeter systems suffer from several basic drawbacks--the velocity signal for each component has a 180-deg directional ambiguity. This presents no difficulty when the velocity direction is known a priori. However, in certain applications, where turbulent and circulating flows exist, the directional ambiguity severely limits the utility of the instrument. In addition most signal processors require a specific number of cycles of information. If a particle traverses the focal region at an angle, which is realistic in the case of turbulent flow conditions, then an insufficient number of cycles of information will be obtained. In other words, a "dead zone" exists. As an example, in Fig. 7A the particle is traversing the focal region at such an angle that only a few fringes are cut and, hence, no horizontal component data were acquired. In Figure 7B the particle path is at such an angle that no vertical component data can be acquired, again because of the insufficient number of cycles. The "dead zones" are characteristic of systems having stationary fringe planes set up in the probe volume.

It has been shown that the directional ambiguity can be resolved with the use of ultrasonic Bragg cells, rotating diffraction gratings, etc., to frequency shift of the portion of the transmitted light such that a carrier frequency can be generated for the Doppler signal (Ref. 12). The direction of the frequency shift about the carrier frequency is then related to the direction of the velocity vector. In the present section the

operation of a Bragg Cell velocimeter system will be described, examples of its operation illustrated and the improvement in performance of an LV will be described.

B. Principles of Operation

The diffraction of light by ultrasonic waves is well understood (Ref. 13 and 14). In a liquid-filled (or solid state) ultrasonic cell, a quartz crystal oscillating at a predetermined frequency generates a traveling wave (although by changing the cell geometry, a standing wave can also be generated). Since the wave oscillates along the direction of propagation, sinusoidal variations in the index of refraction of the liquid are produced. Hence, the device may be visualized as a phase diffraction grating; for standing waves the diffraction grating is imagined to be stationary whereas for traveling waves the grating may be imagined as moving at the speed of sound in the direction of the wave propagation. The diffraction characteristics of the grating are a sensitive function of the orientation of the grating relative to the input illumination (Ref. 14). Only Bragg reflection (where the ultrasonic wave vector is nearly perpendicular to the wave vector of the input light) will be considered. Other diffraction modes, e.g., in the so-called Raman-Nath region (Ref. 14) can be used in self-aligning two-component LV systems, but with considerable difficulty. By carefully adjusting the driving crystal electronics and the cell orientation, the cell may be made to diffract one-half of the input light by the Bragg effect, into a first order "Bragg mode" the other half of the light passes through the cell unaltered. The angle between the beams, θ , satisfies the Bragg equation

$$\sin \theta = \frac{\lambda}{\Lambda} \quad (4-1)$$

where λ is the wavelength of the light and Λ is the wavelength of the ultrasonic wave in the diffracting medium. Λ is given by

$$\Lambda = \frac{c}{f_m} \quad (4-2)$$

where c is the speed of sound in the diffracting medium and f_m is the modulation frequency of the cell-driving crystal and, therefore, the frequency of the ultrasonic wave.

The grating model of the ultrasonic Bragg cell fits well with the fringe interpretation of the LV. The fringe spacing, δ , for stationary fringe LV systems is given by:

$$\delta = \frac{\lambda}{2 \sin \theta/2}$$

$$\delta \approx \frac{\lambda}{\theta} \text{ for } \theta \ll 1 \quad (4-3)$$

where θ is the angle between the beams transmitted to the probe volume. In a moving fringe LV system, the Bragg cell can act as a beam splitter. The angle between the beams (Eq. (4-3)) is usually quite small and must be magnified for practical applications. In any case, a lens system images the dispersive origin of the two beams, to form the probe volume for the moving-fringe LV system (Fig. 8). In this respect care must be taken to mode match (Ref. 15) the optics associated with the Bragg cell. Since a laser produces a Gaussian beam diffraction must be considered to ensure that the beams cross and focus coincidentally. It is also possible for the fringes in the probe volume to be non-equidistant introducing errors in the analysis of data. In general commercial Bragg cell systems will include the mode matching optics (Ref. 16) as part of the unit.

With recourse to geometrical optics, it is straight, forward to show that for a moving fringe LV system

$$\delta = m \Lambda \quad (4-4)$$

$$\frac{\lambda}{\theta} \approx m \Lambda \quad (4-5)$$

where m is the magnification of the system. Equations (4-4) and (4-5) show that the stationary and moving fringe systems are fully equivalent and that the probe volume in the moving fringe case may be thought of as containing the image of the moving diffraction grating. The movement of the grating image, V_m , is given by

$$\vec{V}_m = m \vec{c} \quad (4-6)$$

where \vec{c} is the velocity vector of the wave in the Bragg cell. Hence, the observed velocity component, \vec{V}_{sc} , normal to the fringes, is given by

$$\vec{V}_{sc} = \vec{V}_m \pm \vec{V}_D \quad (4-7)$$

where V_D is the velocity component which would be observed if the fringes were stationary. The (+) D sign is used if \vec{V}_D is in a direction opposite the travel of the grating image, and the (-) sign is used if \vec{V}_D is in the same direction of travel as the image. Transformation

of Eq. (4-7) into one specifying only the frequency is accomplished by

$$\vec{V}_{sc} = \delta f_{sc} \quad (4-8)$$

$$\vec{V}_m = \delta f_o \quad (4-9)$$

$$\vec{V}_D = \delta f_D \quad (4-10)$$

which are forms of the usual equations used for determining velocity components from an LV signal. Using Eqs. (4-8), (4-9), and (4-10) in Eq. (4-7) one obtains

$$f_{sc} = f_m \pm f_D \quad (4-11)$$

Equation (4-11) shows the well-known result that the Doppler signal is centered about a carrier frequency f_m and that the value of this frequency can be used to remove the directional ambiguity.

C. Two-Dimensional Bragg Cell

The primary difficulty in using two individual Bragg cells in a two-component dual-scatter LV system is that considerable effort must be expended to properly align the system. The light input into a focusing lens from each of the cells must be parallel or the respective components will focus at different points. This could lead to considerable errors in attempting to resolve the measured velocity components into a two-dimensional velocity vector. The optics required for maintaining parallel inputs into the transmitting lens is cumbersome, and it is tedious to align with sufficient accuracy for a coincident focus. These difficulties have been circumvented with the development of a two-dimensional Bragg cell (TDBC). The device is shown schematically in Fig. 9. The cell consists of two legs. At the base of each leg is an X-cut quartz transducer. The transducer consists of a quartz disc, a mounting structure for the quartz disc, and impedance matching electronics. The electronics in this particular example comprise two signal generators, two counters to monitor the frequency and two drivers for the Bragg cell. Although 15 and 25 MHz were selected for this example any two frequencies may be selected as dictated by the test program.

The Bragg cell is used both as a beam splitter and as a frequency shifter. It can be imagined to generate two superimposed, linearly independent, diffraction gratings. Hence, for the configuration shown in Fig. 10, light from the TDBC appears to disperse from a common origin. This eliminates any possibility of focusing errors for the optical components of the respective beams.

Several practical advantages in using the TDBC in a LV system are evident. One may immediately observe that the system is automatically self-aligning, i.e., the transmitted beams will have a common focus without further beam adjustment since the beams originate from a common source. Furthermore, since the path length differences between each of the beams are negligible, the fringe contrast at focus will be high, thereby eliminating the need to path compensate the beams prior to transmission and focus. Compared to stationary fringe LV systems, the TDBC system increases the number of cycles of information in the Doppler signal. This increase has significant ramifications in the choice of the type of signal-processing electronics to be used in a particular application.

An estimate of the maximum number of cycles of information that the particle will generate as it passes through the probe volume can be made as follows. Assume that a scatter center with velocity V_{sc} traverses the probe volume with a trajectory which is normal to the fringe planes and passes through the geometric center of the beam cross point (the condition for the maximum number of cycles of information). The signal observed in real time will have a pulse duration time τ , which will be assumed to be the scatter center time of flight between the $1/e^2$ intensity points in the probe volume. The number of cycles of information in the detected signal, N , is then given by

$$N = \tau f_{sc} \quad (4-12)$$

It should be noted that f_{sc} as given by Eq. (4-12) is the frequency of the acoustic wavefronts in the Bragg cell and will not necessarily be the frequency of the signal available to the information processor. For example, experimentally, a more convenient frequency range could be selected by heterodyning the detected signal current with that of a local oscillator in the signal-conditioning electronics. However, to compare the number of cycles of information for the moving fringe system with that of the stationary-fringe system, it will be assumed that f_{sc} as defined by Eq. (4-12) is the same for both the moving- and stationary-fringe systems. Therefore τ , the pulse duration time, may be written as

$$\tau = \frac{N_s \delta}{V_D} \quad (4-13)$$

where N_s is the number of stationary fringes within the $1/e^2$ points of the fringe intensity distribution and δ is the fringe spacing. Using Eqs. (4-10), (4-11), (4-12), and (4-13), the number of cycles of information observed from the moving fringe system relative to that for the stationary-fringe system is

$$\frac{N}{N_s} = \left(\frac{f_m}{f_D} + 1 \right) \quad (4-14)$$

Thus, by always choosing $f_m \gg f_D$, a considerable increase in the number of cycles available for the signal processor can be obtained.

One advantage in using a two-frequency TDBC is that the respective, velocity component frequencies are centered about the Bragg cell modulation frequencies. This allows a multiplicity of components to be detected by a single photodetector and separated electronically, as shown in Fig. 11, rather than optically, after detection. This characteristic of the TDBC simplifies the optic design of an LV system.

V. THREE COMPONENT VELOCIMETER SYSTEMS

There are two basic techniques that are considered in the development of three component, simultaneous, velocity measurements. One technique comprises a two component dual-scatter system for the vertical and horizontal components and the third velocity component is a reference beam system. The latter component determines the velocity parallel to the transmitting beam. In this design, the optical geometry is such that three orthogonal components are acquired. The second technique comprises three dual-scatter components. In this particular case, one component is off-axis and determines either an x-z or y-z velocity measurement. As a result the all dual-scatter system is a bit more complicated in that mathematical reduction of the third component data is required.

A. Dual-Scatter/Reference Beam System

In the event artificial seeding of flow is permitted, or that a sufficient number of particulates are entrained in the flow, then a reference beam system would suffice to determine the third velocity component. This system is schematically illustrated in Fig. 12. From the figure it is seen that the output beam of laser emitting two wavelengths (4880-Å and 5145-Å) is split into several beams by the Bragg cell mode matching optics system. The 4880-Å line is partially removed to serve as the reference beam (1% of the total beam intensity). The remainder is transmitted, along with the 5145-Å beams, to the focal volume. The back-scattered radiation is collected by the same lens as was used for transmission of the beams. To minimize reflected radiation from the transmitting lens, the central region of the lens is removed. The collected radiation is directed to the respective photodetectors by means of mirrors, and dielectric beam splitter (or color separator) and respective line filters. From the photodetectors the signals are transmitted to respective data processing systems. Parallel to the transmitting beam is a local oscillator, or reference beam, system. The design of the two dual-scatter, reference beam system results in a three-dimensional, orthogonal measurement.

B. All Dual Scatter System

In the dual-scatter concept, Bragg cells are used for acquiring both the magnitude and direction simultaneously. Figure 13 is an illustration of the system which has been set up and evaluated in the laboratory. An argon laser is used for the light source and transmits multi-color light through a color separating filter where the 4880-Å line is separated from the 5145-Å line. The 5145-Å beam enters the two-dimensional Bragg cell by means of mode-matched optics. From the two-dimensional Bragg cell three modulated beams are expanded to the desired separation angle, collimated and then focused to the measuring point. The 4880-Å beam is directed by means of a mirror to its respective Bragg cell by means of mode matching optics where it is frequency modulated. The two modulated beams are transmitted to the focal region by means of a similar set of optics as the 5145-Å line. The two 4880-Å beams then traverse the focal lens and are brought to the common focal point with the 5145-Å lines. Three different sets of fringes are formed and a particle traversing the focal volume scatters light which is collected by the collecting-collimating lens combination shown in Figure 13. The scattered radiation, comprising both 4880-Å and 5145-Å lines impinges upon a color separator where the 4880-Å line is reflected to a mirror and then through an aperture lens combination into the photomultiplier tube. The 5145-Å line passes through the color separating lens and is collected on its associated photomultiplier tube and lens-aperture combination. The 5145-Å line contains two components of velocity information, whereas the 4880-Å line contains a y-z or an x-z velocity combination. In this manner, all three components are simultaneously detected and processed by means of an electronics subsystem comprising frequency separators, translators, and data-processing system.

VI. FACTORS AFFECTING SYSTEM DESIGN

In this section the characteristic probe volumes of the cross-beam reference beam and the cross-beam dual-scatter LDV optical systems and other factors affecting system design are discussed. The probe volume is defined to be the region in space from which the amplitude of the Doppler current generated by a moving scatterer is at least $1/e$ of its maximum possible value. The probe volumes of these two optical configurations are seen to be identical.

A. Cross-Beam Reference-Scatter Probe Volume

A reference-scatter (RS), velocimeter of the cross-beam type which operates in a maximum radiation collection mode has an ellipsoidal probe volume which is bounded by the $1/e^2$ intensity contours of the I and R beams (Fig. 14). Both radiation alignment and illuminating intensity are seen to limit the probe volume size.

Two important facts concerning probe volume size are:

1. Scatter center position variations parallel to the axis of the reference beam do not significantly affect alignment of the Scattered and Reference waves at a distant phototube.
2. Scatter center position variations perpendicular to the R beam axis considerably affect wavelength alignment and, thus, the amplitude of the Doppler current generated by a scatter center. When a scatter center is located on the $1/e^2$ intensity contour of the R beam, the relative Doppler current is reduced in amplitude by a factor of $1/e^2$ because of radiation alignment.

In Fig. 15 scatter center is assumed to be positioned such that the scattered wavefronts (dashed) are in phase with reference wavefronts (solid) at a $(0, z_c)$, the center of the R beam on the phototube. The R and S wavefronts are chosen to be 180 deg out of phase at the $1/e^2$ power points (b_o, z_o) of the reference beam. At $(0, z_c)$ the wavefronts reinforce in phase, producing a maximum instantaneous intensity and a maximum elemental phototube current; at (b_o, z_o) the wavefronts are out of phase and tend to cancel one another, producing a minimum intensity and a minimum elemental current contribution. At each point the elemental current will vary with time at the Doppler frequency, as indicated by the I versus t plots to the right of the respective points in Fig. 15. Thus, the net harmonic (a-c) current, obtained by integrating the elemental current contributions over the extent of the R beam on the photocathode, is reduced in amplitude because adjacent elemental current contributions cancel one another. Such would not be the case, however, for a scatter center located near $(0,0)$ because the R and S wavefronts would be parallel over the photodetector and the resulting Doppler current phase variations would be negligible.

The relative Doppler signal strength is affected also by the intensity of the scattered radiation and, thus, by the illuminating beam. Assume an ideal TEM_{00} , diffraction limited, Gaussian laser beam and that $\tan \theta \approx 1/F$ (Fig. 15). The net phototube Doppler current amplitude, I_D , generated by a scatter center positioned at (x, y, z) relative to the cross point of the beam centerlines in the probe region (Fig. 15) is

$$I_D = I_{Do} \exp - \left\{ \left[\frac{2}{b_o^2} \right] \left[x^2 + y^2 \cos^2 (\theta/2) + z^2 \sin^2 (\theta/2) \right] \right\} \quad (6-1)$$

where it is assumed that detector optics similar to those in Fig. 2 are employed, and signal amplitude variations caused by both radiation alignment and illuminating intensity have been considered. I_D falls to I_{Do}/e when a scatter center is positioned on the ellipsoid

$$x^2 + y^2 \cos^2 (\theta/2) + z^2 \sin^2 (\theta/2) = b_o^2/2 \quad (6-2)$$

and to $I_{Do}e^{-a}$ when

$$x^2 + y^2 \cos^2 (\theta/2) + z^2 \sin^2 (\theta/2) = ab_o^2/2 \quad (6-3)$$

for arbitrary $a \geq 0$,

$$b_o = (2/\pi)f = (2/\pi)(\lambda/\Delta \theta) \quad (6-4)$$

which is the $(1/e^2$ intensity) minimum beam radius of the I and R radiations in the focal region, and $f = 1/\Delta \theta$ is the f/number of the I and R beams. Equation (5-3) defines surfaces of constant signal amplitude. As the scatter center passes through the probe region near $0,0,0$, the cross point (and common focal point) of the two beams, it will intersect such surfaces and generate a Doppler signal of varying amplitude.

Let the probe volume be defined as the region of space within which a scatter center will generate a Doppler current amplitude of at least $1/e$ of the maximum amplitude occurring at $0,0,0$. Equation (5-2), which defines the surface of the probe volume, is illustrated in Fig. 14. Note that the entire probe volume is bounded by the $1/e^2$ intensity points of the reference and illuminating beams. The probe volume is

$$V = 2\pi (2b_o^3)/(3 \sin \theta) \quad (6-5)$$

Substituting for b_o from Eq. (5-4), it is found that the probe volume is 10^{-6} cm^3 ($f = 150$, $\lambda = .4880 \mu\text{m}$, and $\theta = 10 \text{ deg}$) and can be as small as 10^{-10} cm^3 (assuming $f = 8$, $\lambda = .4880 \mu\text{m}$, and $\theta = 40 \text{ deg}$) for a velocimeter employing self-aligning optics.

Thus, the cross-beam RS LDV is seen to have a very small characteristic e^{-1} probe volume of ellipsoidal geometry which is limited by radiation alignment and illumination intensity effects. The e^{-1} probe volume is completely contained within the e^{-2}

intensity points of the beam cross-over region.

B. Cross-Beam Dual-Scatter Probe Volume

The two-beam, dual-scatter, cross-beam LV systems, described in Section IV and shown in Fig. 10 provide Doppler information by heterodyning two wavefronts simultaneously scattered from the common crossover region of two illuminating beams. Radiation alignment effects do not enter into the determination of the two-beam probe volume, as two wavefronts simultaneously scattered from the same scatter center must obviously be propagating precisely in the same direction at any point in space. Illumination intensity effects, therefore, solely determine the probe volume of this system.

This system will have excellent spatial resolution since each illuminating beam focuses to a Gaussian spot of $(1/e^2)$ intensity) diameter $2b_0$ (Fig. 14) given by

$$2b_0 = \frac{4}{\pi} f \lambda \quad (6-6)$$

where $2b_0$ is 0.06 mm assuming $f = 100$ and $\lambda = .4880 \mu\text{m}$.

The variables of Eq. (5-6) are shown in Fig. 14. The x , y , z dimensions of the beam crossover (or common overlap) region are

$$\begin{aligned} x &= 2b \\ y &= 2b_0 / \cos(\theta/2) \\ z &= 2b_0 / \sin(\theta/2) \end{aligned} \quad (6-7)$$

Signal contributions of the significant amplitude are generated by scatter centers located within the volume of the beam overlap region which has these maximum dimensions. For a $1/e^2$ focal spot diameter, Eq. (5-6), of $2b_0 = 0.06$ mm and for $\theta = 11$ deg, these dimensions are $\Delta x = \Delta y = 0.06$ mm and $z = 0.60$ mm. Outside this region at least one of the beams is reduced in intensity and contributes very little to the Doppler current amplitude.

A more critical analysis (Ref. 15) will reveal that when a scatter center is located on the ellipsoid:

$$x^2 + y^2 \cos^2 \theta/2 + z^2 \sin^2 \theta/2 = (2b_0)^2 \quad (6-8)$$

the signal current will be of amplitude $1/e$ relative to that signal current which would exist if the same scatterer were located near the geometrical center of the probe volume $0,0,0$. It should be noted that this $1/e$ probe volume is identical to that of a cross-beam, reference-beam, velocimeter (Section IV) and thus the dual-scatter technique provides spatial resolution identical to that of a practical reference-beam velocimeter. In an off-axis configuration the probe volume that is measured can be smaller than the physical probe volume generated by the transmitting optics. This is because the entire lens is used for collecting the scattered light. The following serves as an example: If a 15 cm lens of 90 cm focal length is used for the signal collection then the measuring volume dimensions are:

$$\begin{aligned} 2b_0 &= \frac{4}{\pi} \lambda \frac{F.L.}{D_L} \\ 2b_0 &= 1.2 \times .5 \times 10^{-4} \times \frac{90}{15} \\ &= 3.6 \times 10^{-4} \text{ cm} \end{aligned}$$

The depth of field is

$$\begin{aligned} L &= 3.6 \times 10^{-4} \times 6 \\ &= 21.6 \times 10^{-4} \text{ cm} \end{aligned}$$

which is considerably smaller than the actual probe volume dimensions. In an off-axis mode the dimensions would be further corrected to

$$L_{\text{off axis}} = 2L_0 \cos \theta$$

where θ is the off-axis angle of the collector.

C. Optical Heterodyne Detection

In measuring the Doppler shifted frequency, the most common technique is by optically heterodyning (or homodyning) the signals on the surface of a photodetector. The primary interest is that of optimizing the signal-to-noise (S/N) ratio. Consider two parallel electromagnetic waves that are aligned so that they impinge normally upon a

photodetecting surface. The total electric field vector is given by

$$E_t = E_1 \cos \omega_1 t + E_2 \cos \omega_2 t \quad (6-9)$$

where E_1 and E_2 are the amplitudes of the individual waves. Assume that both electric fields have the same polarization; the intensity of the radiation to which the photodetector responds would be to the square of the electric field, given by:

$$E_t^2 = E_1^2 \cos^2 \omega_1 t + E_2^2 \cos^2 \omega_2 t + E_1 E_2 \cos (\omega_1 + \omega_2) t \\ + E_1 E_2 \cos (\omega_1 - \omega_2) t \quad (6-10)$$

The detector does not respond to the instantaneous values of the optical frequencies (the first three terms) however, it does respond to the average value of these frequencies; e.g., $E_1^2/2$, $E_2^2/2$. The detector does have the capability of following the difference frequency between the two incoming waves. Thus, the response of the detector E_d is given by

$$E_d = E_1^2 + E_2^2 + E_1 E_2 \cos (\omega_1 - \omega_2) t \quad (6-11)$$

It is seen that the photodetector will yield an output current composed of a dc term and an ac term varying at the Doppler frequency f_d . The laser velocimeter technique comprises measuring the signal frequency given by Eq. (6-11) and then converting to velocity by the use of Eq. (3-1). The S/N power ratio of an optical heterodyne detection system (an LV) is

$$\frac{S}{N} = \frac{\eta}{h\nu B} \left[\frac{P_S P_R}{(P_S + P_R + P_B)} \right] \quad (6-12)$$

where P_S is the scattered power from the focal region, collected by a lens and beat with reference radiation power P_R , P_B is the background radiation power, η is the phototube quantum efficiency, h is Planck's constant, ν is the laser light frequency, and B is the (shot noise limiting) bandwidth of the electronic circuitry often the intermediate frequency (IF) bandwidth of a spectrum analyzer. The generated signal power is proportional to the square of the Doppler current which varies in proportion to $P_S P_R$. The noise power (denominator) is usually dominated by the electronic shot noise caused by $(P_S + P_R + P_B)$ the net light power intercepting the phototube. A minimum signal power of 10^{-11} Watts will cause the "other electronic noise" (such as an RCA 931 or 8645 - S20 photomultiplier with a load resistor greater than 50 ohms (Ω) and employing a low noise amplifier) to be negligible. Experience indicates that when P_R is an order of magnitude greater than P_S , it will dominate the denominator of Eq. (6-12). Such a large level of reference beam power will drive most PM tubes into a light insensitive, saturated, condition. However, it is under this condition that maximum (by means of a spectrum analyzer) S/N ratios are observed on reference beam LV systems. Equation (6-12) predicts that above a certain reference beam power, the S/N ratio is a maximum, and this fact is commonly observed experimentally. There exists a range in P_R/P_B of approximately 1000:1 for which even normal room illumination has little effect on S/N ratio since $P_R \gg P_B$, and $P_R \gg P_S$. Equation (6-12) reduces to

$$\frac{S}{N} = \frac{\eta P_S}{h\nu_o B P_B} \quad (6-13)$$

In the dual-scatter systems, with the collecting optics located between the two signal beams, either forward or backscatter configuration and if $P_{S1} = P_{S2}$ then

$$\frac{S}{N} = \frac{\eta P_S}{2 h\nu_o B P_B} \quad (6-14)$$

This implies that the reference beam system S/N is greater than with a dual-scatter system. However, use of a larger collecting lens increases the magnitude of P_S thus reducing this effect. This is a relatively simplified approach to the problem. In general, there is also a relationship between the particle size and fringe spacing which must also be considered when attempting to determine the actual S/N ratio. The Doppler signal is burst-like as shown in Fig. 16. The a-c or high frequency term contains the desired Doppler information whereas the d-c or low frequency term contributes to the degeneration of the signal quality. Therefore the S/N ratio must be modified to properly account for this phenomenon. The modification considers the ratio of particle size to fringe spacing which is related to the Michelson visibility function, defined as

$$V = (I_{S_{\max}} - I_{S_{\min}}) / (I_{S_{\max}} + I_{S_{\min}}) \quad (6-15)$$

where $I_{s_{max}}$ is the maximum scattered intensity from a bright fringe and $I_{s_{min}}$ is the minimum scattered intensity from the adjacent dark fringe. Under ideal conditions it can be shown that the visibility function (Ref. 17) reduces to

$$V = \frac{2J_1\left(\frac{\pi d}{\delta}\right)}{\frac{\pi d}{\delta}} \quad (6-16)$$

where J_1 is a first order Bessel function, d is the particle radius and δ the fringe spacing. The function, plotted in Fig. 17, has zeros at $1.22\pi\delta$, $2.233\pi\delta$ etc. indicating that when a particle has a diameter of $1.22\pi\delta$ etc., no Doppler or a-c signal can be detected. Therefore a means of varying the fringe spacing is therefore a desirable feature to be incorporated into the LV design.

D. Photodetector Frequency Response

Two types of photodetectors are generally used with the various LV systems: (1) a PM tube or (2) a silicon avalanche photodiode. The frequency response characteristics of the photodetector or its associated amplifiers (whether PM tube or photodiode) will ultimately limit the usable frequency range of the LDV system. One PM tube presently in use is the RCA 8644 with a rated anode pulse rise time of 15 nsec. The time-domain parameter, rise time, and the frequency domain parameter, 3-db frequency bandwidth are related for a first-order low-pass device by

$$t_r = \frac{0.35}{f_2} \text{ sec} \quad (6-17)$$

where t_r is defined as the time required for the photodetector output to rise from 0.1 to 0.9 of its final value in response to a step function input. The quantity f_2 is defined as that frequency at which the photodetector output has decreased in magnitude by -3 db from its pass-band value. Equation (6-17) shows that the 8644 PM tube output will have changed by -3 db and will have begun to decrease at a rate of 6 db/octave at a frequency f_2 given by

$$\text{upper 3 db freq.} = f_2 = \frac{0.35}{t_r} = 23.4 \text{ MHz}$$

This represents the approximate upper usable frequency limit disregarding possible response degradation caused by the circuitry attached to the photodetector by the user. The circuitry attached to the photodetector anode could also have a profound effect upon both the sensitivity and the frequency response of the device.

E. Photomultiplier Tube

The conventional (as distinguished from the microwave type) PM tube generally consists of three main sections: (1) a photoemissive cathode, (2) a photoelectron focusing assembly, and (3) a series of secondary electron emission multipliers. Two effects limit the upper usable frequency of the PM tube: (1) a time delay (transit time) between the input radiation and the tube output current and (2) a spread in transit time. The time delays are caused by the finite transit time of the photoemitted and the secondary emitted electrons through the tube. The transit time spread is caused by differences in the initial velocities of the photoemitted electrons and differences in the path length of the electrons through the dynode structure of the tube (Ref. 18). The time constant of the load resistor, R_L , and parasitic capacitance, C_p , associated with the anode lead usually limits the frequency response before the transit time limit is reached. The upper 3-db frequency response dependence upon the $R_L C_p$ time constant is given by

$$f_2 = \frac{1}{2 \pi R_L C_p} \text{ Hz} \quad (6-18)$$

This is an unavoidable frequency response limit and the only alternative is to reduce R_L if higher f_2 limits are needed. However, the reduction of R_L has the undesirable effect of reducing the voltage out of the PM tube since the PM tube is a current source device. Therefore, as a first approximation the anode current is constant (for constant incident radiation intensity) regardless of the value of the load resistor. The inevitable trade-off is between sensitivity (output volts/input watt) and frequency response. For example, the 8644 interelectrode capacitance (anode to all other electrodes) is 3.6 pico farads (pf). With the tube mounted inside a shielded enclosure and electrically connected to output circuitry, an additional 6.4 pf can easily be added to the 3.6 pf for a total C_p of 10 pf. Then if a 3-db frequency of 200 MHz is desired, R_L is

$$R_L = \frac{1}{2 \pi C_p f_2} = 80 \Omega \quad (6-19)$$

an undesirable value for sensitivity but necessary for the desired frequency response.

F. Measurement Uncertainties

Depending upon the optical arrangement of an LV system, velocities are determined from the Doppler shift of electromagnetic radiation scattered from a particle or, for an interference system, the rate at which the particle intercepts fringes in the probe volume. In either case the velocity of each particle is related to the detected frequency by:

$$\vec{v}_i = \delta f_i \quad (6-20)$$

where the subscript refers to the i th data point. The proportionality constant, δ , the fringe spacing is given

$$\delta = \frac{\lambda}{2 \sin \theta/2} \quad (6-21)$$

In lieu of frequency detection some electronic processing systems measure the period of a signal so that

$$\vec{v}_i = \frac{\delta}{\tau_i} \quad (6-22)$$

The uncertainty in velocity measurements attributed to the optical geometry of a stationary fringe system LV is given by (Ref. 19)

$$\frac{\Delta \vec{v}_i}{\vec{v}_i} = \beta + \nu \frac{\tau_i}{\delta} \quad (6-23)$$

where

$$\beta = \frac{\Delta \delta}{\delta} \quad (6-24)$$

and

$$\nu = \frac{\tau_i}{\delta} \quad (6-25)$$

The velocity-to-frequency conversion uncertainty can be shown to be (Ref. 19)

$$\frac{\Delta \delta}{\delta} = \frac{\Delta L}{L} - \frac{\Delta d}{d} \quad (6-26)$$

where L is the distance from the probe volume to a selected measurement, or calibration, plane and d is the spacing between the two beams at the plane. Since the beam diameters are finite it is a task to determine their exact geometric center. Similarly, the determination of the geometric center of the depth of field introduces an additional uncertainty.

As an example, a one-component LV was calibrated where the focal length of the unit was 122 cm and the angle between the beams was 5 deg. From the focal point, or cross-over region, the beams were permitted to expand to a plane 10 m distant. The beam separation, theoretically, should be 87 cm. A series of measurements was made and it was determined that the uncertainty in measuring the distance L was approximately $\Delta L = \pm 0.32$ cm. The uncertainty in the measurement for the distance between the beams, d , was $d = \pm 0.25$ cm. Consequently the value for β was 0.00321 and the conversion for ν was determined to be 8.7×10^{-7} sec/ft. Clearly the second term in Eq. (6-23) is considered negligible and the largest uncertainty lies in measuring distances accurately.

In a Bragg cell or moving fringe, velocimeter system an additional uncertainty exists that is attributed to the modulation frequency f_m . In this particular application the velocity is determined from:

$$\vec{v}_i = \delta \left[f_r - (1/\tau_i) \right] \quad (6-27)$$

where δ is the fringe spacing and f_r is the frequency equal to the difference between the Bragg cell modulation frequency and the local oscillator frequency used in the signal separation electronics as illustrated in Fig. 11. It was shown (Ref. 19) that the uncertainty in the velocity measurement is:

$$\vec{v}_i = \vec{v}_i \left[\frac{\Delta \delta}{\delta} - \frac{\Delta \tau_i}{\tau_i} \right] + \delta f_r \left[\frac{\Delta f_r}{f_r} + \frac{\Delta \tau_i}{\tau_i} \right] \quad (6-28)$$

Equation (6-28) is equally applicable to the stationary fringe system if $\Delta f_r = f_r = Q$. A Bragg cell LV is therefore inherently less accurate than a stationary fringe system because of the frequency-shifting of the beams. Equation (6-28) is equally applicable for other frequency-shifting techniques, such as a rotating grating, etc. In the case of the Bragg cell the uncertainty may be minimized by using a local oscillator to down-beat the signal to a frequency range anticipated by the range of velocities to be measured. The illustration in Fig. 11 indicates the applicability of the technique. Channel 1,

permits velocity measurements of ± 10 m/sec by using a local oscillator frequency of 14.77 Mhz. If the local oscillator is changed to 12.7 Mhz the measurement range is extended to ± 100 m/sec.

Rearranging Eq. (6-28) shows that the uncertainty in the sample velocity measurement is

$$\vec{V}_i = \alpha + \beta \vec{V}_i + v \vec{V}_i^2 \quad (6-29)$$

where

$$\alpha = \delta f_r \left(\frac{\Delta f_r}{f_r} + f_r \Delta \tau_i \right) \quad (6-30)$$

$$\beta = \frac{\Delta \delta}{\delta} - 2 f_r \Delta \tau_i \quad (6-31)$$

$$v = \frac{\Delta \tau_i}{\delta} \quad (6-32)$$

The relationship indicates that in addition to the distance measurement errors an additional term proportional to the square of the sample velocity is introduced. It therefore becomes important to have instrumentation, particularly in high velocity flow fields, that are capable of determining the period very accurately. In addition to the geometrical errors that were discussed there are systematic errors and instrument bias that must also be considered. These factors will be discussed in the next section.

G. Aero Engine Design Problems

The design of a practical LV system is functionally dependent upon the application for which it is intended. No one system is capable of covering the spectrum of requirements hence, specific tradeoff between the numerous parameters are required. In the case of combustion chamber probing of an aero engine the anticipated degree of turbulence and the size of the turbulent eddies must be considered. In this respect, the angle of intersection of the laser beams and the ratio of focal length to diameter of the lens must be determined. The resultant design dictates the probe volume size, fringe spacing, and number of fringes in the probe volume which in turn determines the calibration factor of the system. Assume for the moment that a frequency counting system is used for data processing and has an upper frequency limit of 200 MHz. The velocity to be measured is in the 500-m/sec range and an argon ion laser operating at a frequency of 0.5145 mm will be used. The maximum angle between the beams is determined as

$$\sin \theta/2 \max = \frac{(200 \times 10^6) / \text{sec} \times (0.5145 \times 10^{-6}) \text{ meters}}{2 \times 5 \times 10^2 \text{ m/sec}} = 0.103$$

$$\therefore \theta \max = 11.8 \text{ deg}$$

This angle is relatively large and somewhat impractical; a separation angle of 5 deg would be a more judicious choice. Using a lens of focal length 152.4 cm, the minimum lens diameter is found to be 152.4×0.0872 or 13.3 cm. The dimensions of the probe volume will be dictated by the smallest size of the eddy in the turbulent flow. If the upper limit of the turbulence frequency is v_{\max} , then by Taylor's hypothesis the size of the eddy Λ is

$$\Lambda = \frac{V}{v_{\max}} \quad (6-33)$$

using $V = 500$ m/sec and a turbulent frequency, v_{\max} of 50 khz results in an eddy size of 1 cm. Set the desired probe volume length to 0.5 cm_{\max} . The diameter of the focal volume with a 0.25 cm beam diameter at the last transmitting lens would be Eq. (6-6)

$$2b_o = \frac{4}{\pi} \times 0.5145 \times 10^{-4} \times \frac{152.4}{.25} \\ = 0.04 \text{ cm}$$

$$\text{The probe volume length} = 0.04 / \sin 5 \text{ deg} = 0.46 \text{ cm}$$

The fringe spacing in the probe volume would be Eq. (3-8)

$$\delta = \frac{0.5145 \times 10^{-4}}{0.087} = 6 \times 10^{-4} \text{ cm}$$

Hence the number of fringes, N_f , Eq. (3-10) is:

$$N_f = \frac{400}{6} = 66 \text{ fringes}$$

More than sufficient for accurate measurements using the various frequency-counting techniques. With a probe volume of 0.04 cm diameter and a velocity of 500 m/sec it would take a particle 0.8×10^{-6} sec to traverse the measurement region. If the processor requires 2×10^{-6} sec before another data point can be accepted (instrument dead time

included), and if one particle is assumed to be always in the probe volume, then the data acquisition rate would be approximately $5 \times 10^5/\text{sec}$ which is well within the Nyquist criteria for the 50 kHz turbulence frequency assumed.

VII. STATISTICAL BIAS OF LV DATA

A. Introduction

With the increased use of the LV a number of potential sources of error in the interpretation of data have been identified which are related to the dynamics of particles traversing probe volume. From the dynamics of fluid-particle interactions it has been shown (Ref. 20) that unduly large particles do not respond to fluid transients and may lead to significant errors in the interpretation of the data. Another type of error is concerned with inherent signal processing techniques. Continuous wave systems rely upon frequency tracking electronics to monitor the wave-form of a Doppler signal created by particulates traversing the probe volume. These analog signals are subject to Doppler ambiguities which are attributed to the presence of several particles, simultaneously, in the probe volume in addition to lateral and longitudinal velocity gradients. In general the digital burst-type electronics systems that have been developed minimize these ambiguities. It has been shown, however, (Ref. 21) that individual burst-type processing systems are also subject to statistical bias attributed to a finite sampling time in addition to exhibiting bias toward particles having higher velocities.

In the present section the statistical bias that arises when attempting to acquire the temporal mean of a collection of samples by arithmetic averaging the data will be discussed. The conditions for which this bias occurs is related to the number density of particulates in the fluid. When the number density is sufficiently low and the sampling frequency is less than the velocity equivalent frequency of the flow, no bias occurs. However, when the number density is high the mean velocity is biased in proportion to the turbulent intensity of the flow. It will also be shown that the bias, in determining the mean velocity and the turbulent intensity, may be eliminated by the use of harmonic averages in conjunction with arithmetic averages. The biasing problem, including particle-gas dynamic interactions, has been extensively treated (Ref. 22), therefore, only a brief summary of the salient features will be presented in this section.

B. Processing of Individual Data Points

Depending upon the optical arrangement of a LV system, velocities are determined from the Doppler shift of electromagnetic radiation scattered from a particle or, for an interference system, the rate at which the particle intercepts fringes in the probe volume. In either case, the velocity of each particle is related to the detected frequency by the relation

$$V_i = \delta f_i \quad (7-1)$$

where the subscript refers to the i th data point. The proportionality constant, δ , is given by

$$\delta = \frac{\lambda_0}{2 \sin \theta/2} \quad (7-2)$$

For the dual scatter system V_i is the component of velocity normal to the fringes, λ_0 is the wavelength of the incident radiation, f is the detected frequency and θ is the included angle between the two beams. As an alternative to the frequency detection, some systems measure the period, τ_i , of the signal so that

$$V_i = \frac{\delta}{\tau_i} \quad (7-3)$$

Since the flow is not generally steady, meaningful results are obtained by statistical averaging of the individual results. The arithmetic mean of data is the most direct measure of the mean velocity. For a collection of M samples of the velocity, V_i , the arithmetic mean $\langle \rangle$ is defined by

$$\langle V_i \rangle = \frac{1}{M} \sum V_i \quad (7-4)$$

Introducing (7-1) in (7-4), it is seen that

$$\langle V \rangle = \delta \langle f \rangle \quad (7-5)$$

Due to the direct relation between the mean velocity and frequency, the arithmetic mean velocity may be termed a frequency-averaged velocity. Similarly, the n th moment of the velocity is defined by

$$\langle V^n \rangle = \frac{1}{M} \sum_{i=1}^M V_i^n \quad (7-6)$$

If the sample, M , is sufficiently large, the corresponding central moments of the velocity are

$$\langle V'^n \rangle = \langle V^n \rangle - \langle V \rangle^n \quad (7-7)$$

The concept of frequency-averaging applies for the central moments because the relation to the mean and moments of a frequency is retained.

The relations (7-1) through (7-4), provide a consistent method for analyzing individual data points. It is known (Ref. 21) that if the velocity is a random variable and the number of samples is large, the results obtained by this procedure should provide good estimates of the mean and central moments of velocity. Nevertheless, it has been proposed (Ref. 22 and 23) that these estimates will be biased because the acquisition rate of the samples is related to the velocity. In an effort to resolve this anomaly consideration will now be given to the stimulation of the temporal mean of the velocity by individual realization data.

C. Temporal Average of Velocity

The quantity one wishes to stimulate with an LV system is the temporal mean of the velocity \bar{V} which may be defined as

$$\bar{V} = \frac{1}{\tau} \int_0^{\tau} V(t) dt \quad (7-8)$$

In laser velocimetry, however, data are not taken continuously since a particle will not be located in the probe volume at each instant. Consequently, (7-8) must be approximated by a relation such as

$$\bar{V} = \frac{1}{T} \sum_{i=1}^M V_i \Delta t_i \quad (7-9)$$

where the interval between samples is

$$\Delta t_i = t_{i+1} - t_i \quad (7-10)$$

To evaluate the temporal mean requires a model for the sampling interval. A general model of the sampling process, however, would require knowledge of the history of each particle in the flow. Obviously, this degree of generality is not practical. The approach taken, therefore, must be more heuristic, since knowledge of the instantaneous velocities is all that will be possessed in most cases.

If, in the vicinity of the probe volume, the number density of particles is constant, and velocity changes in the volume are strongly correlated with those immediately upstream, it may readily be shown from the kinematics of a one-dimensional motion that the time interval between successive samples must vary as

$$\Delta t_i = \frac{1}{\bar{V}_i} \quad (7-11)$$

where \bar{V}_i is the average fluid velocity over the interval. Introducing (7-11) in (7-10) and noting

$$T = \sum_{i=1}^M \Delta t_i \quad (7-12)$$

one obtains for the temporal mean

$$\bar{V} = \frac{\sum_{i=1}^M \frac{V_i}{\bar{V}_i}}{\sum_{i=1}^M \frac{1}{\bar{V}_i}} \quad (7-13)$$

Regardless of the complexity of the fluid motion over the interval Δt_i , the velocity can be represented by a series of the form

$$V(t) = \bar{V} + \sum_{n=1}^{\infty} V'_n \cos(W_n t - \beta_n) \quad (7-14)$$

The mean value over the sample interval is then obtained by introducing (7-14) in (7-8) to obtain

$$\begin{aligned} \bar{V}_i &= \bar{V} + \sum_{n=1}^{\infty} V'_n \sin(W_n t_i - \beta_n) \frac{\cos W_n \Delta t_i - 1}{W_n \Delta t_i} \\ &\quad + \sum_{n=1}^{\infty} V'_n \cos(W_n t_i - \beta_n) \frac{\sin W_n \Delta t_i}{W_n \Delta t_i} \end{aligned} \quad (7-15)$$

When $W_n \Delta t_i \gg 1$ that is, if the sampling frequency, $1/\Delta t_i$, is much less than the frequency of flow oscillations, it follows that \bar{V}_i approaches the mean fluid velocity, \bar{V} . For this case, Δt_i is essentially constant and the temporal and arithmetic averages are identical. While this procedure does not prove that the arithmetic average is the true mean velocity of the flow, it should be noted that long time delays between samples destroys any correlation between the instantaneous velocity and the sampling rate. As a result, it

is equally probable that a detected velocity will be greater or less than the mean value. It is, therefore, expected that the arithmetic mean should provide an unbiased estimate of the mean velocity.

On the other hand, if $W \Delta t_i \ll 1$, the sampling frequency is much greater than the frequency of flow oscillations.ⁿ For this case, it may readily be seen that $V_i \sim V_i$. This condition may be achieved by seeding the flow so that the particle number density is very high and the time between realizations short. When the interval is short, moreover, the temporal mean (Eq. 7-9) should be an excellent approximation to (Eq. 7-8). It follows from (Eq. 7-13) that the true temporal mean is given by the harmonic average

$$\bar{V} = \frac{1}{\frac{1}{M} \sum_{i=1}^M \frac{1}{V_i}} \quad (7-16)$$

Equation (7-16) forms the basis for the "statistical" bias of LV data. The nature of this bias may be more clearly understood if one substitutes (Eq. 7-3) in (Eq. 7-16) to obtain

$$\bar{V} = \frac{\delta}{\langle \tau \rangle} \quad (7-17)$$

The harmonic average of the velocity data may thus be interpreted as a "period-averaged" velocity. The period-averaged and frequency-averaged velocity, (Eq. 7-5), are related due to the inverse relation between period and frequency. If one notes that $f_i = 1/\tau_i$ and

$$f_i = \langle f \rangle + f'_i \quad (7-18)$$

it may be shown from (Eq. 7-5), (Eq. 7-17), (Eq. 7-18) and the expansion of $(1 + x)^{-1}$ that for $f'_i \ll \langle f \rangle$

$$\langle V \rangle = \bar{V} \sum_{r=0}^{\infty} \frac{(-1)^r \langle f'^{1r} \rangle}{\langle f \rangle^r} \quad (7-19)$$

It follows then that the frequency-averaged velocity will yield higher mean values than the period-averaged result. To determine the magnitude of this bias in terms of the fluid mechanic parameters, however, it is necessary to consider the higher temporal moments of velocity.

D. Magnitude of Statistical Bias

The n th central moment of velocity may be defined in terms of temporal averages by

$$V'^n = \frac{\sum_{i=1}^M [V_i - \bar{V}]^n \Delta t_i}{\sum_{i=1}^M \Delta t_i} \quad (7-20)$$

From the binominal expansion, one may write

$$[V_i - \bar{V}]^n = \sum_{s=0}^n (-1)^s \binom{n}{s} V_i^{n-s} \bar{V}^s \quad (7-21)$$

If the sampling frequency is high ($\Delta t_i = 1/V_i$) so that introducing (Eq. 7-21) in (Eq. 7-20) and carrying out the indicated average gives

$$V'^n = \sum_{s=0}^n (-1)^s \binom{n}{s} \langle V^{n-s-1} \rangle \bar{V}^{s+1} \quad (7-22)$$

Now the turbulence intensity is defined as

$$\sigma_{\bar{V}} = \left[\frac{V'^2}{\bar{V}^2} \right]^{1/2} \quad (7-23)$$

Setting $n = 2$ in (Eq. 7-22), one obtains

$$\sigma_{\bar{V}} = \frac{\langle V \rangle}{\bar{V}} - 1 \quad (7-24)$$

and

$$\langle V \rangle = \bar{V} (1 + \sigma_{\bar{V}}^2) \quad (7-25)$$

It is seen that the frequency-averaged velocity is biased in proportion to the square of the turbulence intensity. This result which agrees exactly with those of reference 23 and is plotted in Fig. 18. It should be noted, moreover, that for the assumed conditions \bar{v} is the "true" turbulence intensity and equation (Eq. 7-24) could be used to directly compute that quantity without recourse to obtaining central moments.

Arithmetic averaging of the data likewise must lead to biased results for the higher moments of velocity. For example, setting $n = 3$ in (Eq. 7-22), leads to

$$\frac{\bar{v}'^3}{\bar{v}^3} = \frac{\langle v^2 \rangle}{\bar{v}^2} - 3 \frac{\langle v \rangle}{\bar{v}} + 2 \quad (7-26)$$

From (Eq. 7-7), (Eq. 7-23), and (Eq. 7-25), one may obtain

$$\sigma_{\langle v \rangle} = \frac{\sigma_{\bar{v}}}{1 + \sigma_v^2} \left[1 - \sigma_v^2 + \frac{\bar{v}'^3}{\sigma_v^2 \bar{v}^3} \right] \quad (7-27)$$

The turbulence intensity obtained by arithmetic averaging is, therefore, biased with respect to the true value. For turbulent flows, \bar{v}'^3 is expected to be small (Ref. 24) since it is related to the skewness of the velocity probability distribution. Figure 19 presents the bias of the turbulent intensity for such a flow condition. It is seen that arithmetic averaging of the data significantly over predicts the turbulence intensity.

VIII. DATA PROCESSING

A. Introduction

No matter how skillfully the optics assembly is designed and constructed, the data acquisition and processing system is the most important component of an LV system. In the case of aero engine development and testing, the instrumentation requirements are extremely demanding. A lower frequency limit is on the order of 10 kHz because of the thermal motions of the scattering particles. The upper frequency limit for a 500 m/sec flow is on the order of 100 MHz. The highly fluctuating flow conditions that exist--even flow reversal--pose an operational frequency-response requirement of approximately ± 200 MHz. In addition the signal-conditioning electronics must respond to the sudden frequency variations dictated by the turbulent flow conditions (the signal is frequency modulated, say at an upper frequency of 50 kHz). Likewise the instrument should be capable of rejecting noise signals while passing the Doppler information signals. For the case of a large number of scattering centers, the system must not only accept continuous wave (CW) signals but also signals undergoing abrupt changes in amplitude (the so-called signal drop-out condition). On the other hand a small number of scattering centers dictate that the electronics system must accept frequency-burst signals having small amplitude information superimposed upon large amplitude pedestal voltage levels. Furthermore the instrument should be capable of furnishing "on-line" indications of the instantaneous, or average, Doppler frequency or velocity. Finally, the output of the signal-conditioning electronics must be in a form suitable for rapid data acquisition and processing. The stringent demands of the LV electronics requirements for aero-engine development precludes the use of the many analog processing systems available such as signal averagers, spectrum analyzers, tracking filters, etc. The candidate systems that meet these requirements incorporate direct frequency counters operating in conjunction with high speed data acquisition, storage and computing systems. Several of these devices, e.g., Doppler data "burst" type, real-time LV data analyzer along with several modifications of direct-counting techniques will be described. Although the photon-counting techniques could also serve as possible candidates, the data acquisition rate as compared with the real-time LV data analyzer is much too low. A review of the analog techniques for applications in engine development is contained in Ref. 25, and a review of photon counting techniques is contained in Ref. 26.

B. Doppler "Burst" Comparator Counter

The so-called "burst" type comparator counters that have undergone considerable development (Ref. 8, 27, 28) are extensively used in many laboratories. In principle their operation depends upon measuring the period of n cycles and m cycles of signal data and then comparing these periods. If the periods correspond to within a certain set percent called a "data window"; e.g., 0.5%, 1%, 3% etc., the data are accepted for further processing and analysis. If the data do not fall within the set window, they are rejected. There are numerous versions of the processor such as 4/8, 5/8 and 10/16 etc., in addition to dual time interval counters where the data have to pass both comparator tests. The problem with these counters is that they are biased toward the larger particles where good S/N ratios are evident. This is readily shown in Fig. 20 where the results of experiments, using various comparator techniques, were evaluated under poor S/N conditions. In this example the S/N ratio was set at 0.09. After 1000 data points had been evaluated by the various comparator conditions approximately 1% of the data were valid. Of course as the signal quality improves so does the data rate and the number of valid data points as shown in Fig. 21, for the case of the dual comparator. Nevertheless the data acquisition rate is essentially proportional to the S/N ratio; hence, attempts are made to maximize this relationship although all of the contributing factors are difficult to evaluate quantitatively.

C. Real-Time Processor

The newly developed (Ref. 29) "real-time processor" technique is a prototype that is being used for LV applications. When a particle traverses the focal volume, it cuts fringes at a rate proportional to its velocity. The data interval is measured when the particle traverses the first detectable fringe, above a threshold value, and ends when it traverses the third detectable fringe. The time interval for traversing the three fringes is the first data input for the histogram to be generated. A second data input is acquired as the particle leaves the third fringe and arrives at the fifth fringe, etc. After a predetermined number of samples are acquired, a histogram is developed. The data rate has been reported to be on the order of 10^7 /sec. With data rates of this magnitude, power spectral densities and turbulent frequency measurements should be realizable, almost in real time.

The analyzer digitizes the LV "burst" data by counting clock pulses from a 150-MHz clock during the fringe crossing time interval (Fig. 22). Two counters are alternately counting and storing data into a scratch-pad memory which serves as a high-speed buffer. The data generation rate is one-half the LV burst frequency; and expeditious handling is required while the burst signal is present. One of the scratch pad memories is receiving data from the two counters while the alternate memory is passing its data to the address lines of a histogram-generating random access memory block. As each successive address is applied, the memory word so addressed is incremented by one count. The

resultant grouped data in the memory provides a histogram of the LV burst data. The memory address defines the velocity data cell number and the stored word defines the frequency of occurrence within a given cell. Each 14-bit word can store up to 16,384 samples per cell at rates up to 10 million samples/sec. This provides for useful data compression of the large amount of data being processed.

An auxiliary CRT visual display has "on line" access to the memory-stored histogram data being accumulated. The display is a condensed look at the 256 x 16,000-point memory matrix containing over 4 million possible values. When a selected number of samples has been taken, the histogram is rapidly transferred to a first-in first-out (FIFO) buffer memory and the empty histogram memory is free to resume data acquisition. The FIFO data in turn are clocked into a programmable calculator for data reduction. The calculator prints the histogram distribution data and computes the mean and standard deviation of the data set. Approximately 3 sec are required to reduce the histogram data that may contain up to half a million samples. A calculator controlled x-y plotter can be used for plotting a velocity profile of the LV probe volume traverse.

The determination of the measurement accuracy is complicated in actual test environments since it is almost impossible to have steady conditions. The technique was evaluated utilizing a simulated Doppler signal by amplitude modulating a light-emitting diode with a function generator whose frequency can be precisely measured. The diode possesses the required bandwidth (10 to 30 MHz) to simulate a frequency burst. A photomultiplier tube acquires the signal from the light emitting diode. Background radiation is produced by a noncoherent light source to provide sufficient noise to simulate the actual signal obtained in a test program.

A series of 1,000 histograms, each containing approximately 8,000 samples, was taken and the mean of each sample series was determined. During the sampling period the amplitude modulated light frequency was held within $\pm 0.05\%$ of 12 MHz. The mean (X_m) of the 1,000 sample mean values was calculated to be within 0.05% of the standard frequency and the standard deviation of the distribution of the mean values was found to be 0.07% of the mean (X_m). The data provided a 99% confidence level indicating that no individual sample mean will depart more than three standard deviations from the distribution mean or more than 0.25% from the standard test frequency. These data are plotted in Fig. 23b. A similar distribution of the instrument sampling a continuous sine-wave signal is also shown in Fig. 23a for comparison purposes. The distribution sample, where the number of samples per histogram was reduced from 8,000 to 500 samples, showed little change in the computed results when the experiment was repeated. The reduced sample time interval of the smaller sample data group would be significant only when measuring turbulence parameters.

Another experiment was performed where the velocity distribution in a region near a normal shock in a 30-cm transonic wind tunnel at the Arnold Engineering Development Center. The signals stemming from a dual scatter, Bragg cell, laser velocimeter operating in the on-axis backscatter arrangement were processed simultaneously by the real-time LDV data analyzer and with the conventional "burst" counter type processor requiring ten consecutively detected fringe crossings per sample. The best estimate of the Mach number at the shock was between Mach 1.1 and 1.2 resulting in an estimate of the downstream gas velocity of between 277 and 310 m/sec. The data in Fig. 24 show that within only 0.025 to 0.075 cm of the shock, the data processed by the real-time analyzer fall within this range of estimates. The conventional-counter-processed data, for the particular S/N ratio condition, lags the velocity for a distance greater than 1 cm from the shock front. The indications are that the analyzer is processing signals from much smaller particles than the conventional "burst" counter. A theoretical study was performed to ascertain particle lag effects. The results are shown in Fig. 25 where the velocity of various size particles is plotted as a function of average distance from the shock front. From the data in Fig. 25 (Ref. 30) it is estimated that the particle sizes, from which the majority of data were taken, appear to be approximately 0.1 μ m.

The interesting feature concerning the real-time system is that there is no data rejection logic incorporated into the design. The particle lag effect is still evidenced in the data since a skewness in the velocity distribution exists. In evaluating the data the mode value was used to ascertain the mean value of the gas velocity distribution which reduces, and in some cases eliminates, the effects of particle lag (Ref. 30). Both the mode and mean values of the velocity distribution are compared with theory in Fig. 24. Of particular significance are the data acquisition rates of the two techniques. The analyzer required 0.10 sec to acquire 4,000 measurements, whereas the conventional "burst" counter required approximately one minute of sample time. The capability of on-line visual display of the analyzer histogram, as it is being generated is a valuable asset not only monitoring the flow conditions but in monitoring the system operation itself.

D. Computing Counter

Several additional straightforward counting techniques are currently being used (Refs. 31 through 33) as a means for processing the Doppler signals. One of the techniques uses a visibility processor (Ref. 34) that measures the signal amplitude continuously throughout the burst cycle. When the scattered light intensity reaches a pre-set signal threshold level, of the photodetector, the visibility processor triggers a computer counter thereby starting the counting cycle. During the ensuing time-interval both clock pulses and valid zero crossings are counted. The counting period ends on the first valid zero crossing after the signal level falls below a set threshold value. At this time the gate is closed and the system is re-set for the next, burst, data input.

Upon completing the counting cycle the frequency is determined by the following relationship

$$F_d = N_e / N_t (F_c) \quad (7-1)$$

N_e is the number of signal zero crossings obtained during the sampling time, N_t is the total number of clock pulses counted, and F_c is the clock frequency. A schematic illustration of the system is shown in Fig. 26, and the signal characteristics, within the processing system, are shown in Fig. 27. In the proposed arrangement two-component velocity measurements are made simultaneously with particle size measurement. The velocities are determined with HP 5345A computing counters having a clock frequency of 500 MHz. The visibility processor, monitoring the quality of each zero crossing throughout the burst, triggers the computing counters after the first valid zero crossing after the threshold signal amplitude value has been attained.

The determination of the particle size using interferometric techniques has been reported (Refs. 17, 25, 35 and 36) and is currently under development at the AEDC. If the size of the particle, traversing the fringes in the probe volume, is small compared with the fringe spacing the scattered light intensity will be proportional to the incident light intensity through the particle's trajectory. If the size of the particle is comparable in size to the fringe spacing the particle will partially overlap bright fringes even when it is centered on a dark fringe and produce a burst signal as shown in Fig. 16a. A larger particle traversing the same path as a smaller particle might produce a signal as shown in Fig. 16b. A still larger particle could overlap several adjacent fringes and produce a signal such as shown in Fig. 16c. There could also be a range of particle sizes where the relationship between the a-c signal and d-c pedestal is such that there would be no signal detected as shown in Fig. 17 and qualitatively discussed in Section V-C. The conclusion is that the relative amount of signal-oscillation that modulates the d-c pedestal is a function of the size of the particle relative to the fringe spacing--which has been verified both analytically and experimentally.

In the particle size-velocity measuring system described the data acquired and processed, from both the visibility processors and the computing counter electronics, are transmitted to a data acquisition and storage system. A histogram may also be acquired on-line on either the particle size distribution or velocity distribution or any combination thereof depending upon the type data format desired. It has been reported that the application of the direct counting technique can realize an order-of-magnitude improvement in data acquisition rate, over previous "fixed-gate" frequency counting techniques (Ref. 31).

The velocimeter acquires information on the flow-field characteristics, including turbulence, by measuring the motion of particles in the focal volume. If the flow field possesses large velocity gradients and/or if the fluid motion is turbulent the particles will lag the fluid motion by an amount proportional to the particle diameter and density (Ref. 37 and 38). Many studies of LV characteristics (Refs. 38 and 39) considered the response of particles to fluid transients to determine the particle size required to a specified flow-field condition. The results of one such study (Ref. 30) are shown in Fig. 25 for the case of particles traversing through a shock front. If the particles in a given flow were of a single size and chemical composition, the studies would be sufficient to define the effects of particle lag on the LV measurements. In practice, the measurements stem from different types and sizes of particles that traverse the focal volume and the results reflect these variations.

In the case where measurements are made on the inherent impurities contained in the atmosphere, it is obvious that a wide range of particle sizes, shapes and composition will be present. Because of the particle size distribution, hence velocity distribution, and discounting any other errors or bias the LV measurements will appear to indicate the presence of turbulence even under perfect laminar flow conditions. The magnitude of the indicated turbulence intensity is functionally dependent upon (1) the velocity lag of the particle traversing the probe volume, (2) the inability of the LV to discriminate particles of a given size such as in the case of the visibility modification to the S/N ratio, and (3) the size and density distribution of the particles comprising the data set.

By artificially seeding the flow, attempts are made to control the results by introducing particles of known size and characteristics. Unfortunately, even controlled seeding will produce a range of particle sizes albeit narrower than those found in the atmosphere.

IX. OPERATIONAL LV SYSTEMS

A. Introduction

To conclude the present introduction to the fundamentals of LV measuring techniques a brief description of operational installations for aero engine and other fluid dynamic investigations are presented. In this respect it may be affirmed that the LV systems are being seriously adopted for effecting non-intrusive measurements of flow fields where data cannot be accurately acquired by other means.

B. Engine Test Facility Installation

In the present section a few LV installations in test environments and the problems encountered will be briefly discussed. A one component, backscatter, LV system was installed in an altitude chamber at the AEDC to measure the exhaust characteristics of an operating aircraft engine. A unit in such an environment poses a number of problems that must be resolved including the extremely high radiation heat flux, and exposure of the support structure to mechanical and/or acoustic induced vibrations. The LV system therefore requires a suitable isolated enclosure to protect it from the environment even though it does not come in physical contact with the hot exhaust flow from the engine. The housing constructed for the LV unit had a capability of maintaining atmospheric pressure while the engine was altitude tested. This is a necessary requirement to prevent the electrical breakdown of the plasma tube and other high voltage components. The system was isolated from the localized aerodynamic loads in the test cell so that the vibration would not adversely affect the optical alignment. The temperature in the vicinity of the electro-optical components must be controlled to prevent thermally induced component failures and sufficient vibration isolation was utilized to preserve the integrity of the system in addition to maintaining radiation alignment. In addition, in a test environment, oil and fuel spills are not uncommon, and attention had to be directed to the prevention of contamination that could cause signal degradation of any exposed optical components. Figures 28a and b are photographs of the installation. The entire system is enclosed in a thermally insulated housing. The argon ion laser is shown on the left side of the photograph. An umbilical furnishes the electric power and coolant water for the installation. The beam-splitting blocks are located on the top right hand region of the environment enclosure. The two beams traverse a light baffle before entering the transmitting lens in the lens housing by means of a turning mirror. The focusing lens also serves as a scattered light collector. The collected light is transmitted to a focusing lens to the photomultiplier by means of a turning mirror located at the bottom center of the unit. From the photomultiplier tube the signal is sent, by means of a preamplifier and cabling, outside the test cell to the signal-processing electronics. To minimize the background radiation a laser line filter (.5145 μm) was used. As shown in both figures, considerable baffling and heat shielding is required to minimize scattered radiation entering the detection system and to reduce the heat load to the velocimeter enclosure. A heat shield was also placed between the engine exhaust and the optics system to reduce the radiative heat transfer to the optics. As can be seen in Fig. 28b, the heat shield contains a port through which the transmitted and scattered light pass.

Access to the collecting optics was by means of a removable side plate and the entire system was also accessible from a removable top plate of the housing. All of the optical components, with the exception of the transmitting lens, were mated on a base plate containing four optical rails. The base plate was attached to the remaining enclosure and onto the test cell by means of pneumatic vibration isolators located on each of the corners.

B. LV Installation in a Plenum Chamber

A two dimensional, backscattered, Bragg cell unit was installed in the plenum chamber of an AEDC transonic aerodynamic test cell as illustrated in Figs. 29a and b. As in the previous installation a special housing was designed to maintain proper pressure and vibration isolation. Figure 29a shows the LV system skeletal construction. The laser is mounted in a pressured structure, whereas the optics and electronics are mounted on top without any special environmental provisions. Turning mirrors were used to keep the package compact since space was limited. In this particular configuration the transmitting portion of the optics are totally enclosed in metal tubing to minimize the possibility of scattered radiation from entering the collection system optics. Inside the metal tubing another lens is mounted on a small traverse thereby providing a zoom scanning capability. It was possible to scan ± 35 cm from the centerline of the tunnel. The entire unit was operated from the control room of the tunnel. As in the previous case, the electronic processors and associated computing equipment were located external to the tunnel environment.

C. Furnace and Diesel Engine LV

A two-dimensional Bragg cell system was designed to be used for probing an EPA furnace using various fuels. The design of the unit incorporating both forward and backscattering capabilities is schematically illustrated in Fig. 28a. In this particular design the laser is mounted on a rack below the optics and traversing system. The laser beam is directed into the two dimensional Bragg cell by means of mirrors and a mode matching system of optics. From the Bragg cell, positioning mirrors direct the beams to the focusing lens and then into the furnace by means of the output mirror. The back-scattered radiation is collected by the mirror and reflected to the collecting-transmitting lens. At this point the scattered light is reflected by means of another mirror, turned toward the light collecting optics system, and directed to the photomultiplier tube. A photograph of the unit (Fig. 28b) shows the cored mirror and transmitting-collecting lens. This minimizes the probability of parasitic reflections from the transmitting portion of the beam to the collecting-detection system. A laser line filter in front of the photomultiplier reduces the effect of the noise stemming from the light emitted in the combustion chamber. The unit both forward and backscattered component has operated quite satisfactorily in both oil and gas flames. The forward-scattered portion of the system comprises a traversing system that is synchronized with the transmitting traverse system to guarantee alignment between the transmitting and receiving optics. A system of this same design was also used to make two dimensional velocity measurements in the combustion

chamber of a diesel engine (Ref. 40). The fundamental problem that existed in both the experiments was to keep the windows clean from soot and other contaminants. In the diesel engine experiment the problem was more severe in that window fogging occurred within a few minutes after the combustion process was initiated.

X. CONCLUSION

In this brief introduction to the principles of the laser velocimeter both the reference- and dual-scatter system have been described. There are many variations to the concepts, and the individual research worker will invariably develop his own technique in accordance with the experimental program he is pursuing. The reference beam system can be effectively used in fluid flows containing a large number of impurities so that, essentially, a continuous signal is obtained. In this case frequency trackers and similar analog techniques may be used for data acquisition and processing. In the case of the more hostile environments, such as in combustion chambers, compressors etc. the dual-scatter or Doppler differential technique is the preferred system. In this case more expensive counting systems used in conjunction with high-speed data acquisition and storage equipment are required. Particularly in the illustrated case of the real-time processor where 10 million data points and 5,000 histograms per second can possibly be acquired, high speed computing equipment is a necessary adjunct for the processing of data.

In general it is desirable to design an LV system to perform in the back-scattered mode of operation--the preferred orientation. In this mode of operation the optical components are rigidly tied to a base plate thereby minimizing alignment problems. Only one window is required for the entrance and scattered beams thereby facilitating modifications to wind tunnels, combustion chambers etc. The entire unit can then be mounted on a three dimensional traverse system to scan across a flow field, whereas, in the forward scatter mode of operation synchronous motion of transmitter and collector optics is required to maintain alignment--a tedious task. However, one does sacrifice signal intensity in the back-scattered mode of operation. For a given particle size, composition and velocity the intensity of light scattered in the forward direction is approximately two orders of magnitude greater than in the back-scattered direction. For this reason a relatively high powered laser is a dictating requirement for LV operation in the hostile environments encountered in engine research and development. Details concerning the scattering mechanisms, the variations in light intensity as a function of the particle parameters and the peculiarities exhibited in the scattering process is beyond the scope of this lecture, however, good treatments to the subject may be found in Refs. 3, 4, 25 and 41.

Despite the necessity for considerable care in the design of an LV system the accelerated application of the technique as evidenced by the myriad of symposia and workshops during the past decade specifically designated to the presentation of new developments and applications of laser anemometry justify its application as a diagnostic tool. Dr. Wisler in a following lecture will discuss other salient features of the velocimeter in practical aero-engine applications.

REFERENCES

1. Yeh, Y. and Cumming, H. Z., "Localized Fluid Flow Measurements with a He-Ne laser Spectrometer," Applied Physics Letters, Vol. 4, No. 10, May 1964, pp. 176-178.
2. Boutier, A., "A Compact Velocimeter for Measurements in Highly Turbulent Flows," ESA TT-276 Office National d'Etudes et de Recherches Aeronautiques, 29, Avenue de la Division, Leclerc, 92320 Chatillon, France, 24 October 1974.
3. James, R. N., Babcock, W. R., and Seifert, H. S., "Application of a Laser Doppler Technique to the Measurement of Particle Velocity in Two Phase Flows," AFRPL-TR-66-119, May 1966.
4. Morse, H. L., Tullis, V. K., Babcock, W. R., and Seifert, H. S., "Development Application and Design Specifications of a Laser Doppler Particle Sensor for Measurement of Particle Velocities in Two Phase Rocket Exhausts," AFRPL-TR-68-153, Vols. I and II, September 1968.
5. Rolfe, E., Silk, J. K., Booth, S., Myser, K., and Young, R. M., "Laser Doppler Velocity Instruments," NASA CR-1199, December 1968.
6. Lewis, R. D., Chatterton, N. E., and Watson, H. J., "Investigation of Two Dimensional Flow Measurements using the Laser Doppler Technique," Technical Note AST-285 (AD685249), December 1968.
7. Thompson, H. D., and Stevenson, W. H., Editors, Proceedings of Second International Workshop on Laser Velocimetry, Vols. I and II, Purdue University, 1974.
8. Lennert, A. E., et al., "Application of the Laser Velocimeter for Trailing Vortex Measurements," AEDC-TR-74-26 (AD-A002151), December 1974.
9. Durst, F., and Whitelaw, J. H., "Integrated Optical Units in Laser Anemometry," J. Physics, E 4, 1971, pp. 804.
10. Yanta, W. J. and Lee, R. E., "Determination of Turbulence Properties with the Laser Doppler Velocimeter and Conventional Time-Average Mean Flow Measurements at Mach 3," AIAA paper 74-575, 1975.
11. Brayton, D. B., and Goethert, W. H., "A New Dual-Scatter Laser Doppler-Shift Velocity measuring Technique," ISA Transactions, Vol. 10, No. 1, 1971, pp. 40-50.
12. Mazumder, M. K., "Laser Doppler Velocity Measurements without Directional Ambiguity by Using Frequency Shifted Incident Beams," Applied Physics Letters, Vol. 16, No. 11, June 1970, pp. 462-464.
13. Born, M., and Wolf, E., Principles of Optics, 2nd Edition, Pergamon Press, New York, 1964, p. 597.
14. Damon, R. W., Maloney, W. T., and McMahon, D. H., Physical Acoustics, Edited by W. P. Mason and R. N. Thurston, Academic Press, New York, Vol. 7, Chap 5, 1970.
15. Kogelnik, H., "Imaging of Optical Modes-Resonators with Internal Lenses," Bell System Technical Journal, May 1965.
16. Sci-Metrics, Inc., Bragg Cell Handbook, Tullahoma, Tennessee 37188.
17. Farmer, W. M., "Measurement of Particle Size, Number Density, and Velocity Using a Laser Interferometer," Applied Optics, Vol. 11, No. 11, 1972.
18. RCA Electron Tube Handbook, Radio Corporation of America, Harrison, New Jersey.
19. Barnett, D. O., and Giel, T. V., Jr., "Application of a Two-Component Bragg Cell Laser Doppler Velocimeter to Turbulence Measurements in a Subsonic Jet," AEDC-TR-74-34, May 1976.
20. Berman, N. S., "Particle-Fluid Interaction Corrections for Flow Measurements with a Laser Doppler Flowmeter," NASA-CR-124154, 1972.
21. McLaughlin, D. K., and Tiederman, W. G., "Statistical Modeling in Laser Doppler Anemometry," Workshop Proceedings on Theory and Application of Laser Doppler Anemometry, Oklahoma State University, 1973.
22. Proceedings of the LDA Symposium, Copenhagen, August 25-27, 1975, "Theory of Flow Measurement by Laser Doppler Methods," published 1975.
23. Gramer, H., "The Elements of Probability Theory," Wiley, New York, 1959.
24. Townsend, A. A., "The Measurements of Double and Triple Correlation Derivatives in Isotropic Turbulence," Proceedings Cambridge Philosophical Society, Vol. 43, Part 4, pp 560-570, 1947.

25. Durst, F., and Whitelaw, J. H., "Optimization of Optical Aneometers," Proceedings of the Royal Society of London A, 324, 1971, pp. 157-181.
26. Pike, E. R., "Photon Correlation Velocimetry," NATO Advanced Study Institute Proceedings, Capri, Italy, Plenum Press, 1976.
27. Lennert, A. E., et al., "Laser Technology in Aerodynamic Measurements," AGARD LS 49, June 1971.
28. Asher, J. A., "Laser Doppler Velocimeter System Development and Testing," General Electric Technical Information Series Report No. 74CRD295, Corporate Research and Development Distribution, Schenectady, New York, October 1972.
29. Kalb, H. T., and Cline, V. A., "New Technique in the Processing and Handling of Laser Velocimeter Burst Data," Rev. Sci. Instrum. Vol. 47, No. 6, June 1976, pp. 708-711.
30. Cline, V. A., and Lo, C. F., "Application of the Dual-Scatter Laser Velocimeter in Transonic Flow Research," AGARD Symposium on Applications of Non-Intrusive Flow Instrumentation in Fluid Flow Research, St. Louis, France, May 1976.
31. Hoesel, W., and Rodi, W., "A Highly Accurate Method for Digital Processing of Laser-Doppler Velocimeter Signals" Sonderforschungsbereich 80, University of Karlsruhe, December 1975.
32. Melling, A., and Whitelaw, J. H., "Design of Laser Doppler Anemometers for Reciprocating Engines." Report No. CHT/76/6 Imperial College of Science and Technology, London, England, November 1976.
33. Pfeifer, H. J., "Review of High Speed Applications of Laser Anemometry in France and Germany." AGARD Conference Proceedings No. 193 on Applications of Non-Intrusive Instrumentation in Fluid Flow Research, St. Louis, France, May 1976.
34. Roberds, D., "Particle Sizing Using Laser Interferometry," Applied Optics, Vol. 16, No. 7, July 1977.
35. Robinson, D. M., and Chu, W. P., "Diffraction Analysis of Doppler Signal Characteristics for a Cross-beam Laser Doppler Velocimeter," Applied Optics, Vol. 14, No. 9, 1975, pp. 2177-2183.
36. Durst, F., "Scattering Phenomena and Their Application in Optical Anemometry," Journal of Applied Mathematics and Physics, (ZAMP), Vol. 24, 1973, pp. 619-643.
37. Yanta, W. J., "Turbulence Measurements with a Laser Doppler Velocimeter," Naval Ordnance Laboratory Report NOL TR-73-94, May 1973.
38. Maxwell, B. R. and Seasholtz, R. G., "Velocity Lag of Solid Particles in Oscillating Gases and in Gases Passing through Normal Shock Waves," NASA TND-7490, 1974.
39. Barnett, D. O. and Giel, T. V., Jr., "Laser Velocimeter Measurements in Moderately Heated Jet Flows." AEDC-TR-76-156, (AD-A038283), April 1977.
40. Lennert, A. E., et al., "Electro-Optical Techniques for Diesel Engine Research," AIAA Paper No. 76-68, AIAA 14th Aerospace Sciences Meeting, Washington, D.C., January 26-28, 1976.
41. H. C. Van de Hulst, Light Scattering by Small Particles, John Wiley & Sons, Inc., New York 1957.

ACKNOWLEDGEMENTS

The author gratefully acknowledges the permission, to include in this portion of the lecture, the results of work performed by D. O. Barnett, H. T. Kalb, V. A. Cline, B. W. Bomar, and D. W. Roberds. The assistance of R. A. Belz, J. M. Mann, and G. Chumbley and his staff in editing and preparing the lecture notes in final form is greatly appreciated. Finally, the expedient typing of the final copy by Mrs. Melinda Knies is deeply appreciated.

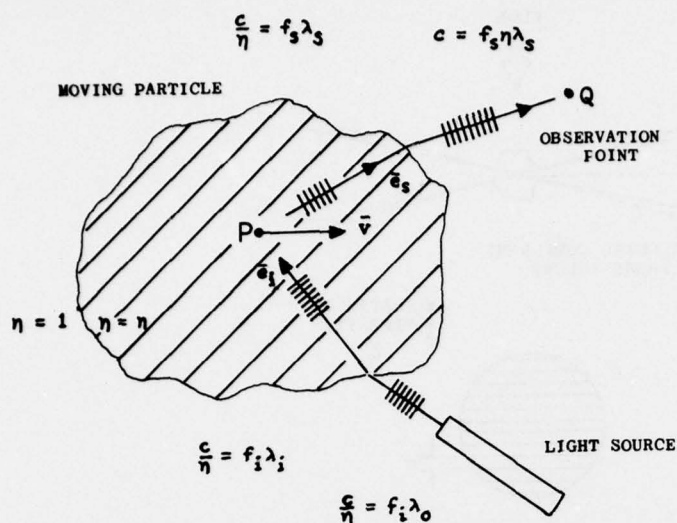


Figure 1a. Isotropic Medium of Index of Refraction η Moving at a Velocity v .

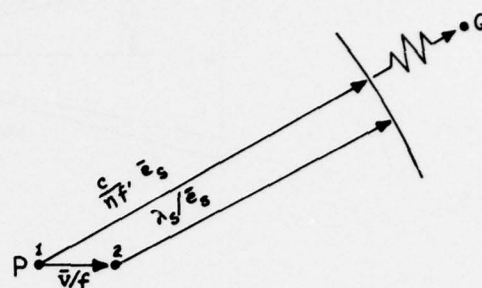


Figure 1b. Doppler Frequency Shift Assuming a Refractive Environment.

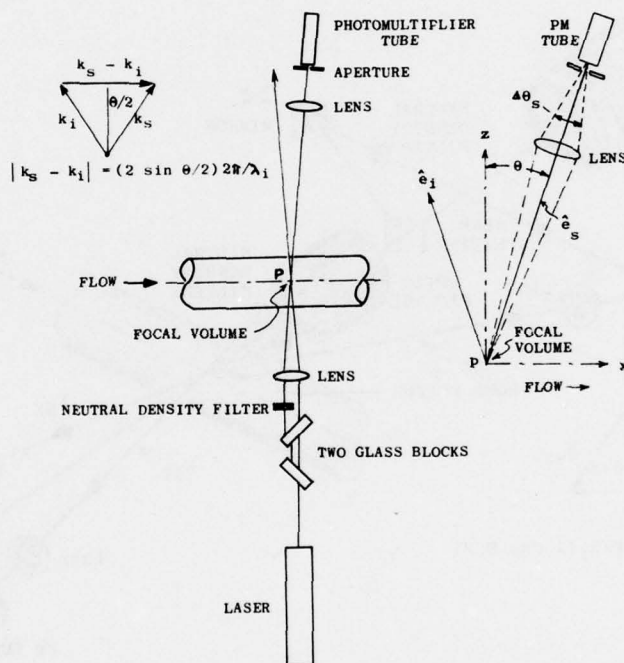


Figure 2a. One Component Reference Beam.

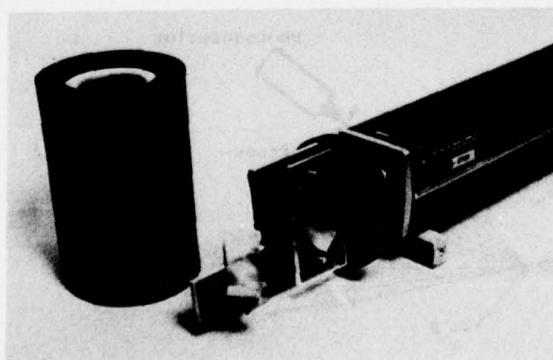


Figure 2b. Optics of Two Component Reference Beam Laser Velocimeter.

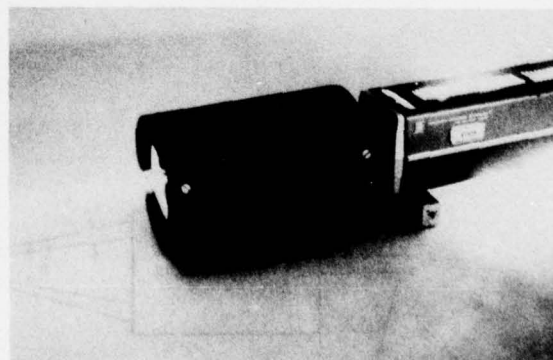


Figure 2c. Operating Two Component Reference Beam Laser Velocimeter.

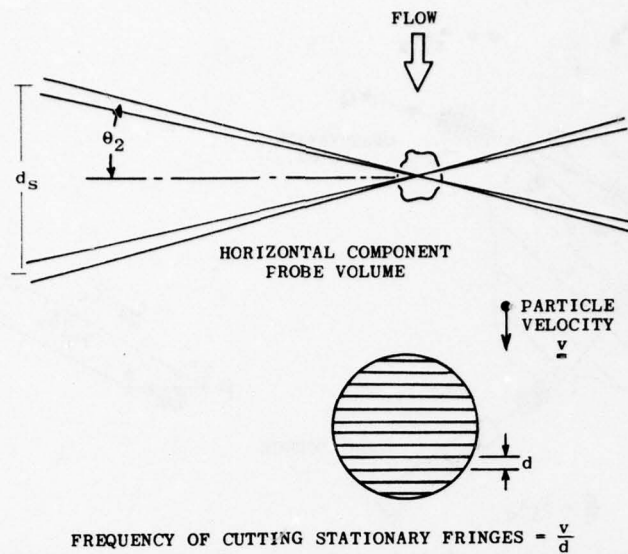


Figure 3. Fringe Analysis of Laser Velocimeter.

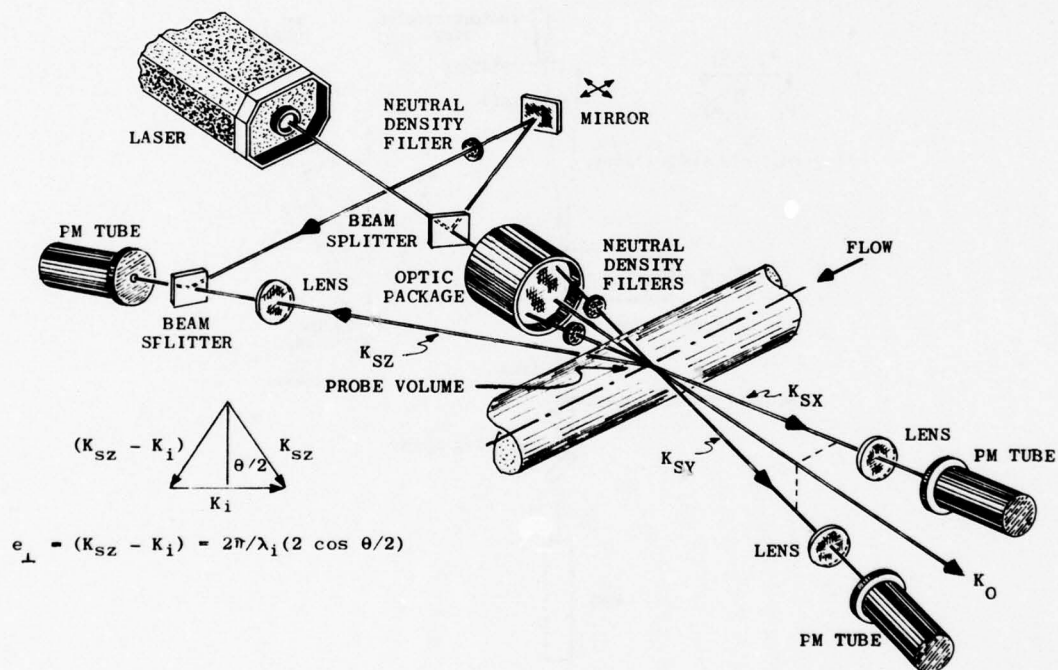


Figure 4. Three Component Reference Beam.

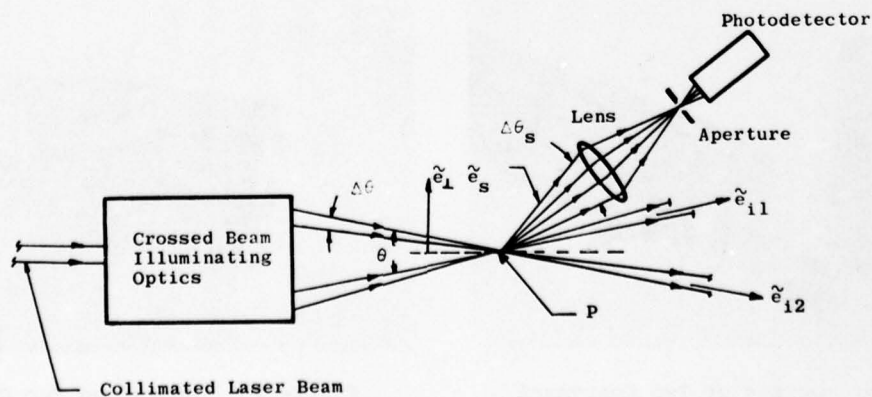


Figure 5. Two Beam Dual Scatter.

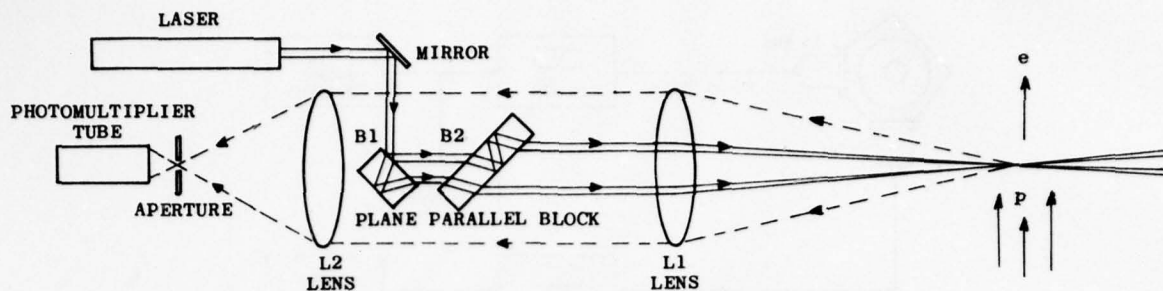


Figure 6. Dual-Scatter, Backscatter Laser Doppler Velocimeter System.

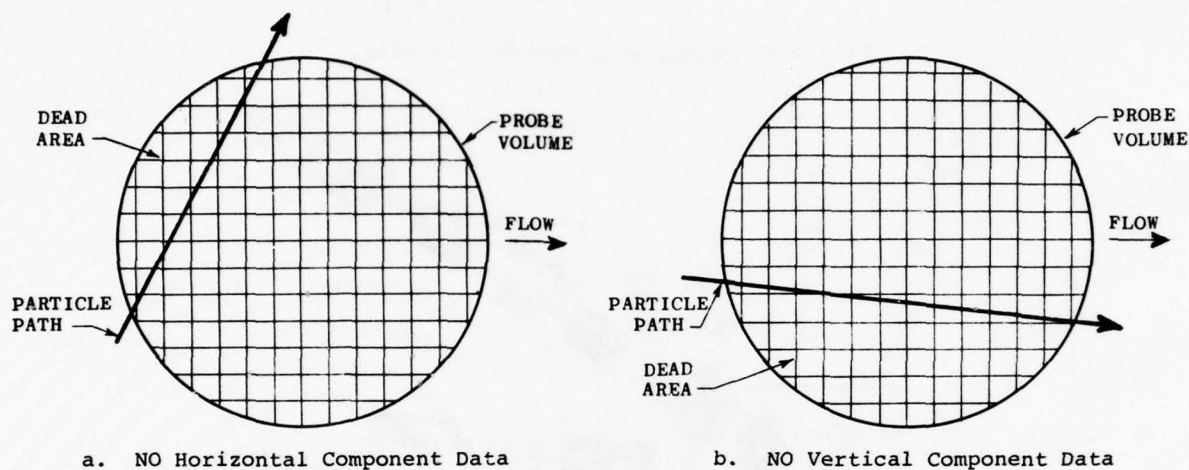


Figure 7. Insufficient Number of Cycles.

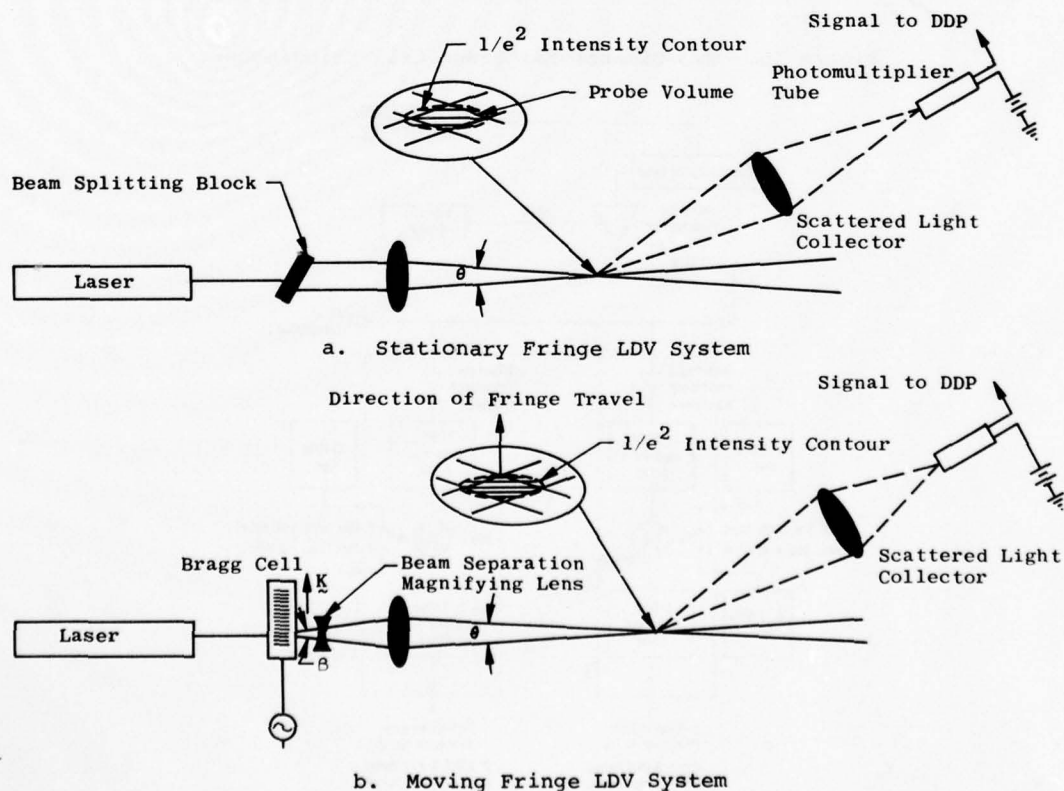


Figure 8. Stationary Fringe and Moving Fringe LDV Systems.

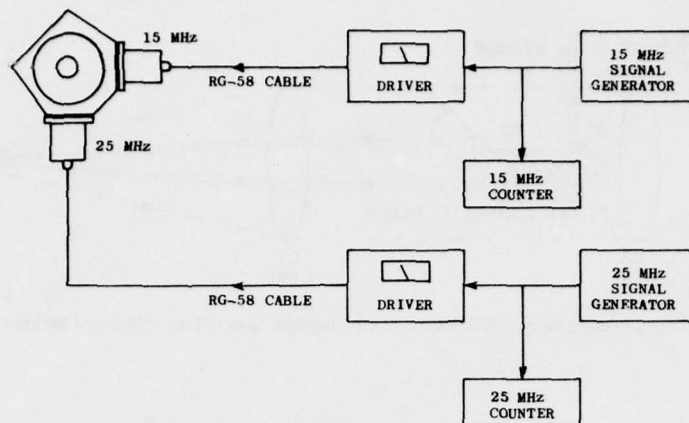


Figure 9. Bragg Cell System Schematic.

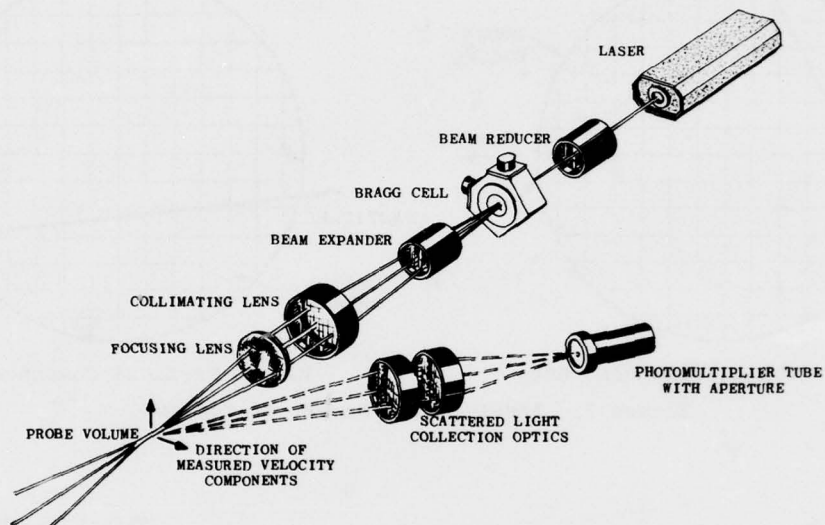


Figure 10. Two-Dimensional Bragg Cell Velocimeter.

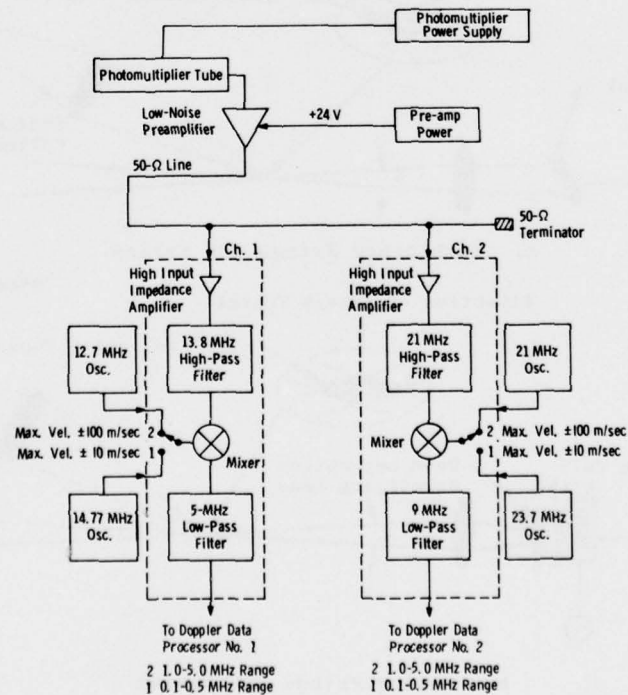


Figure 11. Signal Separation and Spectrum Translation Systems.

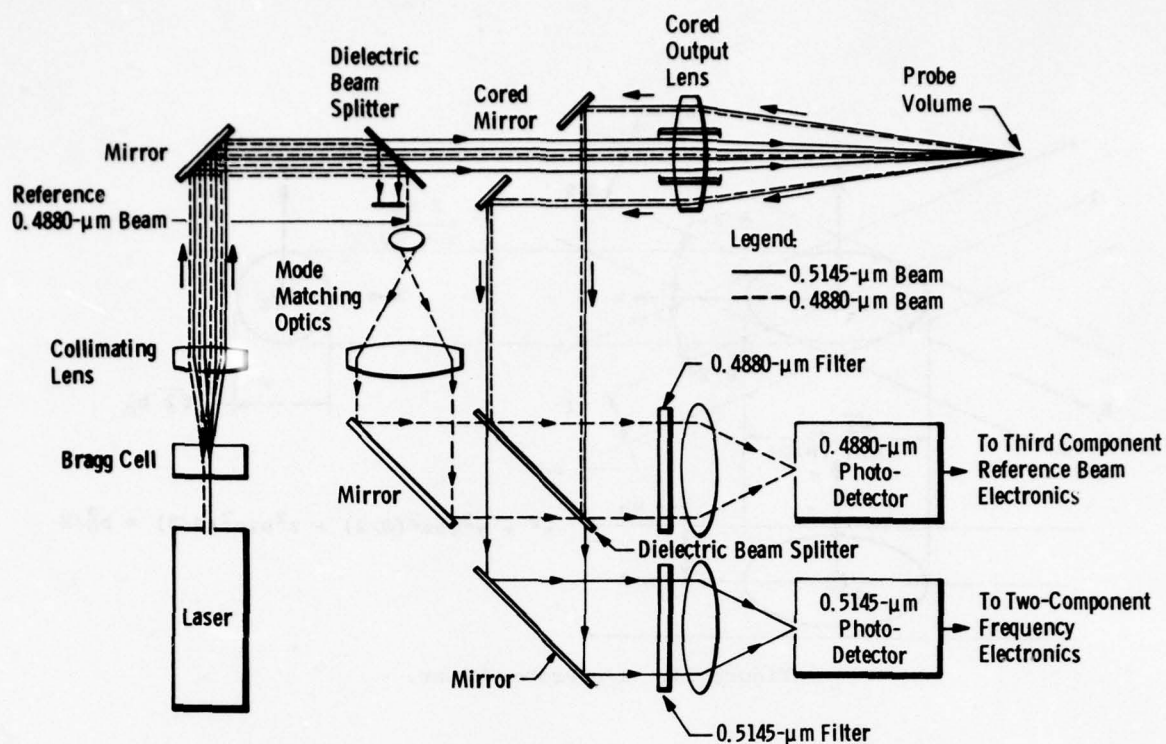


Figure 12. Proposed three component velocimeter schematic.

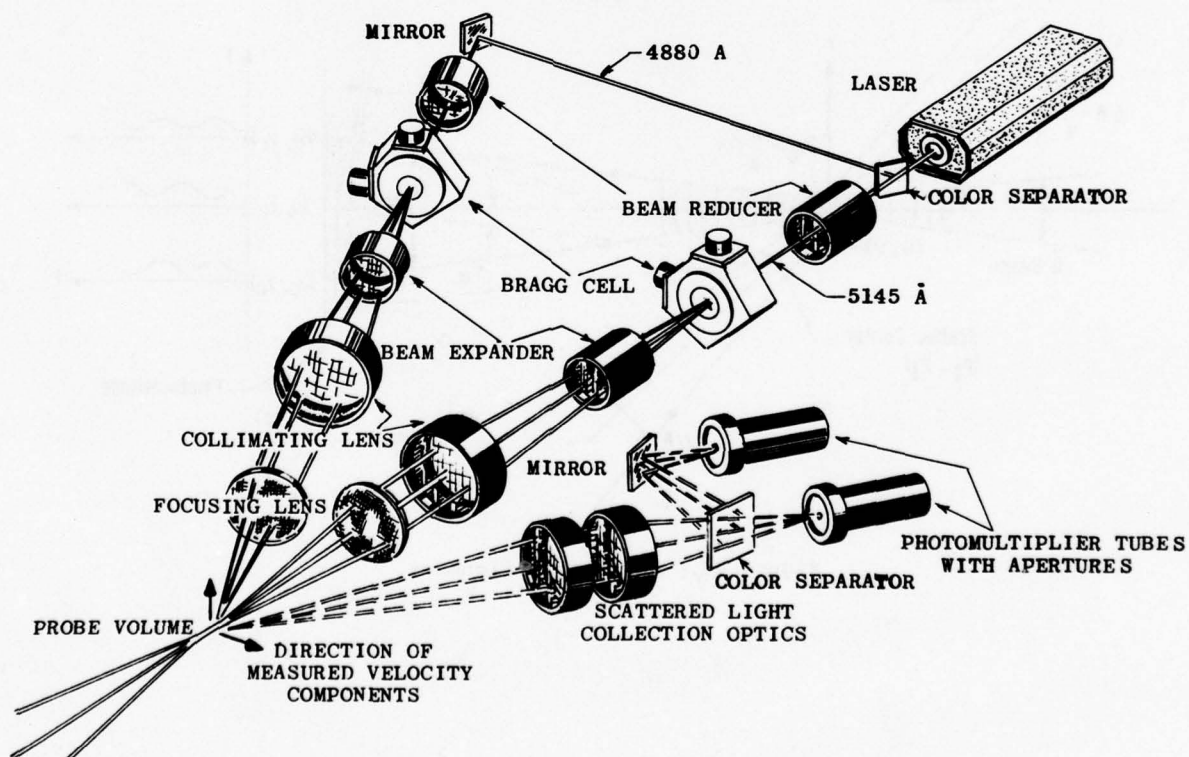


Figure 13. Three Component Dual Scatter - Backscatter Velocimeter.

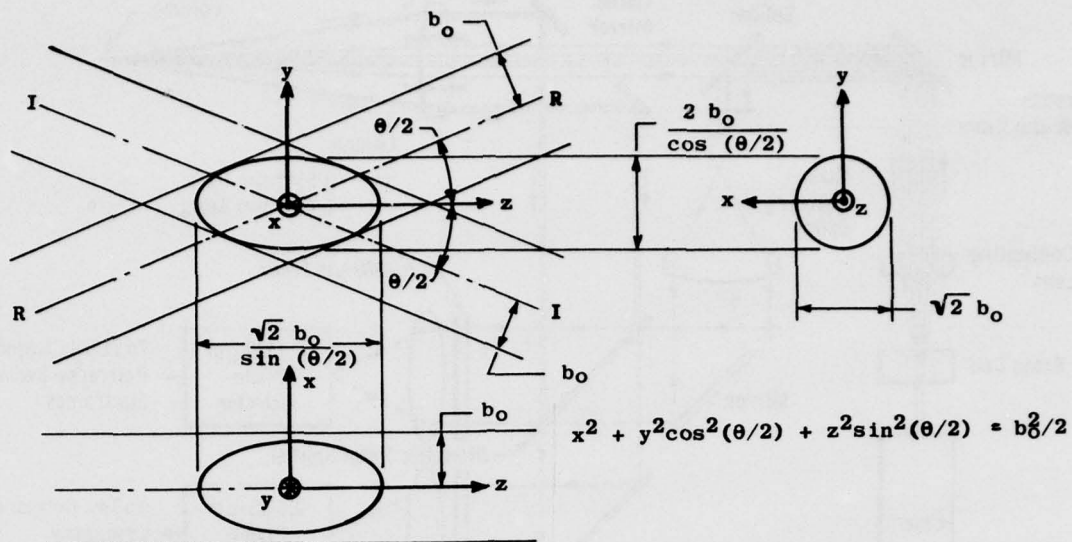


Figure 14. 1/e Probe Volume.

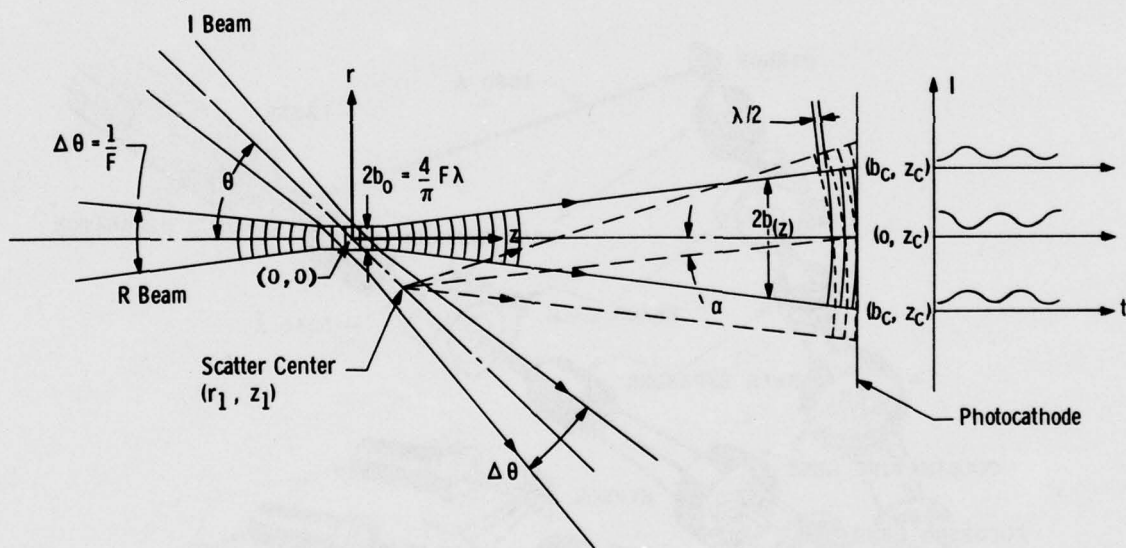


Figure 15. Radiation Alignment.

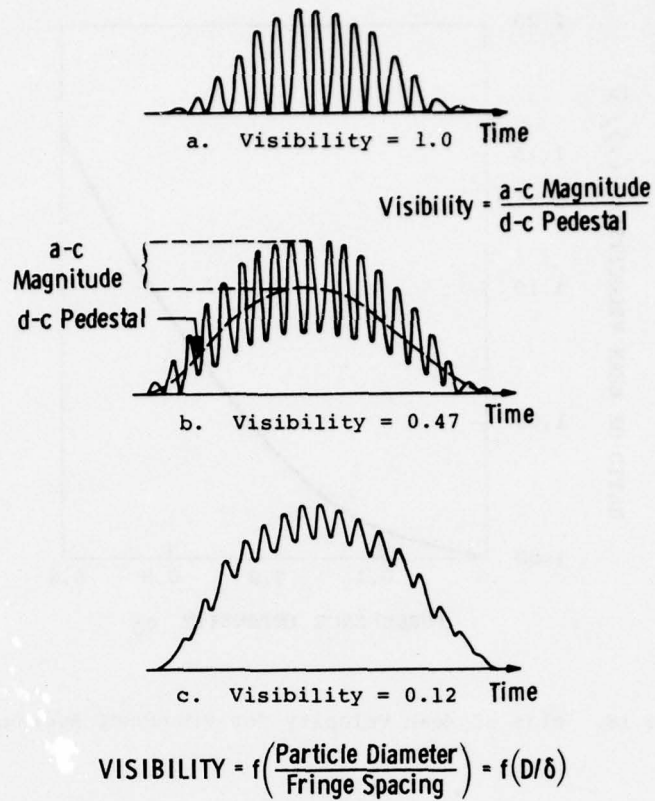


Figure 16. Photodetector Output Signal for Three Values of D/δ .

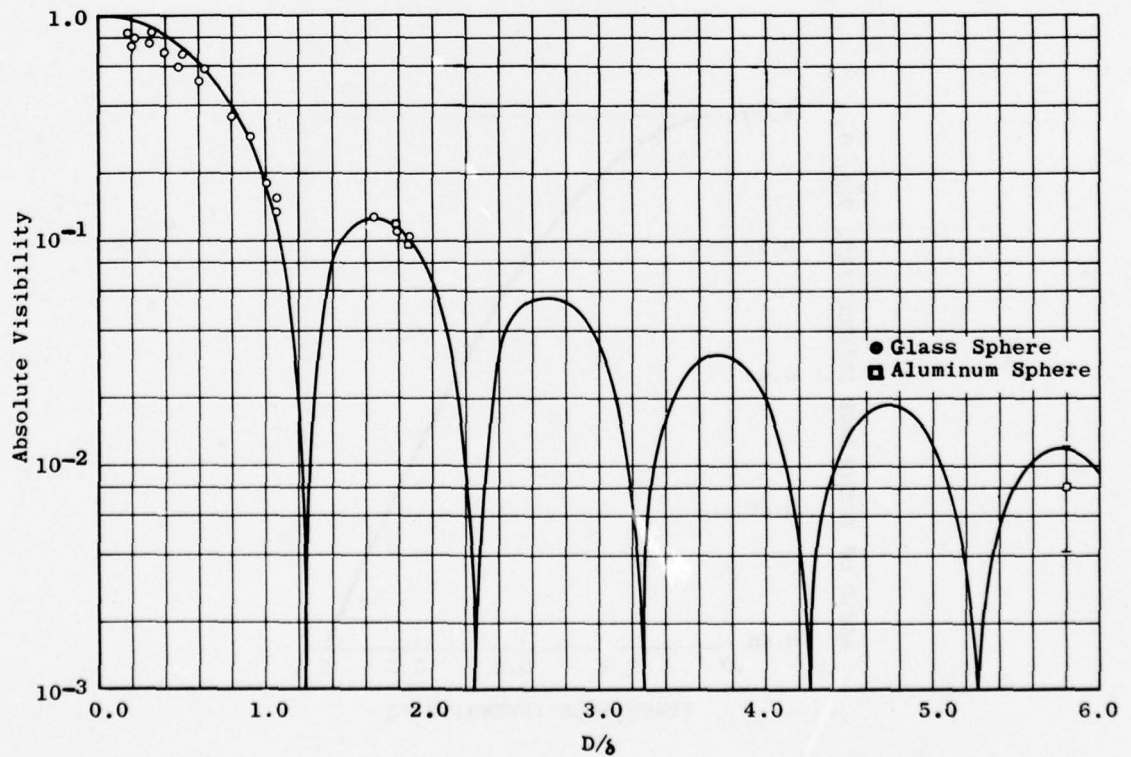


Figure 17. Comparison of Theoretical and Experimental Paraxial Visibility for a Spherical Particle.

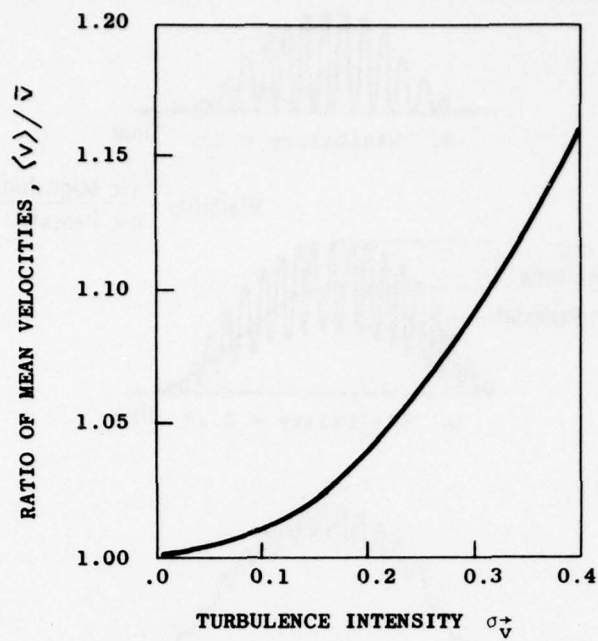


Figure 18. Bias of Mean Velocity for Frequency Average

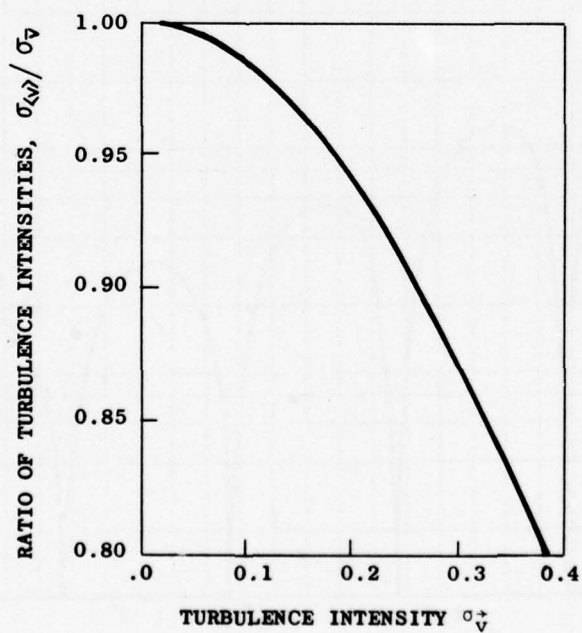
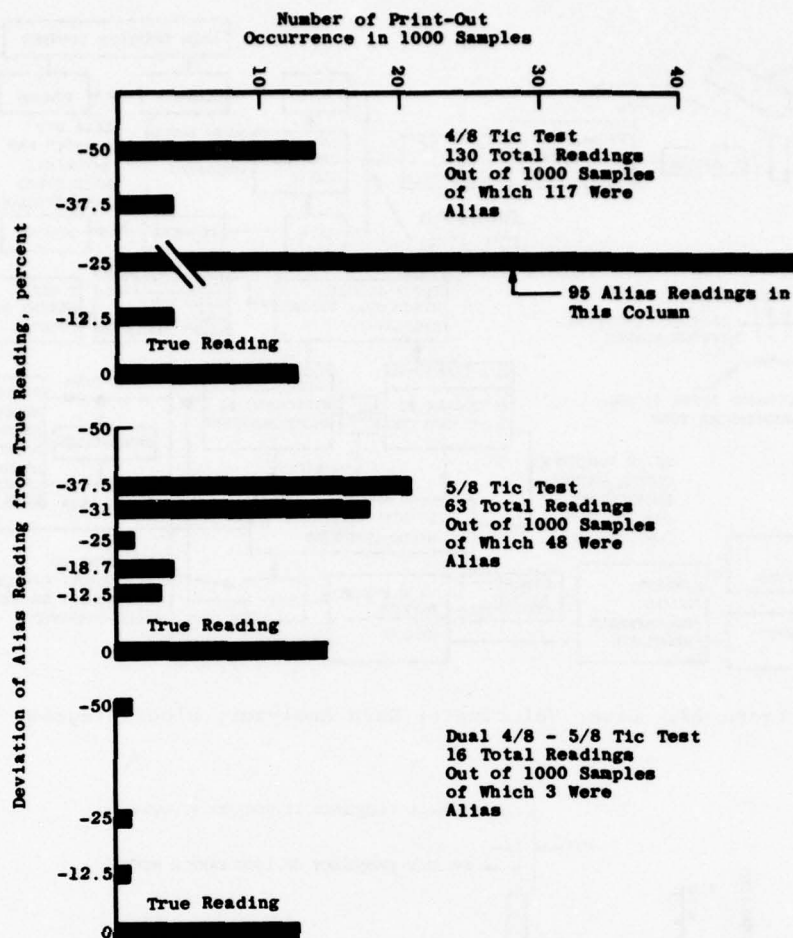
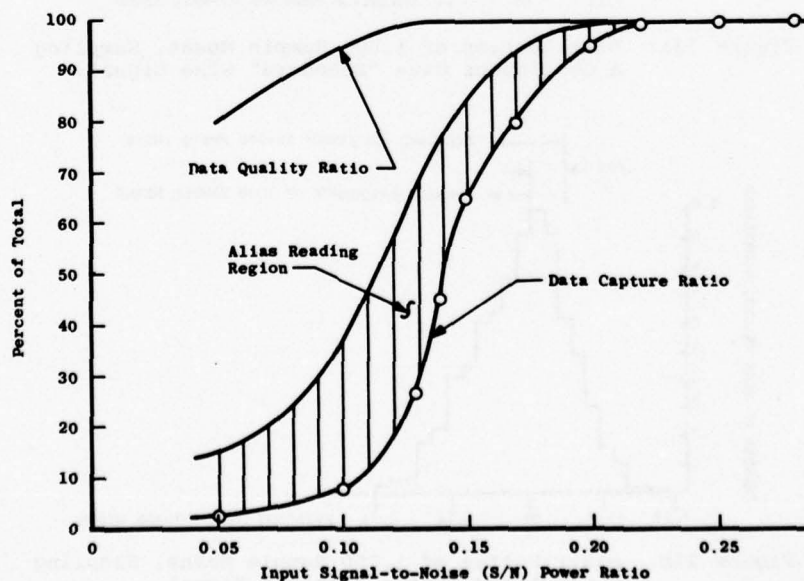


Figure 19. Bias of Frequency-Averaged Turbulence Intensity

Figure 20. Test Data of $S/N = 0.09$.Dual Test Processor Performance in Low S/N Regions

$$\text{Data Capture Ratio (DCR)} = \frac{\text{Total Times Processor Prints}}{\text{Total Sample Cycles Made}}$$

$$\text{Data Quality Ratio (DQR)} = \frac{\text{Total "True" Readings Printed}}{\text{Total Times Processor Prints}}$$

Figure 21. Processor Performance in Regions of Low S/N .

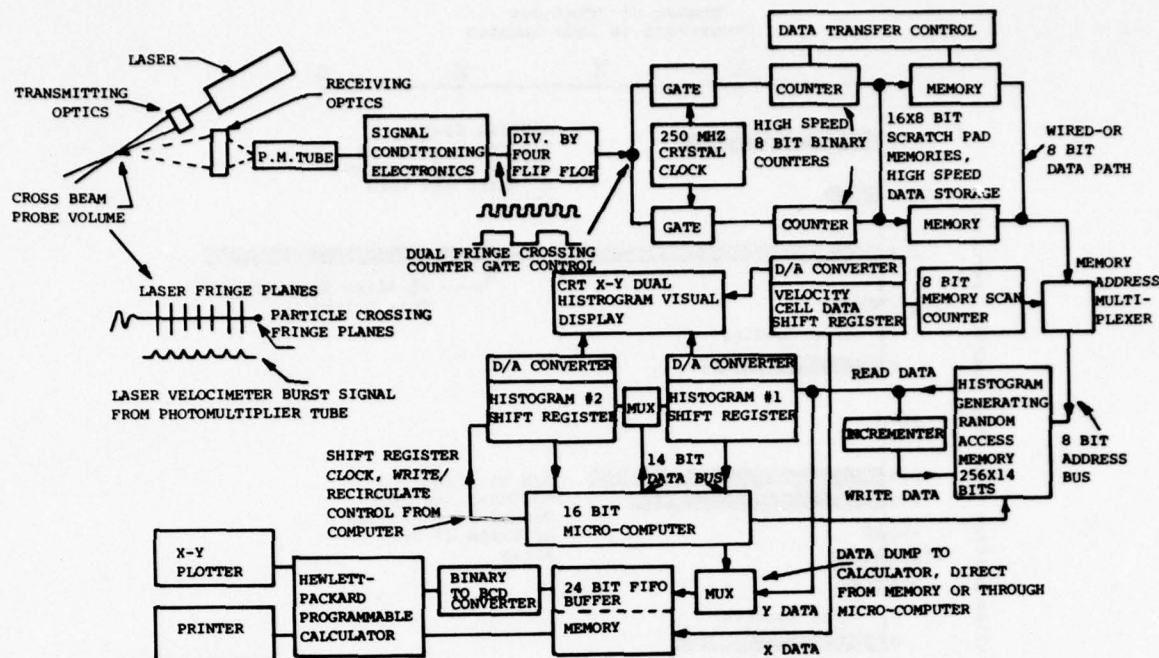


Figure 22. Laser Velocimeter Data Analyzer, Block Diagram.

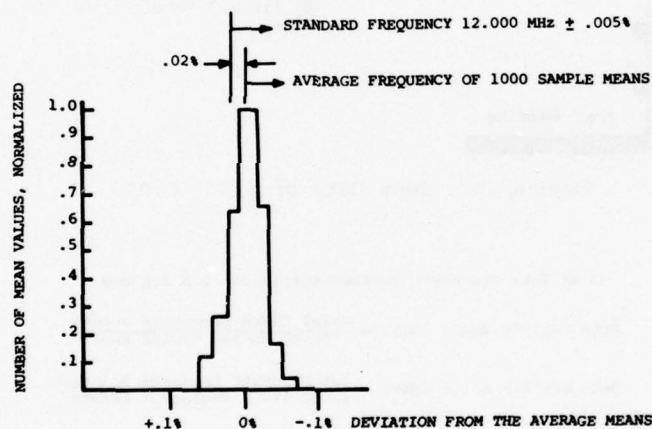


Figure 23a. Distribution of 1,000 Sample Means, Sampling a Continuous Wave "Standard" Sine Signal.

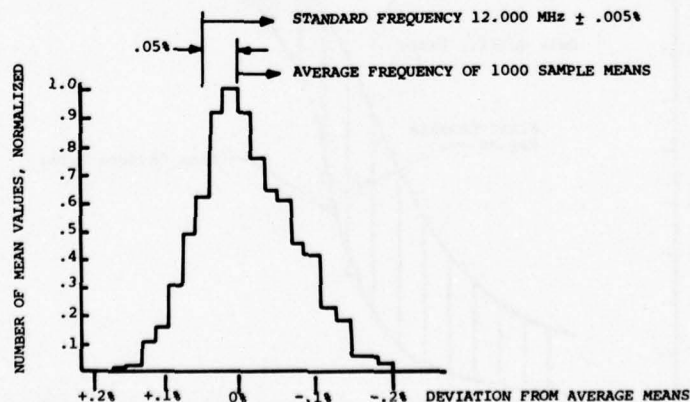


Figure 23b. Distribution of 1,000 Sample Means, Sampling a Simulated Photon Resolved Signal.

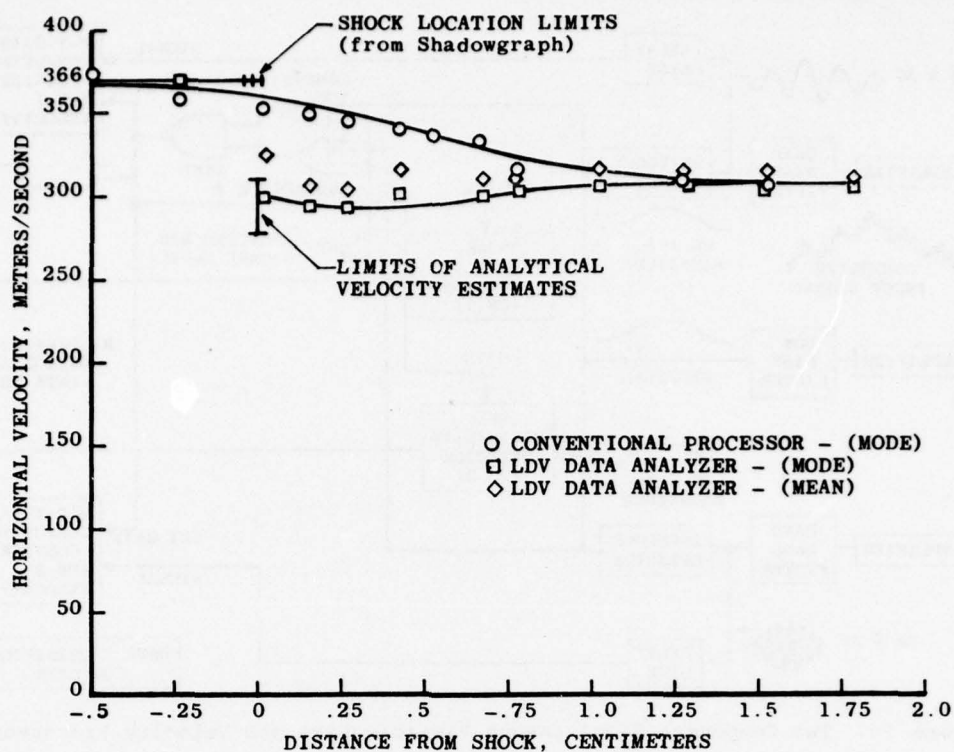


Figure 24. Velocity Profile Across a Shock.

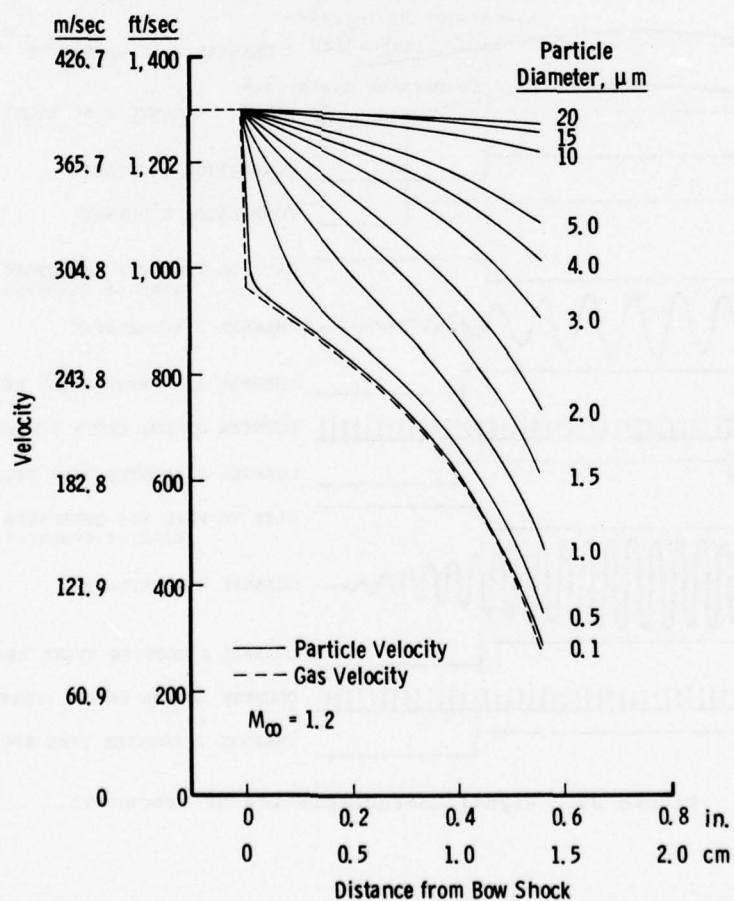


Figure 25. Particle Lag Effect.

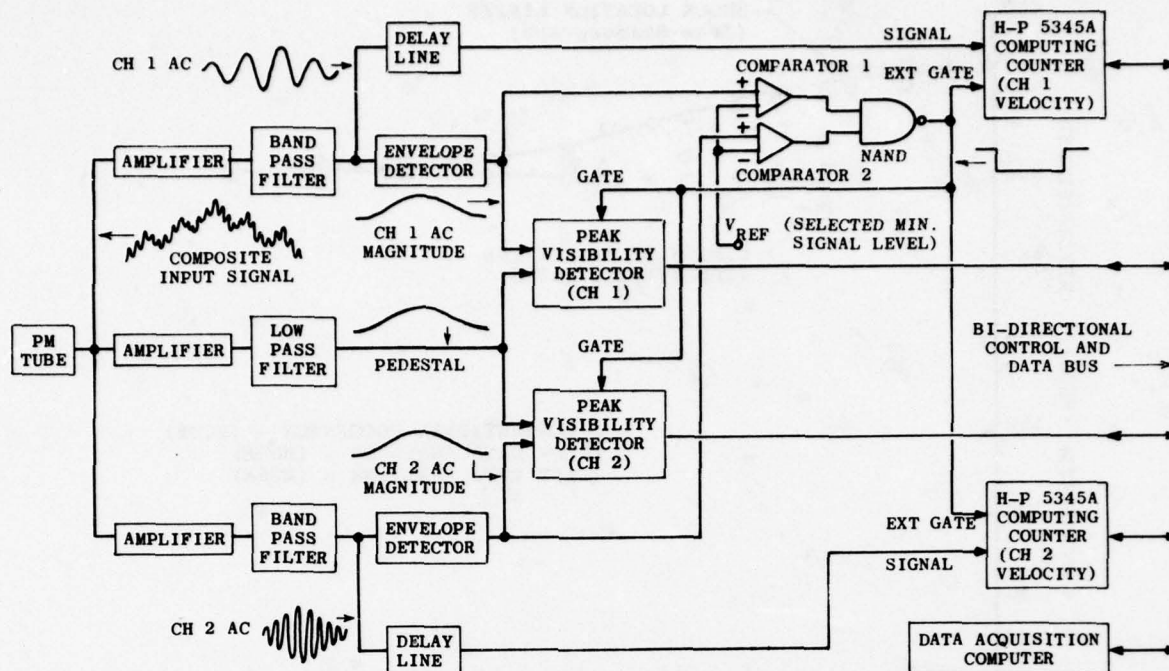


Figure 26. Two Component Simultaneous Particle Size and Velocity Processor.

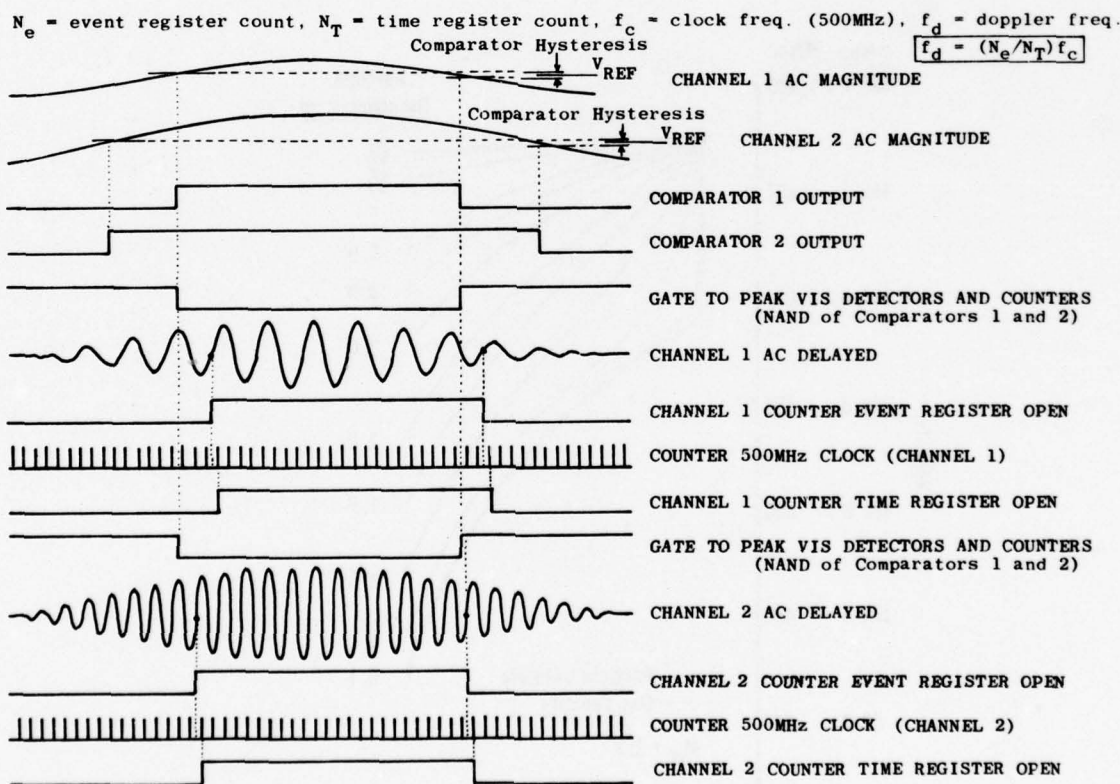


Figure 27. Signal Characteristics of Processor.

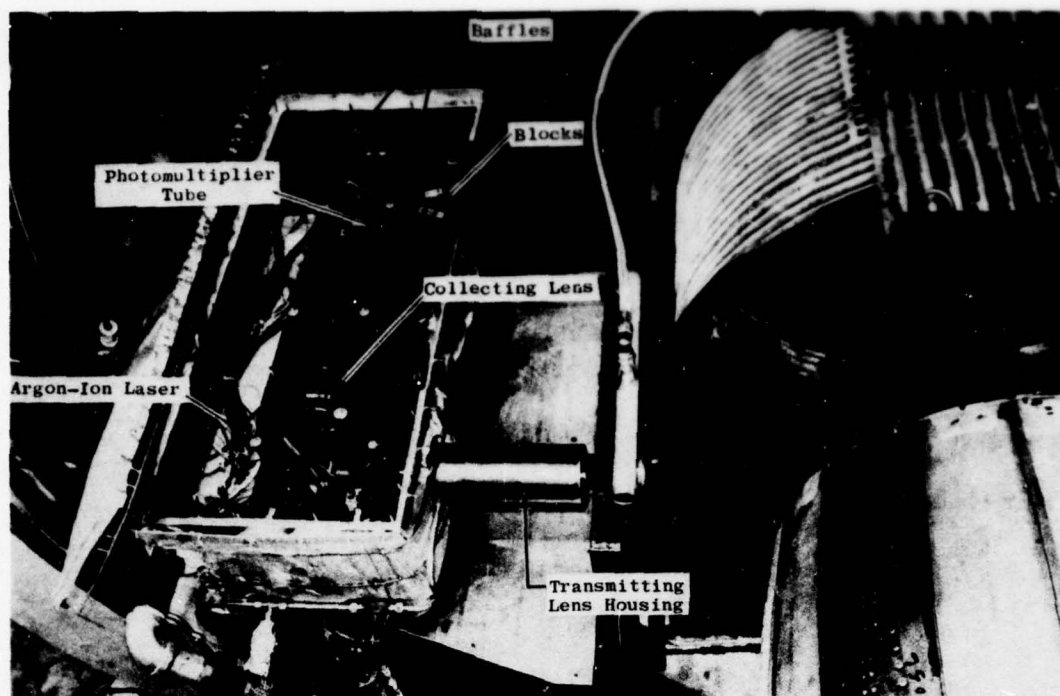


Figure 28a. LV Installation in Engine Test Tunnel (Top View).

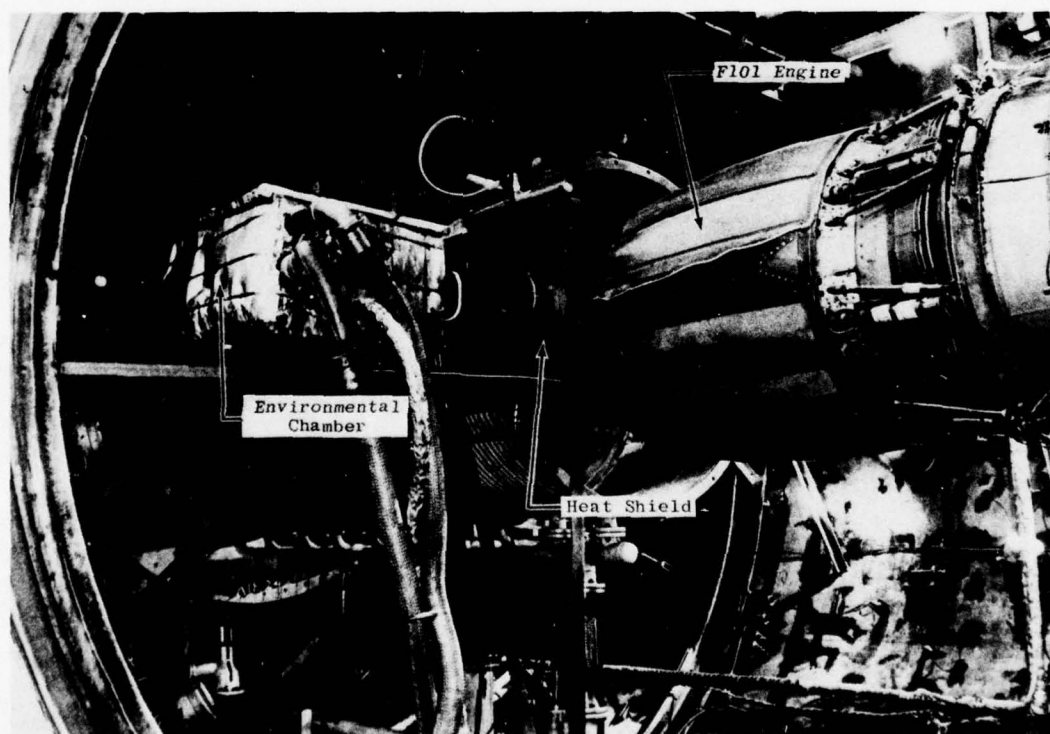


Figure 28b. LV Installation in Engine Test Tunnel (Side View).

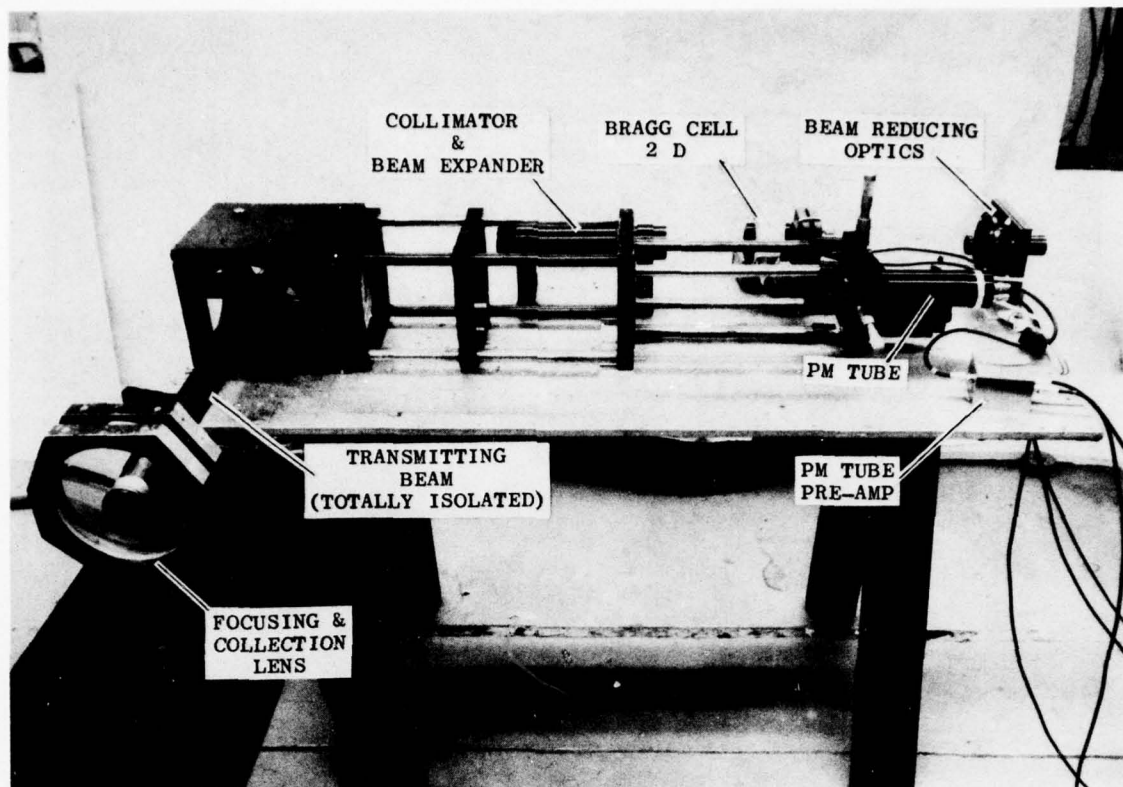


Figure 29a. LV Installation in Plenum Chamber of a Wind Tunnel (Skeletal View).

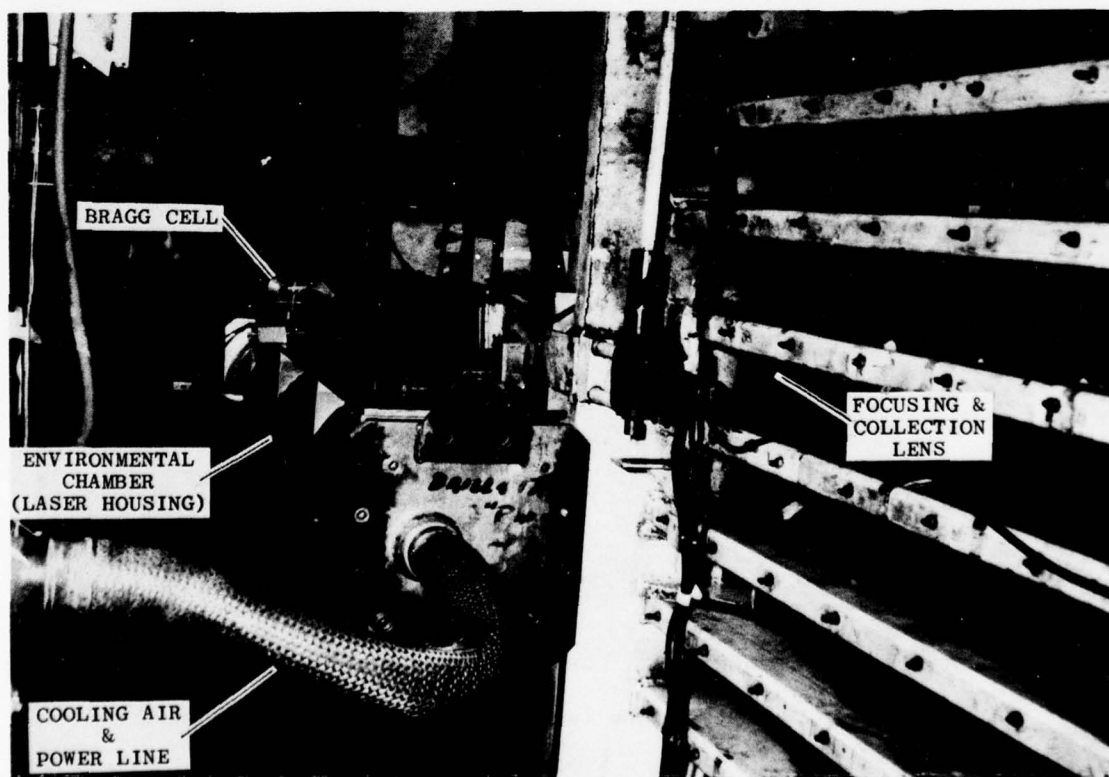


Figure 29b. LV Installation in Plenum Chamber of a Wind Tunnel (Skeletal View).

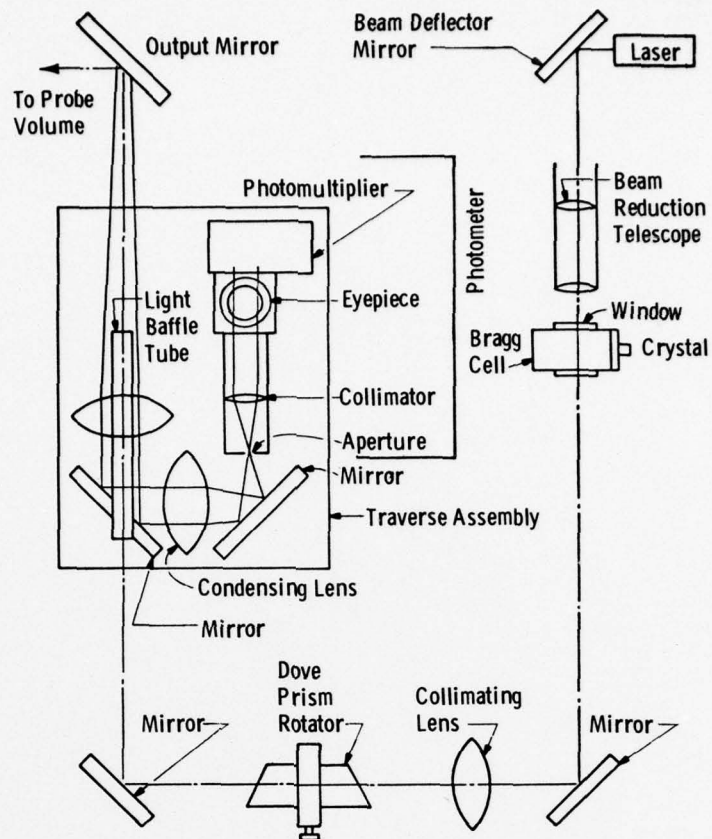


Figure 30a. Schematic of Combustion Analyzer Optical System.

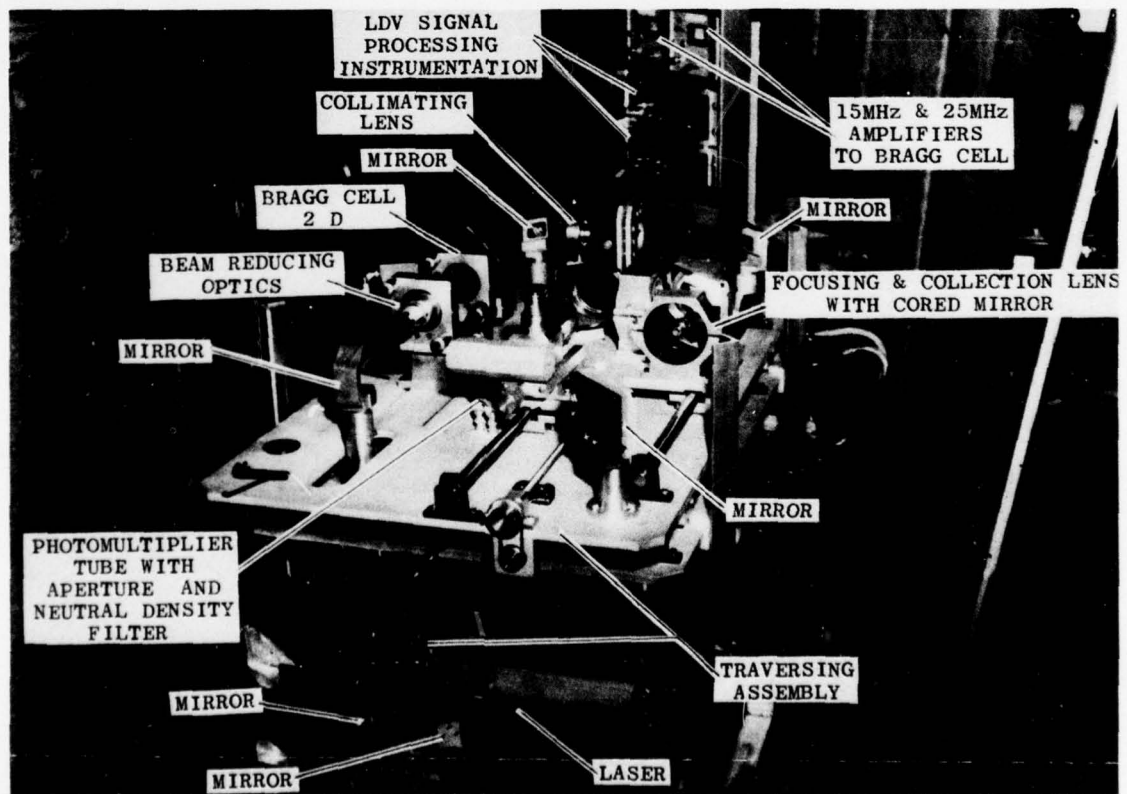


Figure 30b. Combustion Analyzer System.

LASER-TWO-FOCUS VELOCIMETRY (L2F) FOR USE IN AERO ENGINES

BY

R. SCHODL

DFVLR-Institut für Luftstrahlantriebe,
Linder Höhe, 5 Köln 90, W.Germany

ABSTRACT

The fundamentals of a new nonintrusive measuring technique - the L2F method - are reported. Similar in concept to the LDV system, this method measures the velocity of a fluid by utilizing the principle of light scattering of small particles entrained in the fluid. However, a much higher laser light concentration is achieved in the probe volume which helps to overcome the difficulty of obtaining measurements in regions of unfavorable signal-to-noise ratio, e.g. within the narrow blade channels of turbomachines, especially those of centrifugal compressors. For this application a concentric backscatter measuring device was considered and compared with an equivalent LD-system. It can be demonstrated that in principle the L2F-method is less susceptible to the injurious back-ground radiation which is generated from solid surfaces and in the narrow blade channels.

A description of an improved L2F-velocimeter suitable for use in strongly turbulent flows such as those found in turbomachines is presented.

From a series of probability density distributions taken at each measuring location nearly all two-dimensional information about the flow can be calculated; e.g. the magnitude and direction of the mean flow vector, the turbulence intensities, Reynold's shear stresses, etc. Measurement errors and their possible correction are discussed and the measuring accuracy is demonstrated in windtunnel tests.

To apply the L2F-velocimeter to turbomachines requires several additional pieces of equipment. A particle seeding device to increase the number of particles for the purpose of reducing the measuring time, a traversing and time delaying unit for positioning of the probe volume, and a window cleaning device are described and the experiences of operating the L2F-velocimeter are reported. Furthermore some results of L2F-measurements, carried out in a transonic axial and a highly loaded radial compressor are submitted and discussed.

NOMENCLATURE

b	meridional impeller channel width
c_m	meridional component of absolute velocity
dA	diameter of holes within the L2F-aperture
DF	window diameter
DL	diameter of lens system L2
d _p	particle diameter
F _p	velocity function
\bar{F}	mean value of velocity function
f	focal length of lens L1
f ₀	focal length of lens system L2
l	axial length of the L2F-probe-volume
L1, L2	lenses
M	Mach-number
m	mass flow
m_p	index-of-refraction of particle material
n _p	rotational speed
n _A	design speed
p, p*, p**	probability density functions
P _S	scattered-light power of a single particle
P _B	background radiation power
Q _{ΩL}	scattering efficiency of a single particle
r _{ΩL}	beam radius at the probe volume
S _{0, S'}	beam spacing within the L2F-probe-volume
S _m	meridional shroud contour length from inlet to outlet
T _u ', T _v '	turbulence intensities
t	blade spacing
Δt	time difference needed from particles for passing the two beams in the L2F-probe volume
\underline{u}	amount of velocity vector
\bar{u}	mean value of velocity
\vec{u}	velocity vector
u _⊥	amount of velocity component in the plane perpendicular to the beam axis
u'	velocity fluctuation component in the direction of the mean flow vector
u _{op}	optically measured velocity
u _p	velocity calculated from temperature and pressure measurements
u ₂	tip speed at impeller outlet

v'	velocity fluctuation component perpendicular to the mean flow direction
w	relative velocity
x	distance of a scattering solid surface with respect to the probe volume
\vec{x}	position
\vec{x}	local vector
x/S_m	relative meridional shroud contour
$y/H/2$	dimensionless coordinate of the tube width
y/t	relative blade spacing
z/b	relative meridional channel width
α	direction of flow velocity components in the plane perpendicular to the beam axis
$\Delta\alpha$	angle range defined by the finite size of the beams in the L2F-probe-volume
β	relative flow angle
ϵ	magnitude of outstanding edges caused by flat windows and curved casings
ϵ_S	error of beam spacing
φ	angle of particle velocity with respect to the focal plane
λ	vacuum wave length of light
η_0	scattering efficiency of a solid surface
Ω_L	cone angle limiting the spatial angle of scattered light observed
R_A	radius of casing
θ	crossing angle of the beams in the LD-probe volume

1. INTRODUCTION

Future research and development work on turbomachines is dependent upon the experimental investigation of flow phenomena within the blade channels of the rotors. The recently developed non contiguous optically based velocity measurement techniques offer us today methods for conducting such investigations.

Using the well established Laser Doppler technique, flow velocity measurements often become difficult in high speed turbomachinery because of the unfavourable test conditions. This is especially true, when in addition to the high speed problems the flow channels are very narrow. Often strong background-radiation is generated by laser light reflections at the hub and at the casing windows rendering any measurements more difficult.

However, it has been possible to overcome these problems at least in some turbomachinery applications. The first report was published by Wisler and Mossey (General Electric) [1] in 1972. They developed a Laser Doppler Velocimeter (LDV) for use in a transonic fan. A recent paper by Wisler [2] describes the application of the same basic technique to map the local velocity and to determine the shock wave locations within a high speed fan rotor.

Measurements of a similar nature have been carried out by Pratt & Whitney Aircraft. As reported by Walker, Williams and House [3], a two-component LDV was used to measure flow velocities and determine shock locations in an experimental transonic compressor blade row. Also in a research compressor Boutier, Guy Fertin and Languier [4] performed measurements of the periodic flow downstream the rotor blades and Seasholtz [5] describes work going on at the NASA Lewis Research Center to make LDV measurements in axial turbine rotors.

These important papers have presented valuable results of turbomachinery flows however they also mention the difficulties encountered in making measurements in regions which are located less than about 10 mm from solid surfaces. The relatively large dimensions of the LDV probe volume may introduce additional problems, when used in high speed turbomachinery applications.

Because of the rather large dimensions of the machines being examined these restrictions were not so severe. However in small machines or in the outlet part of centrifugal impellers operating at high speeds the already mentioned limitations make measurements very difficult.

Since the frequency limit of LDV electronics is mainly responsible for this drawback, Runstadler and Dolan [6] designed LDV-electronics which work up to about 150 MHz. In that way the probe volume diameter could be decreased and measurements closer to a scattering wall became possible. Results of flow research at the inlet of a small high speed centrifugal impeller and behind the rotor are reported.

In 1972 the DFVLR Institut of Airbreathing Engines started the development of a new laser velocimeter system for use in the study of high mach number turbomachinery flows which differs very much from usual LDV's. The fringe pattern in the probe volume is replaced by two discrete light beams, thus creating a light gate. It was supposed that the much higher intensity concentration in the probe volume could be used to overcome the problems of applicability in turbomachines. The basic idea of such a time of flight anemometer was introduced by Tompson [7], Mesch [8] and Tanner [9]. As Tanner's method was restricted to application in low turbulent flows it was necessary to improve it for use in turbomachinery. This development led to the Laser-Two-Focus (L2F) velocimeter (ref. [10] and [11]), which can be used in any turbulent flows to measure the magnitude and the direction of the mean velocity as well as the turbulence intensities and the Reynolds numbers in the plane perpendicular to the beam axis.

2. PRINCIPLES OF TANNER'S TIME OF FLIGHT ANEMOMETER

Like the Laser-Doppler-Technique the Time of Flight anemometer measures the velocity of small light scattering particles usually present in the fluid.

Fig.1 illustrates the construction of this optical arrangement which resembles that of the Doppler procedure. The incident laser beam is split in two by a beam splitter. The beams are sent forth at such an angle with respect to one another that they cross at the focal point of the subsequently placed lens L_1 . As a result, the beam axes leave the lens parallel to one another whereas the parallel beams are focused on the other focal plane of lens L_1 . As illustrated by Fig.1 in enlargement, two parallel beams are formed each of which is highly focused in plane MV' (the focal point of lens L_1) such that the desired "light-gate" is created. In order to assure sufficient space between the optical apparatus and the measuring sector a second lens system L_2 is interposed between L_1 and the flow channel to increase the distance to the desired length.

For a more exact examination of the conditions at the point of measurement (see detail Fig.1 and Fig.2) it may be observed that both beams in cross-section have - as a result of the focusing - a converging diverging character. The diameter of the beams at their narrowest point is limited by diffraction and the spherical aberration of the lenses. In the present set-up this diameter is about $10\text{ }\mu\text{m}$ which makes it many times smaller than that of the usual Doppler-crossed beam techniques. This gives a laser light concentration in the measuring sector which is about one hundred times greater than otherwise possible. The distance between the two beams-shown in Fig.1 - is between 0.3 and 0.5 mm. The axial depth within which the photodetector is capable of receiving particle-scattered light, depends on the intensity distribution of the laser beams around the measuring (focal) plane and on the spatial resolution of the receiving optical equipment. It can be limited to about $\pm 0.5\text{ mm}$.

A particle passing through both the light beams in the measuring sector, along the focal plane, produces then two successive pulses of scattered light. Given the distance between the two laser beams, the time elapsed between the pulses yields the velocity of the flow perpendicular to the optical axis - at 300 m/s about $2\text{ }\mu\text{s}$. In order to register this double pulse it is necessary, however, that the plane formed by the two laser beams is parallel to the flow direction. Consequently, it is possible to determine the flow direction once the plane of the beams has been established.

However, e.g., in turbulent flows, not every particle entering the probe volume will meet both laser beams and emit a scattered-light double pulse. Moreover, two succeeding light pulses - necessary for the time measurement - may be generated by two different particles. But those measurements yield useless time interval data which are randomly distributed along the time axis. Only the time interval of useful double pulses as they are actually produced by single particles which pass both laser beams has an eminent probability as long as the mean distance between two succeeding particles is just larger than the laser beams distance in the probe volume. For the chosen beam distance of 0.5 mm there are no limitations in any real flows including seeding.

A simple way of determining the time interval between the two scattered-light pulses is to use a storage oscilloscope as proposed by Tanner.

Fig.3 shows a typical oscillogram of the double pulses which are superimposed on the storage screen. The distance between the two peaks yields the time interval between the scattered-light pulses from which, given the spatial distance between the beams, the average flow velocity perpendicular to the optical axis can be evaluated. This simple timing method was used for measurements carried out in a subsonic and a supersonic wind tunnel under exploitation of the weak back-scattering of particles. The results published in ref.[1] demonstrate that - even by employment of a 5 mW laser - the weak back-scattered light of natural dust particles in filtered air generates sufficient signal quality to measure flow velocities higher than Mach 2. The measuring error was about 1.5% and the flow angle resolution about $\pm 1^\circ$.

However, this simple method is only suited to determine the mean flow vector not the turbulence intensities. Furthermore it must be pointed out, that - as a great disadvantage - Tanner's method works only in low turbulent flows. Because of the often higher turbulence intensities found in turbomachines this limitation cannot be tolerated.

3. LIMITING CONDITIONS IN TURBOMACHINES WITH REGARD TO THE APPLICATION OF OPTICAL VELOCIMETERS

Due to the very complicated geometrical conditions in turbomachines one is constrained in applying an optical backscatter arrangement. Thus, only the weak backscattered intensity of small particles can be employed by the photo-detectors leading to low signal amplitudes.

To measure the high velocities found within blade rows very small particles are required to insure that they follow the real streamlines closely so that they provide an accurate measurement of the fluid velocity. This is especially important in flows which contain large gradients or shock waves. These submicron particles should have diameters below $0.5\text{ }\mu\text{m}$. Unfortunately these small particles only scatter very weak intensities of light.

The most important restriction on the application of laser velocimeters in small tur-

bomachines is the background radiation generated by laser light reflections at the hub and at the casing windows. Its order of magnitude is usually from 10^6 to 10^8 times higher than the scattered-light of particles. If it is possible to chose a large angle of observation with respect to the axis of the incident laser beams one has a good chance to suppress the background radiation by spatial filtering. But especially in centrifugal machines such arrangements cannot be employed. It is necessary to have only one casing window for both the incident laser beams and the observed scattered light beam. This window should be flat so that it will not be restrictive in positioning the probe volume. Flat windows installed in the generally highly curved turbomachinery casing generate projecting edges which should be small to avoid flow disturbances. Fig.4 illustrates this conditions. The width of the protruding edge is ϵ , the radius of casing is ρ_A , D_f defines the window diameter and H the blade height from hub to tip.

Taking in account different types of turbomachines it was found that for the most critical measuring point close to the hub a cone angle of less than $\Omega_L = 10^\circ$ - when used simultaneously for the incident and scattered light - is required to avoid edges with ϵ greater than 0.2 mm. Due to this small spatial angle it is very difficult to suppress the mentioned background radiation.

As a result a confocal backscatter arrangement of an optical anemometer should be chosen as the best possible compromise under these limiting conditions.

4. COMPARISON OF CONFOCAL BACKSCATTER SET UPS OF A LASER DOPPLER AND A TIME OF FLIGHT ANEMOMETER WITH RESPECT TO THE INFLUENCE OF BACKGROUND RADIATION

A calculation of the influence of background radiation on Laser Doppler and time of flight anemometers was performed considering two very similar optical set ups. Fig.5 shows the Laser Doppler set up. The observation cone angle of $\Omega_L = 10^\circ$ corresponds to turbomachinery limitations. Taking into consideration a 50 MHz frequency limit of LDV electronics and 500 m/s as a maximum of measurable flow speed the beams crossing angle θ is calculated to 2.9° . Furthermore a beam diameter $2r_0 = 0.2$ mm results assuming 20 fringes in the probe volume. To reduce the background radiation extensively an aperture 0.2 mm in diameter is placed in front of the photomultiplier. This diameter corresponds to the diameter of the beams in the probe volume - the imaging scale is 1 : 1. A working distance of $f_0 = 300$ mm was arbitrarily chosen.

To study the influence of background radiation it was assumed that the aperture is figured into the probe volume. At a certain distance x from the probe volume a solid surface is placed which scatters the incident laser beams into the observation optics. As x is much smaller than f_0 the optics gather the background light nearly by a constant cone angle of $\Omega_L = 10^\circ$.

However, the aperture cuts off a certain part of this light so that the observed background radiation decreases as x increases.

A similar optical set up for a time-of-flight anemometer suitable for use in high speed flow research is shown in Fig.6. The observation cone angle is also 10° , the distance of the beams in the probe volume is 0.4 mm and their diameters $2r_0 = 0.012$ mm. The double hole aperture in front of the photomultiplier has diameters of $d_A = 0.030$ which are somewhat greater than the beams' diameter to make adjustments easier. Again the aperture is assumed to be figured into the probe volume for a simpler understanding of background radiation reduction.

A measure of the influence of background radiation is the ratio of the scattered-light power P_S of a particle and the observed background radiation power P_B . Calculations of this ratio have been carried out under the following assumptions:

1. The distance x is small compared to f_0
2. All the scattered light which passes through the lenses strikes the photomultiplier cathode. The entire area of the lense is used to transmit the backscattered radiation although in actual applications the central portion cannot be used since it is occupied by the incident beams.
3. The solid surface scatters the incident laser light homogeneously into the space angle 2π .

The resulting equation for the power ratio of the LD system is:

$$\frac{P_S}{P_B} = \frac{Q_{\Omega_L}}{n_0} d_p^2 \frac{x^2}{r_0^4} \quad (1)$$

and the corresponding equation for the T.O.F. anemometer is

$$\frac{P_S}{P_B} = \frac{Q_{\Omega_L}}{n_0} d_p^2 \frac{x^2}{r_0^2 d_A^2} \quad (2)$$

Q_{Ω_L} is the scattering efficiency in backwards direction with respect to the observation

cone of 10^0 , n_0 describes scattering efficiency of the solid surface and d_p the particle diameter. The n_0 formulators demonstrate the strong dependency of this ratio on the beam radius r_0 in the probe volume and on the diameter d_A of the aperture.

For the following data: $d_p = 0.5 \mu\text{m}$, the wavelength of light $\lambda = 0.5 \mu\text{m}$, the particles index of refraction $m_p = 0.5$, the scattering cross section of such particles was found to be $Q_{\Omega} = 10^{-3}$. Assuming a solid surface scattering efficiency of $n_0 = 0.01$ the power ratio was calculated. The results are shown in Fig.7.

The minimal allowable distance x of a scattering surface from the probe volume can be estimated by setting $P_S = P_B$. This limiting value is found to be 62 mm for the LD-system and 1.2 mm for the time of flight system. The superiority of the time-of-flight system is mainly due to the much smaller beam diameters in the probe volume and to the additionally smaller aperture. If the inner part of the lenses is excluded from collecting light the limiting distances can be decreased in both cases, but the comparable ratio remains unchanged. Although the time of flight system has this advantages the problem remains that it only works under flow conditions with low turbulence. How to overcome this restriction is part of the following description.

5. STATISTICAL ANALYSIS OF TURBULENT FLOWS

A stationary turbulent flow field can be expressed by

$$\vec{u} = \vec{u}(\vec{x}, t) \quad (3)$$

or in cartesian coordinates

$$\begin{aligned} u_1 &= u_1(x_1, x_2, x_3, t) \\ u_2 &= u_2(x_1, x_2, x_3, t) \\ u_3 &= u_3(x_1, x_2, x_3, t). \end{aligned} \quad (4)$$

Usually the time dependence of flow vector variations is very irregular so that it cannot be related by any time functions. Therefore mean values of the flow parameters are required to describe the most probable flow field.

In the theory of probability $\vec{u}(\vec{x})$ is considered to be a random variable and the probability density function $p(\vec{u}, \vec{x})$ is used to describe the turbulent flow field. The expression $p(u_1, u_2, u_3, x_1, x_2, x_3) du_1, du_2, du_3$ is equal to the probability that at a certain location the velocity component take values of $u_1 + du_1, u_2 + du_2$ and $u_3 + du_3$.

To calculate the mean value of any a function $F(\vec{u})$ which is also considered to be a random variable the space integral

$$\bar{F}(x) = \iiint_{-\infty}^{\infty} F(\vec{u}) p(\vec{u}, \vec{x}) du_1, du_2, du_3 \quad (5)$$

can be applied, but only if the condition of normalization

$$\iiint_{-\infty}^{\infty} p(\vec{u}, \vec{x}) d\vec{u} = 1 \quad (6)$$

is true.

The probability density function contains all information about the flow field except its time dependence. By the inserting the appropriate function $F(\vec{u})$ into the integral the mean values of the flow vectors, the turbulence intensity the Reynold's shearstresses, the skewness factors, etc. can be calculated.

Transforming equation (5) into cylindrical coordinates yields

$$\bar{F}(x) = \int_0^{\infty} \int_0^{2\pi} \int_{-\infty}^{\infty} F(\vec{u}) p^*(u_{\perp}, \alpha, u_3, x_1, x_2, x_3) u_{\perp} du_{\perp} d\alpha du_3 \quad (7)$$

if the velocity components in cylindrical coordinates are

$$\vec{u} = \vec{u}(u_{\perp} \cos \alpha, u_{\perp} \sin \alpha, u_3).$$

Restricting oneself to functions $F(\vec{u})$ which are only defined in the plane perpendicular to u_3 - $F(\vec{u}) = F(u_{\perp}, \alpha)$ - a transformation of equation (7) yields

$$\bar{F}(\vec{x}) = \int_0^{\infty} \int_0^{2\pi} F(u_{\perp}, \alpha) p^{**}(u_{\perp}, \alpha, x_1, x_2, x_3) u_{\perp} d\alpha du_{\perp} \quad (8).$$

p^{**} is the integrated probability density function p^* , which now contains only the information about the flow parameters defined in the plane perpendicular to u_3 .

It is maintained, that $p^{**}(u_{\perp}, \alpha, x_1, x_2, x_3)$ can be measured by a time of flight ane-

nometer or as it was later called the Laser-Two-Focus (L2F) velocimeter.

At a certain measuring point $\vec{x} = \vec{x}(x_1, x_2, x_3)$ $p^{**}(\vec{x})$ is a two-dimensional function

$$p^{**}(\vec{x}) = p^{**}(u_1, \alpha). \quad (9)$$

Due to the flow turbulence the flow vector varied in its magnitude as well as in its direction. If the plane containing the two beams of the L2F-velocimeter is assumed to be approximately aligned with the flow direction only particles which have this direction will be selected for measurements. Measuring the amount of velocity of a certain number of particles entering the probe volume that leads - due to the velocity fluctuations - to a probability histogram as a function of u_1 . Because the axial length of the probe volume is orientated along the coordinate u_3 the velocity component of all particles in the plane perpendicular to the optical axes are measured.

In this way, the measured histogram is already integrated over the velocity component u_3 .

By setting the plane containing the beams to other slightly different angles and by counting the same number of particles entering the probe volume, more velocity histograms can be measured as long as the chosen setting angles of the plane are within the range of the velocity angle fluctuations. This yields a two dimensional probability histogram comparable to the probability density function of equation (9). From equation (8) which should be transformed from an integral to a summation form the desired mean values can then be calculated.

This treatise should demonstrate, that the L2F method has the capacity to measure also in high turbulent flows if one operates it in the above mentioned manner. To turn the plane containing the beams a special construction of the optical beam path is required and in addition a suitable arrangement of data processing electronics must be provided for the measurement of velocity histograms.

6. THE CONCEPTION OF THE L2F-VELOCIMETER

6.1 Optical Set Up

To apply a velocimeter to turbomachines a solid construction is required to make it insensitive to vibrations and for easy in handling it. The optical beam path should not include too many optical components to keep the laser light losses as small as possible. Furthermore any slight misalignment of the initial laser beam should not alter the beams distance or the position of the probe volume.

The arrangement of the final L2F-set up is illustrated schematically in Fig.8. A polarization prism - Rochon prism - is used to split the initial laser beam (detail A) whose middle is located at the focal point of the immediately following lens L_1 .

As a result, the beam axes leave the lens parallel to one another whereas the parallel beams are focused on the other focal plane of lens L_1 . As shown in Fig.8 - detail A - two parallel beams are formed, each of which is highly focused in the focal point of lens L_1 so that the desired "light-gate" is created. In order to assure sufficient space between the optical apparatus and the measuring sector, a second lens complex L_2 is installed to increase the distance between the probe volume and the apparatus to the desired length. The same lens system L_2 also picks up the back-scattered light and forms two discrete light bundles which are deflected by a flat mirror into the observation plane of a microscope optics, where - corresponding to the laser beams in the measuring volume - two scattered light beams of very small diameter occur. By means of the microscope optics, these two beams may now be enlarged and projected on a double hole aperture. The following optics align each of the laser beams to a photomultiplier. The purpose of enlargement is to allow an exact adjustment of the aperture holes in order to minimize any background radiation received by the lens system L_2 .

The use of two photomultipliers - one to deliver the start pulse and the other the stop signal - effects several advantages.

First the influence of background radiation is reduced by a factor of two since one photomultiplier only observes the radiation being generated by one beam while the signal amplitude remains constant.

Second the probability of measuring useless double pulses is decreased since only a particle passing the first beam enables a measuring event to be started.

And third, the two photomultiplier arrangement allows the detection of the sign of the velocity direction.

To carry out measurements inside the rotating blade channels trigger optics are installed to switch the laser beam periodically.

As already mentioned the plane containing the two laser beams must be turned. This is accomplished with a rotation of the Rochon-prism and a synchronized turning of the dual hole aperture, while the respective position is indicated by use of a potentiometer.

Some considerations of the dimensions of the two beams in the probe volume are ne-

cessary. Fig.9 shows an enlarged view of the probe volume.

The contour of the laser beams is defined at the $1/e^2$ -point of intensity distribution inside the laser beams. Due to the focusing of the beams a minimum diameter of $2r_0$ results at the probe volume. To achieve a sufficiently high intensity concentration this diameter should be very small. It was chosen to be $12.8 \mu\text{m}$. The axial length l of the probe volume depends on focussing. If one defines it at the location where the beam diameter is double the minimum diameter, the length l can be calculated to be 0.88 mm .

Usually, the velocity vector \vec{u} is not aligned in the plane perpendicular to the beam axis. To measure its velocity component with respect to this plane a particle crossing the beams at an angle of φ (s.Fig.9a) must be detectable. If φ is set to be $+45^\circ$ this requires a beam distance S smaller than $1/2$. With a choice of $S = 0.4 \text{ mm}$ all dimensions are fixed.

Due to the cylindrical shape of the laser beams a systematical error is introduced which effects the beam spacing. Fig.8b shows this situation. A particle passing the beams centers travels a distance S . But if it tangentially touches the beams as illustrated in Fig.9b the distance travelled is S' . These two distances are related by the equation:

$$S' = S \cos \arcsin \frac{2r_0}{S} \quad (10)$$

Instituting the beam dimensions the error ϵ_S was calculated:

$$\epsilon_S = \frac{S - S'}{S} = 1 - \cos \arcsin \frac{2r_0}{S} \quad (11)$$

A value of about 0.001 results which is small enough to be considered negligible.

6.2 Electronics

To carry out velocity measurements the time difference between the double pulses must be registered. Assuming a beam distance of 0.4 mm , which could be measured with an accuracy of $1 \mu\text{m}$ by enlarging simultaneously the two beams in the probe volume and a micro-scale, a time difference of $0.85 \mu\text{s}$ occurs for a fluid velocity of 500 m/s . Therefore fast electronic equipment is required with a time response of a few nanoseconds. For typical probe volume dimensions and particle seeding rates about 10 000 measurement per second must be registered by collection electronics.

Similar measuring problems occur in nuclear physics. Sufficiently fast electronic equipment has been developed in this field and these devices are well suited for the L2F-application.

Fig.10 shows a block diagram of the data processing system. The start signal for the time measurements is produced by photomultiplier 1 which receives the scattered light from the first laser beam. Photomultiplier 2 which is aligned with the second beam yields the stop signal.

After the amplification of both signals discriminators enable the pulse type signals to be triggered at their maximum independent of the signal amplitudes. This is to avoid a broadening of the time measurement. The discriminator output signals are well defined and have short rise times. They start and stop the time interval measurements which are carried out by a time-to-amplitude converter. A counter counts the started measuring events and after reaching the present number the measuring cycle is stopped. The rectangular shaped output pulse of the time-to-amplitude converter containing the information on the measured time difference in its amplitude is digitized by the ADC of the following multi-channel analyser. The data are stored and arranged along the time axis, such, that a probability histogram of time measurements is generated on the MCA display.

Fig.11 shows an oscillogram containing various probability density distributions corresponding to different angles α with respect to the mean flow direction. The t-axis represents the transit time of the particles between the two beams. The quantity of each time-measurement is arranged along the ordinate. Each distribution represents the same number of measuring events at each measuring cycle. The probability that a particle traveling along the line of flow will be irradiated by both laser beams is maximum at the angle position $\alpha = 0^\circ$ corresponding to the mean flow direction. The peak of the distribution curve indicates the mean velocity, whereas the width of the curve near the baseline indicates the maximum velocity fluctuations. As α increases the probability of particle irradiation by both laser beams decreases rapidly and is - in this case - at $\alpha = 1.5^\circ$ practically nonexistent. Negative values of α yield the same results. A combination of all results leads to a two dimensional probability density distribution depending on time difference (velocity^{-1}) and angle (setting angle α) as it is shown in Fig.12.

At each of about 5 to 6 angle settings 1 000 to 2 000 valid measuring events are necessary to provide sufficient information about the flow. Depending on the particle concentration in the flow this takes nearly 3 to 5 minutes and requires steady flow conditions during this time period.

After the two dimensional probability distribution is measured and stored the data are transmitted to a computer for the calculation of the desired mean values.

The probability distribution as a function of time and setting angle is transformed into an equivalent one as a function of velocity and flow angle. In the case of the L2F-velocimeter the well known particle broadening effect occurs. Assuming the flow density to be constant and independent of flow fluctuations at each measuring point corrections can be carried out by dividing each value of the histogram by the respective velocity.

Another broadening effect is due to the finite size of the probe volume. While its influence on the magnitude of the measured velocities is already corrected by the employment of discriminators triggering each signal pulse at its maximum, the additional broadening of the measured flow angle fluctuations must be considered.

Fig.13 shows the cross-section for the two beams at 3 different angle positions of the measuring plane. A flow fluctuating only in velocity magnitude and not in direction is assumed. Using the L2F-velocimeter different probability distributions will be measured at different angle settings of the measuring plane inside the range $\pm \Delta\alpha$ which depends on the dimensions of beam diameter and beam spacing. In this way the measured two dimensional probability distribution indicates an apparent flow angle variation which does not occur in the flow as presumed.

A theoretical treatment of this problem leads to the calculated correction curve shown in Fig.14. By the mean flow velocity \bar{u} and the components of velocity fluctuations u' and v' parallel and perpendicular to the mean flow direction the turbulence intensities Tu' and Tv' are defined. Because of the broadening effect only the turbulence intensity Tv' calculated from the measured probability distributions deviates from the real flow turbulence. The possible error decreases as the turbulence increases. The magnitude and the direction of the mean flow vector will not be effected. The correction of Tv' was carried out by the computer program.

The remaining measuring error of the L2F-velocimeter depends mainly upon the uncertainties of determining the beam distance, from calibration errors, and from temperature shifting of the electronics. It was found to be 0.25 % at 200 m/s and 0.5% at 500 m/s.

6.3 Experimental Test

The first set of test results have been conducted in a rectangular tube to prove experimentally how close to a reflecting wall measurements would be possible and to determine the accuracy of the measurements, particularly the turbulence intensities. Fig.15 shows some results of these tests.

The fixed wall is left, the tube center right in the diagram. The mean flow velocity with respect to the velocity in the tube center and the degree of turbulence are plotted against the dimensionless coordinate of tube-width. The results performed by means of the L2F technique are compared with those attained by Reichardt using hot-wire anemometry (Ref.[12]). The agreement of the two sets of results is practically exact beginning at the first point of the optical measurement which is located 20% of the tube half width or 1.5 mm from the fixed wall. This value was determined to be a positioning limitation in the test and it agrees very well with the theoretically calculated limit, despite the simplifications which have been presumed. Reichardt could get relatively closer to the fixed wall because he conducted his experiments in a rectangular tube of significantly larger dimensions. However, the Reynolds numbers are, despite the difference in size of the rectangular tubes employed, nearly the same in both cases.

The results of tests performed in a supersonic windtunnel are shown in Fig.16. The related difference of the optically measured velocity u_{op} and the velocity u_p calculated from pressure and temperature measurements are plotted against the Mach- P number. A maximum error of 0.5% is indicated. The reproducibility of two test-series was much better than this even at the high velocities of 570 m/s which corresponds to Mach = 2.8. However, it must be considered that the determination of flow velocity by static and total pressure is not more accurate than 0.5%.

7. APPLICATION PROBLEMS IN TURBOMACHINES

7.1 Positioning of Probe-Volume

Under usual applications of fixed flow channels the measuring position in the flow field is changed by moving the complete device on a x-y-z-coordinate platform (see Fig.17). Depending on the focal length of lens 2 (see Fig.8) the probe volume is positioned at a certain distance - about 350 mm - in front of lens 2. This distance remains constant as long as no refractive material is placed along the beam path. However this distance is altered if planparallel glass window have to be installed in the casings of flow channels or turbomachines. The result is a small change in the probe volume position which can easily be calculated from the glass thickness and its refractive index. But a better way is to adjust the coordinates with the help of a reference point inside the flow channel.

When applying the L2F velocimeter to rotor flow measurements in turbomachines displacements of the probe volume can only be carried out in one or two coordinates - in radial and in axial directions. The reference points inside the blade channels can be for example the position of the hub to adjust the radial coordinate and the small slot between rotor and stator to adjust the axial coordinate, or any other suitable reference points. The complete device is moved along the corresponding coordinates until the probe volume just touches the chosen reference point. This is indicated when the maximum dc-

current of the photomultiplier output is observed. In this way adjustments are possible during machine operation. The positioning of the probe volume is accurate to within 0.1 mm.

In order to define the measuring position in the circumferential direction a Pockel's cell has been installed in the L2F-velocimeter beam path (see Fig.8). The Pockel's cell interrupts the laser beam during the rotation of the rotor and releases it - as directed by a trigger signal from the rotor - at a certain point in each blade channel to take measurement. The adjustable exposure time of the Pockel's cell is so short that the measurement can take place in a very small sector of the flow channel and, thus, under nearly steady-state conditions. The exposure time is determined by the blade frequency and the number of measuring points along the blade spacing; for 10 points this time has to be less than 1/10 of the blade cycle (at a frequency of 10 kHz less than 10 μ s). This time must be necessarily longer than the particle time of flight through the probe volume. It was usually chosen to be 1/20 of the blade passing time. The measurements at the selected spots in the blade channels are repeated during rotor revolution again and again until enough data for an adequate statistical evaluation are gathered.

At first it might appear be sufficient to merely switch the signals from the electronics, but due to sudden changes in background radiation caused by the blade passing through the probe volume this method is not used. If the blade surfaces touch the probe volume a strong radiation is generated which causes the photomultiplier to become saturated for a certain time. During this time period, which is often not small compared to the blade passing time, no measurements can be carried out. Therefore, the use of a Pockel's cell helps to overcome this problem.

To adjust the measuring position in the circumferential direction two methods are possible. One possibility is to calculate the delay time between the trigger signal from the rotor and the selected circumferential position. However, due to changes in rotational speed and due to the twisted blades this calculations becomes very difficult, perhaps even wrong if the blade becomes untwisted by centrifugal forces.

The other method of adjustment is independent of rotor displacements and blade deformations. Observing the photomultiplier output signals on an oscilloscope the circumferential position is clearly indicated (see Fig.18).

This is possible because the laser beam is not completely switched off by the Pockel's cell. The remaining intensity is sufficient to generate a good quality signal on the photomultiplier if a blade surface passes the probe volume. One must pay special attention to whether the blade radiation is caused by the suction or pressure surface of the blade. On the scope two pulses close to each other are periodically produced by the start- and stop-photomultiplier. Between the double pulses displaced by the blade period a region of increased noise is indicated which occurs just in that moment when the laser beam is released by the Pockel's cell for measurement. Due to the short time increase of intensity the background noise will simultaneously be increased, such, that it is detectable by the photomultipliers.

In order to shift the probe volume to any circumferential position adjustable delay electronics were used which work independent of rotational speed.

Before ending this consideration on the positioning conditions in turbomachines a problem must be emphasized which render any measurements impossible in some regions of the blade channel. These regions - called blade shadow - result if the blade cross-section in the plane normal to the rotor axis is not orientated parallel to the optical axis of the velocimeter. The blade tips cut off the laser beams such, that depending on the respective orientation either close to the suction - or close to the pressure side measurements cannot be made. The way to overcome this restriction is to adjust the optical axis, at each axial position, parallel to the respective blade direction. Because these adjustments are often very difficult the small blade shadow regions are tolerated.

7.2 Window Cleaning Device

Preliminary tests inside the rotating blade channels of an axial compressor have revealed additional problems. The most severe of them was that during compressor operation the glass windows in the casing became dirty very quickly, rendering the velocity measurements difficult or even impossible. A cleaning device was developed which worked very successfully. The basic idea was to clean the windows during compressor operation just before each measurement by injecting a cleaning liquid upstream of the windows for a short time (2 seconds). Thus, a liquid sheet covers the glass and cleans it of any dirt. The measurement can then take place immediately after the liquid has evaporated.

The construction of a window mounting device including the window cleaning arrangement is shown in Fig.19. The cleaning liquid - usual Triclorathylen - is forced through the clearance between the window and the mounting device. Due to some slots in a ring shown in the top view the liquid is directed to the upstream part of the window. The cleaning process is accomplished with both chemical and mechanical actions due to the turbulence within the casing shear layer which provides a scrubbing action.

The already mentioned cleaning fluid works very well for dirt or oil usually contained in air flows. But there are some seeding materials - for example TiO_2 - which stick so strongly to the glass windows that no liquid was found to be capable of cleaning the covered surfaces. Therefore when using artificial seeding the window cleaning problem must be given special consideration.

7.3 Particle Seeding Apparatus

Another problem concerned the concentration of dust in the test air, which often is so low that the velocity measurements take a relatively long time. Because the laser beam is triggered to fix the measuring point at a definite circumferential position, the measuring time is extremely short especially at high rotational speeds. This again reduces the probability that a particle is inside the control volume at exactly the same time. Therefore, it is often useful to seed the flow with additional particles. This has to be done to increase the particle concentration but not to get larger particles, as is often necessary in LDV operation.

Today some particle seeding devices are available, but most of them generate liquid particles of a relatively large diameter ($1 - 2 \mu\text{m}$). It is very unfavourable to have liquid particles in compressor work as they will be centrifuged on to the compressor casing and soil the windows. Thus, it is more convenient to seed with solid particles. However, other problems arise because solid particles usually agglomerate to large units, which no longer follow the real flow.

A technique was developed to reduce the size of the agglomerated particles. The principle of this technique is shown in Fig.20.

A fluidised bed of SiO_2 with individual particle diameters of $0.03 \mu\text{m}$ is produced by a small compressor which simultaneously drives a cyclone to separate the large agglomerated particles. A membrane pump sucks the smaller particles out of the cyclone and feeds them with the help of a seeding probe into the flow. Due to the fluctuating flow field induced by the membrane pump the small agglomerated particles become broken into smaller particles which have an area of about $1 \mu\text{m}^2$. Fig.21 shows electron-microscopic photographs of particles caught by wisker meshes. The upper picture shows particles transported by the membrane pump and the lower one the much larger particles which occur when instead of a membrane pump only pressed air is used for transportation.

Because of the very low mass of the particles with respect their area these particles are small enough to accurately follow the streamlines even in supersonic flows. Some tests carried out pointwise across an oblique shock demonstrate that these particles followed the velocity step in the short distance of only 2 mm.

Another great advantage of SiO_2 -particles is that they do not settle out and can easily be removed from the window surface with the already mentioned cleaning device. Furthermore extensive test experience with these particles has shown that they do not damage the blade leading edges.

7.4 Measuring Accuracy of L2F-Velocimeter in Turbomachinery Test

When positioning the probe volume in the circumferential direction a finite measuring region rather than a discreet point results due to the combination of the rotor wheel speed and the finite time interval during which the laser beams are released by the Pockel's cell. The measuring point position is assumed to be localized in the middle of this region which usually occupies $1/20$ of blade spacing. Velocity gradients which may occur in the circumferential direction lead to a broadening of the measured velocities with respect to the assumed measuring point resulting in a measured turbulence intensity which is usually too high. Depending on the velocity gradients the measured mean values can deviate additionally. To estimate the possible error the shape of measured circumferential velocity distribution must be taken into account.

Equivalent uncertainties arise if the axial length of the probe volume ($\pm 0.4 \text{ mm}$) is not small with respect to the velocity gradients in the radial direction. This happens especially in the regions of hub and wall shear layers.

In order to decrease the measuring time measurements should be carried out in each of the blade channels. Due to small errors in manufacturing the blade shapes the flow in each blade channel is somewhat different. As a result, in addition to the real flow turbulence, some flow unsteadiness is superimposed on the velocity measurements. Therefore the measured turbulence intensities are a result of both turbulence and flow fluctuations.

Considering all this uncertainties it was found that generally an accuracy of flow angle detection within $\pm 1^\circ$ can be achieved, whereas the error of mean velocity measurement does not exceed $\pm 1\%$. Only in the region of three dimensional shock waves, within the blade wakes, and within close proximity of the hub and outer casing walls measuring errors will be somewhat increased.

8. COMPRESSOR TESTS

The compressor that has been investigated is a single-stage transonic axial compressor without inlet guide vanes, designed for a total pressure ratio of 1.51 and mass flow of 17.3 kg/s at $20,260 \text{ rpm}$. The rotor has 28 blades with an inlet tip diameter of 399 mm and a radius ratio of 0.5. The rotor tip solidity is 1.34. The blades are composed of multiple-circular-arc profiles, having the shape of a DCA-profile near the hub and of a wedge type profile in the supersonic position near the tip. The stator consists of 60 blades having NACA-65-profiles with a circular arc camber line.

The flowpath of this stage, illustrated in Fig.22, has been designed such that the

blade loading is properly balanced between rotor and stator and does not exceed critical values. The stage design data are submitted in detail in [13].

The tests were carried out in the point of maximum efficiency at 70- and 100-percent-speed (mass flow 11.7 and 16.8 kg/s, respectively).

In Fig.22 the lines denoted by the numbers 2 - 8 designate the streamlines as they are drawn from conventional measurements outside the blade rows at design speed. The vertical lines, numbers 3 - 16, represent the various measuring planes distributed throughout the rotor. The points of the optical measurements are indicated by the circular symbols. At each point, up to 15 distinct measuring positions were realized over one blade spacing, especially downstream of the rotor to analyse the blade wakes; however, also inside of the blade channels to determine the shock positions accurately.

Within the blade channels, however, measurements in the actual vicinity of the blade surfaces were often impossible due to the blade twisting which causes as already mentioned shadow areas.

Fig.23 illustrate the complex flow field within the rotor blade row for 70 percent speed at the compressor's best point (11.7 kg/s). Each plot shows the distribution of the relative velocity as lines of constant local Mach number on surfaces of revolution from blade-to-blade and on planes from hub to tip over one blade channel.

Fig.23 demonstrates the relative flow field at 18 percent blade height (stream surface 2, Fig.22). The flow - subsonic throughout the blade channel - decelerates by flow turning to a Mach number of about 0.46. Along the blade suction side the deceleration takes place quite steadily whereas on the pressure side it happens primarily in the blade entrance region of lower velocity.

Fig.24 presents the flow field on stream surface 8 at 89 percent blade height. This plot reveals a reasonable effect of the blade row on the upstream flow which enters the rotor at a mean Mach number of 0.86. On the suction side the flow accelerates to weak supersonic velocities. The static pressure increases steadily within the blade channel by subsonic flow turning.

In Fig.25 the relative Mach number distribution is plotted over the blade passage at rotor outlet, seen with flow direction (plane 16, Fig.22). The blade wake can be clearly identified in this picture by the region of low velocity. The wake position varies with radius due to variations of the relative flow direction and also to the increasing distance from blade trailing edge to plane 16. Outside of the wake the Mach number increases uniformly from hub to tip.

Fig.26-28 present the results of the experimental flow study at 100 percent speed with a mass flow of 16.8 kg/s.

In Fig.26 the relative velocity distribution - again as lines of constant Mach number - is shown on stream surface 4 (45 percent blade height). The inlet Mach number is now slightly supersonic ($M_{aw} = 1.05$) due to the increased rotor speed. The detached shock waves appear at the blade channel entrance with a subsonic bubble downstream around the blade leading edges. Along the front part of the suction side the flow accelerates to reasonable supersonic velocities before being reduced to subsonic values through a normal shock. After an additional subsonic diffusion in the rear part of the blade channel an outlet Mach number of about 0.7 is achieved.

Fig.27 demonstrates the flow field on stream surface 6 at 63 percent blade height. Mach number is now about 1.2, and a typical bow shock is located ahead of each blade. Its oblique branch (dashed line) travels upstream and interferes with the expansion waves, which are caused by the supersonic acceleration around the blade leading edge and along the convex suction side. The normal shock within the blade passage impinges on the suction side of the adjacent blade at nearly 50 percent chord. Due to shock-boundary-layer interaction, a λ -shock appears at the blade suction side, which is indicated by the spreading of the Mach lines in this region. The normal shock reduces the flow to subsonic velocities and contributes essentially to the static pressure rise within the rotor. The pressure increase in the normal shock does not agree with the theoretical value of a one-dimensional supersonic flow, which is probably due to three-dimensional flow effects as annulus contraction and flow interactions on adjacent stream surfaces. The subsonic flow is further decelerated by flow turning in the rear part of the blade channel.

Fig.28 shows the relative Mach number distribution throughout two blade passages on stream surface 8 (89 percent blade height near the blade tip). The inlet Mach number has increased up to 1.3. The shock wave is attached to the blade leading edge and has an oblique branch also within the blade channel which impinges on the adjacent blade at nearly 80 percent chord. This flow type is typical for a back pressure case in transonic cascade.

As indicated in Fig.28 the deceleration from supersonic to subsonic velocities does not occur within a normal shock, but gradually over a larger portion of the blade channel. This supersonic diffusion is probably caused by the smooth stream tube convergence.

This diagrams presented here demonstrate some typical flow phenomena within a transonic compressor rotor. More detailed interpretation and a comparison with results of a corresponding through-flow calculation is published in [14].

As a second example velocity measurements in the internal flow field of a radial discharge impeller, running at a tip speed up to 400 m/s, are presented (inlet diameter 280 mm, outlet diameter 400 mm). The flow investigations are carried out at a test point near stage optimum - at $n = 14\,000$ rpm and $m = 5.31$ kg/s a stagnation pressure ratio $PR = 2.1$ and an isentropic stage efficiency $\eta_{is} = 0.88$ were reached.

The centrifugal impeller flow field was determined from inducer inlet to impeller discharge in 5 measuring areas, designated by I - V, the positions of which are illustrated in the Fig.29.

The described L2F principle renders it possible to measure the amount, the direction of the statistically averaged absolute velocity vector in the laser focal plane. After calculating the local circumferential velocity from impeller speed, geometry and the relative width position z/b of the measuring volume, the complete velocity triangle including relative velocity w and flow angle β can be determined.

Fig.17 shows the centrifugal compressor test rig and the L2F velocimeter set-up on the left. The laser beam passes through a cylindric casing window (5 - 20 mm diam. depending on blade height), which is normally aligned to the shroud contour.

The Figures 30, 31, 32, 33 and 34 represent the continuous development of the flow distribution within the centrifugal impeller from inducer inlet (meas.area I) to impeller discharge (meas.area V).

The perspective views show the locally measured meridional components of the absolute velocity c_m , referred to the tip speed at impeller outlet u_2 . In the diagrams the form of the measuring areas has been simplified to trapezium shapes at which the blade spacings and widths are equally scaled; the shroud-side casing wall lies in the front ($z/b = 0$), the hub in the rear ($z/b = 1$) and the hatched areas along the pressure side PS ($y/t = 0$) and suction side SS ($y/t = 1$) designate half of the blade thickness respectively.

A check of the relative flow pattern showed that the measured relative flow directions β coincide within ± 1 deg. with the local blade angles of plane I. This indicates that the flow has already largely adjusted to the blade surface at this plane about 11 mm aft of impeller leading edge. Similar conclusions can be drawn from Fig.31 for the conditions in the next measurement area II in the transition range from the axial inducer to the radial impeller. The flow is again very regular at a comparatively low blade loading and has still preserved its potential-theoretical character.

First marked distortions of the impeller flow pattern appear a short distance downstream at measurement area III, as can be observed in Fig.32. Here - at $x/s_m = 0.59$ in the range of highest blade loading - a pronounced velocity "dip" in the shroud stream tube ($z/b = 0.07$) marks a beginning flow separation. In the rest of the blade channel the flow is preserving its theoretically predictable pattern, but compared to the foregoing measuring areas with a clearly steeper blade-to-blade velocity gradient. This is especially true at the shroud stream tube ($y/t < 0.4$) where additionally a distinct thickening of the casing wall boundary layer may be observed.

The beginning flow separation in measuring area III rapidly enlargens downstream, as shown in Figures 33 and 34 for the subsequent areas IV and V, developing a pronounced wake. This wake area covers about 30 percent (IV), respectively 35 percent (V) of the corresponding flow channel area. The wake region is characterized by

- a low mass-flow component, the wake comprises about 15 percent of the total mass-flow at impeller discharge,
- a high fluctuation intensity,
- a steep, relatively stable velocity gradient to the surrounding main flow.

It is apparent from the velocity distribution, Fig.32, that there is still, at least in the circumferential direction, a substantially potential-theoretical flow character. The thickening shroud wall boundary layer and the increasing displacement effect of the rapidly growing wake region initiate then a shift of the main flow towards the pressure side and the hub wall region.

Eckardt [15] and [16] has published more details about these measurements as well as an extensive interpretation of these results. It was shown, that the impeller flow pattern, which coincide largely with potential-theory calculations in the axial inducer, become more and more reversed when the flow separates from the blade suction side, developing a rapidly increasing wake in the radial impeller. The observed secondary flow pattern and effects of channel curvature and system rotation on turbulence structure are discussed with respect to separation onset and jet/wake interaction.

8. THE L2F-FLUORESCENT TECHNIQUE

As it was demonstrated by the results taken within the centrifugal impeller, measurements were possible up to a minimum probe volume distance of 2 to 3 mm close to the hub or to the shroud. An unsteady background radiation was generated, due to machine vibrations and differences of hub curvature, leading to a somewhat greater minimum probe volume distance than that observed in windtunnel tests.

Additionally, measurements somewhat closer to the flow channel walls are still of interest to study flow separation effects and boundary layers in more detail.

Therefore the L2F-velocimeter was modified, so that now measurements became possible very close - about 0.5 mm - to a reflecting wall.

This improvement could be achieved by using fluorescent particles for flow seeding. The solid fluorescent particles - called "lumogene" - are stimulated by incident light of high frequency - as e.g. the blue or green light of an argon⁺-laser - and emit immediately low frequency light, which is well separated in its wave length from the incident light.

The unfavourable background radiation is almost completely eliminated, if optical filters are used to prevent the photomultiplier from observing the incident laser light frequencies, but which allow the passage of the fluorescent light frequencies.

Although the fluorescent particle light intensity is two orders lower than the back-scattered light, the signal-to-noise ratio was found to be much improved, especially in the case of measurements close to the walls. A signal amplitude, sufficient for data processing was achieved due to the high light concentration in the L2F-volume.

Fig.35 shows the new L2F measuring device which can be operated both, with scattered as well as fluorescent light.

Some results of a preliminary test, carried out within the above mentioned centrifugal impeller, are shown in Fig.36,

The results correspond to a measurement area at $x/s_m = 0.73$, located between the measurement areas III and IV. Measurements with the L2F scattered light technique are marked by triangles, whereas the circles designate the measurements with the fluorescence technique, demonstrating the improved possibilities for measurements within the immediate vicinity of the shroud wall.

A limiting distance of $\Delta b \approx 1$ mm resulted from the background radiation which could not be eliminated completely by the applied optical filters. However, a further reduction of this minimum distance would not be very reasonable, for the finite axial length of the probe volume and the steep velocity gradients in the wall boundary layers would cause significant errors.

9. CONCLUSIONS

An extremely high light concentration can be achieved in the probe volume with the L2F-velocimeter. Thus, measurements using the weak backscattered light are possible even in the vicinity of metal surfaces. This was proved by measurements in compressors where the test conditions are normally more severe than in windtunnels.

The L2F-velocimeter measures time differences instead of frequencies (as LDV systems do). Thus, measurements can be performed up to 1 000 m/s without reaching the limits of the electronic data processing equipment.

Furthermore, the L2F device is a compact unit which allows modifications of the measuring volume without any realignment in the optical part. It is well-suited to determine the amount and the direction of the velocity vector. Very often this procedure is more accurate than the determination of the velocity components. It yields also information on the flow turbulence and on the sign of velocity vector.

Detailed investigations by means of the L2F-velocimeter revealed an excellent survey of the internal flow in a transonic axial compressor rotor at subsonic and supersonic speeds and in a centrifugal compressor impeller.

The results demonstrate the capability of the technique for experimental studies of the complex real flow pattern: the shock-wave system within the blade row was investigated with respect to position and intensity. Effects of blade wakes were revealed. In the future the study of boundary-layers and flow separation appears to be possible.

These experimental investigations will help to develop more realistic internal flow models as a valuable basis for more complete calculation methods and more reliable loss and flow turning prediction techniques.

REFERENCES

- [1] Wisler, D.C., Mossey, P.W.: "Gas Velocity Measurements Within a Compressor Rotor Passage Using the Laser Doppler Velocimeter". Presented at the Winter Annual Meeting of the American Society of Mechanical Engineers, New York, N.Y., Nov. 26-30, 1972, ASME Publication No. 72-WA/GT-2.
- [2] Wisler, D.C.: "Shock Wave and Flow Velocity Measurements in a High Speed Fan Rotor Using the Laser Velocimeter". Presented at the American Society of Mechanical Engineers Gas Turbine Conference and Products Show, New Orleans, La., March 20-25, 1976. ASME Publication No. 76-GT-49.
- [3] Walker, D.A., Williams, M.C., House, R.D.: "Intra-Blade Velocity Measurements in a Transonic Fan Utilizing a Laser Doppler Velocimeter". Minnesota Symposium on Laser Anemometry, University of Minnesota, October 22-24, 1975.
- [4] Boutier, A., Fertin, G., Larguier, R.: "Laser Anemometry Applied to a Research Compressor". Proceedings of the ISL/AGARD Workshop on Laser Anemometry, May 5-7, (1976).
- [5] Seasholtz, R.G.: "Laser Doppler Velocimeter Measurements in a Turbine Stator Cascade Facility". Technical Paper presented at Laser Velocimetry Workshop, West La Fayette, Indiana, March 27-29, 1974, NASA TMX-71524.
- [6] Dolan, F.X., LeBlanc, F.R., Runstadler, P.W., Jr.: "Design, Development, and Test of a Laser Velocimeter for High Speed Turbomachinery. Presented at the LDA Symposium Technical University of Denmark, Lyngby, Denmark, August 25-28, 1975. Create Technical Note TN-234.
- [7] Thompson, D.H.: "A Tracer Particle Fluid Velocity Meter Incorporating a Laser". J.Scientific Instruments (J.Phys.E.), Series 2, Vol.1, pp.929-932, 1968.
- [8] Mesch, F., Daucher, H.H., Fritsche, R.: "Geschwindigkeitsmessung mit Korrelationsverfahren". Meßtechnik 7, pp.152-157, 1971.
- [9] Tanner, L.H.: "A Particle Timing Laser Velocity Meter". Optics and Laser Technology, pp.108-110, June 1973.
- [10] Schodl, R. "On the Development of a New Optical Method for Flow Measurements in Turbomachines". Paper presented at the ASME Gas Turbine Conference in Zürich, Switzerland, 1974.
- [11] Schodl, R.: "Advanced Testing Techniques in Turbomachines; A Laser Dual Focus Velocimeter for Turbomachine Applications". Von Karman Institute for Fluid Dynamics Lecture Series; April 14-18, 1975.
- [12] Reichardt, H.: "Messungen turbulenter Schwankungen". Naturwissenschaften 404 (1938), Comp.ZAMM 13, p.177-180, 1933 and ZAMM 18 p.358-361 (1938).
- [13] Strinning, P.E., Dunker, R.J.: "Aerodynamic- and Blade-Design of a Transonic Axial Compressor Stage"(in German). DFVLR, Institute for Air Breathing Engines, Internal Report No. IB-352-75/7, 1975, p.87.
- [14] Dunker, R.J., Strinning, P.E., Weyer, H.B.: "Experimental Study of the Flow Field Within a Transonic Axial Compressor Rotor by Laser Velocimeter and Comparison With Through Flow Calculations". ASME-paper No. 77-GT-28.
- [15] Eckardt, D.: "Instantaneous Measurements in the Jet-Wake Discharge Flow of a Centrifugal Compressor Impeller". Trans.ASME, Journal of Engineering for Power, Vol.97, No.3, July 1975, pp.337-346.
- [16] Eckardt, D.: "Detailed Flow Investigations Within a High-Speed Centrifugal Compressor Impeller". ASME, Journal of Fluids Engineering, Vol.98, No.3, Sept.1976, pp.390-402.

LIST OF FIGURES

- Fig. 1 Scheme of Tanner's Time of Flight-Velocimeter
- Fig. 2 Principle sketch of the time of flight velocimeter measuring volume
- Fig. 3 Oscillogram of signals from the time of flight velocimeter
- Fig. 4 Installation of flat windows in curved turbomachinery casings
- Fig. 5 LD-set up for turbomachinery application
- Fig. 6 Optical set-up of a time of flight anemometer for turbomachinery application
- Fig. 7 Influence of background radiation
- Fig. 8 Optical set-up of the L2F-velocimeter
- Fig. 9 Dimensions of L2F-probe volume
- Fig.10 Data processing of L2F-velocimeter
- Fig.11 Output signal of the electronic data processing system
- Fig.12 Measured two dimensional probability distribution
- Fig.13 Broadening effect on flow angle turbulence due to finite size probe volume
- Fig.14 Influence of finite size probe volume on flow turbulence
- Fig.15 Optical measurements of flow velocities in a rectangular tube in comparison to hotwire measurements of Reichardt
- Fig.16 Optical measurements in a supersonic windtunnel
- Fig.17 L2F-velocimeter for impeller flow studies at the centrifugal compressor test rig positioned on a x-y-z-coordinate platform
- Fig.18 Detection of the circumferential measuring position
- Fig.19 Mounting and cleaning device of a casing window
- Fig.20 Particle seeding apparatus
- Fig.21 SiO_2 -particles (ISL photographs)
- Fig.22 Compressor flowpath with the laser measuring stations
- Fig.23 Lines of constant relative Mach number through the blade passage at 18 percent blade height (70 percent speed)
- Fig.24 Lines of constant relative Mach number at 89 percent blade height (70 percent speed)
- Fig.25 Lines of constant relative Mach number downstream of the rotor plotted over one blade channel (plane 16); (70 percent speed)
- Fig.26 Lines of constant relative Mach number through the blade passage at 45 percent blade height (100 percent speed).
- Fig.27 Lines of constant relative Mach number at 63 percent blade height (100 percent speed)
- Fig.28 Lines of constant relative Mach number at 89 percent blade height (100 percent speed).
- Fig.29 Centrifugal compressor impeller with arrangement of optical measurement areas in the blade channel (impeller blackened by anodic treatment to reduce back-ground-radiation)
- Fig.30 Velocity distribution c_m/u_2 at measurement area I,
 $n = 14\ 000\ \text{rpm}$, $\dot{m} = 5.31\ \text{kg/s}$, $x/s_m = 0.08$
- Fig.31 Velocity distribution c_m/u_2 at measurement area II,
 $n = 14\ 000\ \text{rpm}$, $\dot{m} = 5.31\ \text{kg/s}$, $x/s_m = 0.43$
- Fig.32 Velocity distribution c_m/u_2 at measurement area III,
 $n = 14\ 000\ \text{rpm}$, $\dot{m} = 5.31\ \text{kg/s}$, $x/s_m = 0.59$

AD-A045 240

ADVISORY GROUP FOR AEROSPACE RESEARCH AND DEVELOPMENT--ETC F/G 17/8
LASER OPTICAL MEASUREMENT METHODS FOR AERO ENGINE RESEARCH AND --ETC(U)
JUL 77

UNCLASSIFIED

AGARD-LS-90

NL

2 OF 2

AD
A045 240

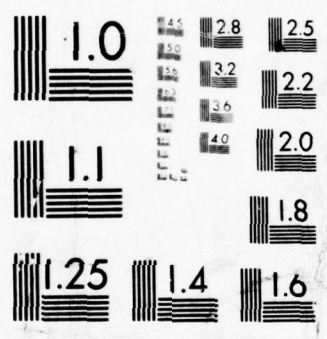


END

DATE
FILMED

11-77

DDC



MICROCOPY RESOLUTION TEST CHART
NATIONAL BUREAU OF STANDARDS-1963-A

Fig.33 Velocity distribution c_m/u_2 at measurement area IV,
 $n = 14\ 000$ rpm, $\dot{m} = 5.31$ kg/s, $x/s_m = 0.87$

Fig.34 Velocity distribution c_m/u_2 at measurement area V,
 $n = 14\ 000$ rpm, $\dot{m} = 5.31$ kg/s, $x/s_m = 1.01$

Fig.35 L2F-fluorescence-velocimeter

Fig.36 L2F-fluorescence-velocimetry within centrifugal compressor impeller

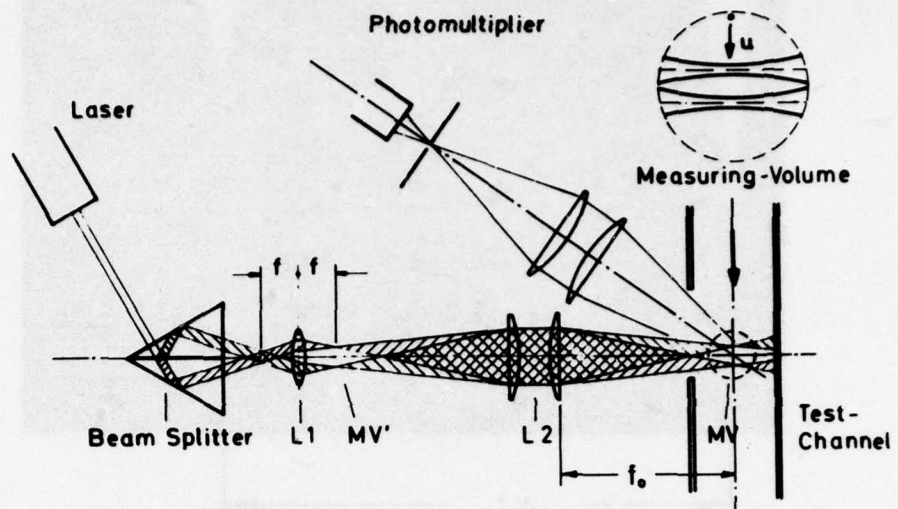


Fig. 1 Scheme of Tanner's Time of Flight-Velocimeter

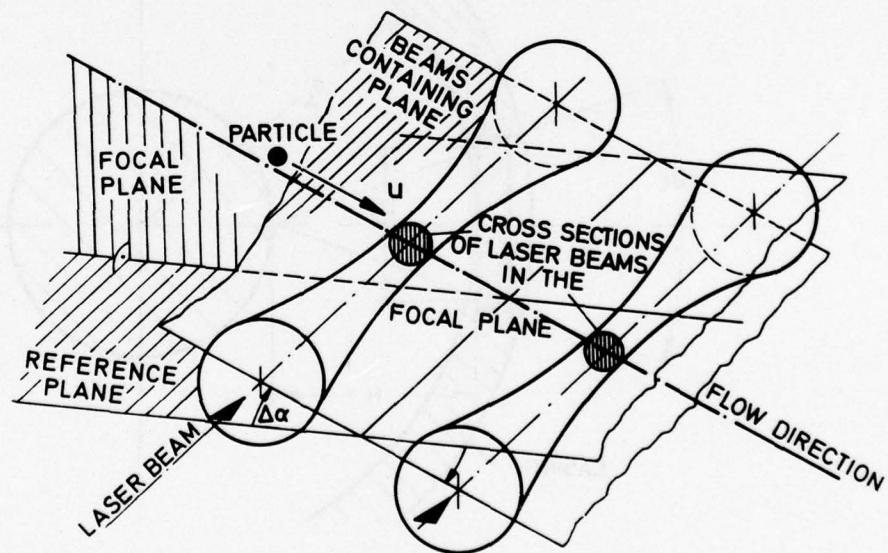


Fig. 2 Principle sketch of the time of flight velocimeter measuring volume

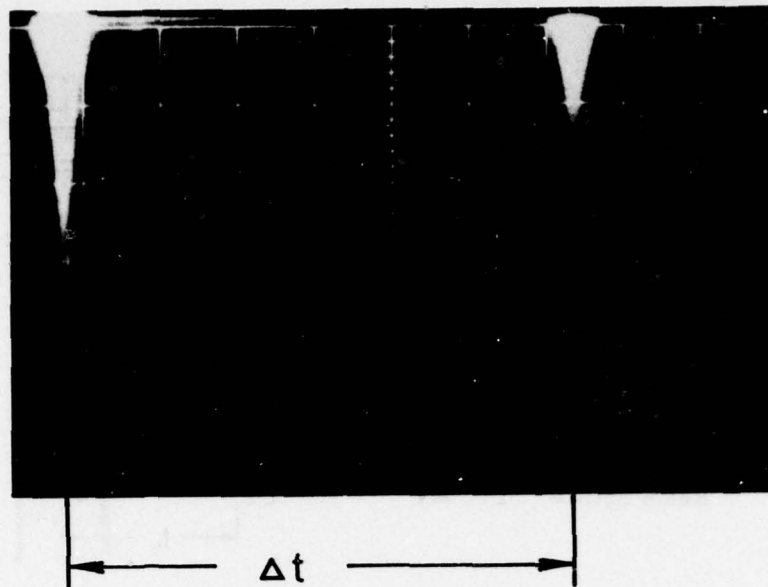


Fig. 3 Oscilloscope of signals from the time of flight velocimeter

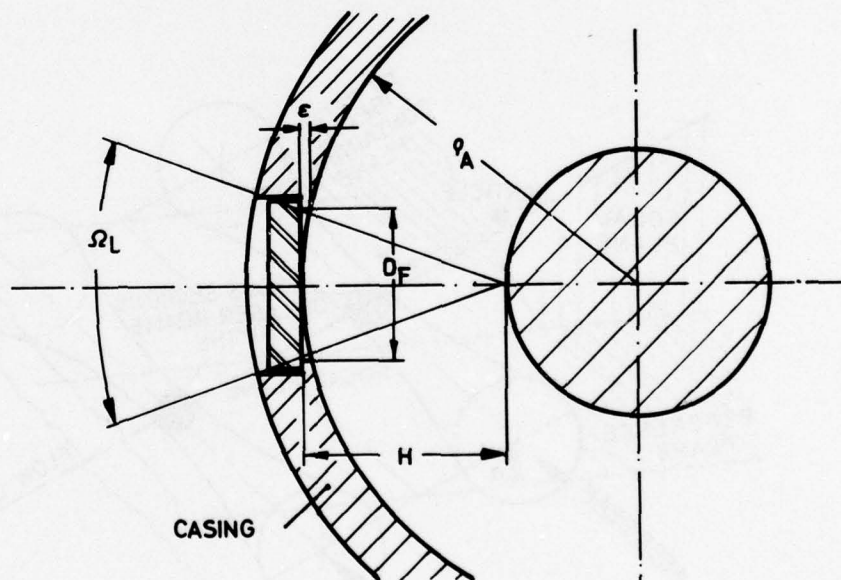


Fig. 4 Installation of flat windows in curved turbomachinery casings

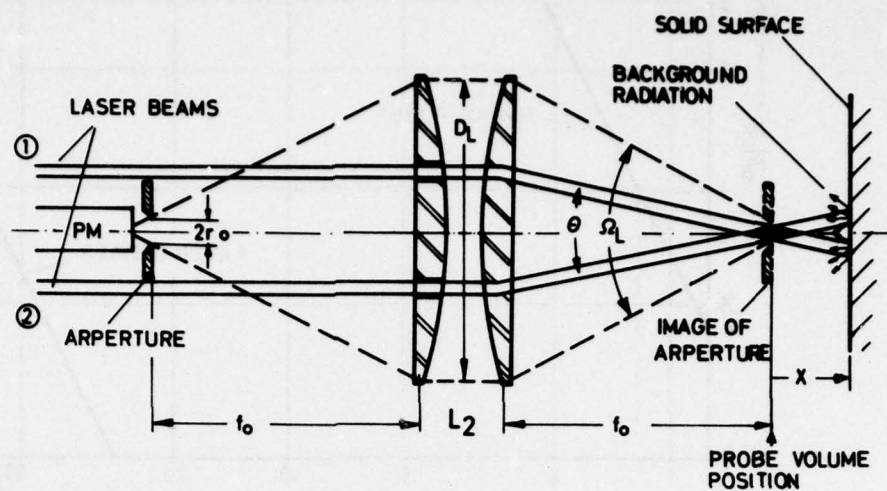


Fig. 5 LD-set up for turbomachinery application

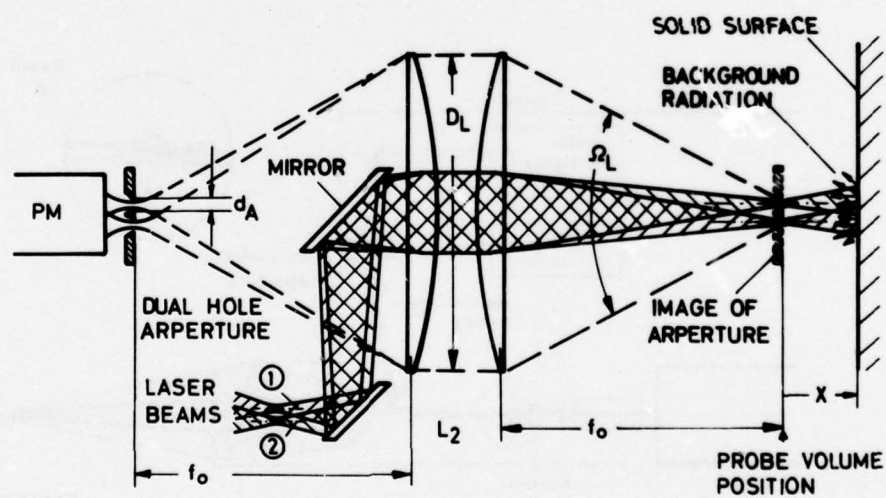


Fig. 6 Optical set-up of a time of flight anemometer for turbomachinery application

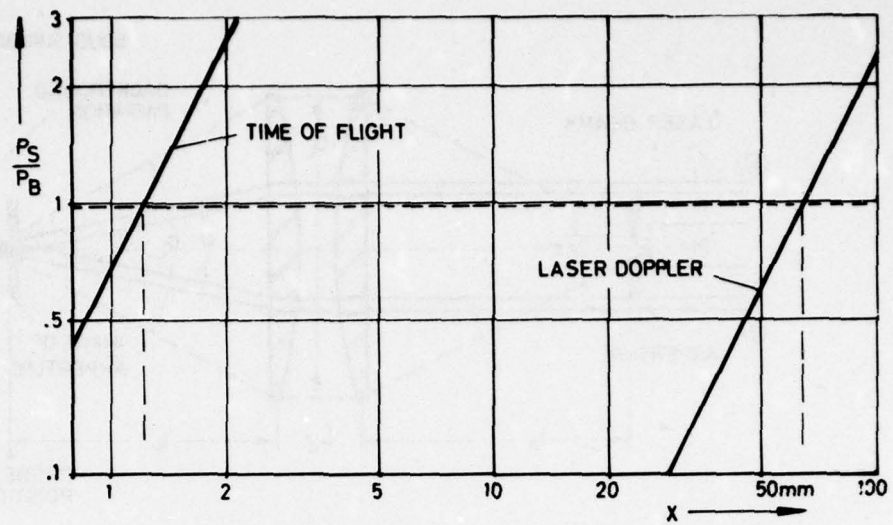


Fig. 7 Influence of background radiation

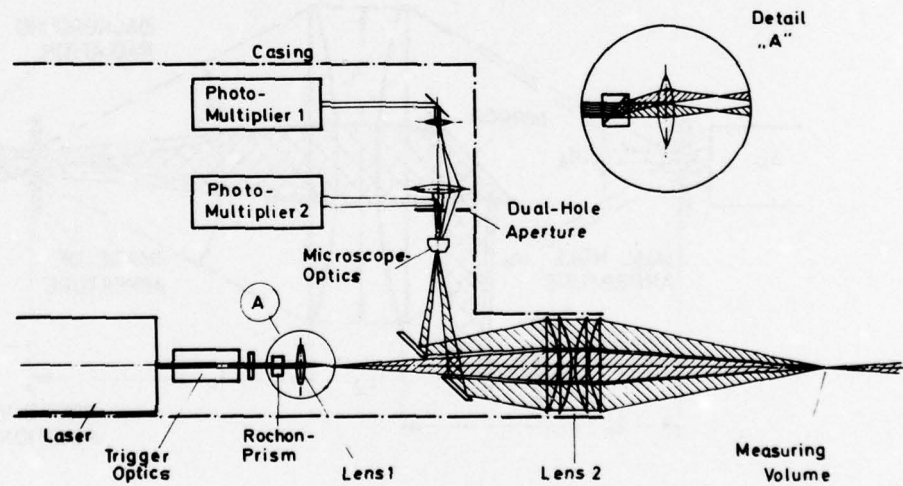


Fig. 8 Optical set-up of the L2F-velocimeter

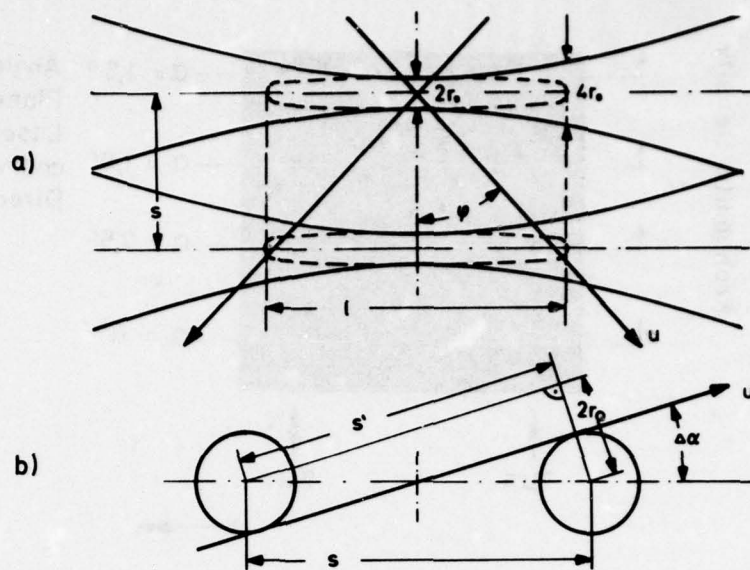


Fig. 9 Dimensions of L2F-probe volume

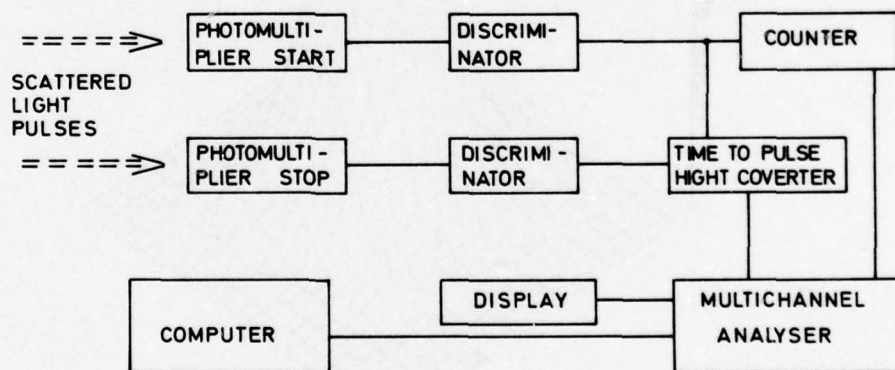


Fig.10 Data processing of L2F-velocimeter

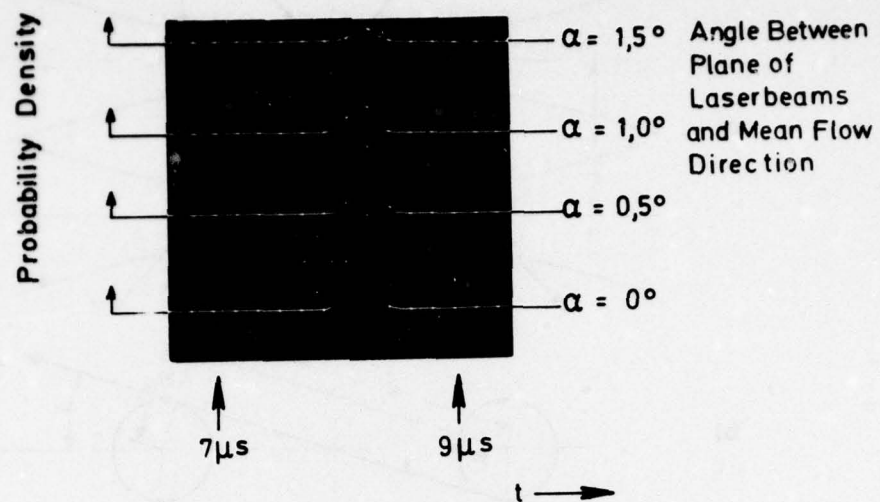


Fig.11 Output signal of the electronic data processing system

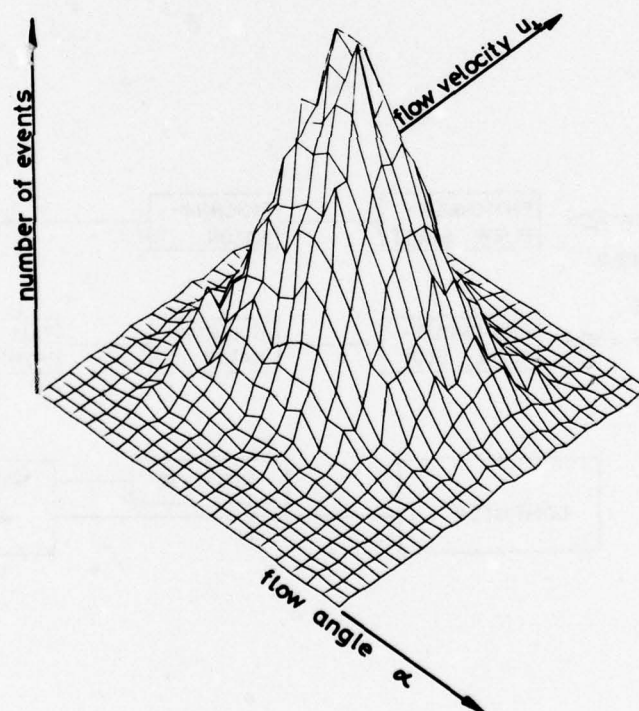


Fig.12 Measured two dimensional probability distribution

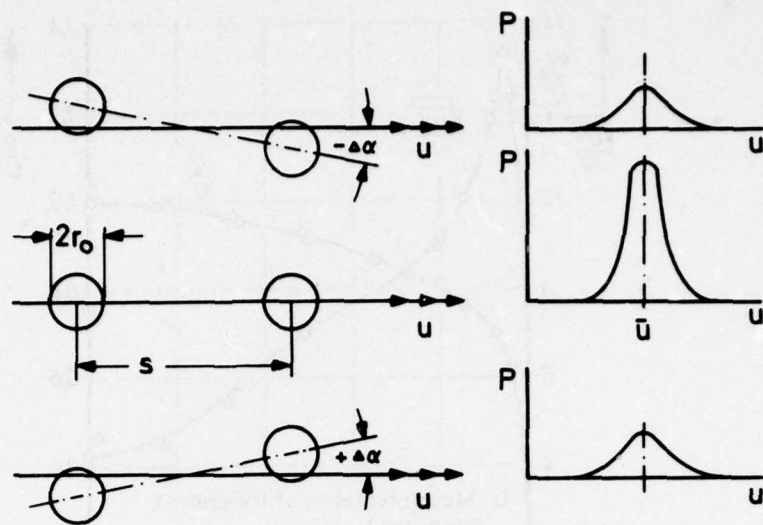


Fig.13 Broadening effect on flow angle turbulence due to finite size probe volume

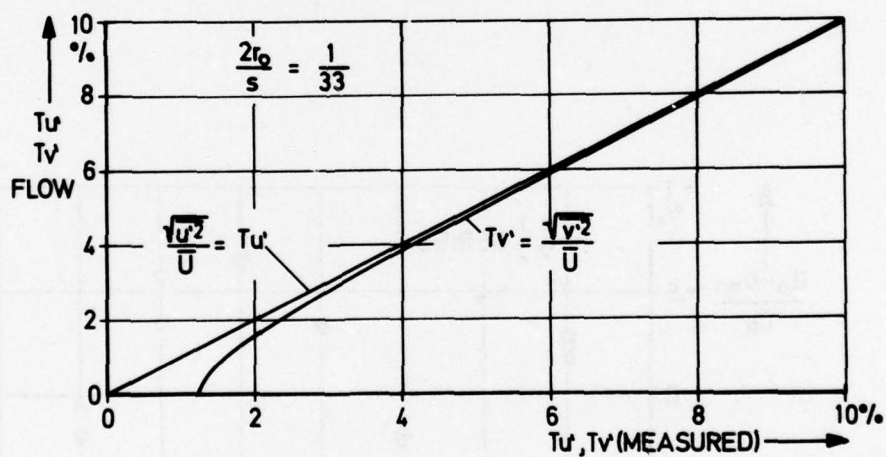


Fig.14 Influence of finite size probe volume on flow turbulence

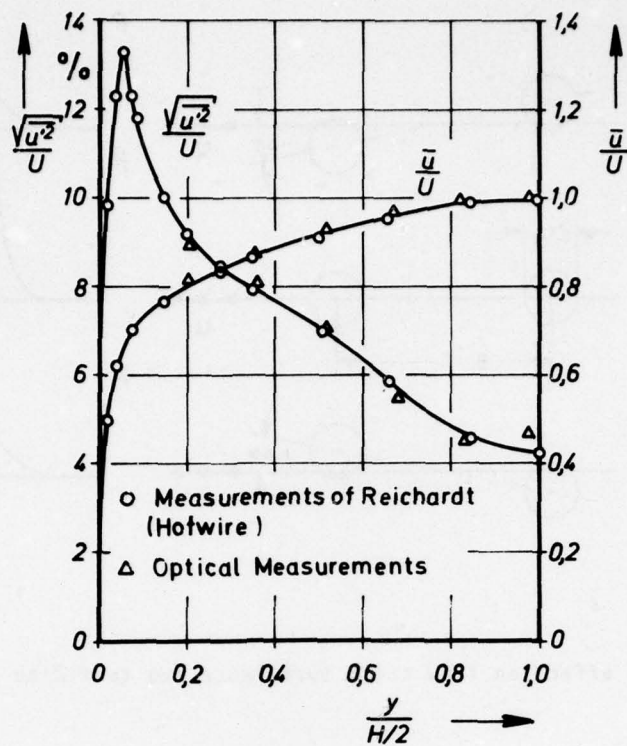


Fig.15 Optical measurements of flow velocities in a rectangular tube in comparison to hotwire measurements of Reichardt

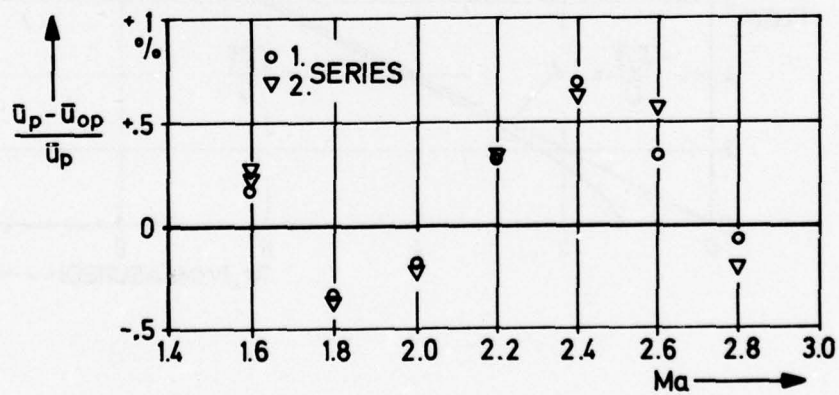


Fig.16 Optical measurements in a supersonic windtunnel

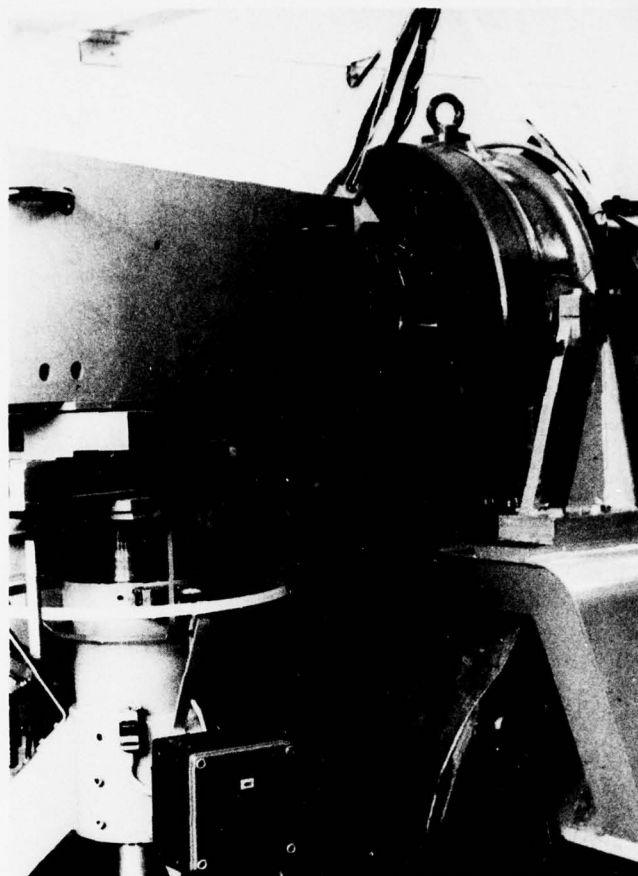


Fig.17 L2F-velocimeter for impeller flow studies at the centrifugal compressor test rig positioned on a x-y-z-coordinate platform

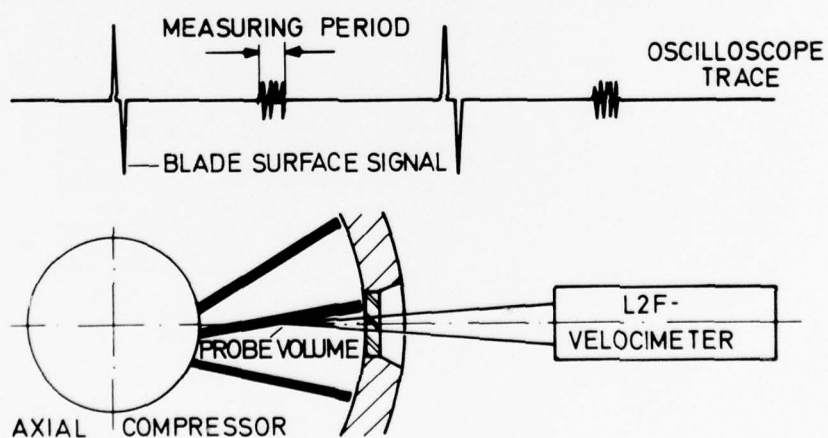


Fig.18 Detection of the circumferential measuring position

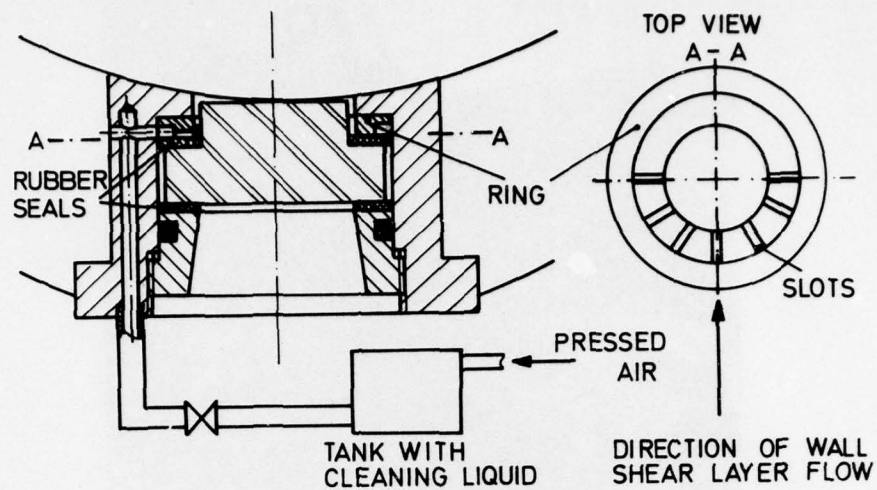


Fig. 19 Mounting and cleaning device of a casing window

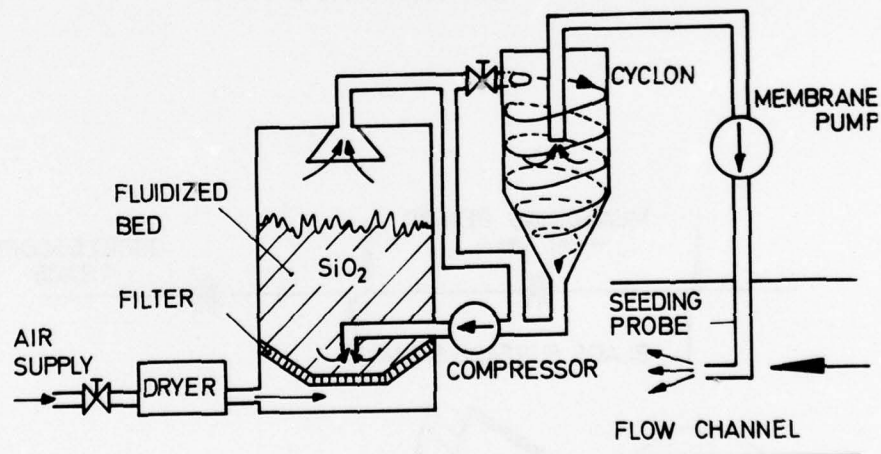


Fig. 20 Particle seeding apparatus

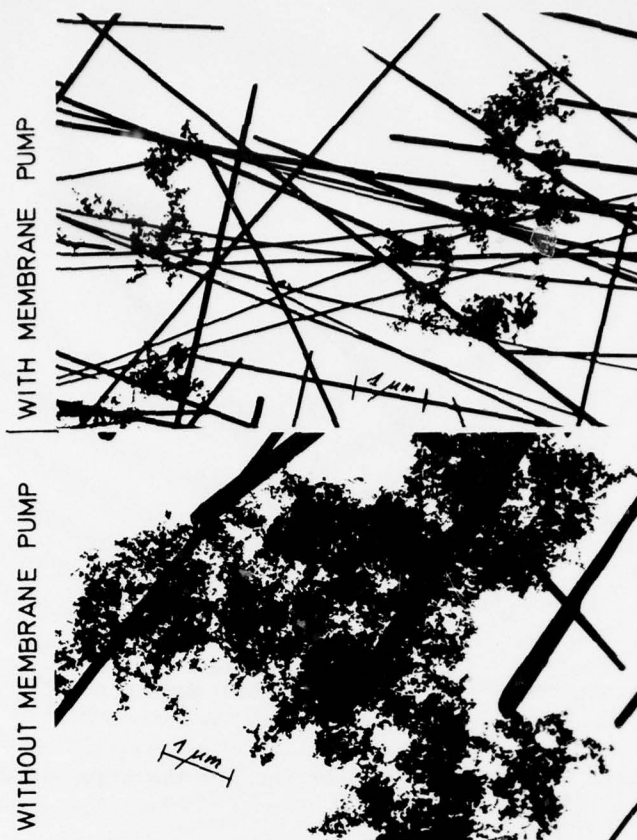


Fig.21 SiO_2 -particles (ISL photographs)

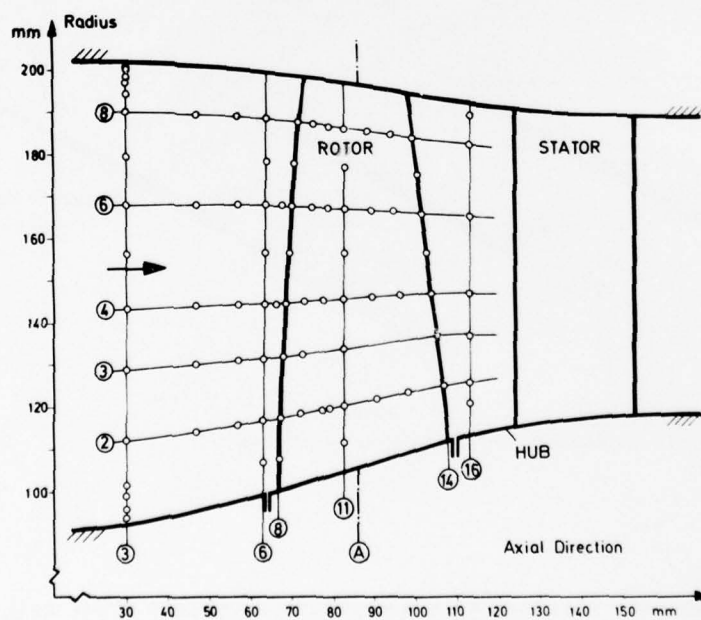


Fig.22 Compressor flowpath with the laser measuring stations

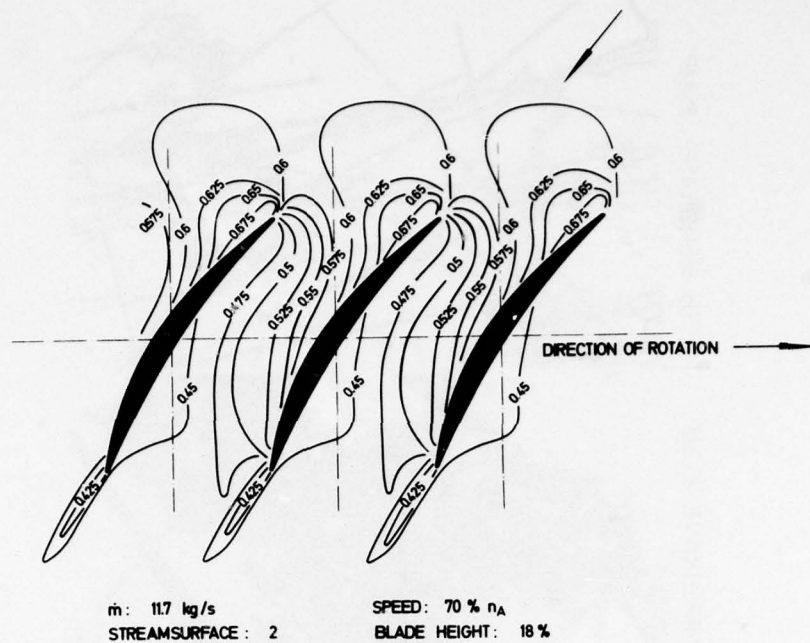


Fig.23 Lines of constant relative Mach number through the blade passage at 18 percent blade height (70 percent speed)

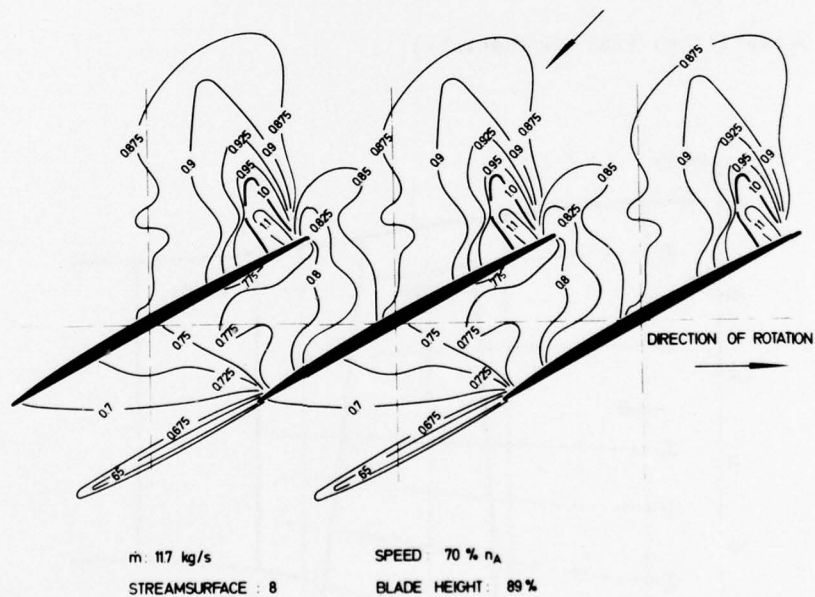


Fig.24 Lines of constant relative Mach number at 89 percent blade height
(70 percent speed)

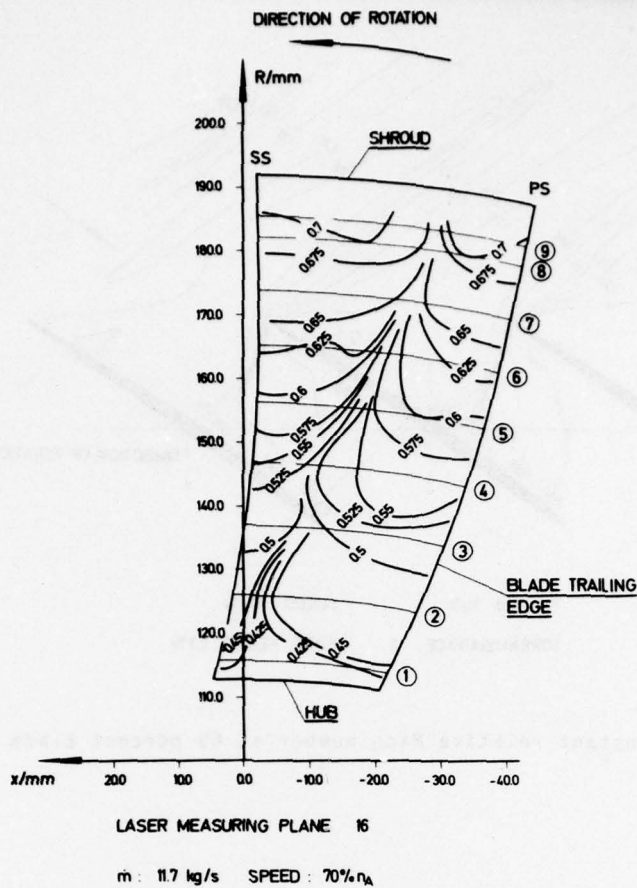


Fig.25 Lines of constant relative Mach number downstream of the rotor plotted over one blade channel (plane 16); (70 percent speed)

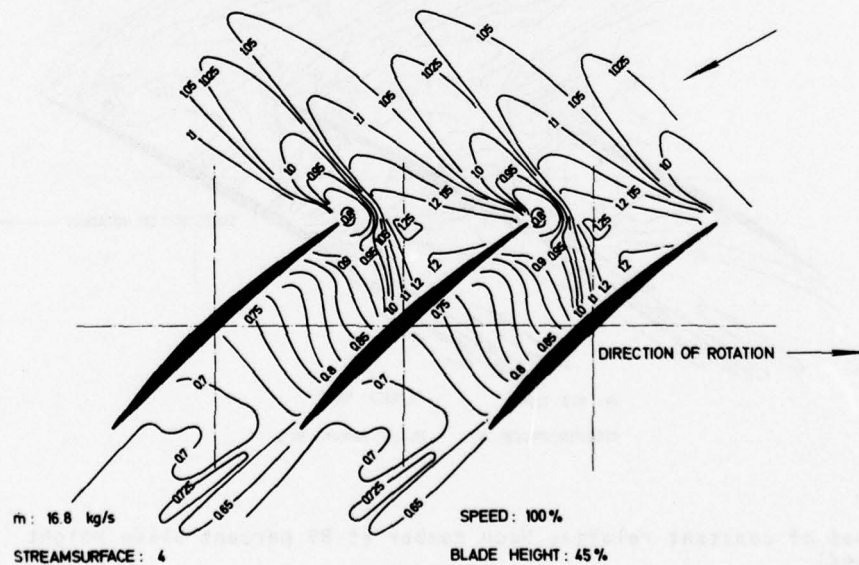


Fig.26 Lines of constant relative Mach number through the blade passage at 45 percent blade height (100 percent speed)



Fig. 29 Centrifugal compressor impeller with arrangement of optical measurement areas in the blade channel (impeller blackened by anodic treatment to reduce back-ground-radiation)

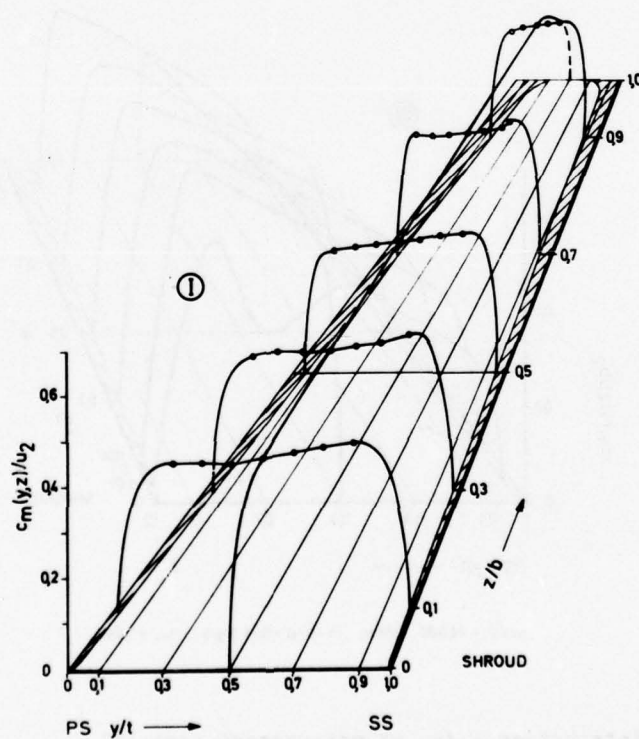


Fig. 30 Velocity distribution c_m/u_2 at measurement area I, $n = 14\,000$ rpm, $\dot{m} = 5.31$ kg/s, $x/s_m = 0.08$

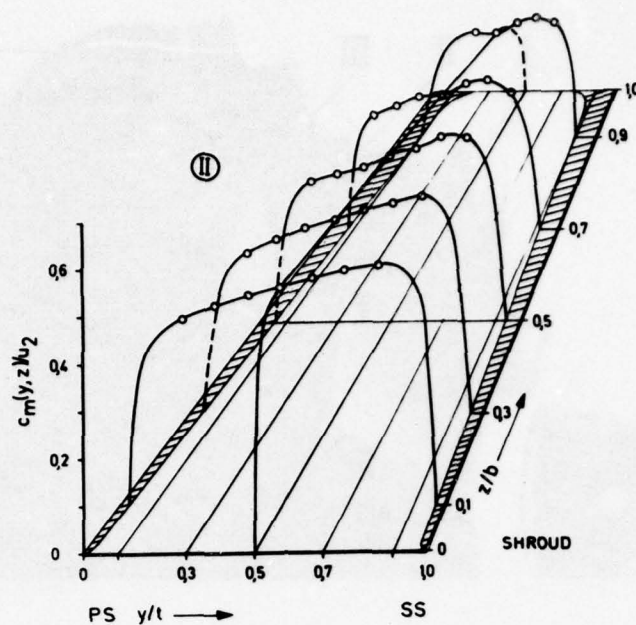


Fig.31 Velocity distribution c_m/u_2 at measurement area II,
 $n = 14\,000$ rpm, $\dot{m} = 5.31$ kg/s, $x/s_m = 0.43$

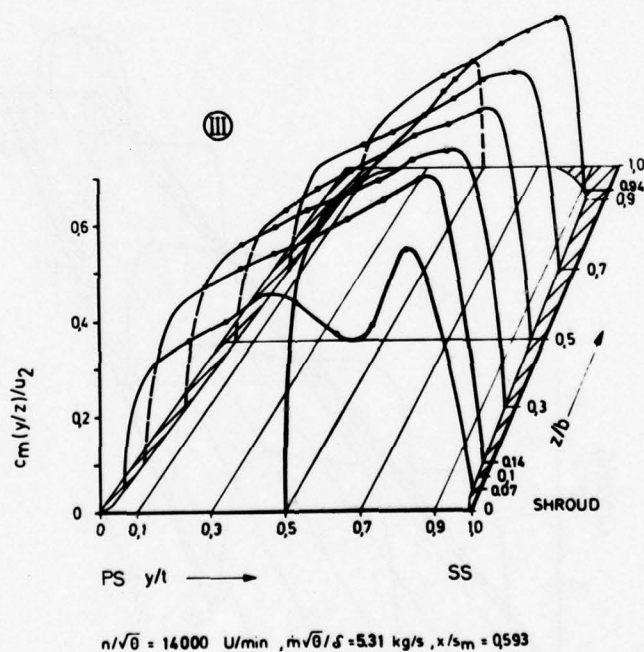


Fig.32 Velocity distribution c_m/u_2 at measurement area III,
 $n = 14\,000$ rpm, $\dot{m} = 5.31$ kg/s, $x/s_m = 0.59$

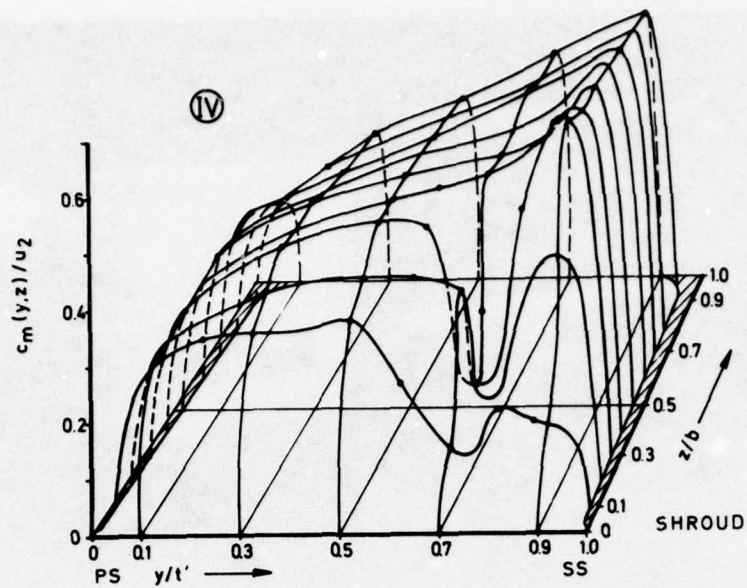


Fig.33 Velocity distribution c_m/u_2 at measurement area IV,
 $n = 14\ 000\ \text{rpm}$, $\dot{m} = 5.31\ \text{kg/s}$, $x/s_m = 0.87$

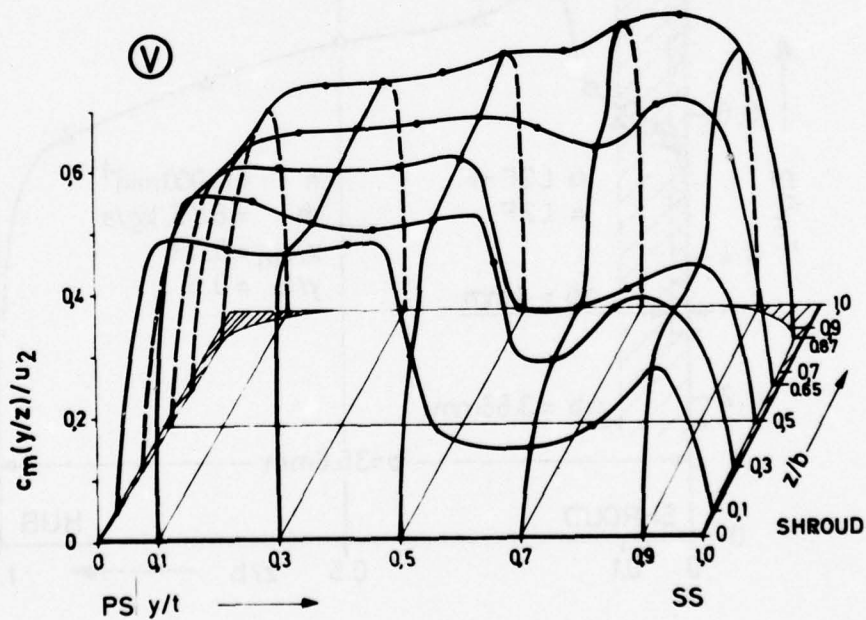


Fig.34 Velocity distribution c_m/u_2 at measurement area V,
 $n = 14\ 000\ \text{rpm}$, $\dot{m} = 5.31\ \text{kg/s}$, $x/s_m = 1.01$

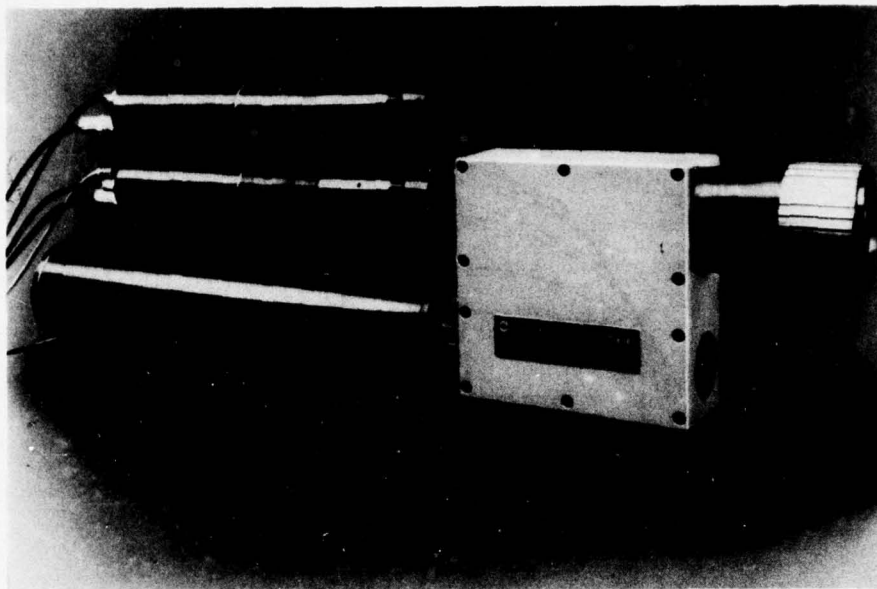


Fig.35 L2F-fluorescence-velocimeter

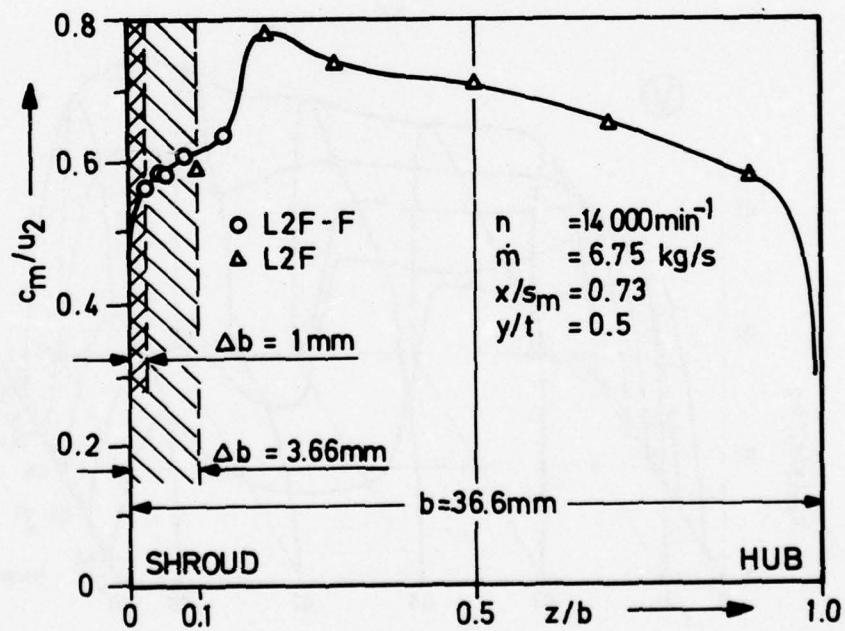


Fig.36 L2F-fluorescence-velocimetry within centrifugal compressor impeller

PRACTICAL APPLICATION OF LV SYSTEMS TO AERO ENGINE RESEARCH AND DEVELOPMENT

by

D.C. Wisler and P.W. Mossey

Aircraft Engine Group
General Electric Company
Mail Drop H43
Cincinnati, Ohio 45215 USA

ABSTRACT

Laser velocimeter (LV) measurement technology has been applied to aircraft gas turbine research and development. The velocimeter operates by measuring the transit time of a seed particle across interference fringes produced at the intersection of a split and crossed laser beam. The LV system has been used to make nondisturbing gas velocity measurements in front of bellmouth inlets, within jet exhausts for acoustic studies and within the rotating bladerows of axial flow compressors, fans and turbines, including the mapping of shock locations. The rotor flowfields were obtained at several radial immersions for operating-line and near-stall throttle settings. The results show the effects of blade loading on the flowfield and, for the supersonic fan, show the change in shock pattern as stall is approached. Analytical predictions of the various flowfields were obtained using potential flow theory, the method of characteristics and a time-dependent, finite difference solution of the fluid dynamic equations of motion. The analytical results and the flowfield measurements are considered to be in good agreement. Typical results are presented from the compressor and fan studies, the turbine studies, the acoustic studies and the inlet flow studies. The practical benefits of these results are briefly discussed.

1.0 INTRODUCTION

At the present time the laser velocimeter (LV) is the only practical method of making nondisturbing velocity measurements within the rotating blade rows of compressors, fans and turbines, particularly when these components are operating in the transonic or supersonic flow ranges. Although the concept of measuring the velocity of a gas flow by the Doppler shift of light is well known [1,2] and in recent years has been used to study many types of flowfields [3-8], the practical application of the LV to making measurements in the rotating components of turbomachinery was complicated by the fact that access to only one side of the stream was available. A particular version of the LV, known as differential Doppler [9,10], was developed using a geometry which permitted measurements of fluid flow velocities in situations where there is access to only one side of a stream. The first publication of laser velocimeter measurements in a turbomachinery application was that reported by Wisler and Mossey [11] in 1972. This work was part of a continuing research and development program at the Aircraft Engine Group of the General Electric Company, Cincinnati, Ohio USA to investigate the flowfields within turbomachinery using the laser velocimeter. The work reported in Reference 11 formed the basis for continued development of the laser velocimeter and for its use in transonic fan measurements in 1973 as reported by Wisler in Reference 12. Measurements of a similar nature on a transonic fan have also been reported by Pratt and Whitney Aircraft [13]. Runstadler and Dolan [14] have described the use of the LV for studying the basic fluid dynamics of the impeller and diffuser regions of a high pressure ratio, small centrifugal compressor. Seasholtz [15] has described work being conducted at the NASA Lewis Research Center, Cleveland, Ohio to make LV measurements in a turbine cascade. Work has been in progress at DFVLR in Germany for some years to develop an LV system that does not use a fringe pattern. Schodl has described the development of this system in References 16 and 17 and Eckardt, in Reference 18, has presented the results of using this type of LV system to measure the flowfield in a radial compressor.

The present paper discusses the application of the laser velocimeter to aero engine research and development in the areas of compressor, fan, turbine, inlet and jet acoustic technology. Both the experimental results and the analytical correlation are discussed.

2.0 LASER VELOCIMETER

The laser velocimeter determines velocity by measuring the time taken by a particle to traverse laser fringes of known spacing. This time is obtained by analyzing the light scattered by the particle as it traverses the fringes. A discussion of the design of the velocimeter, the electronics for analyzing the scattered light, the seeding of the flow and the data reduction techniques are presented in the following.

2.1 Design of the Laser Velocimeter

The arrangement of the General Electric laser velocimeter system used to obtain measurements within rotating blade rows of turbomachinery is shown in Figure 1. The laser, the optics and the photomultiplier assembly are enclosed in a cylindrical housing that can be electrically actuated over 380 mm axially, 150 mm radially, and +90 degrees about the beam bisector. A continuous argon-ion laser with a power of 1.4 watts is operated at a wavelength of 514.5 nm. The laser output beam is split into two beams by a beamsplitter. Each of these half power beams is brought to a common focus, called the measurement zone, by the mirrors and lens assembly shown in Figure 1.

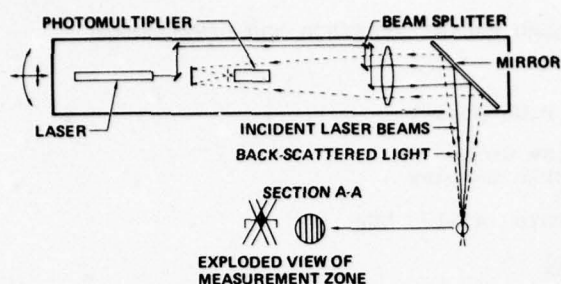


Fig. 1 Illustration showing the laser velocimeter and the optical system

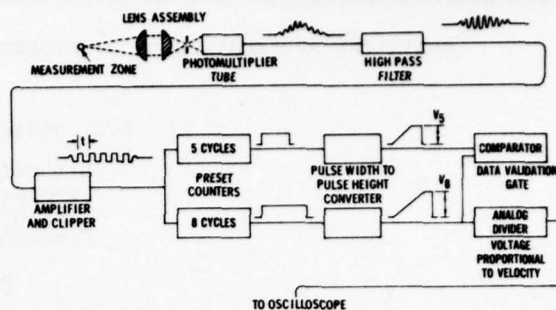


Fig. 2 Schematic showing the LV electronics

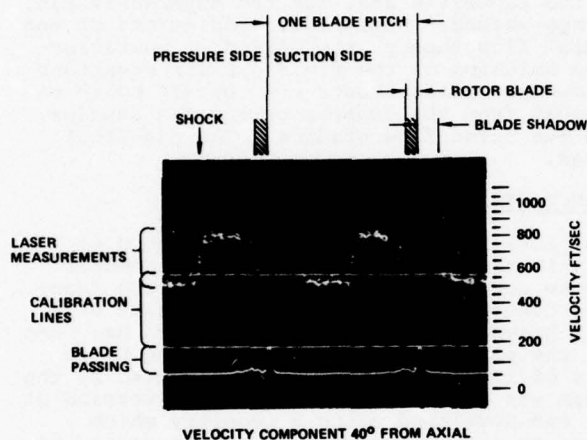


Fig. 3 Typical LV oscillogram showing fan intrarotor velocity measurements and shock wave location for the 30 percent flow streamline, 37 percent axially projected chord

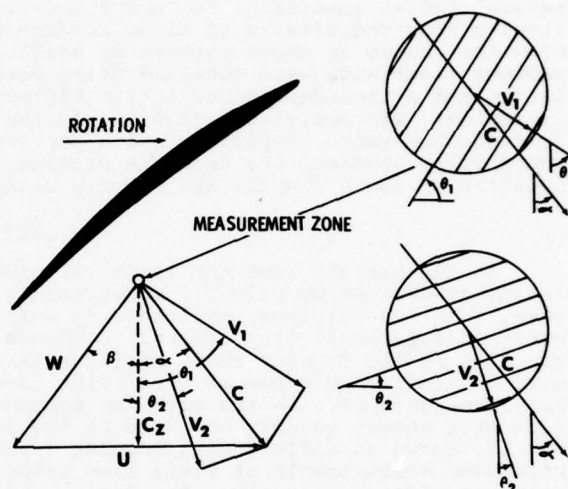


Fig. 4 Rotor vector diagram and orientation of laser fringes

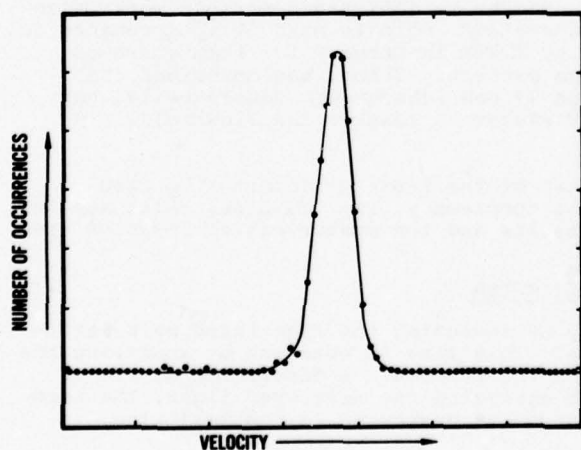


Fig. 5 Probability density distribution obtained from laser velocimeter measurements

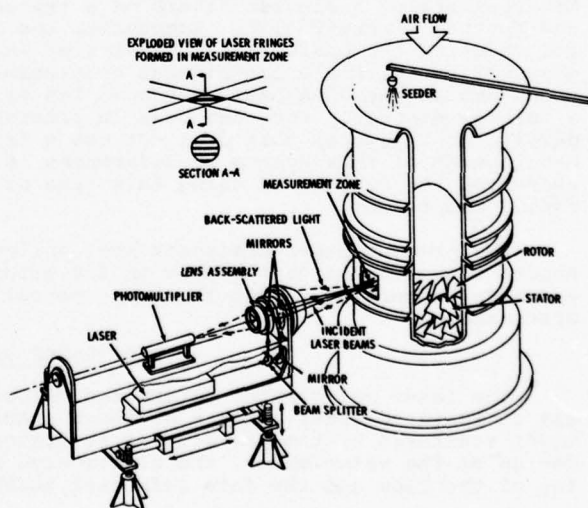


Fig. 6 Isometric drawing showing the Low Speed Research Compressor and the Laser Velocimeter

Optical access to the blading is provided by an anti-reflection window which is flat to $\lambda/10$. The insert in Figure 1 shows an enlarged view of the laser beam interference fringes formed in the measurement zone. There are 572.07 laser fringes per cm in the measurement zone. The beam diameter at Section A-A is about 0.305 mm and the included angle of the beams is 1.9 deg, providing 4.06 mm of common crosscover. Seed particles, which are sprayed into the flow upstream of the blading, pass through the laser fringes in the measurement zone and scatter the laser light in all directions. A small 11-deg cone of back-scattered light is collected and converged through an aperture to a photomultiplier tube. For turbomachinery applications within rotating blade rows, an optical working distance from the velocimeter to the measurement zone of 64 cm (25 in.) is acceptable. For acoustic measurement applications, the optical arrangement of the system shown in Figure 1 is modified by removing the mirror and using lenses which provide a long working distance of 216 cm (85 in.). The velocimeter is capable of making measurements from 8 to 1200 m/sec.

When a particle passes through the laser fringes, it scatters light in all directions. The backscattered mode of operation was chosen for use because only one visual access to the flow is needed. This is ideally suited to turbomachinery applications because, generally, only one-sided entry through the casing is available to observe the flow. In addition the receiver and transmitter can be integrally contained resulting in better thermal equalization, one acoustic housing and best alignment stability. For acoustic applications using long working distances, stringent requirements on laser divergence and beam alignment are necessary to obtain a small control volume at long working distances.

The intensity of forward-scattered light is approximately 100 times greater than the intensity of back-scattered light. Consequently, a laser power of 1 to 2 watts (single line) is necessary to assure sufficient back-scatter intensity. The continuous 1.4 watt argon-ion laser, which is fairly reliable and widely available, provides this intensity in the 514.5 nm green line. It is advantageous to work with the visible light rather than infra-red light because the scattering cross section is better and set-up and alignment is more convenient. The photomultiplier used to detect the back-scattered light needs to have high gain, low noise and a frequency response up to approximately 100 MHz. The S20 cathode chosen is ideal for the 514.5 nm green line. The photomultiplier is protected against acoustic and vibratory inputs with mass damping material (lead sheet and foam rubber).

The laser fringe spacing determines the resultant Doppler burst frequency for a given velocity. The design goals are (1) to keep the control volume as small as possible so that spacial resolution is high and (2) to keep at least 12 to 20 fringes in the control volume. The frequency corresponding to the highest velocity should be within the signal processor's range but well below the laser's cavity Δf which is about 140 MHz for a 1 meter cavity. Theoretically there is no lower velocity limit, but in practice the dynamic range, V_{\max}/V_{\min} , can be the item that determines complexity and therefore cost of the signal processor. The dynamic range of the GE processor is 150 to 1.

Adaptation of the laser velocimeter to turbomachinery applications requires certain compromises. The LV head must be kept compact to keep clear of probes, etc. In order not to disturb the flow, the window size is usually limited which in turn limits the viewing volume available. In addition an X, Y, Z and tilt actuation system, which is expensive and complex, is often needed to reduce blade shadow volume. Finally, the necessity to keep the window clean in order to keep good fringe quality for signal processing must be balanced against the cost of having to shut down to clean windows during engine and component testing.

2.2 Electronics

The counter-timer (also called the burst counter) type of signal processor was chosen for use because of the low seed density employed. The frequency tracker, spectrum analyzer and correlation processors are not capable of single-particle velocity measurements and therefore cannot be used.

A schematic of the GE counter-timer signal processor is shown in Figure 2. The processor uses a 5 cycle/8 cycle comparator as a validation check. A brief description of the operation of the processor, developed by W.B. Jones [10], is given in the following. Since the scattered light intensity varies sinusoidally as the particle moves from one fringe plane to the next, the photomultiplier output during this time is an amplitude modulated sine wave burst. If the spacing of the fringes is known, then the velocity component can be found by measuring the frequency of the burst. This burst is made symmetrical about a line of zero volts by using a high pass filter. This symmetrical burst is highly amplified and clipped on the top and bottom to yield a nearly square wave. The square wave enters preset counters whose outputs are single pulses of time duration equal to five consecutive cycles and eight consecutive cycles of the burst wave respectively. The preset counter output gates a pulse-width-to-pulse-height converter. The converter output is a linear ramp ending in a constant voltage whose magnitude is proportional to the elapsed time for five cycles and eight cycles respectively. The comparator validates the signal and outputs a gate pulse only if the five-cycle elapsed time is equal to 5/8 of the eight-cycle elapsed time within a tolerance band. The analog divider converts the eight-cycle elapsed time to a voltage proportional to the velocity. The voltage is recorded if the data validation gate appears. All circuits are then reset for the next signal pulse. The maximum attainable data rate was 67,000 data/sec. The signal processor was calibrated as input frequency

versus output voltage by using a variable frequency oscillator as a signal source into a "burst generator." With a typical processor setting of $N = 8$ counts, the overall calibration limit was ± 0.6 percent. The signal-to-noise ratio required by this wide-band processor is about 20 to 25 dB. As the signal-to-noise ratio falls below 20 dB the validation percentage falls.

2.3 Seeding

The LV operation depends upon the detection of frequency shifted scattered light from micron-sized tracer particles. Seeding is generally necessary because air molecules do not usually scatter sufficient laser light and because the data from existing natural dust is too low. Two types of seeding are used. The first type is a 1 micron diameter polystyrene latex particle manufactured for use in calibration of electron microscopes. These particles have a low density (1.0 gm/cc). Seeding is accomplished by spray-atomizing a dilute suspension of the particles into the air entering the test compressor. Unfortunately they have a temperature limit of about 95°C (200°F). Latex particle seeding was used in the compressor tests described in this paper.

The other type of seed particle used is the refractory type such as Al_2O_3 , MgO or TiO_2 . Seeding is accomplished by use of a fluidized bed and an auxiliary dry air supply. Although refractory particles can withstand higher temperatures, they have higher densities (4 gm/cc) and for a given diameter tend to show more slip in high-g fields. Refractory seeding was used in the turbine tests and the acoustics tests described in the paper.

The accuracy of the LV system is limited by the accuracy with which the tracer particles follow the fluid flow. A detailed particle trajectory analysis was conducted and the results shown in the Appendix of Reference 12 indicate that the seed particles should follow the flowfield within 1 to 2% outside of the region of the shocks and that the particles should recover rapidly after passing through the shocks. This conclusion is also supported by the crisp shock wave indication in the oscillogram in Figure 3.

2.4 Data Recording and Reducing Techniques

The laser velocimeter processor-validated measurements of velocity are available as either a brief (5 μsec) sample or as a sample and hold output which lasts as long as the interval to the next sample. The various types of data recorders which can be used include: the X-Y plotter for mean velocity profiles, the pulse height analyzer for construction of probability density distributions of velocity, the digital data acquisition computer with core, disc and magnetic tape storage mediums, and the oscilloscope/camera for data collection, storage and display. The oscilloscope/camera recording technique and the pulse height analyzer recording technique are discussed in the following.

A typical oscillogram showing LV measurements obtained within the rotating blade rows of a high speed fan is shown in Figure 3. A velocity scale which starts at the baseline is shown on the figure. Each of the short dashes on the oscillogram in the zone marked "Laser Measurements" represents an individual velocity measurement. The horizontal lines appearing at 55.4 m/sec and 176 m/sec are used for calibration purposes. The blade spacing marks on the oscillograms were obtained by recording the flash of the blade as seen by the photomultiplier and by-passing the LV electronics. These blade passing marks were used to position the data circumferentially relative to the blade surface. Since the laser beam was blocked by the twist and camber of the blade, a void, indicated as a blade shadow in the figures, appeared in the data at circumferential locations near the blade surface. The LV oscillogram in Figure 3 shows measurements taken at 37% axially projected chord for the 30%-flow streamline. There is clear indication of the shock wave location and of the pre-shock and postshock velocity levels. The velocity component measured was 40° from axial. The shock wave was usually more clearly detected using this fringe orientation.

In order to obtain the circumferential and axial velocity components which are of interest, measurements at two fringe orientation angles were necessary. The radial components of velocity were not measured. A schematic in Figure 4 shows the orientation of the laser fringes, the two velocity components V_1 and V_2 obtained from the oscillograms, and the vector diagram of the rotor. Since the LV measures the velocity component perpendicular to the fringes, the absolute velocity, C , and flow angle, α , are obtained by solving Equations (1a) and (1b) simultaneously. This results in Equation (2) for the flow angle, α . Numerical values for α and C are obtained from Equation (2) and either Equation (1a) or (1b) by using the measured velocity components V_1 and V_2 and the measured orientation angles of the laser fringes θ_1 and θ_2 .

$$V_1 = C \cos (\theta_1 - \alpha) \quad (1a) \qquad V_2 = C \cos (\alpha - \theta_2) \quad (1b)$$

$$\tan \alpha = \frac{V_1 \cos \theta_2 - V_2 \cos \theta_1}{V_2 \sin \theta_1 - V_1 \sin \theta_2} \quad (2)$$

The relative velocity, W , and the relative flow angle, β , are then obtained from the usual equations involving the blade speed U ,

$$W = [C^2 + U^2 - 2UC \sin \alpha]^{1/2} \quad (3) \qquad \beta = \tan^{-1} \left[\frac{U - C \sin \alpha}{C \cos \alpha} \right] \quad (4)$$

Another method of recording data is by using the pulse height analyzer. This allows the velocity measurements to be classified, providing the necessary information for the construction of probability density distributions. These distributions are particularly useful for jet plume turbulence (acoustic noise) studies. An example of such a distribution is shown in Figure 5. The mean velocity, \bar{V} , can be calculated from the discrete velocity samples by

$$\bar{V} = \sum_{\text{All Class Intervals}} \left(\frac{V_{i+1} + V_i}{2} \right) \frac{f_i}{N} \quad (5)$$

where $(V_{i+1} + V_i)/2$ is the value of the sample velocity component at the center of the class interval, f_i is the number of occurrences (the weighting factor) of a classified velocity interval (such as from 100 to 100.5 m/sec) and N is the total number of samples taken. The turbulence velocity, v' , at a point is found from the standard square root of the statistical variance,

$$v' = \left[\sum_{\text{All Class Intervals}} \left(\frac{V_{i+1} + V_i}{2} - \bar{V} \right)^2 \frac{f_i}{N} \right]^{1/2} \quad (6)$$

The turbulence level is then v'/\bar{V} .

3.0 COMPRESSOR AND FAN APPLICATIONS

The General Electric Company is conducting research programs aimed at the development of high performance turbomachinery components. As part of this effort, the laser velocimeter is being used to provide detailed flowfield measurements within the rotating blade rows of fans and compressors. Such measurements have proven to be very useful in mapping shock wave locations, in determining diffusion rates and in assessing the performance of turbomachinery blade rows. Two applications of the laser velocimeter to these types of flowfield measurements are presented.

3.1 Low Speed Research Compressor Application

The Low Speed Research Compressor (LSRC) is an experimental facility which is used for testing the aerodynamic characteristics of various compressor and fan designs. The compressor has a tip diameter of 1.52 m (5 ft) and is mounted vertically, as shown in Figure 6. A large flow straightening screen (not shown), which fits over the bellmouth, was used to ensure uniform disturbance-free flow into the compressor. The discharge of the LSRC is covered with a large movable plate for throttling the flow. The experiments were performed using a two-stage 0.5 radius ratio compressor having an average rotor tip speed of 46 m/sec (150 ft/sec). The laser measurements were confined to the region of the first stage rotor. The 55 blades of this stage had a modified NACA 65-Series thickness distribution on a circular arc meanline. At 50 percent immersion the solidity was 1.61, the camber was 18.2 degrees, and the stagger angle, measured from axial, was 52 degrees.

The arrangement of the LV system is also shown in Figure 6. The laser, the optics and the photomultiplier assembly were mounted on a platform that could be electrically actuated over 380 mm (15 in.) of radial distance and 150 mm (6 in.) along the compressor axis. In addition, it could be rotated $\pm 90^\circ$ about the beam bisector. Measurements were taken at the entrance and exit planes of rotor 1 and at various radial immersions from the leading edge to the trailing edge within the first rotor passage for three throttle settings: wide open, mid-range and near stall. Data were recorded across a blade pitch and were reduced using equations (1)-(4) as discussed in Section 2.4.

Test Results

There were two fundamental objectives of the experimental program. The first was to make velocity (magnitude and direction) measurements at those positions where conventional instrumentation, such as hot film anemometers, pitot static probes, and flow angle measuring devices, could be used for comparison. To carry out this objective, velocity measurements were made at the inlet and exit planes of the first stage rotor. The velocity obtained from the laser velocimeter, the hot film anemometer and the pitot static probe all agreed generally within 2 or 3 percent. An example of these velocity comparisons across the rotor pitch at 50% immersion for the midrange throttle setting is shown in Figure 7a for the rotor inlet plane. The velocity distribution across the inlet plane from the pressure surface to the suction surface of the rotor varied from 18.3 m/sec (60 ft/sec) to 20.5 m/sec (67.2 ft/sec). The pitot static and hot film measurements fell within the distribution of the LV measurements. Good agreement was also obtained between flow angles measured by the LV, the tuft and the wedge angle probe. An example of such measurements is shown in Figure 7b for the rotor exit plane.

After confidence in the laser velocimeter measurements had been achieved, the rotor intra-blade flow angles and velocities were then measured. The data were taken at 50 percent radial immersion in equally spaced planes from the leading edge to the trailing edge of the rotor. The relative flow angles and velocities are shown in Figures 8 and 9a, b, and c. The small solid circles in Figures 9a, b, and c indicate

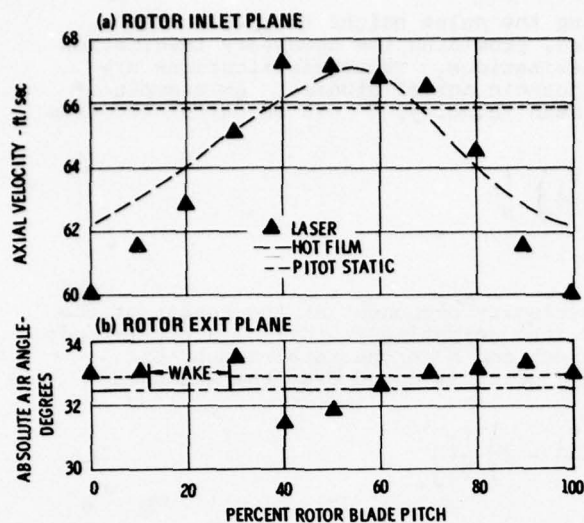


Fig. 7 Comparison of velocity and air angle measurements across the compressor rotor pitch, (m/sec = 0.3048 x ft/sec)

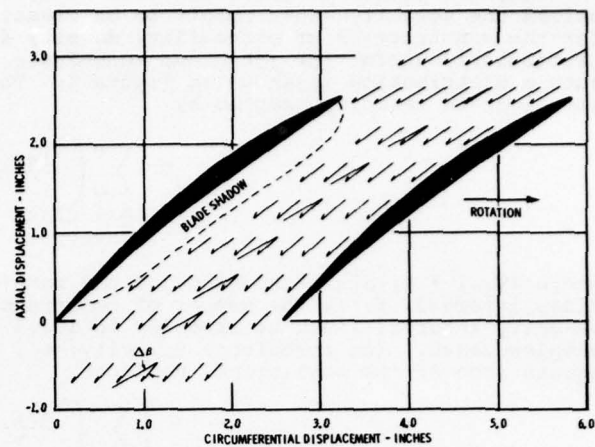


Fig. 8 Relative flow angle measurements within the first compressor rotor passage for the midrange throttle setting and 50 percent immersion. $\Delta\theta$ indicates the flow turning

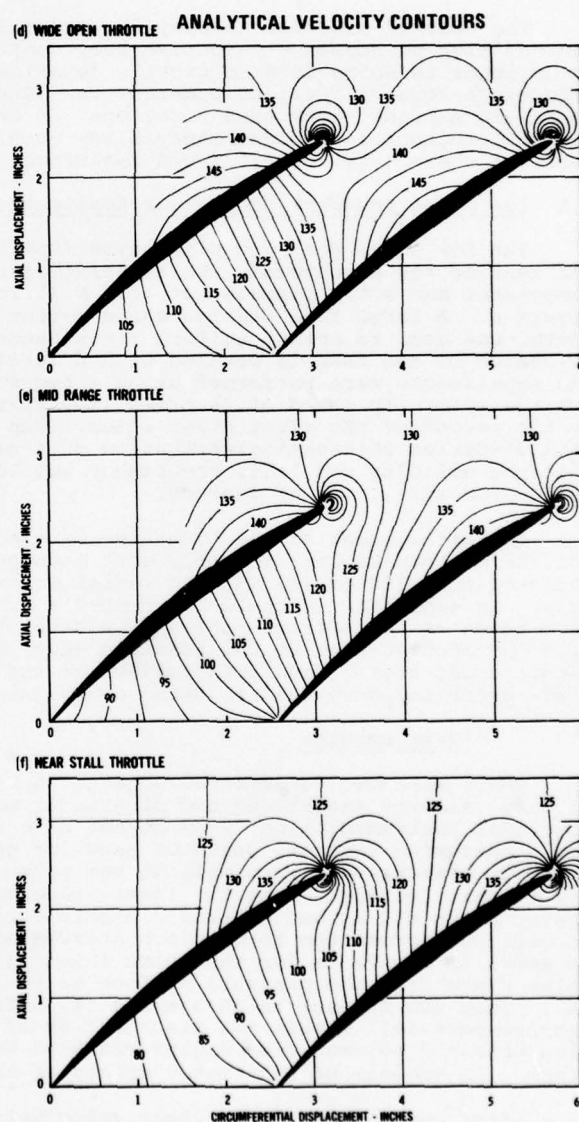
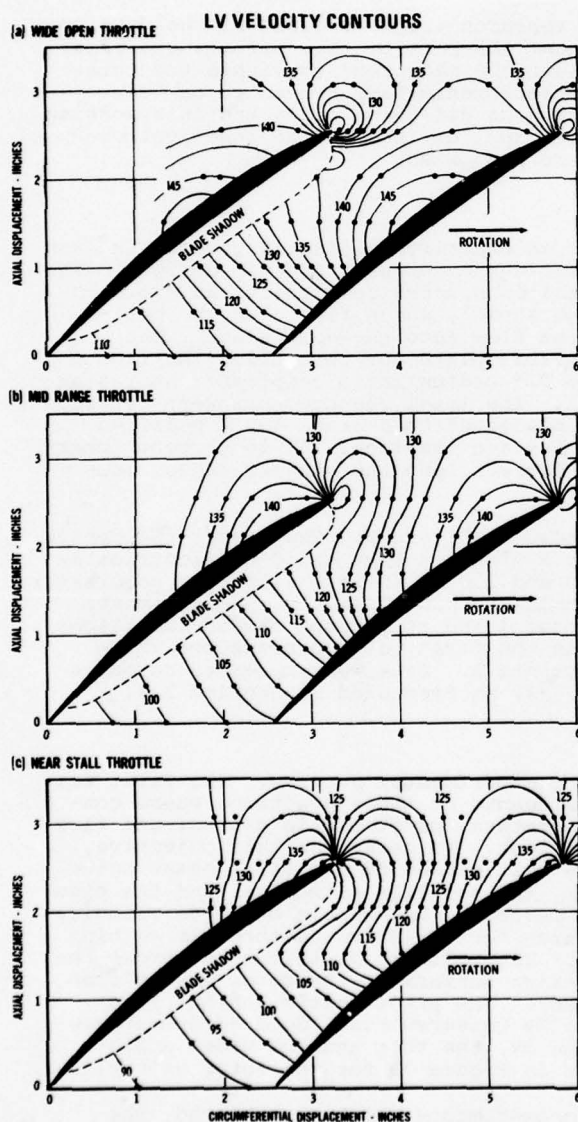


Fig. 9 Comparison of experimental and analytical velocity contours within the first compressor rotor passage for wide open throttle, midrange throttle and near stall throttle. Velocity is in ft/sec, (m/sec = 0.3048 x ft/sec)

measured data points. Velocity contour lines were then drawn through the measured data points assisted by a knowledge of general isobar shapes typical of the potential flow-field about an airfoil. Since the laser beam was blocked by the twist and camber of the blade, a void appeared in the data near the pressure surface. This void is indicated in the figures by "blade shadow". The intra-blade relative flow angles for the mid-range throttle show a smooth turning of the flow from the entrance plane to the exit plane with no evidence of flow separation; see Figure 8. The relative velocity measurements, seen as contour plots in Figure 9, show the effects of blade loading as the compressor is throttled from wide open (Figure 9a) to mid-range (Figure 9b) to near stall (Figure 9c). These figures will be discussed in detail in the next section.

Theoretical Analysis and Discussion

The flowfield in the first stage rotor passage was analyzed theoretically by applying Laplace's Equation to an incompressible, irrotational, two-dimensional cascade. For these conditions, Laplace's Equation can be written in terms of the stream function, ψ , as

$$\frac{\partial^2 \psi}{\partial x^2} + \frac{\partial^2 \psi}{\partial y^2} = 0 \quad (7)$$

The computer program, which also incorporates compressibility corrections, performed a relaxation solution for the stream function within a strip corresponding to one rotor pitch with the airfoil surfaces forming fixed boundaries. Solutions to Equation (7) were obtained for the wide open, midrange and near stall throttle settings by using the measured rotor inlet and exit flow angles. Velocity components were then found by differentiating the stream function,

$$u = \frac{\partial \psi}{\partial y} \text{ and } v = - \frac{\partial \psi}{\partial x} \quad (8)$$

The resultant velocity contour plots are shown in Figures 9d, e, and f.

The overall qualitative agreement between the LV measurements and the potential flow solution is quite good, as can be seen by comparing Figures 9a, b, c and 9d, e, and f. For the wide open throttle in Figures 9a and 9d, the peak velocity on the suction surface occurs near the 45% chord point as measured from the leading edge. Also the contours around the leading edge compare favorably. When the compressor is throttled to the midrange setting, the location of the peak velocity on the suction surface moves toward the leading edge; see Figures 9b and 9e. Again the contours around the leading edge and the free stream velocity contour of 130 ft/sec compare favorably. For the near stall throttle settings, Figures 9c and 9f, the position of peak velocity has moved very near the leading edge.

Examination of Figure 9 from approximately the mid-chord point to the trailing edge reveals that more diffusion occurs in the potential flow analysis than is present in the experimental results. The local diffusion parameter [19] is defined as

$$D_L = \frac{V_{\max} - V_{\text{exit}}}{V_{\max}} \quad (9)$$

where V_{\max} is the maximum suction surface velocity and V_{exit} is the rotor exit velocity. Based on the velocity contours in Figure 9, the experimental and potential flow D_L values are respectively 0.24 and 0.28 for the wide open throttle, 0.29 and 0.34 for the midrange throttle and 0.35 and 0.42 for the near stall throttle. Thus the potential flow analysis has over-estimated the amount of diffusion by about 17% for the wide open and midrange throttles and 20% for the near stall throttle. This overestimate is, of course, primarily due to the fact that boundary layer growth and flow separation were not incorporated into the flow model. Thus the use of the LV for determining "calibration factors" for potential flow cascade models appears feasible.

Additional information on this test program is given in Reference 11.

3.2 High Speed Fan Application

As part of another comprehensive test program, the laser velocimeter was used to determine shock wave locations and to make gas velocity measurements within the rotating blade row of an advanced 550 m/sec (1800 ft/sec)-tip speed fan rotor, shown schematically in Figure 10. The rotor contained 30 titanium blades having an inlet tip diameter of 559 mm (22 in.) and a radius ratio of 0.45. The rotor tip solidity was 1.27 and the stagger angle was 72°. There were 26 variable IGV's and 48 variable stators in the assembly. The fan was tested in the General Electric Scale Model Test Facility at Evendale, Ohio. The tests were conducted at an inlet pressure of 0.55 atmosphere and an inlet temperature of 32° C (-90° F). A flow straightening screen and bellmouth (not shown in the figure) were used to ensure uniform disturbance - free flow into the fan.

The laser, the optics and the photomultiplier assembly, also shown in Figure 10, were enclosed in a cylindrical housing that could be electrically actuated over 38 mm axially, 150 mm radially and + 90 deg about the beam bisector. Measurements were taken from the leading edge to the trailing edge within the fan rotor passage for the opera-

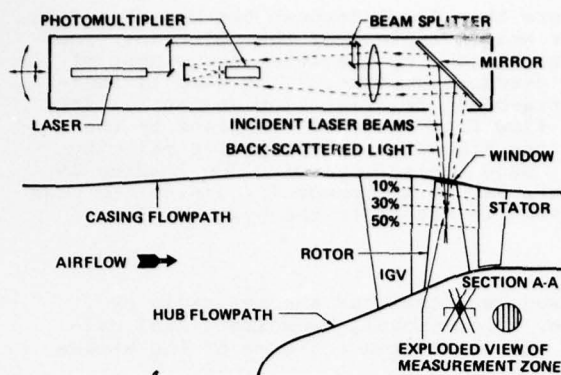


Fig. 10 Illustration showing the laser velocimeter and the high-speed fan test vehicle.

drawn to scale and indicate the direction of the flow. Each "tick" mark below an arrow represents 152 m/sec (500 ft/sec). For the operating line condition shown in Figure 11a, there are two shocks in the rotor passage. The first shock is an oblique shock. Due to window contamination, measurements of this shock location could not be obtained near the leading edge; however, the data that were obtained, when extrapolated, indicate that the first shock was oblique. The second shock is approximately a normal shock originating on the pressure surface at about 60% chord from the leading edge. The normal shock is positioned outside the passage well past the trailing edge of the adjacent blade. The measured flow velocity entering the oblique shock is about 510 m/sec (1675 ft/sec). The flow turning and supersonic Mach number behind the oblique shock as well as the subsonic flow behind the normal shock are clearly shown by the measurements. It is recognized that the velocity jump across the normal shock does not follow the classical normal shock relations. This difference, verified by over-the-rotor pressure measurements, may result from the three dimensional nature of the flow in which the shock is not normal in the plane in which the measurements are made, but is rather curved in the radial direction.

At the near-stall throttle setting shown in Figure 11b, the higher back pressure has eliminated the second strong shock and pushed the leading edge shock upstream in the rotor passage. The measured velocity entering the shock is about 521 m/sec (1710 ft/sec) which has been reduced from the inlet velocity of about 533 m/sec (1750 ft/sec) by the precompression on the suction surface. The shock is still mostly oblique and is pulled back into the passage. It is nearly attached to the leading edge, indicating that rather little flow spillage has occurred. The flow at the near-stall condition is slightly less than at the operating line, so not much flow spillage would be expected. The post-shock velocity is very slightly supersonic, $M \approx 1.06$, decelerating to subsonic Mach numbers with no evidence of a shock of any significant strength. The flow continues to decelerate in the enlarging passage and exits from the rotor at a subsonic Mach number.

The flowfields for the 30%- and 50%-flow streamlines, shown in Figures 11c, d, e, and f are qualitatively the same as those for the 10% flow streamline. There is an acceleration of the flow behind the oblique shock shown in Figure 11c which is caused by an expansion on the pressure surface. In addition, the normal shock has moved closer to the trailing edge of the adjacent blade in Figure 11c and has moved into the rotor passage in Figure 11e. Due to window contamination, measurements could not be obtained forward of the 50%-chord point; consequently, an assumed oblique shock is shown as a dashed line for graphic presentation. The near-stall flowfields shown in Figures 11d and 11f are qualitatively the same as that shown in Figure 11b, except that the Mach numbers behind the shock are more clearly subsonic.

In summary, the measurements at the operating line show a distinct two-shock system in the rotor that exists at least to the pitchline radial immersion and probably beyond. In contrast, at the near stall condition a single shock system is present in the rotor. In all cases the flow exits the rotor at subsonic Mach numbers.

Theoretical Analysis

In order to determine the consistency between the experimental measurements and the analytical prediction of the rotor flowfield, a time dependent calculation procedure and a method of characteristics analysis of the rotor flowfield, were carried out. These procedures are discussed below.

A numerical procedure has been developed at General Electric by P.R. Gliebe for computing inviscid transonic flowfields in turbomachinery cascades. The procedure uses a finite difference scheme to solve the time-dependent conservation equations of mass, momentum and energy written in cylindrical coordinates relative to a rotor rotating with angular speed ω . With the time dependent computation (TDC) approach, the steady-state solution of these equations is obtained as the asymptotic limit for large times of an initial flow distribution which is allowed to vary with time. The solution is

ting line and the near-stall throttle settings. The three radial immersions surveyed were the 10%-, 30%- and 50%-flow streamlines (approximately) where 0%-flow represents the outer casing. Typical oscillograms showing LV measurements for this test have previously been presented in Figure 3. There is clear indication in this oscillogram of the shock wave location and of the pre-shock and post-shock velocity levels. The data were reduced using equations (1)-(4) as discussed in Section 2.4.

Test Results

The flowfields obtained from the LV measurements along the 10%-flow streamline for the operating line and the near-stall throttle settings at 100% corrected speed are shown in Figures 11a and 11b respectively. On Figure 11 the small arrows are

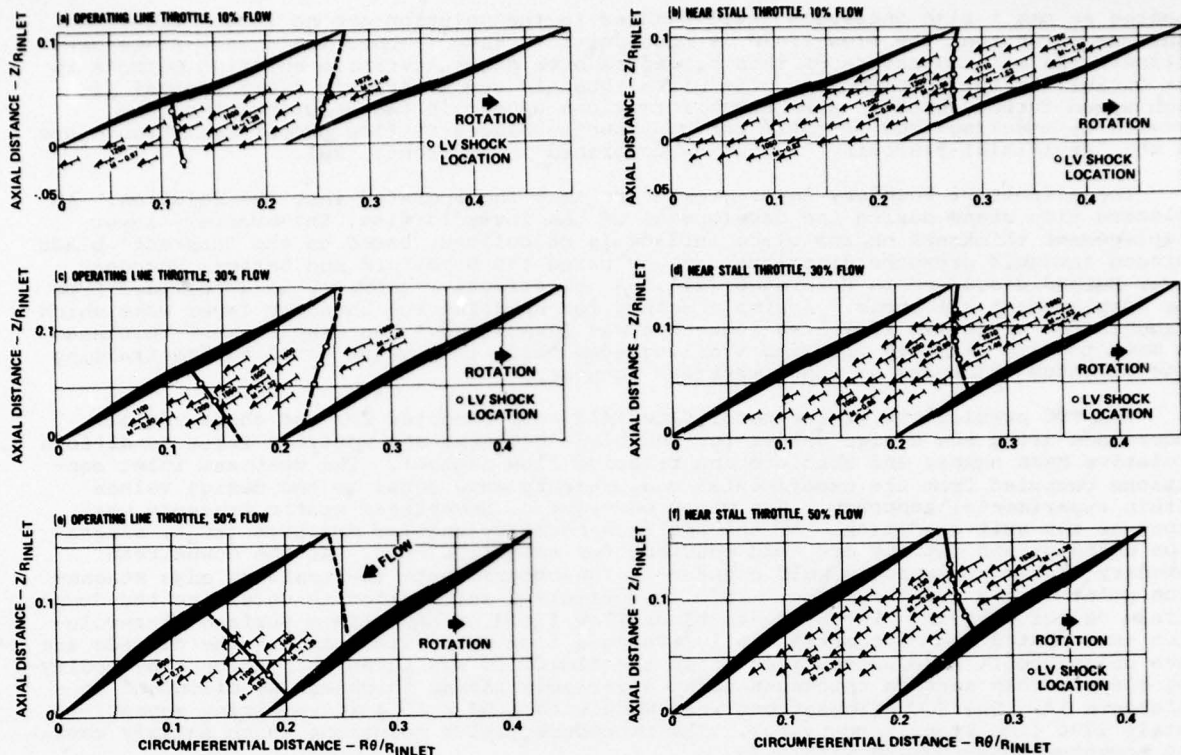


Fig. 11 Comparison of fan intrarotor LV velocity measurements for the operating line and near stall throttle, 100 percent corrected speed. Velocity is in ft/sec, conversion factor (m/sec = 0.3048 x ft/sec)

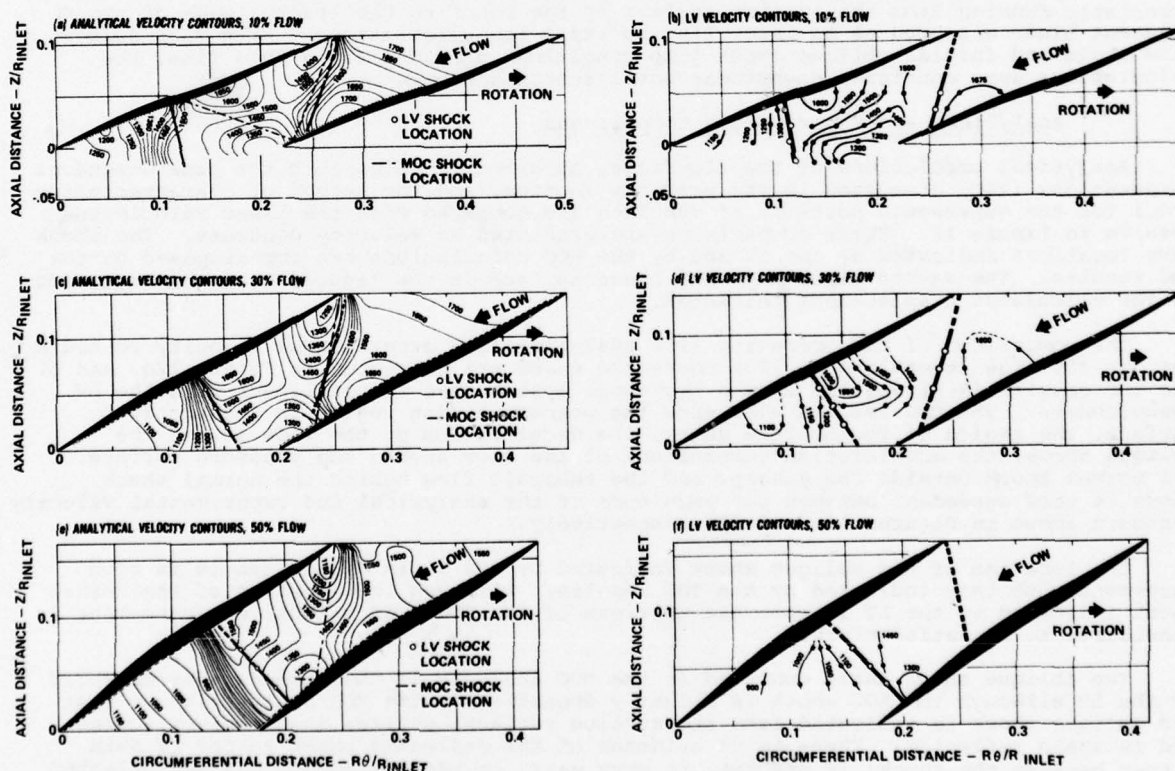


Fig. 12 Comparison of analytical and experimental fan velocity contours for the 10%, 30% and 50% flow streamlines, 100 percent corrected speed, operating line throttle, velocity is in ft/sec, conversion factor (m/sec = 0.3048 x ft/sec)

updated at small time intervals until changes in the solution are no longer significant, at which time the flow field is considered to have reached its steady-state condition. The main advantage of this procedure over other iterative solution methods is its capability for accommodating the mixed subsonic and supersonic flows typical of high-speed turbomachines. When shock formations appear in the solution, they are treated by modeling them as rapid but continuous changes in flow properties through use of the "artificial-viscosity" technique described in Reference [20].

The effects of boundary layer growth are also incorporated into the solution. At selected time steps during the development of the inviscid flow, the boundary layer displacement thickness on the blade surface is calculated, based on the "current" blade surface inviscid pressure distributions, by using the Stratford and Beavers Boundary Layer Method discussed in Reference [21]. A new effective geometry is determined from the displacement thickness. A simple method for handling the boundary layer wake which accounts for effective flow area reduction was formulated. The displacement thickness is made to vary linearly from its trailing edge value to a value equal to the trailing edge momentum thickness at the downstream boundary.

The TDC predictions of the rotor flowfield were computed for the three radial immersions using the design values for the blade geometry and upstream inlet conditions (relative Mach number and absolute and relative flow angles). The upstream inlet conditions computed from the experimental measurements were equal to the design values within experimental accuracy. The measured value of downstream static pressure was input as the exit condition. At the upstream boundary angular momentum (rC_u), stagnation enthalpy and entropy are held constant for each time step. At the downstream boundary static pressure is held constant. The program puts the trailing edge stagnation point at the trailing edge. This is sufficient information to determine the downstream vector diagram. The blade-to-blade flow field on the stream surface-of-revolution is computed and circumferentially averaged flow properties through the cascade are then calculated. Annulus contraction in the flowfield was taken into account by modifying blade stream surface thickness using a variable lamina thickness as discussed in Reference 12. The TDC calculations were made with a 50 x 15 grid requiring approximately 1700 time steps to converge. The procedure yields solutions which satisfy mass and momentum conservation within 4%.

The supersonic portion of the rotor flowfield was also determined analytically by using General Electric's Method of Characteristics (MOC) computer program. This program solves the steady state conservation equations using the method of characteristics. In addition it includes provisions for automatic initiation and reflection of oblique shock waves in the flowfield and for a variable lamina thickness as described in the previous section. The MOC calculations were performed within a strip corresponding to one rotor pitch with the airfoil surfaces forming the fixed boundaries. A right characteristic running from the suction surface of the rotor to the leading edge of the adjacent blade was used as an inlet line to start the calculations. With Mach number, flow angle and initial oblique shock jump conditions provided along this line, the calculations were continued downstream until subsonic flow appeared.

Analytical and Experimental Comparisons

Analytical predictions of the flowfield, obtained by using both the time dependent computations (TDC) discussed in the previous section, and the method of characteristics (MOC) for the supersonic portions of the flow are compared with the laser velocimeter results in Figure 12. These comparisons are presented as velocity contours. The shock wave locations indicated by the LV and by the MOC calculations are superimposed on the TDC results. The dashed lines near the blade surface in the figures show the magnitude of the calculated displacement thickness.

The comparison of the operating line analytical and experimental velocity contours for the 10% flow streamline at 100% corrected speed are presented in Figure 12a, and b. The TDC results in Figure 12a show a two-shock system that is consistent with the LV measurements. The TDC results also show the precompression region on the suction surface, the region of the oblique shock, the deceleration of the flow across the oblique shock, the acceleration (expansion) of the flow around the pressure surface, the normal shock outside the passage and the subsonic flow behind the normal shock. There is good agreement between the magnitude of the analytical and experimental velocity contours shown in Figures 12a and 12b respectively.

The location of the oblique shock indicated by the LV in Figure 12a is in good agreement with that indicated by the TDC results. Although the location of the normal shock indicated by the LV is somewhat upstream of the TDC predictions, the agreement is considered to be satisfactory.

The oblique shock angle computed in the MOC analysis is the same as that measured by the LV although the MOC shock is slightly downstream. The MOC analysis shows that the oblique shock is reflected from the suction surface, strikes the pressure surface and is again reflected. There is no evidence of the reflected shock in the LV data either because the shock, if present, is very weak, or because the LV was not oriented in a manner that would detect it. Similarly there is little evidence of the reflected shock in the TDC predictions, probably due to the grid orientation and size. The MOC analysis indicates that subsonic flow would be obtained at approximately the same location as predicted by the TDC results.

Similar analytical and experimental comparisons are made for the 30%- and 50%-flow streamlines in Figures 12c, d and 12e, f respectively. The agreement in these comparisons is also reasonably good. The TDC predictions show that the normal shock moves toward the trailing edge of the adjacent blade in Figure 12c and finally into the passage in Figure 12e. The agreement between the magnitude of the velocity contours is also good.

Although reasonably good agreement between the analytical and experimental results has been demonstrated, significantly better agreement should probably not be expected because: (1) the analytical models do not include three-dimensional effects, and (2) shock-induced boundary layer separation and the resultant thickening of the boundary layer is not incorporated in the calculations (although a boundary layer displacement thickness model is incorporated), (3) the lamina thickness in the TDC and MOC models varied only in the axial direction, (4) all of the losses in the flowfield could not be determined and modeled, and (5) the LV system has inaccuracies associated with positioning the measuring zone and reducing the data.

Additional information is presented in Reference 12.

4.0 TURBINE APPLICATIONS

Modern aircraft gas turbine engines often employ advanced, highly-loaded, single-stage high pressure turbines and highly loaded low pressure turbines. As a result of this advancement of turbine technology, losses associated with transonic and supersonic flow in the blading, secondary flow effects and cooling air injection have become more important and applied research programs to reduce them have been undertaken. As a part of this effort, the laser velocimeter is being used to investigate the complex flow fields within turbine rotors.

4.1 Test Program

Turbine component and development testing is conducted in the General Electric Warm Air Turbine Test Facility, a dual purpose facility capable of evaluating either high pressure turbine or fan drive turbine performance. The facility will accommodate turbine configurations ranging from a minimum hub diameter 356 mm (14 in) up to a maximum tip diameter of 81 mm (32 in) with operational capabilities up to 11,200 kw (15,000 horsepower) at 15,000 rpm.

For the test program being described, a research turbine having 94 blades was tested at 7550 rpm with inlet conditions of 422° K (760° R) and 41.4 KPa (60 psi). The laser velocimeter was mounted in a manner similar to that described in Section 3.2 in order that axial, radial and circumferential traverses of the flowfield could be obtained. The flow was seeded with magnesium oxide particles having a diameter of 1 micron or less. The LV measurements were reduced using equations (1)-(4) as discussed in Section 2.4.

4.2 Test Results

A typical turbine rotor flowfield obtained from the LV measurements is shown in Figure 13. The solid arrows in the figure represent the LV vector measurements in magnitude and direction. The dashed arrows represent the corresponding results obtained from time-dependent calculations similar to those discussed in Section 3.2. A calculated flow streamline and a calculated particle path for a 1 micron diameter MgO particle are also shown in the figure.

There is good agreement between the LV measurements and the analytical predictions at the rotor inlet. As one proceeds to axial measurement planes downstream of the inlet, the agreement remains reasonably good near the pressure surface of the blade. However from the suction surface to beyond mid-pitch in the high turning region of the blade, the inertia of the particles apparently causes them to lag; consequently, there are larger differences between the LV measurements and the analytical predictions in this high turning region. At the exit plane the particles have had a chance to make up the turning (although not completely near the suction surface), and the overall flow turning determined from the LV measurements is in fair agreement with the turning predicted by the analytical model.

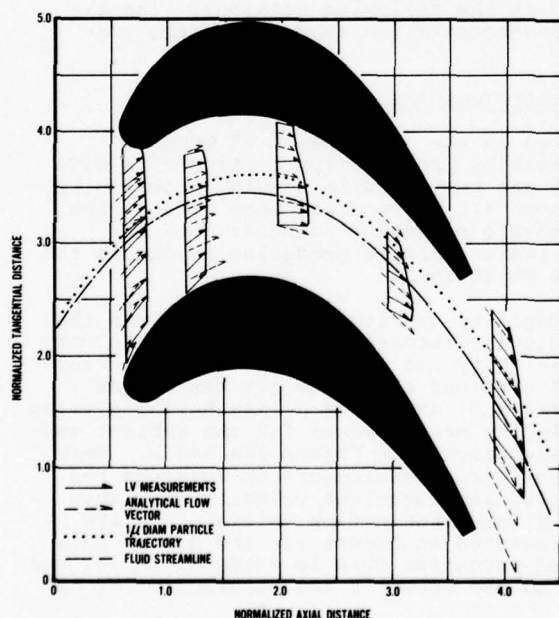


Fig. 13 Comparison of LV velocity measurements and analytical results obtained within a turbine rotor passage

Since flow seeding was used to obtain LV measurements, particle trajectory calculations were performed in an attempt to follow a 1 micron diameter particle through the rotor flowfield. These results are compared with a flow streamline in Figure 13. The particle and the streamline do not start at the same location in the rotor inlet plane because the particle was assumed to have entered the flow upstream of the preceeding vane and some migration of the particle relative to the streamline has already occurred. Two questions arise. First, where does the particle go? And secondly, when the particle gets there, how well does its velocity compare with the local flow velocity at that point? To answer the first question, the results in Figure 13 indicate that the particle path can migrate substantially from the streamline. This result, coupled with the fact that reasonably large amounts of cooling flow were injected into the flow along the suction surface, would explain why there is a void in measurements near the suction surface. However, in answer to the second question, the particle trajectory analysis indicates that even though the 1 micron particle migrates, it is still able to represent the local flow velocity reasonably well at that point. The deviation in the high turning region between the LV measurements and the analytical predictions are larger than would be predicted by the 1 micron diameter particle trajectory analysis. Consequently it is believed that the MgO seed particles clumped together forming particles of at least 2 or 3 microns in diameter and the LV measurements were obtained from these particles.

Overall the results are quite encouraging and work is still continuing in the analysis of this data.

5.0 JET NOISE (ACOUSTICS) APPLICATIONS

With the advent of larger and more powerful commercial and military aircraft propulsion systems, it has become increasingly important to improve the general community environment affected by these systems. Consequently General Electric has conducted a number of major research programs aimed at improving this environment, and in particular aimed at understanding the mechanisms of noise generation and reduction. In one such program, sponsored jointly by the US Air Force and Department of Transportation, an investigation of supersonic jet exhaust noise was undertaken to develop a mathematical model capable of providing aeroacoustic design data for future supersonic jet exhaust noise suppressors. As a part of this program reported in Reference 22, a comprehensive turbulent mixing aeroacoustic model was developed which is capable of computing detailed aerodynamic flow properties such as velocity (mean and turbulent), pressure, temperature, density and length scale of turbulence as well as the main acoustic properties such as overall sound power level, power spectra, overall sound pressure level, sound pressure level spectra and jet directivity. The computational scheme was designed to yield acoustic predictions based on aerodynamic input which can be computed or measured. It is at this point that the General-Electric-developed laser velocimeter was utilized. The LV provides a means of measuring the flow properties of high velocity/high temperature jets without disturbing the flow. It also provides an accurate method of measuring not only rms mean velocity and turbulent velocity distributions but also of obtaining spectral and cross-correlation type of information which is important for direct noise source location. A brief discussion of the LV measurements obtained in this study is presented in the following sections. The extensive test results and the LV-to-far-field cross-correlation experiments are presented in References 22 and 23.

5.1 Laser Velocimeter Mean and Turbulence Velocity Measurements

The laser velocimeter measurements were taken in the jet exhaust of General Electric's Jet Acoustics Test Facility. This facility provides for testing of a wide variety of interchangeable exhaust nozzles using gas temperatures ranging from ambient to 3000° K and using pressure ratios of up to about 4. Two nozzles were used in the tests described below: a converging-diverging nozzle producing subsonic flow and shock-free supersonic flow and an underexpanded conical nozzle producing shocks in the flow. The exit diameter of both nozzles was 152 mm (6 in).

Velocity measurements were obtained as probability density distributions and the data were reduced by using the statistical techniques discussed in Section 2.4 to compute mean values and standard deviations (mean velocity and turbulence velocity) respectively. The data were obtained at various axial stations along the jet centerline (radius of measurement plane/diameter of jet $\equiv r/D = 0$) and along a line having a value of $r/D = 0.5$. Typical mean and turbulent LV velocity measurements for the ambient subsonic jet are compared with hot film/hot wire measurements in Figure 14a and b. Very good agreement between the LV and the hot film/hot wire measurements is obtained for the subsonic jet. LV measurements of mean velocity and turbulent velocity were then obtained for the high-temperature 833° K (1500° R) supersonic flow exiting from the convergent-divergent nozzle. The results are presented in Figure 14c and d. In both Figures 14a and 14c the existence of the extended potential core is evident. Also, the difference in the turbulence distributions between the subsonic and supersonic jet can be seen by comparing Figure 14b and d.

Further experimental measurements were obtained using the converging-diverging shock-free nozzle flow and the shocked conical nozzle flow. For both cases the exit Mach number of the jet was 1.55 and the total temperature was 833° K (1500° R). Radial profiles of mean axial velocities were obtained for various axial positions, X , in the jets of both nozzles. The results, presented in Figure 15a and b, are plotted using a parameter, η , which collapses all of the data onto one curve and clearly defines the

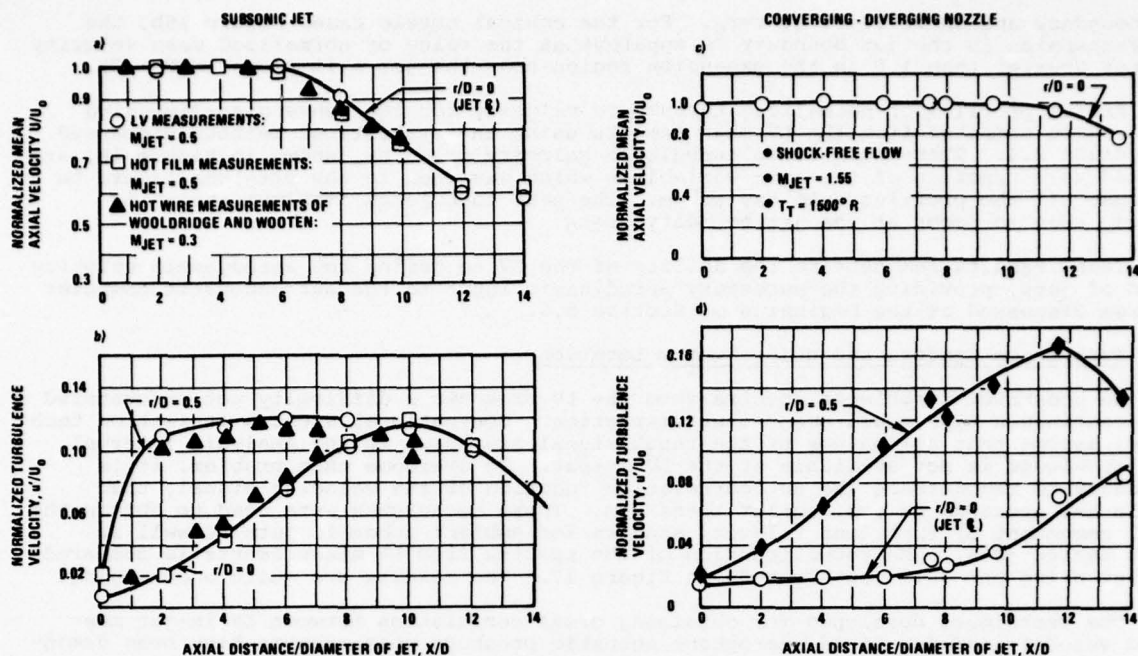


Fig. 14 Normalized mean axial velocity and normalized turbulence velocity for a) the subsonic jet and b) the supersonic shock-free jet

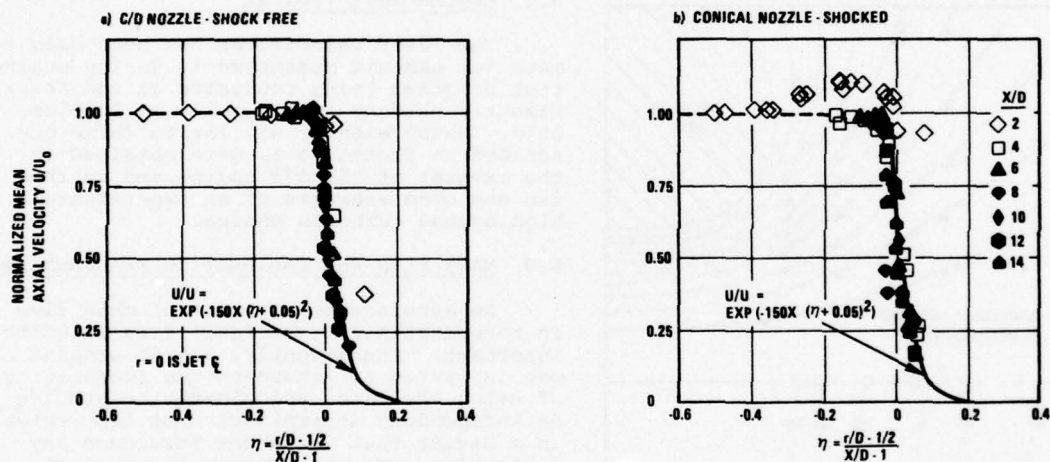


Fig. 15 LV-measured radial profiles of normalized mean axial velocity for a) the converging/diverging nozzle and b) the underexpanded conical nozzle, $M_{jet} = 1.55$, $T_T = 833^\circ K$ ($1500^\circ R$)

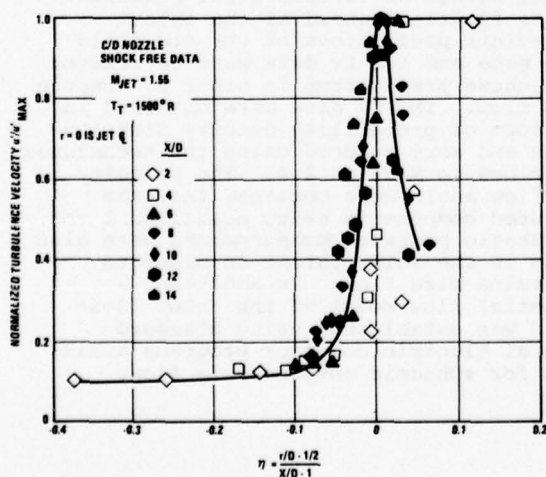


Fig. 16 LV-measured radial profiles of normalized turbulence velocity

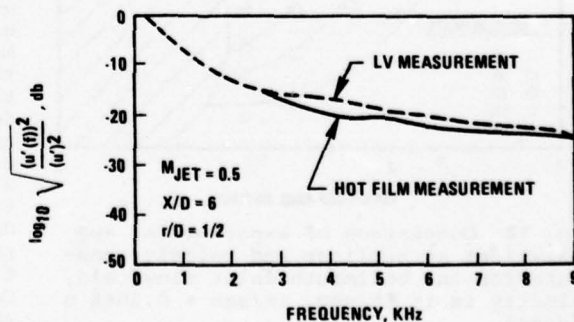


Fig. 17 Comparison of LV-measured and hot film-measured axial turbulence velocity spectra

jet boundary and shear layer at $r=r_0$. For the conical nozzle case, Figure 15b, the underexpansion in the jet boundary is apparent as the value of normalized mean velocity becomes greater than 1.0 in the expansion region near the jet exit plane ($X/D = 2$).

Radial profiles of normalized turbulence velocity for the converging-diverging nozzle were computed from the LV measurements using the statistical methods discussed in Section 2.4. These normalized turbulence velocity profiles, shown in Figure 16, are plotted as a function of the same variable η which was used in the previous figure to collapse all the profiles onto one curve. The peak turbulence (maximum shear) is clearly seen to occur at the jet boundary, $r=r_0$.

These results demonstrate the ability of the LV to define the aerodynamic velocity field of jets, providing the necessary aerodynamic input to the aero-acoustic computer program discussed at the beginning of Section 5.0.

5.2 Turbulence Spectra and Noise Source Location

To construct turbulence spectra from the LV presents a difficulty not encountered with continuous-type measurement instrumentation. Conventional spectra estimation techniques assume that all values of the input signal are known in the analysis interval. Such knowledge is not available at the LV output. To overcome this problem, it is necessary to reconstruct the autocorrelation function of the velocity signal, then obtain the spectrum as its Fourier transform. These techniques were used to obtain the axial component of turbulent velocity spectra for ambient subsonic jets as well as sonic heated jets. The reconstruction of the spectra from LV measurements is compared to that using hot film measurements in Figure 17. The results are quite encouraging.

The techniques developed for obtaining cross-correlation between LV in-jet measured velocity and far-field microphone acoustic pressure measurements have been demonstrated and the results are discussed in References 22 and 23.

5.3 Engine Test Program

The laser velocimeter has been used to make jet exhaust measurements during engine test programs being conducted at the General Electric outdoor test complex at Peebles, Ohio. Measurements, similar to those described in Section 5.1, were obtained in the exhaust of the J79 engine and in the fan and core exhausts of an experimental high bypass turbofan engine.

6.0 MASS FLOW AND CALIBRATION MEASUREMENTS

An accurate measurement of mass flow in turbomachinery test facilities is quite important. Consequently, a test program was initiated to determine the feasibility of using the laser velocimeter to provide an independent determination of flow rates in a manner that would not introduce any distortion into the turbomachinery test facility. The test program was conducted using a small-scale, calibrated bellmouth inlet. LV measurements were taken in radial planes at various axial positions in the flowfield ahead of the inlet. Analytical predictions of the flowfield were made and the LV data were correlated with these predictions in order to compute mass flow. The LV data were obtained in the form of probability density distributions and were reduced using the techniques described in Section 2.4. The velocity and flow angle were obtained from the measured components using equations 1 and 2. Static pressure measurements were also taken in the inlet throat in order to determine mass flow. In addition, a potential flow model of the inlet flowfield was established using standard General Electric computer programs available for subsonic compressible flow.

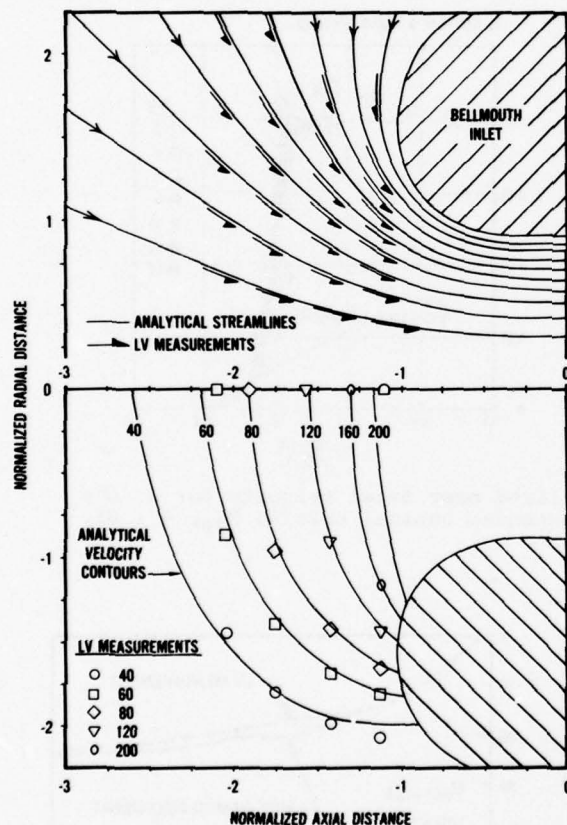


Fig. 18 Comparison of experimental and analytical streamlines and velocity contours for the bellmouth inlet flowfield, velocity is in ft/sec, (m/sec = 0.3048 x ft/sec)

The LV measurements and the analytical determination of the flowfield are presented in Figure 18 in the form of velocity vectors, flow streamlines and lines of constant velocity. The good agreement obtained between the LV-velocity vectors and the analytical streamlines and between the velocity magnitude measurements and the analytical velocity contours is evident in the figure. The LV-determined mass flow was 0.209 kg/sec (0.460 lbm/sec) while the nozzle throat measurements of static pressure yielded 0.212 kg/sec (0.467 lbm/sec). Further refinement of the data is still in progress.

The laser velocimeter is also being used to calibrate an annular cascade designed for airfoil aeroelastic instability studies. Radial and circumferential surveys of velocity (magnitude and direction) are being made in the cascade over a range of subsonic and transonic Mach numbers.

7.0 AREAS REQUIRING FURTHER DEVELOPMENT

In the practical application of laser velocimetry to the turbomachinery environment, it must be remembered that this environment is different from the somewhat well-controlled conditions of the wind tunnel or research laboratory. For example, the use of the LV to obtain jet exhaust measurements at outdoor engine test sites presents a challenging set of environmental problems which include high noise and vibration levels, high exhaust temperatures and products of combustion in the core exhaust stream. In component and scale model testing the general approach has been to adapt the LV system to the specific hardware and flow situation, wherever possible, rather than to modify the hardware. In such testing the experimentalist has had to deal with a number of problem areas which include: accessibility to the flowfield, clouding and dirt collection on optical windows, measurements close to solid surfaces, measurement accuracy and economics of operation. These problem areas, which are receiving further attention, are discussed in the following.

Complete optical access to the flowfield is often limited in turbomachinery applications. As discussed previously in Section 2.1, a forward-scattering system would require the optical axis to pass through blades, discs, shafts, etc, which is not possible. Consequently, the back-scatter mode is used even though there is a substantial decrease in signal-to-noise ratio. Also the optical path is often blocked by tip shrouds or part span shrouds and optical accessibility is often hindered by the twist and camber of the blades which results in a "shadow" problem. These types of access problems have generally been solved by using a reorientation of the optical axis. However, a remote-controlled actuation system for reorientation is complicated and expensive. Another real accessibility problem has been the clouding and dirt collection on optical windows by seed materials and other contaminants. This problem, which also presents signal resolution difficulties, has been greatly reduced by employing ingenious window protection procedures during testing.

Making measurements in close proximity to solid surfaces, where reflected light tends to completely dominate the back-scattered flow signal, presents another difficulty. In some cases this swamping has been reduced by using selective, non-reflective wave length coatings or by a reorientation of the optical axis. Measurements have been made as close as 0.75 cm (0.3 inch) from solid surfaces and in some cases, by using special techniques, at the boundary. Photomultiplier tube saturation, and a subsequent recovery problem, results when the rotor blade tips, or blade surfaces, pass through the measurement zone and reflect laser light back to the phototube. If the phototube recovery time is small compared to the blade-to-blade passing time, this does not present a significant problem. When there is a problem, a gating system can be employed.

The accuracy of LV measurements is influenced by a number of factors: the size of the measurement volume, ability of particles to track the flow, particle agglomeration, the degree of turbulence and the size of any separated flow region. The dimensions of the measurement zone where the two laser beams cross were presented in Section 2.1. For most cases of relatively larger turbomachinery flow paths, these dimensions are small compared to the flow field dimensions. However, in very small turbomachinery flow passages or in regions of very large velocity gradients, the size of the measurement volume becomes important. For the large gradient case, the velocity measurements can be biased away from the average velocity which is assumed to occur at the center of the measurement zone. The accuracy with which the tracer particles track the local fluid velocity (direction and magnitude) also limits the accuracy of the LV measurement. The use of small, uniform seed material has minimized this problem. As discussed in the particle trajectory analysis in Reference 12, the seed particles used should track the flowfield within acceptable limits even in the high acceleration regions such as those which occur through shocks. The real problem arises when the seeding material agglomerates or when contaminants (diameter > 2 microns) enter the flow field giving erroneous velocity measurements due to large particle lag or lead. This in general is easily recognizable as a large spread or scatter in the data. Electronic discrimination can also be employed to eliminate measurements from large particles.

In highly turbulent flow, LV measurements can be biased toward preferred velocity vector orientations because of the way the particle trajectories cross the fringe field. Also, in highly turbulent separated flow regions, the measurements may be biased because of non-uniformity of seed material in the separated flow region.

Finally the cost and time involved in making laser velocimeter measurements in turbomachinery is a practical and important consideration. Component and engine test-

ing is expensive, often involving a large number of personnel and a complex test facility. Consequently sufficient time is not always available to take the detailed measurements one would like to take, to shut down and clean windows or to "iron out the bugs".

Overall, the experimentalist has produced meaningful LV aerodynamic measurements in turbomachinery under rather adverse operating conditions. Developmental work is continuing in an effort to reduce or eliminate those problem areas discussed above.

8.0 CONCLUSIONS

The laser velocimeter has been used in aircraft gas turbine research and development to make nondisturbing gas velocity measurements in bellmouth inlets and cascades, to make flowfield measurements within jet exhausts for aero-acoustic correlation and to make flowfield measurements within the rotating bladerows of compressors, fans and turbines, including the mapping of shock locations. Analytical predictions of the various flowfields were obtained by using a potential flow analysis, method of characteristics analysis, and a time-dependent, finite-difference solution of the fluid dynamic equations of motion, where applicable. The analytical predictions were, in general, consistent with the experimental measurements. The application of the LV to jet exhaust (acoustic) measurements and to compressor/turbine intra-rotor flowfield measurements was of particular encouragement. For acoustic applications, the LV provides an accurate method of obtaining not only rms mean velocity and turbulent velocity distributions but also of obtaining spectral and cross-correlation type information which is important for direct noise source location. For compressor/turbine applications the LV provides detailed intra-rotor flow measurements which include the location of shock waves. The high speed fan operating line results showed a two-shock system in the rotor passage consisting of an attached oblique shock at the leading edge and a nearly normal shock further downstream in the rotor passage. As the rotor was throttled toward stall, a one-shock pattern appeared as the higher back pressure eliminated the second shock, and pushed the leading edge shock upstream in the rotor passage. Based on these experimental and analytical results, it is concluded that the laser velocimeter provides an accurate and practical method for obtaining detailed flowfield measurements in turbomachinery research and development programs.

9.0 REFERENCES

1. Yeh, Y.; and Cummins, H.Z.; "Localized Fluid Flow Measurements with He-Ne Laser Spectrometer", Applied Physics Letters, Vol. 4, 1964, p. 176.
2. Cummins, H.Z.; Knable, N.; and Yeh, Y.; "Observation of Diffusion Broadening of Rayleigh Scattered Light", Physical Review Letters, Vol. 12, 1964, p. 150.
3. Goldstein, R.J.; and Kreid, D.K.; "Measurement of Laminar Flow Development in Square Duct Using Laser-Doppler Flowmeter", ASME Paper No. 67-APM-37.
4. Goldstein, R.J.; and Hagen, W.F.; "Turbulent Flow Measurements Utilizing the Doppler Shift of Scattered Laser Radiation", Physics of Fluids, Vol. 10, 1967, p. 1349.
5. Welch, N.E.; and Tomme, W.J.; "The Analysis of Turbulence from Data Obtained with a Laser Velocimeter", AIAA Paper No. 67-179, AIAA 5th Aerospace Sciences Meeting, New York, 1967.
6. Denison, E.B.; and Stevenson, W.H.; "Oscillatory Flow Measurements with a Directionally Sensitive Laser Velocimeter", Review of Scientific Instruments, Vol. 41, No. 10, October 1970, p. 1475.
7. Sullivan, J.P.; Widnall, S.E.; Ezekiel, S.; "Study of Vortex Rings Using a Laser Doppler Velocimeter", AIAA Journal, Vol. 11, October 1973, p. 1384.
8. Cliffone, D.L.; and Orloff, K.L.; "Far-Field Wake-Vortex Characteristics of Wings", Journal of Aircraft, No. 5, May 1975, p. 464.
9. Penney, C.M.; "Differential Doppler Velocity Measurements", IEEE Journal of Quantum Electronics, Vol. QE-5, June 1969, p. 318.
10. Jones, W.B.; "Laser Fluid Velocity Sensor", Paper No. 2-8-82, Symposium on Flow, Pittsburgh, Pennsylvania, Sponsored by AIAA, AIP, and NBS, May 1971.
11. Wisler, D.C.; and Mossey, P.W.; "Gas Velocity Measurements Within a Compressor Rotor Passage Using the Laser Doppler Velocimeter", ASME Winter Annual Meeting, November 26-30, 1972, NY, NY, Paper No. 72-WA/GT-2 and ASME Transactions, Journal of Engineering for Power, April 1973, p. 91.
12. Wisler, D.C.; "Shock Wave and Flow Velocity Measurements in a High Speed Fan Rotor Using the Laser Velocimeter", ASME International Gas Turbine Conference, New Orleans, La, March 20-25, 1976, Paper No. 76-GT-49 and ASME Transactions, Journal of Engineering for Power, April 1977.
13. Walker, D.A.; Williams, M.C.; and House, R.D.; "Intra-Blade Velocity Measurements, in a Transonic Fan Utilizing a Laser Doppler Velocimeter, Minnesota Symposium on Laser Anemometry, University of Minnesota, October 22-24, 1975.

14. Dolan, F.X.; LeBlanc, F.R.; and Runstadler, P.W., Jr.; "Design, Development, and Test of a Laser Velocimeter for High Speed Turbomachinery", Presented at the LDA Symposium, Technical University of Denmark, Lyngby, Denmark, August 25-28, 1975. Creare Technical Note TN-234.
15. Seasholtz, R.G.; "Laser Doppler Velocimeter Measurements in a Turbine Stator Cascade Facility", Technical Paper presented at the Laser Velocimetry Workshop, West LaFayette, Indiana, March 27-29, 1974, NASA TMX-71524.
16. Schodl, R.; "On the Development of a New Optical Method for Flow Measurements in Turbomachines", Paper presented at the ASME Gas Turbine Conference in Zurich, Switzerland, 1974.
17. Schodl, R.; "Advanced Testing Techniques in Turbomachines; a Laser Dual Focus Velocimeter for Turbomachine Applications", Von Karman Institute for Fluid Dynamics Lecture Series, April 14-18, 1975.
18. Eckardt, D.; "Detailed Flow Investigations Within a High-Speed Centrifugal Compressor Impeller", Presented at the Gas Turbine and Fluids Engineering Conference, New Orleans, La., March 21-25, 1976, ASME Publication No. 76-FE-13.
19. Johnsen, I.A.; and Bullock, R.O.; (editors), "Aerodynamic Design of Axial Flow Compressors", U.S. Government Printing Office, Washington, D.C., NASA SP-36, 1965, p. 203.
20. Richtmyer, R.D.; and Morton, K.W.; "Difference Methods for Initial Value Problems", Interscience Publishers, John Wiley and Sons, 2nd Ed., ch. 13, 1967.
21. Stratford, B.S.; and Beavers, G.S.; "The Calculation of Compressible Turbulent Boundary Layer in an Arbitrary Pressure Gradient - A Correlation of Certain Previous Methods", ARC R&M No. 3207, September 1959.
22. Knott, P.R.; "Supersonic Jet Exhaust Noise Investigation, Volume I-IV", Final Report, USAF and Department of Transportation Technical Report No. AFAPL-TR-76-68, July 1976.
23. Scott, P.; The Theory and Implementation of LV Spectra Measurements, Second International Workshop on Laser Velocimetry, 23 March 1974.

10.0 ACKNOWLEDGEMENTS

The authors wish to thank the Aircraft Engine Group of the General Electric Company for its permission to publish this paper. The authors also wish to express appreciation to Mr. C.J. Studerus and to Dr. P.R. Knott, respectively, for allowing us to use their turbine and acoustic analysis in this paper.

SPECIAL PROBLEMS OF LASER ANEMOMETRY IN DIFFICULT APPLICATIONS

by

Dr. A. E. Smart
Rolls-Royce Limited
Advanced Research Laboratory
P.O. Box 31
DERBY DE2 8BJ.

SUMMARY

Many difficulties with this technique of laser anemometry arise from engineering constraints and seemingly trivial problems may take much time and effort to overcome. A few solutions to some of these problems are outlined. Data retrieval from very low signal is possible using photon correlation and this is now popular in many engineering applications because of its high efficiency. We have obtained good measurements in aero-engine exhaust and in unsteady combustion systems with this method. For real time measurements it is necessary to seed the flows and use frequency tracking (or equivalent). Phase noise is serious here but may be compensated by separate assessment. Transit anemometry is shown to be superior in conditions of bad flare, such as blade passages, but takes longer to make a given measurement. However, shear stresses may be derived from the same measurement. The disparity between particle and fluid velocity field is related to its practical consequences. More application topics are included, such as window installation and cleanliness, vibration and noise, thermal problems, laser safety and finally information presentation.

1. INTRODUCTION

This paper comprises a large number of topics and ideas which may be useful in the application of this relatively new technology to the measurement of velocity and turbulence parameters in engineering situations. By 'engineering situations' we mean areas where quantification is a necessary step forward in the understanding of a device or machine - the important factor being a 'measurement' rather than a meticulous theoretical guess. The engineering constraint also means in many cases that the device to be investigated already exists and may not be designed to facilitate optical measurements. This makes it necessary to adapt the instrumentation, sometimes with considerable loss of optical performance to get results. That is not to say that we are not concerned with accuracy, but more that we are concerned to pick out factors which may affect our confidence level and attend to these at the expense of those interesting sophistries which may divert.

Some of the problems here would be too trivial to include if it were not for the large amount of wasted time which may be avoided simply by arranging that they do not occur. Other, more serious, problems such as what to do to optimise information retrieval in low signal cases, and how much trust may be placed in data so obtained, merit more detailed study.

2. SOME TRIVIAL CONSIDERATIONS

We at Rolls-Royce have spent some years developing and trying to understand laser anemometry, and to applying it to measuring fluid mechanical properties within and near aero-engines and component test rigs.(13)(14) In most of these applications the major problems have been those associated with operating conditions and environment. Many systems of anemometry may be constructed and used in the laboratory but only the naive would suppose that the transition to real test stands was easy. The sort of optics and electronics which it has become necessary to use for anemometry measurements tends to be sensitive to rain, snow, and ice: large changes in temperature, humidity or electrical surroundings all conspire to prevent successful measurements. To some extent care and forethought may minimise the effects, but perhaps examples may be instructive.

Many of our applications have been in the open air as is necessary for rigs used for noise field measurements, or in large but cluttered buildings with a lot of environment changes. In England weather changes may be very rapid and keeping a forward scatter anemometer with a 5m throw (because it was the only suitable system for that application) in good alignment posed problems. Although these tests are always scheduled for summer it often seems that the final programme actually happens

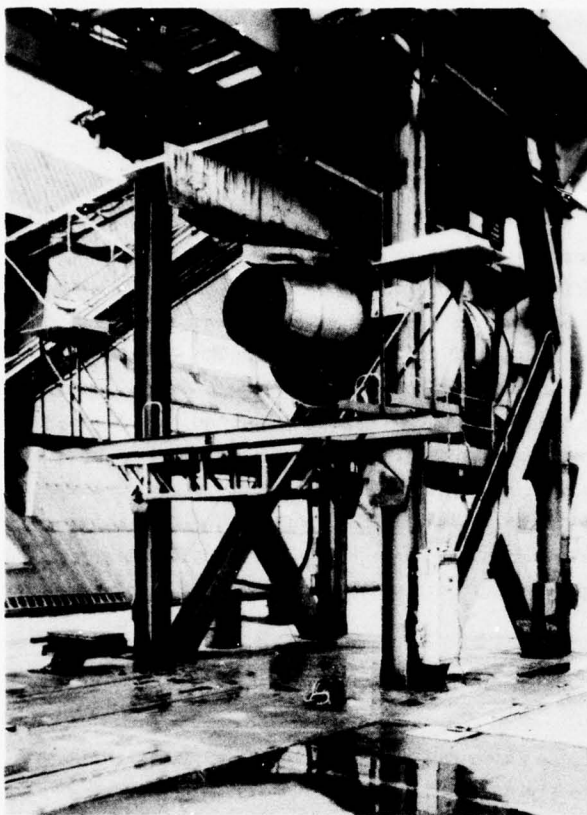


Fig. 1 RB211 Quiet Engine Demonstrator with LDA on a Test Stand.

in January and the final corrective adjustment must be made on a gantry 7m from the ground in wind and rain (Fig. 1). Anticipation of these conditions can make life easier. Environmental protection for the optical and electronic components is always to be recommended; in cases where an anemometer is in a cold environment but exposed to a hot rig some form of thermal control is necessary. Aluminium foil coated asbestos is a very good protection from radiant heat and also provides some thermal buffering.

Simplification cannot be too highly recommended. In the laboratory one can get away without parsimony of components but in the field the fewer separate items requiring adjustment, cleaning or even rigid mounting the more reliable is the final unit likely to be and the higher the chance of success. Every component should be viewed critically to see if it may be omitted without excessive penalty. Even the layout of Fig. 2 may be simplified if the rig is not self luminous by the omission of the narrow band laser filter and its collimating lens.

It is usually impossible to obtain access to the data acquisition part of the laser

anemometer when a rig or engine is running, so all control functions and adjustments if necessary must be made remotely, and the signal must be transmitted through long leads. Signal attenuation is no problem; what has been troublesome is electrical interference and pick up. Many large rigs have associated electrical plant and heavy switching produces unpleasant transients. Where long distances of tens of metres are involved there can be problems with earthing. That this is an irritating problem was evidenced by one of our magnetic tapes recording the output from a Cambridge Physical Sciences Tracker processing the signal from a life size combustion rig.

The FM tape recording of the real time continuous output from the frequency tracker was later played for analysis. We have developed the habit of putting such signals through an audio channel because the ear is very good at picking out odd anomalies; in this case hidden beneath the noise and scuffling represented by the turbulence and phase noise was a distorted but intelligible demodulation of a radio programme whose transmission frequency was near that represented by the mean velocity.

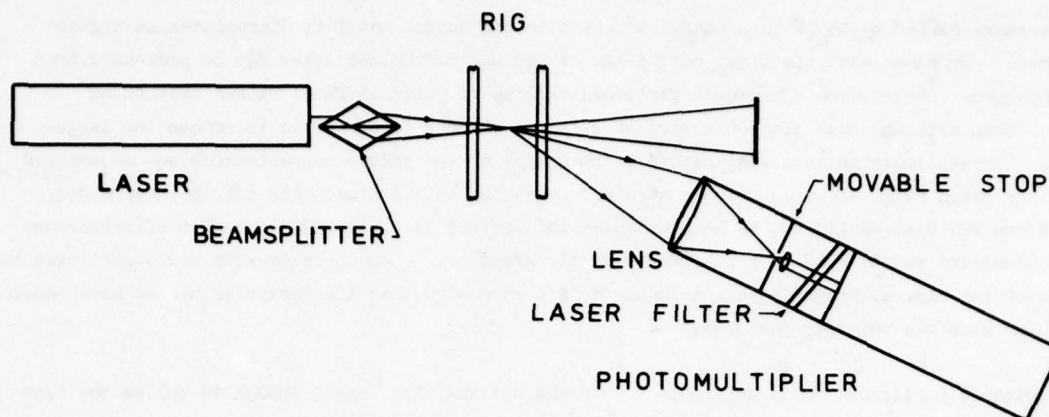


Fig. 2 Layout of Typical Fringe Anemometer

When working on engines with mass flow up to 700Kgs^{-1} doping is normally infeasible. The quantity and quality of signal, determined as it is by the natural particles present may vary radically. In England a south west wind, a harbinger of rain, is usually the most satisfactory, but other conditions may operate to provide particles. In industrial areas, particularly those in medium to heavy manufacturing there are usually adequate supplies of particulates despite pollution legislation. The best natural signal we ever obtained was from a test stand in farming area on a sultry summer day several fields away from a combine harvester.

3. PARTICLE PROBLEMS

The most serious problem in optical anemometry is almost always directly attributable to particles and may be divided into two parts:-

- (a) The provision of suitable particles
- (b) The disparity between particle and fluid velocity.

We offer some general notes on these subjects but no more than an introduction to a very complex aggregate of ideas.

By 'provision' particles must exist in the flow or be added to it. Homogeneous mixing is almost always assumed but not always guaranteed. A simple test of the Poisson nature of distributed particles added to a mixing chamber and subsequently sampled in the core of a jet showed very high correspondence between theory and measurement, but it is a large step to infer that this may hold true in cases such as turbomechanical applications. Indeed it is known to be untrue for large particles (8). The addition of particles to the flow may be achieved in a number of ways - none especially satisfactory.

For liquid particles a sheared membrane is probably the easiest method. Acoustic or air driven 'atomisers' are most suitable but a settling chamber must be provided to allow removal of large particles, and the particle loaded gas must be conveyed to the point of its addition to the flow in question by sufficiently large pipes, and at sufficiently slow speeds to prevent 'reclassification' and 'wetting out'. Many liquids may be used but inert systems of low vapour pressure are preferred. In general, water is not good as the final particle size depends more on the proximity to dew point in the gas than on more closely controllable factors.

Solid particles are preferred for hot flows as they may be refractory or otherwise have very high boiling points. Methods of production are fluidised beds, crystallisation from solution, or condensation from gas. Examples of these three methods might be MgO particles, NaCl from water and TiO_2 from TiCl_4 and water vapour. An added advantage of the last is that if the HCl is rendered harmless

by NH_3 , the smoke formed by NH_4Cl is a useful addition to the dopant until it dissociates at higher temperatures. Problems with the first method are caused unless the particles may be prevented from becoming charged. Aggregates of charged particles will be of quite different sizes from those intended. Even with the best methods a form of settling chamber is desirable to remove the largest particles. Crystallisation is a good method in many ways as the solute concentration can be changed to obtain any given range of sizes from an atomiser producing only a fixed size cut, perhaps widely different from the desired size. We have extended this method to a stirred suspension of refractory particles (emulsion paint) with an air driven acoustic atomiser. One problem with solid particles may be erosion of the rig, although if this happens it is a sure sign that the particles are or have become too large for sensible velocity measurements.

To have 'suitable particles' it is desirable to use the optimum size, small enough to follow the flow acceptably and large enough to scatter sufficient light. The range of this optimum may be extended by such considerations as reducing the differential specific gravity between particle and fluid, increasing the complex component of refractive index of the scatterer, using a fluorescent seed, etc. The refractive index merits some mention. The real part corresponds to absorption and is little use for anemometry. The backscatter from a good conductor is smaller than that from a bad in ranges of interest here. Scatter in other directions may be very complicated but can, if one has the time, energy and need, be calculated from Mie theory. The complex component of refractive index, indicative of the reflected or transmitted component should be large, as that implies that light hitting the particle is redirected into possibly useful directions. Many books are available which discuss these mechanisms. Usually a stronger constraint than the esoteric theoretical ideals is the real practicality of obtaining any usable dopant that is just acceptable, given all the constraints placed on the system by more pragmatic circumstances, for example, toxicity, cost, availability etc.

The second problem, of disparity between particle and fluid velocities (7) is not easily resolved. It has been referred to as particle sampling bias but this concept was shown to be in error by Dr. F. Durst at Capri '76 who pointed out that the difficulties only exist in the difference of fluid velocity from the measured particle velocity. In those few cases, such as fluid sprays, where the particle velocity field is under investigation there can be no problem. However most researchers require measurements of the fluid field and attempts to infer it from particles embedded in the flow has led to interminable argument. We propose to illustrate only the skeleton of this problem.

If particles are uniformly distributed throughout a container of gas at rest and subsequently moved past a fixed point in space the rate of observing particles depends on several things. For a perfect incompressible flow the rate of particle events depends on the modulus of velocity of the gas at that time and place and the mean separation of particles. The distribution of rate depends on Poisson statistics skewed by the velocity dependence. For degrees of compressibility the velocity dependence becomes a fractional power. This assumes that there is no velocity slip, i.e. the particle velocity is identical with that of the fluid.

The criterion on particles following the flow is that the difference between their velocity and that of the local gas shall be below a given small percentage - implying an upper size limit for other parameters fixed. This is only the first part of the constraint as there is a much tighter limit for results to a given accuracy.

Although the particles may follow the flow velocity to the acceptable degree discussed above and are thus bounded in behaviour by a given tolerable acceleration, both velocity and acceleration are vector fields and need not be everywhere aligned. Hence if a particle experiences an acceleration field associated with vorticity, although its differential velocity is a small value its consistent effect will sort particles such that there will be a correlation of particle concentration with vorticity history. This concentration heterogeneity interferes with assumptions about uniform particle distribution and can bring statistical inferences into serious question.

In summary then there are two criteria about particle flow following properties, minimisation of differential velocity due to slip, and changes in local concentration correlated with fluid acceleration properties.

Having outlined many of the problems with particles it is useful to discuss the sort of errors which arise and what level of tolerance is necessary. Here it is most important to obtain engineering measurements and what would be totally unacceptable to an academic purist can be very useful data in an awkward problem area. We have found that the errors which accrue from using seed particles which are theoretically much too large are not so serious as to cause concern. Although errors in absolute values of velocity or turbulence (albeit quite small) may occur, in many situations a comparative measurement says all that needs to be decided about a rig configuration. Engineering and design decisions are often taken in the absence of measurements - for the measurements to be a few percent in error need not invalidate their relevance and usefulness.

Most flows may be adequately sampled up to 10kHz or so by particles around or below $2\mu\text{m}$ to $3\mu\text{m}$ diameter although the accepted figure in the literature is nearer $1\mu\text{m}$, presupposing a density of about 103Kg m^{-3} for the particles in air. Viscosity and density effects may be allowed for by simple linear scaling. In the case of photon correlation measurements, particles may be much smaller to give adequate signal and often there are sufficient naturally occurring particles. As an aside, the particle biasing problems are quite different for the use of photon correlation since the velocity dependence of sampling rate is suppressed - there are more high velocity particles but each scatters less photons. The wide range of size of naturally occurring particles does not necessarily lead to serious error with photon correlation as large particles operate to lock out the correlator by excessive photon rate saturating the shift register, and very small particles give on average less than one photon and contribute only to the uniform background.

4. INFORMATION RETRIEVAL FROM LOW SIGNAL

In most engineering applications there is less signal than would be ideal. This arises from various constraints but may be divided into two groups (a) adequate size of particles to give a good velocity estimate from each but possibly long intervals between them, and (b) particles which may be rare or frequent but give rise to only a few photons each. We have restricted this part of the discussion to real fringe systems, optimal when the mean number of scattering centres in the sampling volume is less than one. The case where many particles at a time favours the reference beam approach is rarely met in our experience, except in over-rich combustion where large numbers of small particles may be created in the zone of interest - even then the natural particles are often large enough to be discerned above the background light. This case has been recently met again near the dew point line of a supersonic tunnel.

In case (a) above the retrievable information is determined by the frequency and statistical distribution of particle arrivals which we touch upon in the next section. The estimate of velocity from any one particle presents no significant problems when the signal is sufficiently great, as we have postulated. Case (b) is not only more difficult to handle, it is much more common. Fig. 3 shows the photomultiplier output from particles scattering progressively less power. The effect of quantum limitations is clearly illustrated in going from a - d. Low signal from each particle may arise in a number of ways such as:-

- (a) Small particles - desirable because they follow the fluid flow field better than large and may be present in larger numbers for a given mass fraction of contaminant.
- (b) Small laser - large lasers are expensive, fragile, require more extensive services such as three phase mains supply and water cooling, are difficult to hold in a single mode in a bad environment and may possess hazard levels unacceptable to the personnel who staff test rigs.
- (c) Small viewing cone - high pressure or hot rigs only allow small windows which may severely limit the detected signal on direct geometrical grounds.

- (d) Backscatter - highly desirable for traversing, retention of alignment and ease of rigging, but ruinous on signal level for the most appropriate particle sizes.

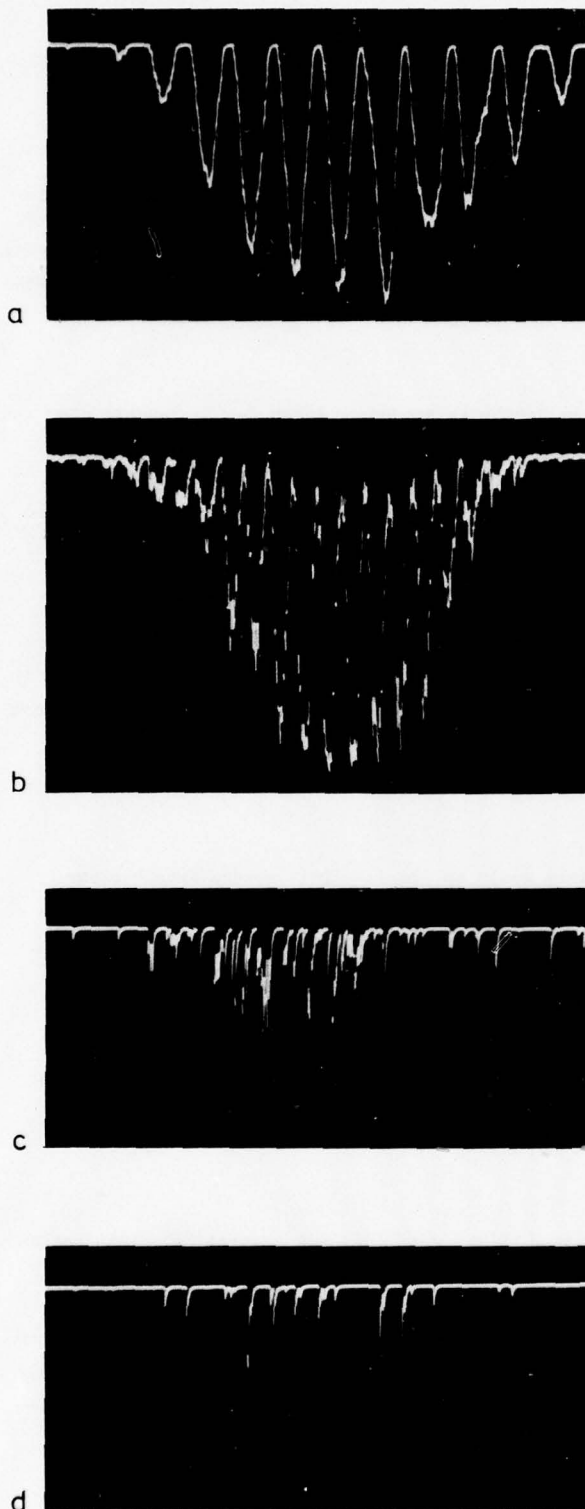


Fig. 3 Photomultiplier Output with Reducing Signal. Quantum Effects become more Apparent from a - d.

Given that in some cases a low signal is inevitable and in many others there are factors which make it desirable to use a small signal we must use methods of information retrieval as efficiently as possible. For many signal processing methods e.g. frequency analysis, tracking, counting, parallel filter bank etc. the signal is taken to be the idealised case with some inevitable noise looking like case a in Fig. 3. In the absence of flare the dominant source of 'noise' for a well contrived set up is of course shot noise, which can be considered more closely. Firstly we must temporarily discard the notion of 'signal to noise ratio'.

In an ideal classical world where the scattered optical fields were representable by electrodynamic continua we may define the fields unequivocally. This is still a useful idea when the energies involved are large compared with quanta. In many real cases of laser anemometry (and more especially so when attempting to apply Raman Spectroscopy to gaseous systems) this assumption does not hold and the classical parameters are only identifiable as expectation values whose immediate realisation is through the detection of single quantum events - photon arrivals.

Looking again at the signal from a quasi-classical scattering theory the optical intensity will be detected as a smooth analogue signal with some 'noise', which is no more than a statistical fluctuation of the photon arrival rate. As the total number of photons for particle transit becomes less so the classical envelope is less well identified until all that remains is a few quantum events which appear, on the classical model, to be entirely noise. This is not true, as the time distribution of the photons depends firstly on the statistics of the optical field, a consequence of source and scatterer, and secondly on the probability distribution relatable to the classical field estimator in the sampling region sampled by particle velocity.

So the time of arrival of photons is closely related to the classical signal and a measurement of the probability distribution of intervals between

photons may be used to make estimates of mean velocity and turbulence (9). So far the most satisfactory way of deriving the required interval probability is to use a fast digital correlator and that produced by Malvern Instruments is at present the most satisfactory commercial machine. It has a 50ns

acquisition time and using the esoteric mathematics of Pike and others (1), (10) may be used successfully without total comprehension of all of the subtleties. Fig. 4 shows a schematic layout of the clipping correlator, adequately described elsewhere (1).

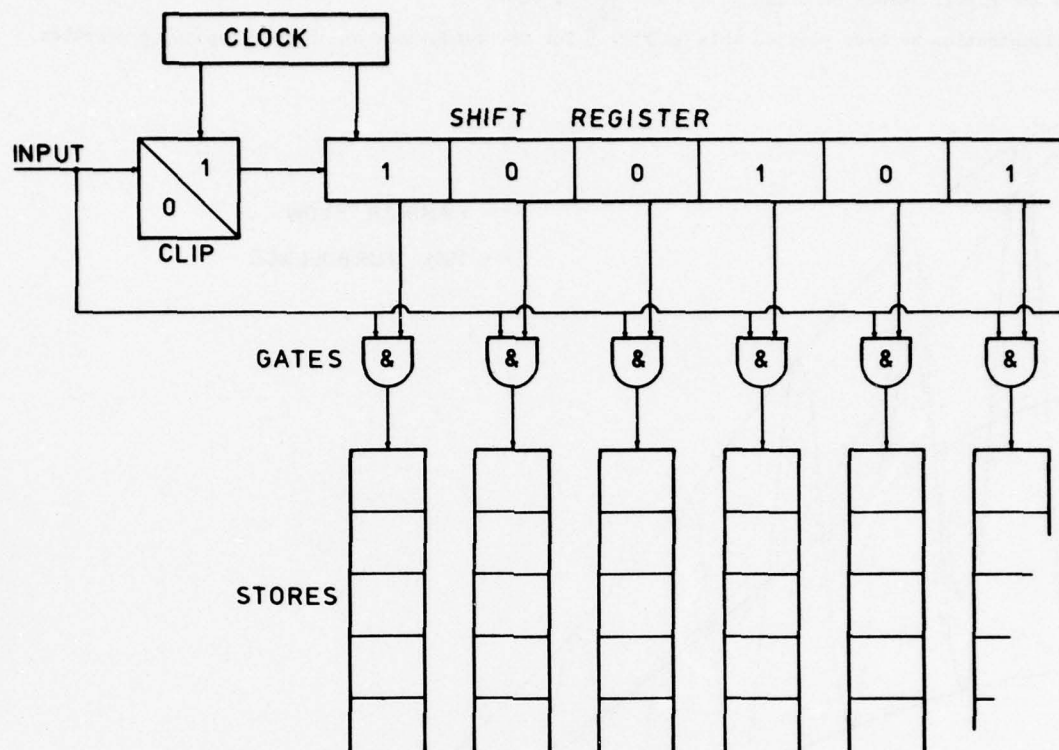


Fig. 4 Block Diagram of Correlator

It may be useful to go into some detail about how the correlator performs. We write the expression for equivalent field intensity in the sampling volume, bearing in mind that this is a gross conceptual oversimplification (11) but is sufficient description for our purposes. In the notation of Ref. 14,

$$I \propto \exp - \left(\frac{x^2 + y^2 + z^2}{2l_0^2} \right) \left[1 + r \cos \frac{2\pi x}{l} \right] \quad (1)$$

where x, y, z are Cartesian co-ordinates of the space of the spherical volume, l_0 is the distance to $e^{-1/2}$ intensity of the illuminated region, l is the fringe spacing in the sensitive direction x and r is the 'fringe' contrast. An ideal particle which scatters this field gives rise to the appropriate detected analytic signal which may be auto-correlated to yield

$$G^2(\tau) \propto \exp - \left(\frac{(u^2 + v^2 + w^2)\tau^2}{4l_0^2} \right) \left[1 + \frac{r^2}{2} \cos \frac{2\pi u\tau}{l} \right] \quad (2)$$

where u, v, w are resolved velocities in x, y, z and τ is correlation time. We have reverted to using $G^2(\tau)$ for the second order optical field correlation as it is more accepted. In general it is not possible with present correlators to extract the complete value of $G^2(\tau)$, although there may be quite enough signal to produce it in the time before the velocity changes because the internal organisation of the store makes data readout take a relatively long time compared with the desirable time between estimates. The most common use to date has been to accumulate estimates of $G^2(\tau)$ from a statistically representative number of particles and note that the function will, for Gaussian Turbulence only, look like

$$G^2(r) \propto \frac{1}{\sqrt{K_x K_y K_z}} \exp - \left(\frac{r^2}{l_o^2} \left(\frac{\bar{u}^2}{K_x} + \frac{\bar{v}^2}{K_y} + \frac{\bar{w}^2}{K_z} \right) \right) \left[1 + \frac{r^2}{2} \exp \left(- \frac{2}{K_x} \left(\frac{\pi \sigma_x}{l} \right)^2 \right) \cos \frac{2\pi u}{l K_x} \right] \quad (3)$$

where σ_x is the r.m.s. spread on u and $K_x = 1 + \left(\frac{\sigma_x r}{2l_o} \right)^2$, etc.

By way of illustration we have plotted this in Fig. 5 for two conditions which show typical properties.

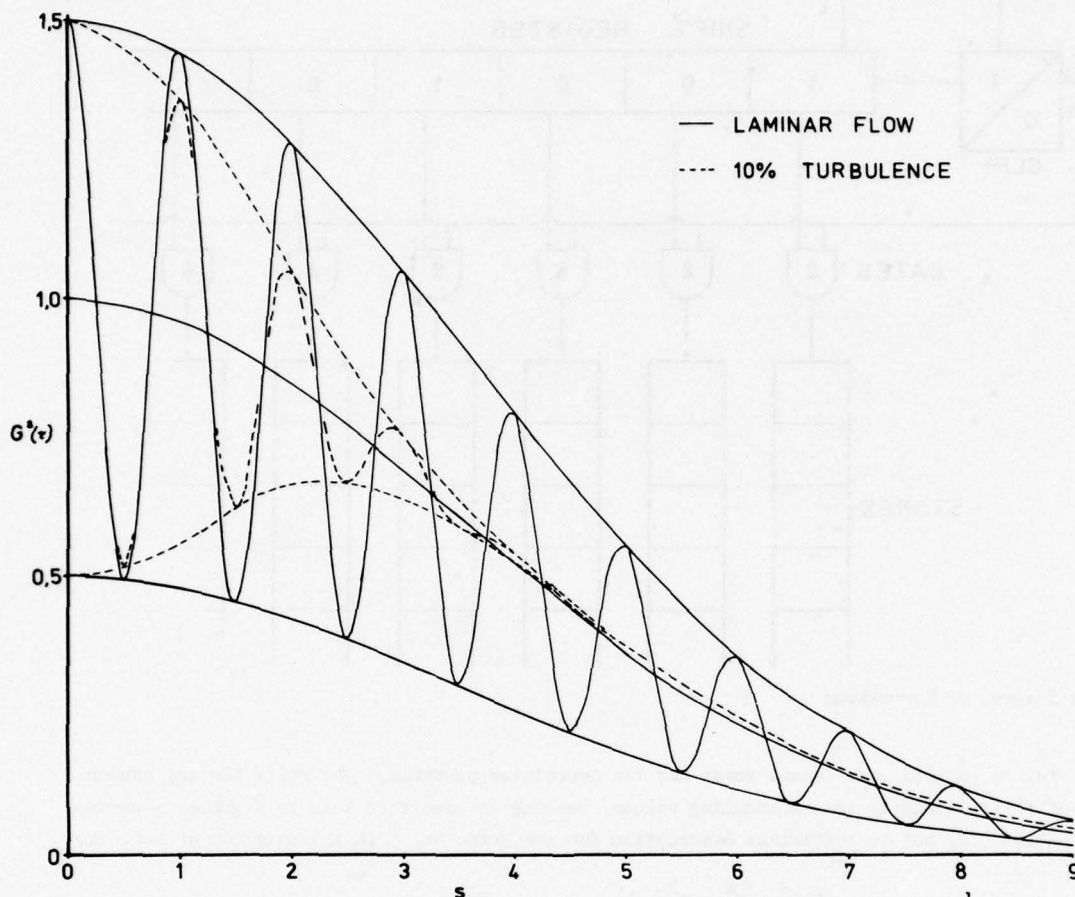


Fig. 5 Calculated Correlogram for 0 and 10% Gaussian Turbulence for 10 Fringes to $\frac{1}{62}$ Diameter.

For not atypical conditions we assume that $r \rightarrow 1$ and that $l_o = 2.5 l$. We further use the reduced parameter $s = \frac{ur}{l}$ and assume that the mean velocity is normal to the fringes i.e. $\bar{v} = \bar{w} = 0$.

For purely laminar flow the above expression reduces to

$$G^2(r) = \exp - \frac{s^2}{25} \cdot \left(1 + \frac{1}{2} \cos 2\pi s \right) \quad (4)$$

which is plotted on Fig. 5 as the solid curve.

For 10% isotropic Gaussian turbulence - an idealised concept -

$$G^2(r) \propto K^{\frac{2}{3}} \exp - \frac{s^2}{25K} \cdot \left(1 + \frac{1}{2} \exp \left(\frac{-2}{K} \left(\frac{\pi s}{10} \right)^2 \right) \cos \left(\frac{2\pi s}{K} \right) \right) \quad (5)$$

plotted as the dotted curve on Fig. 5.

Many interesting features may be noted but are outside our scope here. For those who wish to pursue the subject further there are many challenging areas.

These equations show how the measured function derives from various turbulent conditions. The inversion of the relationship leads to an estimate of velocity probability. For the more useful methods of inversion it is not necessary to make any assumptions about the nature of the turbulence (9).

Although the above calculations have been performed using a continuous model it has been shown that the clipping correlator may realise a very close approximation to this in many situations. For further technical details of the limits of accuracy and the mathematical and physical approximations the reader is referred to the Capri Notes (Refs. 1 & 11).

It has been noted (11) that 60 to 100 photons must be used to obtain a reasonable correlogram from which a velocity accurate to a percent or two may be extracted. It is more satisfactory to obtain all these from one particle but a few from each of several particles in the same fluid environment, with respect to velocity field, will suffice. Of course there is now a great range of 'real time' possibilities, but some changes in hardware design are necessary to realise the potentially high rate of velocity estimates. A correlator which allows parallel extraction of each correlogram, obtained over as little as μ s, with some hard wired method of reducing the correlogram to magnitude of the speed in the resolved direction, would be capable of operating as a real time velocity tracker with several orders more sensitivity than the conventional analogue device for the equivalent purpose. The nature of this efficiency improvement is also likely to reduce the problems of biasing and sampling errors, so much a problem in the more classical situations. The reasons for this are immediately obvious on examination of the mechanisms involved.

With due reference to section 3 we may consider that each particle gives an estimate of velocity in cases such as counting and tracking. This will be a certain introduction of 'bias' but has only been incompletely considered in the literature. Part of the problem is propounded in Ref. 7 and a good analysis is given by George (6) with other useful papers in the same volume. For photon correlation the consequences are somewhat different as the weighting depends on the number of photons collected from each particle. As faster particles, of which there are more, scatter fewer photons each (the intensity is the same but the time is shorter) a correction in incompressible flow is automatically applied to first order. Hence the simple linear dependence of sampling rate on velocity is cancelled. Other biasing still exists and compressibility now makes the correction worse rather than better as in the case of individual particle velocity realisations.

Photon correlation will not help directly in the case of dependence of particle concentration on acceleration history, the tendency for particles to clump and attenuate in turbulent flows because of local centrifugation due to vorticity. This problem can be very serious and I know of no satisfactory treatment of the problem as yet. In ordered flows such as a von Karman street we have looked at velocity probability histograms to find that there is a very sharp decline in particle numbers near the centre of a vortex which has existed for some time. This is a much more restrictive specification on maximum permitted particle size than the conventional particle slip leading to a velocity error. Both are controlled by Stokes drag but affect the observed data very differently. There is some small crumb of comfort to be obtained by the use of photon correlation, capable as it is of retrieving good measurements from particles much smaller than are usually used, and hence less prone to 'turbulent vorticity sorting'.

The advantages of photon correlation may then be summarised. Good velocity estimates may be obtained from about three to four orders of magnitude less optical signal than is usual for other processors. A statistically stationary estimate of turbulence is possible in a time controlled only by the turbulence phenomena, because small particles may be available at greatly increased frequencies. Biasing is correlated for incompressible flow at low turbulence and reduced from other causes, primarily due to the use of smaller particles. Another advantage, at least as important is the extreme conceptual simplicity of digital correlation from the users' point of view. The intellectual hurdle between correlogram and velocity is the only area which may deter people, but is easily crossed by a little thought. The extra step of having to process data with a computer is now becoming more

accepted and the failure to have a machine with a dial on the front calibrated in metres per second is no hardship for the engineers who are really forced to use these methods because no others will suffice. The necessity of slight extra processing also performs the essential function of inducing the user to think about the information, what it means and the constraints on its accuracy.

5. REAL TIME MEASUREMENTS

Many parameters may be extracted from optical measurements of the laser anemometer type, and which presentation format is desirable depends on the purposes for which the measurement is needed. In the earlier section we have illustrated how time averaged data may be obtained from very low signal cases via photon correlation. If we invoke the ergodic hypothesis in the case of turbulence and assume that there exists a characteristic period during which statistics remain constant to a given accuracy from one sample to the next we may derive a 'stationary' estimate of the turbulence statistics. If we observe over one or more such periods with a photon correlation experiment it is possible to extract mean velocity immediately and, by one of various methods, a probability of velocity v.s. velocity histogram from which the rms ('turbulence') values, skewness and perhaps kurtosis, depending on data quality, are obtainable.

There are many situations where real time, or continuous velocity histories are required and since this is not yet available from correlation and existing hardware the price of greatly increased signal must be paid. Even then all is not well as arguments about the accuracy of real time measurements, particularly with regard to results of later processing and the validity of inferences are still raging. In general each particle, tested for suitability yields a measurement of velocity. From a counting system, of which several excellent machines are produced commercially this yields a train of data which suffers all the problems of biasing. In principle this can be 'smoothed' (a general term meaning that some of the data is altered in the belief that this will somehow improve understanding) and assumed to indicate velocity fluctuation, or, more precisely, fairly random samples of it. By extracting two pieces of data from each particle, the velocity and the time at which the sample took place it is possible with adequate computing facilities to construct not very biased probability plots and spectra (4) but the real time or continuous natures are lost. Depending upon the requirement this may not matter. With frequency tracking systems it is conventional to hold the last velocity value until the next opportunity to update. We must mention as an aside that counting and tracking are merely different methods of achieving any or all of the reduced parameters we are discussing, but some measurements favour one method, some another.

An unfortunate artefact of tracking is phase noise, which again is discussed by George (5) and is a consequence of randomly distributed sampling (4). For derivation of spectra from the tracker output this must be corrected. Phase noise arises when more than one particle contributes significant power to the signal. Even though the two particles may have the same velocity, because they are embedded in the same slug of fluid, and hence emit the same frequency there will be an arbitrary phase change between them. The equivalent output excursion which is caused by tracking this phase change has no relation to velocity, but depends rather on the particle arrival statistics. The spectral distribution of those spurious excursions is flat to the upper bandwidth of the tracker for Poisson distributed particles; the level depends on the particle rate via the probability of seeing two particles at once.

Spurious excursions such as phase noise will not lead to serious errors if the retrieved signal is to be correlated with some other parameter since they will be uncorrelated with most phenomena and hence merely enlarge the background and reduce the level of correlation. Slight errors may be manifest if the phenomenon with which velocity is being correlated contains a dependence on vorticity since this may also correlate weakly with fluctuations in local particle concentrations and hence phase noise magnitude. In any real experiment the possible significance of these effects will have been considered and if necessary the conclusions verified by pilot experiment - on a well understood system for example.

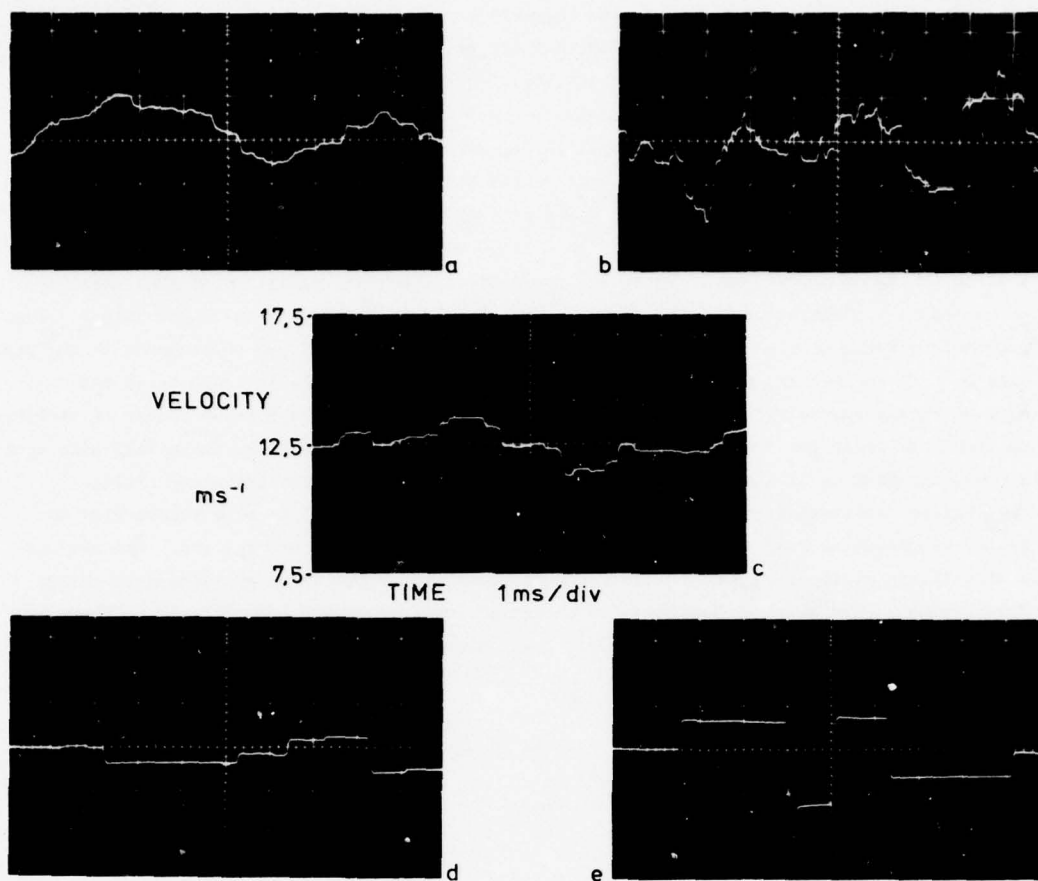


Fig. 6 Tracker Output Showing Good and Bad Time Series Estimates.

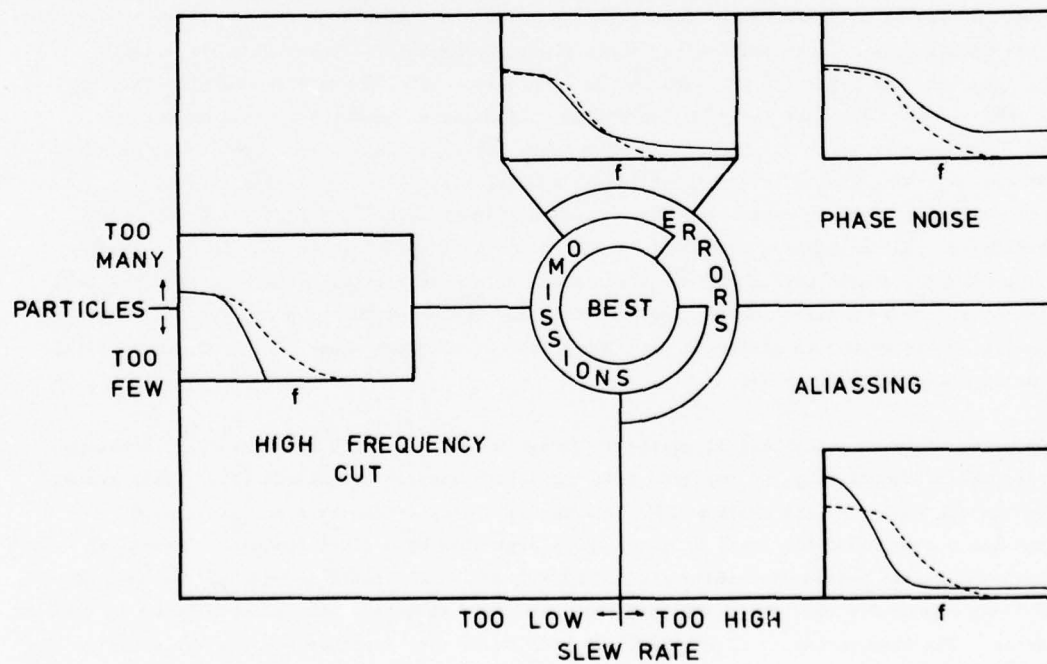


Fig. 7 Tracking Domains Corresponding Qualitatively with Fig. 6.

As a somewhat rough working guide some figures are suggested. If using a frequency tracker in the sample and hold mode, that which for subsequent correlation or spectral analysis is most appropriate, it is necessary to restrict the slew rate of the tracker. A working figure is something of the order of five changes in output level for each cycle of the highest turbulence frequency present. The signals shown in Fig. 6 are typical Cambridge Physical Sciences tracker output from a very turbulent jet at 7 diameters downstream. The fringe anemometer used a HeCd laser with $25\mu\text{m}$ fringes with about 20 fringes in the $\frac{1}{2}$ diameter. The qualitative appearance of the signal is clearly seen as different in the different conditions. This also dictates an optimum dopant concentration with the possibility of errors if this is not chosen correctly. There are two criteria, neither exact. (a) The particles should be at the right concentration and (b) the slew rate should be limited to the right value. Fig. 7 shows a schematic diagram of what can happen if the conditions are not met and corresponds to the same layout as Fig. 6. It is seen that the best estimate is still not perfect as it could be if the particles were uniformly spaced giving an associated Nyquist frequency. The Poisson nature of particle distribution serves to smear the frequency about which aliasing may occur into an infinitely wide zone of possible frequency folding limits yielding a flat background over the lower frequency region. Deviation from Poisson statistics tends to narrow this zone but it may still be some orders wide in frequency space, complicating rather obscurely the interpretation of turbulence spectra. An obvious consequence of sampling at too slow a rate (too few particles) is the inclusion of turbulence energy from high frequencies in the spectrum indicated to obtain at low frequencies (see Fig. 7). There is much more to be said on these topics as experience becomes wider, but it is not appropriate to go into greater depth here.

For many engineering purposes the above discussion is to be considered and should be included in the intellectual background of the informed user.

6. TRANSIT ANEMOMETRY

Using the now conventional system of fringe anemometry a large number of interesting cases may be, and some have been, investigated. It may be used in forward scatter, which makes traversing cumbersome or impossible; it may be used at more or less right angles where scattering efficiency may be very low and access not always possible, or backscatter where signal is usually lower still and spatial sensitivity, including the rejection of flare can be very poor. Fig. 8 shows a schematic and very qualitative look at the figures of merit for selecting collection angle for a typical anemometer application. The factors important for obtaining results useful in engineering are (a) signal level, (b) flare rejection linked to (c) longitudinal spatial resolution (d) ease of traversing and (e) single sided access. It is clear from Fig. 8 that different situations will favour different angles of scattered light collection according to the relative significance of the above properties. We look at the most favourable criterion for making measurements in a rotating machine and find that near backscatter is the only direction in which we stand any chance of making a measurement. Even at the optimum a fringe system is likely to pose many problems although these have been overcome with great success in one application (17).

A way of improving flare rejection was suggested by Thompson (16), extended by Tanner (15) developed to engineering use by Schodl (12) and employed with impressive success by Eckardt (3). This system exists under various names, 2 spot system, L2F, dual focus, transit anemometer and consists of directing the laser power into two small Gaussian spots separated by a fixed distance, instead of forming a larger Gaussian region containing sinusoidal fringes. The power density at the spot may be some 300 times higher for the same laser power and the flare rejection stop reduced by an equivalent factor on area. The improvement in flare light suppression is very considerable but the price to pay is that fewer particles cross the illuminated region. In practice smaller particles are now discernable events, but the statistical accuracy depends on total number and uniformity of events.

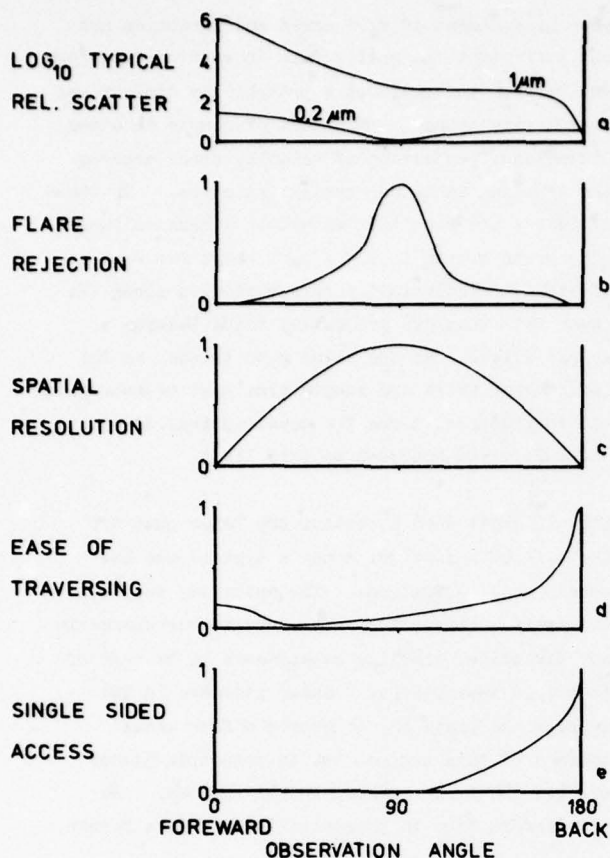


Fig. 8 Schematic Dependence of Collection Angle on Various Parameters.

We will include a brief discussion of the data available from a transit anemometer. It may be shown that using two illuminated regions of space and two detectors a good method of data retrieval is by cross correlation of events on the two channels. There have been techniques which use a multichannel analyser but for a non-gated application this is seen to be less efficient in situations of high seeding, and slightly more efficient for low turbulence and low data rate, depending somewhat on the methods of specifying 'efficiency'. We require the time of transit of a particle going through the first spot (A) and subsequently the second spot (B). Those which go through either A or B contribute nothing but background.

If multichannel analysis is used a sweep is triggered by an event on A and events on B during the subsequent sweep time are recorded in the appropriate time domain store. For high turbulence most particles which go through A do not go through B but distract the analyser from triggering again until one full sweep time later, missing some of the 'useful' events on A and B. A second method of operation is to re-enable A as soon as the next event occurs on B. This misses less events but the background is no longer flat and hence more difficult to correct for by subtraction. If correlation is used the

distribution of probable event times of ALL particles which cross A and ALL particles which cross B is recorded.

The usual ways of operating transit anemometers are to measure the correlogram or multichannel analysis of detected events at different orientations of the two spots. Each correlogram must be transformed from its function of probability of transit time versus time by some suitable non-linear process depending on particle concentration biasing to yield a distribution of velocity probability against velocity. A convenient transform for incompressible homogeneously seeded flow is point by point division by velocity cubed and linearisation of the abscissa. The noise is then non-uniform but if sufficient particle transits are observed this need not be serious. Consequences of biasing errors are almost completely insignificant for all flow compressibilities if the turbulence is low, less than a few percent (say). The way of identifying the flow direction from such measurements is to observe the transformed correlogram at a number of spot orientation angles. A plot of the velocity magnitude at each angle is only weakly dependent on direction, as $\cos \theta$, where θ is the angle of rotation; more sensitive is to plot the number of correlated events normalised by the number which gave a signal from the first spot.

This may be used to identify the mean direction to very high accuracy. For a few percent turbulence and typically 4000 correlated events per correlogram at worst 0.5° arc accuracy is easily achieved. Performance of this exercise yields redundant estimates of speed which may be combined to yield typical accuracies of 0.5% or better. Plotted on Fig. 9 are the speed estimates from the same data and the inferred cosine dependence from the mean of the speeds for the angle less than 1.5° arc. The rms error is less than 0.2%. The scatter is great for longer distances from the mean angle because the data are based on a much smaller number of correlated events.

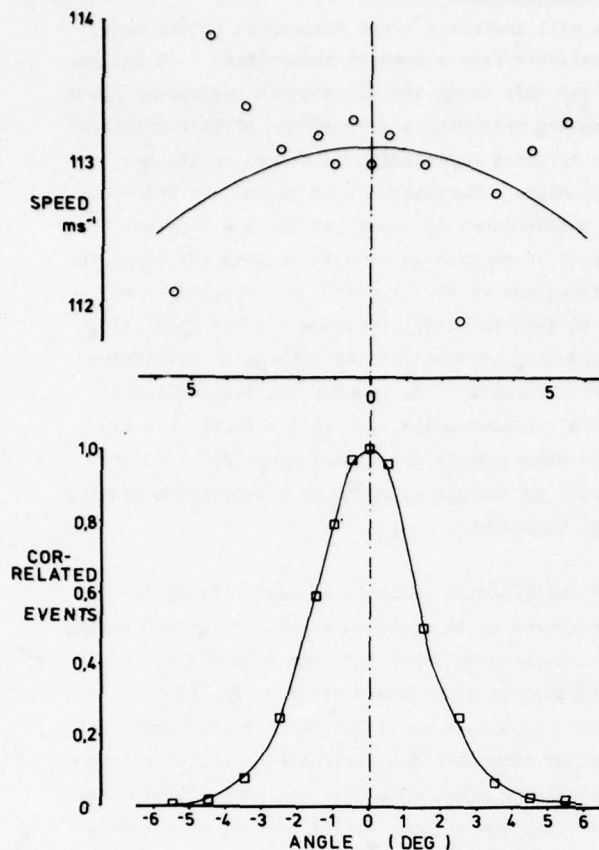


Fig. 9 Direction Identification Using a Transit Anemometer.

Although this will be discussed extensively elsewhere it is worthwhile to illustrate a trivial point. For correlation analysis it is usual to enable the transit anemometer system at a fixed point each cycle of the rotating assembly. This has been done by gating the laser beam by electro- or acousto-optic switches or by gating the correlator clock time. It is quite obviously more satisfactory to leave one correlator channel fully operational all the time and enable the other one at the required time and for the required periods. This obviates any windowing convolution within the correlogram. It may be possible in some future application to gate the system with software thus enabling all points in rotor co-ordinates to be obtained at the same time. But this requires time division multiplexing of cross correlated reductions of the input signal.

7. FURTHER PRACTICAL CONSIDERATIONS

A few other problems which are often mentioned or actually occur may be shown to be irrelevant or prevented by foreknowledge. Again these seem trivial when written out formally.

Vibration is often quoted as a source of error but is unlikely to be serious in rigs and engines. Vibration velocities of metal components, computed as frequency times amplitude, tend not to exceed about ms^{-1} as much more than this leads to physical damage. Aerodynamic velocities in rigs and engines are greater than this by typically two orders of magnitude. If the vibration operates through an 'optical lever' problems could occur but competent design eliminates this. Some uncertainty of sampling position may occur in a vibrating assembly but this must be tolerated or the differential vibration between rig and laser anemometer minimised in some appropriate way; rigid coupling with flexible support for the whole experiment will suffice in some cases. Damage to the laser anemometer may occur if the whole system vibrates. I have been rather careful with mountings since I shook a laser to pieces on a rough running engine with a nearly rigid cradle.

When measurement of flow speed and direction are not sufficient the entire data in each correlogram may be used to construct a probability contour map in velocity space. This must of course be a two dimensional projection of velocity space because the sampling spots are really cylinders. If these cylinders are long then we obtain a true collapsed projection but if they are made short for reasons of spatial resolution in this direction along the laser beam then our projection tends towards a sample slice. As the slice gets thinner so the information falls and sample time must be increased but in practical terms the usual optical designs preclude close approach to this limit.

Fig. 10 shows such a contour map taken just off the axis of a free jet - not a typical use but merely an illustration. The shape may be used to assess a figure for time averaged turbulence in any direction, enabling assessments to be made of isotropic assumptions. Shear stresses in the appropriate plane may be obtained from cross moments of this contour but in principle higher moments are fully represented by the map. No time information is presented in this data format.

A mode of machine operation which has been commonly used is to look at flows in rotating assemblies.

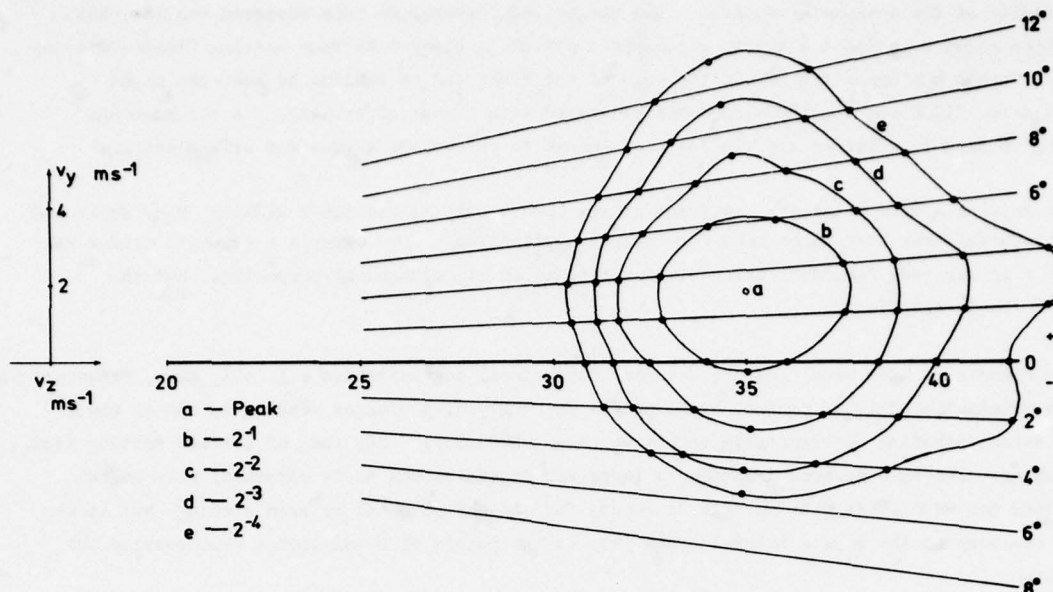


Fig. 10 Contour Plot of Turbulence Probability Just Off Axis in a Free Jet.

In very high noise fields we have noticed that there is acoustic modulation of the laser output by pressure changes in the laser resonator cavity. Acoustic lagging is a cumbersome but effective cure. Other modulation problems have been noted, especially with photon correlation, which were first attributed to vibration but later found to be due to photomultiplier gain modulation. Electron trajectories in the tube were affected by cyclic magnetic fields from nearby electrical machines: the cure was to improve the quality of mumetal magnetic screening of the detector. There can be a tendency to ascribe to vibration curious things which are observed in association with rig work but arise from other causes.

Vibration of windows can cause odd effects, especially if the surface is not perfectly flat nor free from contamination. Beam walkoff at a few percent per reflection can give rise to scattered light from surface dust. If this is inadvertently within the collection cone it may contribute unpleasantly large background even though it may be a long way from the focal region of the detector, or its image.

Windows themselves can cause a lot of problems, most often because those who design and build rigs have little or no experience of window design, properties and handling. Where different windows are to be used for input and output light they have different criteria. The input must be of optical quality - that is it must be free from inhomogeneities or surface defects which might impose wavefront aberrations on the input laser beam. Quite small defects can cause a bad deterioration of fringe pattern in both spacing and contrast. In a two spot system any spreading of the spot or angular separation leads to ambiguity and systematic error. Although the output window distortion may change the spatial resolution, the quality is not so important as the information is now encoded upon the light beam as a frequency modulation. Even serious attenuation does not cause errors but merely reduces the detectable power.

Some general comments on window materials and design may help. For cold rigs we have found that selected float glass is cheap and readily available, easy to work and clean. Always choose the cheapest material and order lots of spare blanks - they will be needed as some damage almost always occurs. Arrange that the window is mounted as a removable cell, both for cleaning and avoidance of accidental damage as it can be placed in the completed rig just before the test. The physical mounting of the transparent component should permit good sealing if pressure differentials are to be met and if thermal loading is to be expected a form of expansion compensation should be included. The sealing is not merely important as a sophistry - it may be essential to prevent hot gases from leaking

into the vicinity of the anemometer optics. One unexpected disaster we once observed was that hot rich combustion gases oozed past a quartz window in a stainless blank with face sealing (inadequate) on both faces. Carbon was deposited around the edge of the blank and on cooling to sub zero night temperatures after 1100K running the window disintegrated with a mass of crazing. A second blank crazed during cooling long before the rig was cool enough to remove the window for safe keeping.

The two most popular window materials are fused quartz (Spectrosil A) and float glass. Many other and more exotic materials may have to be used for unusual applications; for example a sapphire window was necessary in a roller race for lubrication studies because of its mechanical properties, but the essence should be on simplicity.

For cleaning windows we have used 'Analar' Methanol for general contamination e.g. oil, dust, fingerprints; and for more substantial dirt or stains, burnt on oil for example, prolonged soaking in one of the proprietary decontaminating detergents is effective (e.g. DECON 90). Any form of surface pitting will need repolishing. We once sprayed a window, a large and expensive one as it happened, with molten stainless steel and were pleased to be able to remove the streaks of metal by acid etching, but it was not a total recovery as the minute thermal craze pits at the points of metal impact much reduced the window quality.

One almost superfluous comment about windows is that they should be in the right place. Hot rigs often expand many millimetres when operating and it is frustrating to set up a system and have the window translate away from it as the measurements begin to get interesting. This is easily overcome by constraining the rig near the plane of the window, translating the anemometer or enlarging the window.

There has been some pressure to keep to small lasers for rig anemometry from the safety angle. Most test crews unfamiliar with laser techniques are very interested in the laser and are uncertain what, if any, hazard may be present. Even though every effort is made to contain the beam at all times it is always worth while taking some time and trouble to explain some of the details and potential dangers to those who may work near the installation.

8. INFORMATION PRESENTATION

Assuming that the foregoing has enabled us to obtain the measurements of fluid velocities and related parameters the next problem is to transfer this as lucid concepts with adequate quantification into the heads of those who will use it. If the anemometer application is in response to a specific query then this is made easier by the mutual co-operation of the parties concerned. If, as in many cases, the application of laser anemometry yields information in a new and unfamiliar form there is a barrier of conservatism to be crossed. It is difficult to offer universal guidance but new forms of information must be considered in great depth. It is often in the interests of the experimenter to show justification of the validity of his data and a well thought out approach to data reduction and presentation format can help. Tables of numbers may be necessary but should not be the 'first line' in the presentation of results, but a group of pictures or even a physical model is better.

There has been a tendency to assume that fundamental properties with conventional names exist regardless of the method of measurement but in extreme cases this is not entirely true. Let us consider 'mean velocity'. The pitot probe is of course a non-linear device and if used to assess mean velocity has a transfer function which has an effect on the measurement depending on the waveform and other characteristics of the velocity. The laser anemometer is a linear device and produces (with many reservations not relevant to this point) a 'mean velocity' which may or may not differ from that derived by other methods. Without wishing to enter the arguments of time series analysis and the theory of measurement of fluctuating parameters we hope the trivial example shows that care must be exercised in statements of the anemometer measurements.

The availability of this linear technique, together with several others currently becoming popular, is causing a closer look at information theory applied to real measurements. Although it in no way precludes the original use and presentation of data it offers a new tool to look in greater detail at the fundamental processes upon which engineering realisations so firmly depend.

9. CONCLUSIONS

We have tried to stress the practical aspects of applications of laser anemometry and a number of disparate topics have been discussed. Several ideas are discussed in the light of our own experience of the simple and usually unexpected things which may go wrong. As with the man who requested fried hippopotamus sandwiches and was told that there was no bread, the most elaborate and clever instrumentation can fail entirely for reasons that, because each is trivial, do not get even the attention they deserve.

REFERENCES

1. Cummins H. Z. & Pike E. R.
Photon Correlation and Light Beating Spectroscopy
NATO Advanced Study Institute, Capri 1973. Plenum Press New York - London.
2. Durst F, Melling A. and Whitelaw J. H.
Principles and Practice of Laser Doppler Anemometry
Academic Press 1976.
3. Eckardt D.
Detailed Flow Investigations Within a High Speed Centrifugal Compressor Impeller
ASME 76-FE-13 (1976).
4. Gaster M. and Roberts J. B.
Spectral Analysis of Randomly Sampled Signals
J. Inst. Maths. Applics. (1975) 15, pp 195-216.
5. George W. K.
The Measurement of Turbulence Intensities Using Real Time Laser Doppler Velocimetry
J. Fluid Mechanic (1974) Vol. 66 Pt. 1 pp 11-16.
6. George W. K.
The Accuracy of Flow Measurements by Laser Doppler Methods
Proc. of LDA Symposium, Copenhagen 1975, PO Box 70, DK-2740, Skovlunde, Denmark, June 1976.
7. McLaughlin D. K. and Tiederman W. G.
Biassing Correction for Individual Realisation Laser Anemometer Measurements in Turbulent Flows
Phys. of Fluids Vol. 16 No. 12 Dec. 1973 pp 2082-88.
8. Maxwell B. R.
Particle Flow in Turbomachinery with Application to Laser Doppler Velocimetry
AIAA Journal Vol. 12 No. 10 Oct. 1974 pp 1297-1298.
9. Moore C. J. and Smart A. E.
Retrieval of Flow Statistics Derived from Laser Anemometry by Photon Correlation
Journal Phys. E. Scientific Instruments Nov. 1976 Vol. 9 pp 977-981.
10. Pike E. R. and Jakeman E.
Photon Statistics and Photon Correlation Spectroscopy
Advances in Quantum Electronics Ac. Press 1972.

11. Pike E. R. and Cummins H. Z.
Capri 1976, NATO Advanced Study Institute.
12. Schodl R.
A Laser Dual Beam Method for Flow Measurement in Turbomachines
ASME Paper No. 74-GT-157 (1974).
13. Smart A. E., Jones B. and Jewell N. T.
Measurements of Unsteady Parameters in a Rig Designed to Study Reheat Combustion Instabilities
AIAA Paper No. 76-141.
14. Smart A. E. and Moore C. J.
Aero Engine Applications of Laser Anemometry
AIAA Journal Vol. 14 No. 3 March 1976 pp 363-370.
15. Tanner L. H.
A Particle Timing Laser Velocity Meter
Optics and Laser Technology, June 1975 pp 108-110.
16. Thompson D. H.
A Tracer Particle Fluid Velocity Meter Incorporating a Laser
J. Sci. Inst. (J. Phys. E) Series 2 Vol. 1 1968 pp 929-932.
17. Wisler D. C.
Shock Wave and Flow Velocity Measurements in a High Speed Fan Rotor Using the Laser Velocimeter
ASME Paper 76-GT-49.

Bibliography on Laser Optical Measurement Methods
for Aero Engine Research and Development

1. Flow Measurement

INSPEC 76A44573

Measurements in an Axi-Symmetric Jet

J.B. Abbis, L.J.S. Bradbury

Royal Aircraft Establ., Aldershot, England Tech. Univ. Denmark

LDA-Symposium 1975 Accuracy of Flow Measurements by Laser Doppler Methods, Conference Paper, Aug. 1975, 1975, 198, 119. Copenhagen, Denmark, Lyngby, Denmark

A76-41144

Results from a Two-Dimensional Laser Doppler Anemometer

C.J. Bates

University College, Cardiff, Wales

Journal of Physics, Part E - Scientific Instruments, vol. 9, Aug. 1976, p. 616-618, 3 p. Refs. 7

A74-36614

Laser Velocimeter Measurements of the Helicopter Rotor-Induced Flow Field

J.C. Biggers and K.L. Orloff

NASA, Ames Research Center, Moffett Field, Calif.

American Helicopter Society, Annual National V/STOL Forum, 30th Washington, D.C., May 7-9, 1974, Preprint 800, 8 p. 21 refs.

A76-14566

Laser Velocimeter Measurements of Rotor Blade Loads and Tip Vortex Rollup

J.C. Biggers, S. Chu and K.L. Orloff

NASA, Ames Research Center, Moffett Field, Calif.

In: American Helicopter Society, Annual National Forum, 31st, Washington, D.C., May 13-15, 1975, Proceedings

New York, American Helicopter Society, Inc., 1975, 7 p, 9 refs.

A76-45326

The Accuracy of Flow Measurements by Laser Doppler Methods; Proceedings of the LDA-Symposium, Copenhagen, Denmark, August 25-28, 1975

Edited by P. Buchhave, J.M. Delhay, F. Durst, W.K. George, K. Refslund and J.H. Whitelaw

Skovlunde, Denmark, Proceedings LDA-Symposium Copenhagen, 1976, 735 p.

Far-Field Wake-Vortex Characteristics of Wings

D.L. Cliffoe and K.L. Orloff

Journal of Aircraft, no. 5, p. 464-470, May 1975

Design, Development, and Test of a Laser Velocimeter for High Speed Turbomachinery

F.X. Dolan, F.R. LeBlanc and P.W. Runstadler, Jr.

Presented at the LDA-Symposium Technical University of Denmark, Lyngby, Denmark, August 25-28, 1975

Create Technical Note TN-234

A76-20966

Progress in Turbomachine Research Owing to a New Optical Measuring Method for Flow Vectors (Fortschritte in der Turbomaschinenforschung durch ein neues optisches Meßverfahren für Strömungsvektoren)

R. Dunker, R. Schodl, and H. Weyer

Deutsche Forschungs- und Versuchsanstalt für Luft- und Raumfahrt, Institut für Luftstrahlantriebe, Cologne, West Germany

Zeitschrift für Flugwissenschaften, vol. 24, Jan.-Feb. 1976, p. 17-25, 14 refs.

In German

Detailed Flow Investigations within a High-Speed Centrifugal Compressor Impeller

D. Eckardt

Presented at the Gas Turbine and Fluids Engineering Conference; New Orleans, La., March 21-25, 1976

ASME Publication no. 76-FE-13

A74-28283

Instrumentation for Airbreathing Propulsion; Proceedings of the Symposium, U.S. Naval Postgraduate School, Monterey, Calif., September 19-21, 1972
 Symposium sponsored by the U.S. Air Force, U.S. Navy, U.S. Army, and NASA
 Edited by A.E. Fuhs and M. Kingery
 Progress in Astronautics and Aeronautics, vol. 34
 MIT Press, Cambridge, Mass., 1974, 547 p.

N76-31197

Velocity Surveys in a Turbine Stator Annular-Cascade Facility Using Laser Doppler Techniques
 Louis J. Goldman, Richard G. Seasholtz, and Kerry L. McLallin, Washington Sept. 1976, 27 p., refs.
 National Aeronautics and Space Administration, Lewis Research Center, Cleveland, Ohio
 NASA-TN-D-8269; E-8637

A76-18048

A Two-Component Optical Doppler Velocimeter with Ultrasonic Modulator
 A.M. Kolychev, B.S. Rinkevichius, V.L. Chudov
 Radiotekhnika i Elektronika, vol. 20, Oct. 1975, p. 2215-2219. In Russian. Refs. 9

A76-16945

Three-Component Optical Doppler Velocimeter
 V.M. Kulybin
 Moskovskii Energeticheskii Institut, Moscow, USSR
 Fizika, vol. 18, no. 10, 1975, p. 82-86, 5 refs. In Russian

A75-10839

Measurement of Model Helicopter Rotor Flow Velocities with a Laser Doppler Velocimeter
 A.J. Landgrebe and B.V. Johnson
 United Aircraft Research Laboratories, East Hartford, Conn.
 American Helicopter Society, Journal, vol. 19, July 1974, p. 39-43, 6 refs.

N74-17014

Particle Flow in Blade Passages of Turbomachinery with Application to Laser-Doppler Velocimetry. Final Report
 Barry R. Maxwell, Feb. 1974, 36 p. refs.
 Bucknell Univ., Lewisburg, Pa.
 NASA-CR-134543

INSPEC 76A38277, 76B22338

A Technique for Simultaneous Velocity and Concentration Measurements
 A. Melling
 Dept. of Mech. Eng., Imperial Coll., London, England Tech. Univ. Denmark
 LDA-Symposium 1975 Accuracy of Flow Measurements by Laser Doppler Methods
 Conference Paper, Aug. 1975, 1975, 198, 69-70. Copenhagen, Denmark. Lyngby, Denmark

Laser Velocimeter Measurement of Developing and Periodic Flows

K.L. Orloff and J.C. Biggers
 Presented at the International Workshop on Laser Velocimetry, Purdue University, March 1974

A76-20923

Simultaneous Laser Velocimeter and Laser Induced Photoluminescence Measurements of Instantaneous Velocity and Concentration in Complex Mixing Flows
 F.K. Owen
 United Technologies Research Center, East Hartford, Conn.
 American Institute of Aeronautics and Astronautics, Aerospace Sciences Meeting, 14th, Washington, D.C., Jan. 26-28, 1976, 5 p., 5 refs.

N75-30474

Optical Measurements in Turbomachinery
 Jacques Paulon
 In: AGARD Modern Methods of Testing Rotating Components of Turbomachines (Instrumentation) Apr. 1975, p. 123-139, refs.
 AGARD-AG-207

Proceedings of the ISL/AGARD Workshop on Laser Anemometry May 5-7, 1976
H.J. Pfeifer, J. Haertig, Auriol, Schall

N75-30471

Modern Methods of Testing Rotating Components of Turbomachines (Instrumentation)
M. Pianko, ed. (ONERA) Apr. 1975, 186 p. refs.
AGARD-AG-207; AGARDograph-207

A76-34499

A Laser Velocimeter System for Small Radial Turbomachinery
P.W. Runstadler, Jr.; F.X. Dolan
Creare, Inc., Hanover, N.H.
U.S. Navy, SQUID Workshop on Transonic Flow Problems in Turbomachinery, Monterey, Calif.,
Feb. 11-13, 1976, Paper. 20 p.

Special Applications and New Technical Aspects of Laser Anemometry, Review Paper
Peter W. Runstadler, Jr.
Creare Incorporated, Hanover, New Hampshire, USA 03755

On the Development of a New Optical Method for Flow Measurements in Turbomachines
R. Schodl
Paper presented at the ASME Gas Turbine Conference in Zurich, Switzerland, 1974

A74-27493

A Laser Dual-Beam Method for Flow Measurements in Turbomachines
R. Schodl
Deutsche Forschungs- und Versuchsanstalt für Luft- und Raumfahrt, Institut für Luft-
strahlantriebe, Porz-Wahn, West Germany
American Society of Mechanical Engineers, Gas Turbine Conference and Products Show,
Zurich, Switzerland, Mar. 30 - Apr. 4, 1974, Paper 74-GT-157, 7 p., 6 refs.

Advanced Testing Techniques in Turbomachines; a Laser Dual Focus Velocimeter for
Turbomachine Applications
R. Schodl
Von Karman Institute for Fluid Dynamics Lecture Series, April 14-18, 1975

A74-27774

Laser Doppler Velocimeter Measurements in a Turbine Stator Cascade Facility
R.G. Seasholtz
NASA, Lewis Research Center, Cleveland, Ohio
Laser Velocimetry Workshop, West Lafayette, Ind., Mar. 27-29, 1974, Paper. 11 p. 8 refs.

A76-32581

Aero-Engine Applications of Laser Anemometry
A.E. Smart and C.J. Moore
Rolls-Royce /1971/, Ltd., Derby, England
AIAA Journal, vol. 14, Mar. 1976, p. 363-370, 20 refs.

A75-28691

Determination of the Turbulence Characteristics of Gas Flows and Flames by the Method
of Optical Expansion in Fourier Series of the Amplitude of the Probing Laser Emission
(Poluchenie turbulentnykh kharakteristik gazovykh potokov i plamen metodom opticheskogo
Fur'a-razlosheniia amplitudy zondiruiushchego lazernogo izlucheniia)
V.A. Suiushev
Fizika Goreniia i Vzryva, vol. 11, Jan.-Feb. 1975, p. 67-72, 5 refs. In Russian

A74-26916

A Two-Component Laser Doppler Velocimeter for Periodic Flow Fields
J.P. Sullivan and S. Ezekiel
MIT, Cambridge, Mass.
Journal of Physics, Part E - Scientific Instruments, vol. 7, Apr. 1974, p. 272-274, 5 refs.

Intrablade Velocity Measurements in a Transonic Fan Utilizing a Laser Doppler Velocimeter
D.A. Walker, M.C. Williams, R.D. House
Minnesota Symposium on Laser Anemometry, University of Minnesota, October 22-24, 1975

N75-30475

Unsteady Flow Measurements in Turbomachinery

H. Weyer and R. Schodl

In its Modern Methods of Testing Rotating Components of Turbomachines (Instrumentation)

Apr. 1975, p 141-182, refs.

AGARD-AG-207

Shock Wave and Flow Velocity Measurements in a High Speed Fan Rotor Using the Laser Velocimeter

D.C. Wisler

Presented at the American Society of Mechanical Engineers Gas Turbine Conference and Products Show, New Orleans, La., March 20-25, 1976

ASME Publication no. 76-GT-49

INSPEC 73A59602, 73B35753

Gas Velocity Measurements within a Compressor Rotor Passage Using the Laser Doppler Velocimeter

D.C. Wisler, P.W. Mossey

General Electric Co., Cincinnati, Ohio, USA

Trans. ASME Ser. A (USA), Journal Paper, vol. 95, no. 2, April 1973, 91-96

Bibliography on Laser Optical Measurement Methods
for Aero Engine Research and Development

2. Combustion Flow Measurement (incl. Pollution)

N77-11221

Applications of Non-Intrusive Instrumentation in Fluid Flow Research
Advisory Group for Aerospace Research and Development, Paris (France)
May 1976, 309 p., refs. In English; partly in French
Presented at the Fluid Dynamics Panel Symp., Saint-Louis, France, 3-5 May 1976
AGARD-CP-193

A76-45326

The Accuracy of Flow Measurements by Laser Doppler Methods; Proceedings of the
LDA-Symposium, Copenhagen, Denmark, August 25-28, 1975
Edited by P. Buchhave, J.M. Delhay, F. Durst, W.K. George, K. Refslund and J.H. Whitelaw
Skovlunde, Denmark, Proceedings LDA-Symposium Copenhagen, 1976, 735 p.

N75-30374

Measurement in Turbulent Flows with Chemical Reaction
N.A. Chigier
In: AGARD, Anal. and Numerical Methods for Invest. of Flow Fields with Chem. Reactions.
Especially Related to Combust. May 1975, 18 p, refs.
AGARD-CP-164

A75-40802

Laser Anemometer Measurements in Flames with Swirl
N.A. Chigier and K. Dvorak
In: International Symposium on Combustion, 15th, Tokyo, Japan, August 25-31, 1974,
Proceedings
Pittsburgh, Pa., Combustion Institute, 1975, p. 573-582; Comments, p. 582-585, 23 refs.
Research supported by the Science Research Council of England

A76-18747

Combustion Diagnostics by Laser Velocimetry
N.A. Chigier
American Institute of Aeronautics and Astronautics
Aerospace Sciences Meeting, 14th, Washington, D.C., Jan. 26-28, 1976, Paper 76-32, 10 p.,
24 refs.

N77-11234

Laser Raman Diagnostics of Aerodynamic Flows and Flames
Sylvie Druet, Robert Bailly, Michel Pealat, and Jean-Pierre Taran
In: AGARD, Appl. of Non-Intrusive Instr. in Fluid Flow Res., May 1976, 12 p., refs.
In French; English summary

A76-43139

Raman Techniques for Studying Flows and Flames (Techniques Raman d'etude des écoulements
et des flammes)
S. Druet, R. Bailly, M. Pealat, and J.P. Taran
NATO, AGARD, Conférence Générale sur les Applications de l'Instrumentation de Mesures à
Distance dans la Recherche sur les Ecoulements Fluides, Saint-Louis, Haut-Rhin, France,
May 3-5, 1976
ONERA, TP no. 1976-40, 1976, 13 p., 22 refs. In French

A74-28283

Instrumentation for Airbreathing Propulsion; Proceedings of the Symposium, U.S. Naval
Postgraduate School, Monterey, Calif., September 19-21, 1972
Symposium sponsored by the U.S. Air Force, U.S. Navy, U.S. Army, and NASA
Edited by A. Fuhs and M. Kingery
Cambridge, Mass., MIT Press (Progress in Astronautics and Aeronautics, vol. 34), 1974,
547 p.

A76-35880

Absorption Coefficients for Fourteen Gases at CO₂ Laser Frequencies
B.D. Green, J.I. Steinfeld
MIT, Cambridge, Mass.
Applied Optics, vol. 15, July 1976, p. 1688-1690, 3 p., 8 refs.

A76-18750

Methods for Turbulence Measurement in Flames

R. Günther

Karlsruhe, Universität, Karlsruhe, West Germany

American Institute of Aeronautics and Astronautics, Aerospace Sciences Meeting, 14th, Washington, D.C., Jan. 26-28, 1976, Paper 76-36, 9 p., 19 refs.

A76-26071

Optical Diagnostics of Combustion Processes

M. Lapp

General Electric Co., Schenectady, N.Y.

In: Optical methods in energy conversion; Proceedings of the Seminar, Rochester, N.Y., June 23-25, 1975

Palos Verdes Estates, Calif., Society of Photo-Optical Instrumentation Engineers, 1975, p. 42-50, 22 refs.

A76-18743

Modern Diagnostics of Combustion

S. Lederman

New York, Polytechnic Institute, Farmingdale, N.Y.

American Institute of Aeronautics and Astronautics, Aerospace Sciences Meeting, 14th, Washington, D.C., Jan. 26-28, 1976, Paper 76-26, 9 p., 6 refs.

A75-28649

Raman and Fluorescence Measurements of Combustion Emissions

D.A. Leonard

Avco Everett Research Laboratory, Inc., Everett, Mass.

American Meteorological Society and Optical Society of America, Conference on Laser Atmospheric Studies, 6th, Sendai, Japan, Sept. 3-6, 1974, Paper, 44 p., 10 refs.

A75-32321

Raman and Fluorescence Lidar Measurements of Aircraft Engine Emissions

D.A. Leonard

Avco Everett Research Laboratory, Inc., Everett, Mass.

Optical and Quantum Electronics, vol. 7, May 1975, p. 197-209, 10 refs.

A76-40304

A Review of Drop Size Measurement in Fuel Sprays

C.G. McCreath, J.M. Beer

Sheffield, University, Sheffield, England

Applied Energy, vol. 2, Jan. 1976, p. 3-15, 13 p., 25 refs.

INSPEC 76A38277, 76B22338

A Technique for Simultaneous Velocity and Concentration Measurements

A. Melling

Dept. of Mech. Eng., Imperial Coll., London, England Techn. Univ. Denmark

LDA-Symposium 1975 Accuracy of Flow Measurements by Laser Doppler Methods,

Conference Paper, Aug. 1975, 1975, 198, p. 69-70. Copenhagen, Denmark. Lyngby, Denmark

A76-25946

Measurements of Air Pollutants over a Los Angeles Freeway with a Bistatic Laser System

R.T. Menzies, M.S. Shumate

California Institute of Technology, Jet Propulsion Laboratory, Pasadena, Calif.

In: International Conference on Environmental Sensing and Assessment, Las Vegas, Nev., September 14-19, 1975, Proceedings, vol. 2

New York, Institute of Electrical and Electronics Engineers, Inc., 1976, p. 1 22-5 to 3 22-5, 3 p., 6 refs.

A75-37374

Raman Spectral Measurements of Gaseous Combustion Products from Flames

W. Mueller, S.M. Klainer, and P.J. Miller

Block Engineering, Inc., Cambridge, Mass.

In: Impact of lasers in spectroscopy; Proceedings of the Seminar, San Diego, Calif., August 19, 20, 1974

Palos Verdes Estates, Calif., Society of Photo Optical Instrumentation Engineers, 1975, p. 120-126

A76-18748

Laser Velocimeter Measurements of a Confined Turbulent Diffusion Flame Burner

F.K. Owen

United Technologies Research Center, East Hartford, Conn.

American Institute of Aeronautics and Astronautics, Aerospace Sciences Meeting, 14th, Washington, D.C., Jan. 26-28, 1976, Paper 76-33, 11 p.

A76-20923

Simultaneous Laser Velocimeter and Laser Induced Photoluminescence Measurements of Instantaneous Velocity and Concentration in Complex Mixing Flows

F.K. Owen

United Technologies Research Center, East Hartford, Conn.

American Institute of Aeronautics and Astronautics, Aerospace Sciences Meeting, 14th, Washington, D.C., Jan. 26-28, 1976, Paper 76-35, 5 p., 5 refs.

Proceedings of the ISL/AGARD Workshop on Laser Anemometry May 5-7, 1976

H.J. Pfeifer, J. Haertig, Auriol, Schall

A75-40540

Optimal Optoacoustic Detector Design

L.-G. Rosengren

Volvo, AB, Goteborg, Sweden

Applied Optics, vol. 14, Aug. 1975, p. 1960-1976, 40 refs.

Special Applications and New Technical Aspects of Laser Anemometry, Review Paper

Peter W. Runstadler, Jr.

Creare Incorporated, Hanover, New Hampshire, USA 03755

A75-37360

Impact of Lasers in Spectroscopy; Proceedings of the Seminar, San Diego, Calif., August 19, 20, 1974

Seminar sponsored by the Society of Photo-Optical Instrumentation Engineers

Palos Verdes Estates, Calif., Society of Photo-Optical Instrumentation Engineers (SPIE Proceedings, vol. 49), 1975, 163 p.

A76-38616

Temperature Measurement in Conical Flames by Laser Interferometry

R. South, B.M. Hayward

Combustion Science and Technology, vol. 12, no. 4-6, 1976, p. 183-195, 13 p., 21 refs.

A75-28691

Determination of the Turbulence Characteristics of Gas Flows and Flames by the Method of Optical Expansion in Fourier Series of the Amplitude of the Probing Laser Emission

(Poluchenie turbulentnykh kharakteristik gazovykh potokov i plamen metodom opticheskogo Fur'a-razlozheniia amplitudy zondiruiushchego lazernogo izlucheniia)

V.A. Suiushev

Fizika Goreniia i Vzryva, vol. 11, Jan.-Feb. 1975, p. 67-72, 5 refs. In Russian

A75-35784

Measurements of SO₂ Absorption Coefficients Using a Tunable Dye Laser

R.T. Thompson, Jr., J.M. Hoell, Jr., and W.R. Wade

Journal of Applied Physics, vol. 46, July 1975, p. 3040-3043, 11 refs

A76-22802

Laser Absorption Methods for Simultaneous Determination of Temperature and Species Concentrations through a Cross Section of a Radiating Flow

J.Y. Wang

General Dynamics Corp., Convair Div., San Diego, Calif.

Applied Optics, vol. 15, Mar. 1976, p. 768-773, 8 refs.

Bibliography on Laser Optical Measurement Methods
for Aero Engine Research and Development

3. Noise and Vibration Measurement

A76-37218

Experience in Using Holographic Interferometry for Investigating the Vibration of Rotor Elements in Gas Turbine Engines (Opyt primeneniia golograficheskoi interferometrii dlia issledovaniia vibratsii rotornykh elementov GTD)

D.M. Bavel'skii and V.V. Trofimovskii

Nevskii Mashinostroitel'nyi Zavod, Leningrad, USSR

Vsesoiuznaia Nauchno-Tekhnicheskaya Konferentsiia po Konstruktsionnoi Prochnosti

Dvigateli, 3rd, Kuibyshev, USSR, Oct. 15-17, 1974

Problemy Prochnosti, May 1976, p. 85-87. In Russian

A75-36315

Remote Vibration Measurement of Rough Surfaces by Laser Interferometry

R.A. Bruce and G.L. Fitzpatrick

U.S. Bureau of Mines, Denver Mining Research Center, Denver, Colo.

Applied Optics, vol. 14, July 1975, p. 1621-1626, 12 refs.

A76-11074

Laser Doppler Vibration Measurements Using Variable Frequency Shift

P. Buchhave

Disa Elektronik A/S, Herlev, Denmark

DISA Information, Sept. 1975, p. 15-20, 10 refs.

A75-43264

Lasers Applied to Noise and Vibration

J.N. Butters and J.A. Leendertz

Loughborough University of Technology, Loughborough, Leics., England

Acustica, vol. 33, Aug. 1975, p. 211-216, 5 refs

A75-35117

Holographic Interferometry Applied to Rotating Disks

Y. Chen

Rutgers University, New Brunswick, N.J.

ASME, Transactions, Series E - Journal of Applied Mechanics, vol. 42, June 1975, p. 499-501

INSPEC 76A24202, 76B13454

Use of the Optical Doppler Effect to Measure Vibration in Industrial Conditions

A.I. Ilyankov

Avtometriya (USSR), Journal Paper, No. 5, Sept.-Oct. 1975, p. 85-87. In Russian

INSPEC 73A66144, 73B35749

Laser Doppler Instrument for Measurement of Vibration of Moving Turbine Blades

W.K. Kulczyk, Q.V. Davis

Univ. Surrey, Guildford, England

Proc. Inst. Electr. Eng. (GB), Journal Paper, vol. 120, no. 9, Sept. 1973, p. 1017-1023

Proceedings of the ISL/AGARD Workshop on Laser Anemometry May 5-7, 1976

Dr. H.J. Pfeifer, J. Haertig, Auriol, Dr. Schall

Special Applications and New Technical Aspects of Laser Anemometry, Review Paper

Peter W. Runstadler, Jr.

Creare Incorporated, Hanover, New Hampshire, USA 03755

Bibliography on Laser Optical Measurement Methods
for Aero Engine Research and Development

4. Physical Principles

A75-15337

Laser Doppler Anemometry

J.B. Abbiss, T.W. Chubb, and E.R. Pike

Optics and Laser Technology, vol. 6, Dec. 1974, p. 249-261, 27 refs.

INSPEC 76A38290, 76B22350

Frequency Measurement Errors Due to Noise in LDV Signals

R. Adrian, J.A.C. Humphrey, J.H. Whitelaw

Univ. of Illinois, Urbana, IL, USA Tech. Univ. Denmark

LDA-Symposium 1975 Accuracy of Flow Measurements by Laser Doppler Methods, Conference Paper, Aug. 1975, 1975, 198, 110-11. Copenhagen, Denmark. Lyngby, Denmark

A76-45326

The Accuracy of Flow Measurements by Laser Doppler Methods; Proceedings of the LDA-Symposium, Copenhagen, Denmark, August 25-28, 1975

Edited by P. Buchhave, J.M. Delhay, F. Durst, W.K. George, K. Refslund, and J.H. Whitelaw

Skovlunde, Denmark, Proceedings LDA-Symposium Copenhagen, 1976, 735 p.

A75-40534

SNR in Optical Velocimeters - Effect of Particle Number Density

J.H.C. Chan and E.A. Ballik

McMaster University, Hamilton, Ontario, Canada

Applied Optics, vol. 14, Aug. 1975, p. 1839-1846, 13 refs.

Research supported by the National Research Council and Defence Research Board of Canada

INSPEC 76A67106, 76B34955

Doppler Velocimetry by Spectral Modulation

P. Cielo, C. Delisle

Dept. de Phys., Univ. Laval, Quebec, Canada

Can. J. Phys. (Canada), Journal Paper, vol. 54, no. 12, 15 June 1976, 1199-207. In French

N75-29000

Bibliography of Laser-Doppler-Anemometry Literature

F. Durst and M. Zare, Nov. 1974, 59 p., refs.

Karlsruhe Univ. (West Germany). Sonderforschungsbereich 80 Ausbreitungs- und Transportvorgänge in Strömungen

INSPEC 75A31845, 75B15836

Raman Lasers (Review)

A.Z. Grasyuk

Kvantovaya Elektron., Moskva (USSR), Journal Paper, vol. 1, no. 3, vol. 4, no. 3, March 1974, Sept. 1974, 485-509, 269-82

INSPEC 75A31425

Simultaneous Raman and Laser Velocimeter Measurements

M.E. Hillard, Jr., W.W. Hunter, Jr., J.F. Meyers, W.V. Feller

NASA, Hampton, Va., USA

AIAA J. (USA), Journal Paper, vol. 12, no. 10, Oct. 1974, 1445-7

A76-18048

A Two-Component Optical Doppler Velocimeter with Ultrasonic Modulator

A.M. Kolychev, B.S. Rinkevichius, V.L. Chudov

Radiotekhnika i Elektronika, vol. 20, Oct. 1975, p. 2215-2219. In Russian. Refs. 9

INSPEC 74A74189

Laser-Doppler Velocimeter Measurements in Nonuniform Flow: Error Estimates

D.K. Kreid

Tennessee Technol. Univ., Cookeville, USA

Appl. Opt. (USA), Journal Paper, vol. 13, no. 8, Aug. 1974, 1872-81

INSPEC 76A43121
 Light Scattering Particles for Laser Velocimeter Measurements
 D.K. Kreid, D.S. Rowe
 Tennessee Technol. Univ., Cookeville, TN, USA
 Appl. Opt. (USA), Journal Paper, vol. 15, no. 2, Feb. 1976, 321-2

A76-16945
 Three-Component Optical Doppler Velocimeter
 V.M. Kulybin
 Moskovskii Energeticheskii Institut, Moscow, USSR
 Fizika, vol. 18, no. 10, 1975, p. 82-86, Refs. 5. In Russian

INSPEC 76A56351, 76B30230
 Processing of Laser Doppler Anemometry Signals
 L. Lading
 Danish Atomic Energy Comm., Res. Establ. Riso, Roskilde, Denmark
 DISA Inf. (Denmark), Journal Paper, no. 19, March 1976, 12-18

INSPEC 76A16166
 Data Acquisition System for Laser Doppler Velocimeters
 J.A. Maynard, T.K. Gaylord, J.H. Rust
 School of Electrical Eng., Georgia Inst. of Technol., Atlanta, GA, USA
 Rev. Sci. Instrum. (USA), Journal Paper, vol. 46, no. 11, Nov. 1975, 1469-73

INSPEC 76A51142
 Frequency Error of Doppler Beat Signals Due to Extended Scattering Particles
 H. Mishina, Y. Kawase, T. Asakura
 Res. Inst. of Appl. Electricity, Hokkaido Univ., Sapporo, Hokkaido, Japan
 Jap. J. Appl. Phys. (Japan), Journal Paper, vol. 15, no. 4, April 1976, 633-40

INSPEC 76A43134, 76B22361, 76C13118
 The Application of Laser Velocimeter Signal Processing Electronics to Complex Aerodynamic Flows
 K.L. Orloff
 NASA, Ames Res. Center, Moffett Field, CA, USA Tech. Univ. Denmark
 LDA-Symposium 1975 Accuracy of Flow Measurements by Laser Doppler Methods,
 Conference Paper, Aug. 1975, 1975, 198, 153-5. Copenhagen, Denmark. Lyngby, Denmark

INSPEC 73A32281, 73B20422
 Use of Laser for Local Measurement of Velocity Components, Species Densities, and Temperatures
 S.S. Penner, T. Jerskey, M. van Dyke, W.G. Vincenti, J.V. Wehausen
 Univ. California, San Diego; La Jolla, USA Annual Reviews
 Annual review of fluid mechanics, vol. 5, Book Chapter, 1973, 9-30. Palo Alto, Calif. USA

Proceedings of the ISL/AGARD Workshop on Laser Anemometry May 5-7, 1976
 H.J. Pfeifer, J. Haertig, Auriol, Schall

A76-10438
 Photon Correlation Methods - Laser Doppler Velocimeter Signal Analysis
 E.R. Pike
 Royal Radar Establishment, Malvern, Worcs., England
 In: International Workshop on Laser Velocimetry, 2nd, West Lafayette, Ind., March 27-29, 1974, Proceedings, vol. 1, West Lafayette, Ind., Purdue University, 1974, p. 271-285, p. 286-289, Refs. 6

INSPEC 76A43133, 76B22360
 Experimental Comparison of Hot Wire and Different Information Retrieval Methods in Laser Anemometry for Measurement of Mean Flow and Turbulence
 A.E. Smart
 Rolls Royce 1971 Ltd., Derby Engine Div., Derby, England Tech. Univ. Denmark
 LDA-Symposium 1975 Accuracy of Flow Measurements by Laser Doppler Methods, Conference Paper, Aug. 1975, 1975, 198, 148-9. Copenhagen, Denmark. Lyngby, Denmark

INSPEC 73A56685, 73B32576
 Applications of Laser Velocimeters for Flow Field Investigations
 F.H. Smith, A.E. Lennert, R.R. Roberts
 ARO Inc., Arnold Air Force Station, Tenn., USA
 Proceedings of the 18th International ISA Aerospace Instrumentation Symposium, vol. 18, Conference Paper, 15-17 May 1972, 1972, 345 p, 9-16. Miami, Fla., USA. Pittsburgh, Pa. USA

INSPEC 76A16161, 76B10700
Counting Techniques Applied to Laser Doppler Anemometry
F.V. Steenstrup
DISA Inf. (Denmark), Journal Paper, no. 18, Sept. 1975, 21-5

INSPEC 76A07765
A Laser Velocimeter Utilizing Laser-Induced Fluorescence
W.H. Stevenson, R. dos Santos, S.C. Mettler
Appl. Optics Lab., Purdue Univ., West Lafayette, IN, USA
Appl. Phys. Lett. (USA), Journal Paper, vol. 27, no. 7, 1 Oct. 1975, 395-6

INSPEC 74A30502, 74B19319
A Two-Component Laser Doppler Velocimeter for Periodic Flow Fields
J.P. Sullivan, S. Ezekiel
MIT, Cambridge, Mass., USA
J. Phys. E (GB), Journal Paper, vol. 7, no. 4, April 1974, 272-4

INSPEC 73A57026, 73B32635
A Particle Timing Laser Velocity meter
L.H. Tanner
Brighton Polytech., England
Opt. + Laser Technol. (GB), Journal Paper, vol. 5, no. 3, June 1973, 108-10

INSPEC 74A08603
Laser Doppler Velocimeter
Yu.G. Vasilenko, Yu.N. Dubnitshev, V.S. Sobolev, A.A. Stolpovski, V.P. Koronkevich,
E.N. Utkin
Inst. Automation + Electrometry, Acad. Sci., Novosibirsk, USSR
1973 IEEE/OSA Conference on Laser Engineering and Applications Digest of Technical Papers,
Conference Paper, 30 May - 1 June 1973, 1973, 101 p., 40-1. Washington, D.C., USA.
New York, USA

INSPEC 74A30670, 74B19408
Laser Doppler Velocimetry: Experimental Study
C.P. Wang, D. Snyder
Univ. California, San Diego, La Jolla, USA
Appl. Opt. (USA), Journal Paper, vol. 13, no. 1, Jan. 1974, 98-103

REPORT DOCUMENTATION PAGE												
1. Recipient's Reference	2. Originator's Reference	3. Further Reference	4. Security Classification of Document									
	AGARD-LS-90	ISBN 92-835-1248-0	UNCLASSIFIED									
5. Originator	Advisory Group for Aerospace Research and Development North Atlantic Treaty Organization 7 rue Ancelle, 92200 Neuilly sur Seine, France											
6. Title	LASER OPTICAL MEASUREMENT METHODS FOR AERO ENGINE RESEARCH AND DEVELOPMENT											
7. Presented	on 25-26 August 1977 Trenton, New Jersey, USA, 30-31 August 1977 London, UK, and 5-6 September 1977 Urbino Italy.											
8. Author(s)	Various		9. Date July 1977									
10. Author's Address	Various		11. Pages 166									
12. Distribution Statement	This document is distributed in accordance with AGARD policies and regulations, which are outlined on the Outside Back Covers of all AGARD publications.											
13. Keywords/Descriptors	<table border="0"> <tr> <td>Aircraft engines</td> <td>Flow measurement</td> <td>Holography</td> </tr> <tr> <td>Optical measuring instruments</td> <td>Lasers</td> <td>Fluid flow</td> </tr> <tr> <td>Flow distribution</td> <td>Raman spectra</td> <td></td> </tr> </table>			Aircraft engines	Flow measurement	Holography	Optical measuring instruments	Lasers	Fluid flow	Flow distribution	Raman spectra	
Aircraft engines	Flow measurement	Holography										
Optical measuring instruments	Lasers	Fluid flow										
Flow distribution	Raman spectra											
14. Abstract	<p>→ In recent years many optical measuring methods, most using lasers, for determining flow velocity (with turbulence and fluctuations), temperature and species concentration have been studied. The main advantage is that the flow is not disturbed. They are of great value for research and development on engines and components and for the understanding of fundamental flow processes.</p> <p>The proposed Lecture Series will inform propulsion specialists of the techniques that are currently available, how to use them and their limitations. It will review experience to date in practical applications. Laser-velocimetry will be emphasized since it is the only technique which has achieved practical importance up until now. Raman scattering and holography interferometry will also be addressed. Commonly-used techniques and qualitative type methods such as infrared for surface temperature and Schlieren techniques will not be addressed.</p> <p>A bibliography of 98 items is included in the publication. ↗</p>											

<p>AGARD Lecture Series No. 90 Advisory Group for Aerospace Research and Development, NATO LASER OPTICAL MEASUREMENT METHODS FOR AERO ENGINE RESEARCH AND DEVELOPMENT Published July 1977 166 pages</p> <p>In recent years many optical measuring methods, most using lasers, for determining flow velocity (with turbulence and fluctuations), temperature and species concentration have been studied. The main advantage is that the flow is not disturbed. They are of great value for research and development on engines and components and for the understanding of fundamental flow processes.</p> <p>P.T.O.</p>	<p>AGARD-LS-90</p> <p>Aircraft engines Optical measuring instruments Flow distribution Flow measurement Lasers Raman spectra Holography Fluid flow</p>	<p>AGARD Lecture Series No. 90 Advisory Group for Aerospace Research and Development, NATO LASER OPTICAL MEASUREMENT METHODS FOR AERO ENGINE RESEARCH AND DEVELOPMENT Published July 1977 166 pages</p> <p>In recent years many optical measuring methods, most using lasers, for determining flow velocity (with turbulence and fluctuations), temperature and species concentration have been studied. The main advantage is that the flow is not disturbed. They are of great value for research and development on engines and components and for the understanding of fundamental flow processes.</p> <p>P.T.O.</p>	<p>AGARD-LS-90</p> <p>Aircraft engines Optical measuring instruments Flow distribution Flow measurement Lasers Raman spectra Holography Fluid flow</p>
<p>AGARD Lecture Series No. 90 Advisory Group for Aerospace Research and Development, NATO LASER OPTICAL MEASUREMENT METHODS FOR AERO ENGINE RESEARCH AND DEVELOPMENT Published July 1977 166 pages</p> <p>In recent years many optical measuring methods, most using lasers, for determining flow velocity (with turbulence and fluctuations), temperature and species concentration have been studied. The main advantage is that the flow is not disturbed. They are of great value for research and development on engines and components and for the understanding of fundamental flow processes.</p> <p>P.T.O.</p>	<p>AGARD-LS-90</p> <p>Aircraft engines Optical measuring instruments Flow distribution Flow measurement Lasers Raman spectra Holography Fluid flow</p>	<p>AGARD Lecture Series No. 90 Advisory Group for Aerospace Research and Development, NATO LASER OPTICAL MEASUREMENT METHODS FOR AERO ENGINE RESEARCH AND DEVELOPMENT Published July 1977 166 pages</p> <p>In recent years many optical measuring methods, most using lasers, for determining flow velocity (with turbulence and fluctuations), temperature and species concentration have been studied. The main advantage is that the flow is not disturbed. They are of great value for research and development on engines and components and for the understanding of fundamental flow processes.</p> <p>P.T.O.</p>	<p>AGARD-LS-90</p> <p>Aircraft engines Optical measuring instruments Flow distribution Flow measurement Lasers Raman spectra Holography Fluid flow</p>

<p>The proposed Lecture Series will inform propulsion specialists of the techniques that are currently available, how to use them and their limitations. It will review experience to date in practical applications. Laser-velocimetry will be emphasized since it is the only technique which has achieved practical importance up until now. Raman scattering and holography interferometry will also be addressed. Commonly-used techniques and qualitative type methods such as infrared for surface temperature and Schlieren techniques will not be addressed.</p>	<p>The proposed Lecture Series will inform propulsion specialists of the techniques that are currently available, how to use them and their limitations. It will review experience to date in practical applications. Laser-velocimetry will be emphasized since it is the only technique which has achieved practical importance up until now. Raman scattering and holography interferometry will also be addressed. Commonly-used techniques and qualitative type methods such as infrared for surface temperature and Schlieren techniques will not be addressed.</p>
<p>A bibliography of 98 items is included in the publication.</p> <p>The material in this publication was assembled to support a Lecture Series under the sponsorship of the Propulsion and Energetics Panel and the Consultant and Exchange Programme of AGARD, presented on 25-26 August 1977 Trenton, New Jersey, USA, 30-31 August 1977 London, UK, and 5-6 September 1977 Urbino, Italy.</p> <p>ISBN 92-835-1248-0</p>	<p>A bibliography of 98 items is included in the publication.</p> <p>The material in this publication was assembled to support a Lecture Series under the sponsorship of the Propulsion and Energetics Panel and the Consultant and Exchange Programme of AGARD, presented on 25-26 August 1977 Trenton, New Jersey, USA, 30-31 August 1977 London, UK, and 5-6 September 1977 Urbino, Italy.</p> <p>ISBN 92-835-1248-0</p>
<p>The proposed Lecture Series will inform propulsion specialists of the techniques that are currently available, how to use them and their limitations. It will review experience to date in practical applications. Laser-velocimetry will be emphasized since it is the only technique which has achieved practical importance up until now. Raman scattering and holography interferometry will also be addressed. Commonly-used techniques and qualitative type methods such as infrared for surface temperature and Schlieren techniques will not be addressed.</p> <p>A bibliography of 98 items is included in the publication.</p> <p>The material in this publication was assembled to support a Lecture Series under the sponsorship of the Propulsion and Energetics Panel and the Consultant and Exchange Programme of AGARD, presented on 25-26 August 1977 Trenton, New Jersey, USA, 30-31 August 1977 London, UK, and 5-6 September 1977 Urbino, Italy.</p> <p>ISBN 92-835-1248-0</p>	<p>A bibliography of 98 items is included in the publication.</p> <p>The material in this publication was assembled to support a Lecture Series under the sponsorship of the Propulsion and Energetics Panel and the Consultant and Exchange Programme of AGARD, presented on 25-26 August 1977 Trenton, New Jersey, USA, 30-31 August 1977 London, UK, and 5-6 September 1977 Urbino, Italy.</p> <p>ISBN 92-835-1248-0</p>

AGARD

NATO  OTAN

7 RUE ANCELLE · 92200 NEUILLY-SUR-SEINE
FRANCE

Telephone 745.08.10 · Telex 610176

**DISTRIBUTION OF UNCLASSIFIED
AGARD PUBLICATIONS**

AGARD does NOT hold stocks of AGARD publications at the above address for general distribution. Initial distribution of AGARD publications is made to AGARD Member Nations through the following National Distribution Centres. Further copies are sometimes available from these Centres, but if not may be purchased in Microfiche or Photocopy form from the Purchase Agencies listed below.

NATIONAL DISTRIBUTION CENTRES

BELGIUM

Coordonnateur AGARD — VSL
Etat-Major de la Force Aérienne
Caserne Prince Baudouin
Place Dailly, 1030 Bruxelles

CANADA

Defence Scientific Information Service
Department of National Defence
Ottawa, Ontario K1A 0Z2

DENMARK

Danish Defence Research Board
Østerbrogades Kaserne
Copenhagen Ø

FRANCE

O.N.E.R.A. (Direction)
29 Avenue de la Division Leclerc
92 Châtillon sous Bagneux

GERMANY

Zentralstelle für Luft- und Raumfahrt-
dokumentation und -information
Postfach 860880
D-8 München 86

GREECE

Hellenic Armed Forces Command
D Branch, Athens

ICELAND

Director of Aviation
c/o Flugrad
Reykjavik

ITALY

Aeronautica Militare
Ufficio del Delegato Nazionale all'AGARD
3, Piazzale Adenauer
Roma/EUR

LUXEMBOURG

See Belgium

NETHERLANDS

Netherlands Delegation to AGARD
National Aerospace Laboratory, NLR
P.O. Box 126
Delft

NORWAY

Norwegian Defence Research Establishment
Main Library
P.O. Box 25
N-2007 Kjeller

PORTUGAL

Direccao do Servico de Material
da Forca Aerea
Rua de Escola Politecnica 42
Lisboa
Attn: AGARD National Delegate

TURKEY

Department of Research and Development (ARGE)
Ministry of National Defence, Ankara

UNITED KINGDOM

Defence Research Information Centre
Station Square House
St. Mary Cray
Orpington, Kent BR5 3RE

UNITED STATES

National Aeronautics and Space Administration (NASA),
Langley Field, Virginia 23365
Attn: Report Distribution and Storage Unit

THE UNITED STATES NATIONAL DISTRIBUTION CENTRE (NASA) DOES NOT HOLD
STOCKS OF AGARD PUBLICATIONS, AND APPLICATIONS FOR COPIES SHOULD BE MADE
DIRECT TO THE NATIONAL TECHNICAL INFORMATION SERVICE (NTIS) AT THE ADDRESS BELOW.

PURCHASE AGENCIES

Microfiche or Photocopy

National Technical
Information Service (NTIS)
5285 Port Royal Road
Springfield
Virginia 22151, USA

Microfiche

Space Documentation Service
European Space Agency
10, rue Mario Nikis
75015 Paris, France

Microfiche

Technology Reports
Centre (DTI)
Station Square House
St. Mary Cray
Orpington, Kent BR5 3RF
England

Requests for microfiche or photocopies of AGARD documents should include the AGARD serial number, title, author or editor, and publication date. Requests to NTIS should include the NASA accession report number. Full bibliographical references and abstracts of AGARD publications are given in the following journals:

Scientific and Technical Aerospace Reports (STAR),
published by NASA Scientific and Technical
Information Facility
Post Office Box 8757
Baltimore/Washington International Airport
Maryland 21240, USA

Government Reports Announcements (GRA),
published by the National Technical
Information Services, Springfield
Virginia 22151, USA



Printed by Technical Editing and Reproduction Ltd
Harford House, 7-9 Charlotte St, London W1P 1HD

ISBN 92-835-1248-0